eman ta zabal zazu

Universidad del País Vasco
Euskal Herriko Unibertsitatea

# On-Surface Synthesis and Electronic Structure Characterization of Graphene Nanoribbons

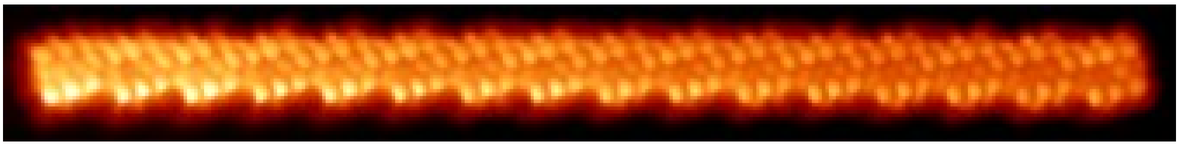

**DOCTORAL THESIS IN**
**Physics of Nanostructures and Advanced Materials**
**submitted by**

**Néstor Merino Díez**

**Supervised by**

**Dimas García de Oteyza**
**and**
**José Ignacio Pascual Chico**

***San Sebastián - Donostia, September 2019***

(c)2019 NESTOR MERINO DIEZ

This thesis has been carried out at *Donostia International Physics Center (DIPC)*,
*Centro de Física de Materiales - Materials Physics Center (CFM-MPC)*,
and *CIC nanoGUNE: nanoscience cooperative research center.*

*Perhaps hapiness is always to be found in the journey uphill,*
*and not in the fleeting sense of satisfaction awaiting at the next peak.*

# Abstract

This thesis presents a comprenhensive study on the on-surface synthesis and characterization of the electronic structure of different types of graphene nanoribbons (GNRs) formed on coinage metallic surfaces, being gold the most present substrate. Graphene nanoribbons (GNRs) are a new emergent material which is gaining considerable attention within the scientific community due to its wide-range potential applications derived from its exotic physical and chemical properties. Since GNRs derive from graphene, they preserve many of its interesting properties, such as the highest electron conductivity. In adittion, the reduced dimensionality of GNRs provide them with a tunable non-zero electrical band gap, no present in graphene, and required for its implementation into electronic devices. Moreover, and again in contrast with graphene, the presence of edges in GNRs brings the emergence of magnetic edge states with promising applications in spintronics.

We employ on-surface chemistry startegies based on the use of aromatic molecular precursors for synthesizing the different GNRs studied here. By thermal annealing, we induce a controlled two-step reaction pathway to form these nanostructures onto different coinage metallic substrates, since their catalytic activity is needed for the product formation. The two chemical reaction accounted involves firstly, the merging of the molecular precursors into commonly linear polymric chains thorugh the well-known and controlled Ullmann coupling. In a second stage, higher temperatures induce the ciclodehydrogenation of the former polymers, giving rise to the formation of planar graphene nanoribbons.

Most of the experimental results were acquired by means of Low-Temperature Scanning Tunneling Microscopy and Spectroscopy (LT-STM/STS) at temperatures of $\sim$ 5K with the use of liquid nitrogen and helium cryostates. Measurements and sample preparations were performed in ultra high vacuum conditions. The main STM equipments used in this work are located at CIC nanoGUNE cooperative research center and the Materials Physics Center-Centro de Física de Materiales (MPC-CFM), being both located in San Sebastián (Spain). Complementary surface-sensitive techniques, such as X-ray and angle-resolved photoemission spectroscopy (XPS and ARPES), were employed for supplementing the STM/STS results. These complementary measurements were done in collaboration with the 'Nano Physics Laboratory' group, headed by prof. Enrique Ortega in the Materials Physics Center-Centro de Física de Materiales (MPC-CFM); as well as with the 'APE' beamline staff at Elettra syncrotrone in Triestre (Italy). In the acquisition of the experimental results have contributed the pre-doctoral researchers Niklas Friedrich, Mohammed Sabri G. Mohammed, Alejandro Berdonces Layunta, and Ana Barragán; and the doctors Jincheng Li, Jorge Lobo Checa, Luciano Colazzo, Martina Corso, Eduard Carbonell Sanromà, James Lawrence, Guillaume Vasseur, Celia Rogero and Francesco Sedona. The different calculations and simulations included in this work were developed by the doctors Aran García-Lekue, Daniel Sanchez Portal and Alejandro Pérez Paz. The molecular precursors employed in this work were synthesized by the group of prof. Diego Peña, in the 'CIQUS' Research Institute (in Santiago de Compostela, Spain).

This thesis is divided in three different parts. In the first one, we introduce the scientific background underlying the context and the motivation of this work. In addition, we explain the different experimental techniques employed including a specific description of the main

equipments used, together with a theoretical explanation of the electronic properties of GNRs. The second part of this thesis focuses on the experimental results obtained with armchair GNRs (aGNRs) and involves two different chapters. In the first one, we synthesize different aGNRs members of the *3p* family on Au(111) and demonstrate how their semiconducting band gap can be precisely modulated by the width of these nanostructures. Moreover, we observe a Fermi level pinned scenario since the valence band (VB) of each nanoribbon is located at very similar, near-Fermi energy values. In the second chapter of this part, we show how the random synthesis of aGNRs from poly-*para*-phenylene (PPP) nanowires on Au(111), can be limited into the formation of aGNRs of a single width (sizx dimers lines, in this case) by the use of the vicinal surface as Au(322) as substrate template, what result into a system of highly aligned nanoribbons allowing the characterization of their electronic structure by averaging surface sensitive techniques like ARPES. The third part of this thesis comprises the experimental results obtained in the study of chiral GNRs (cGNRs) and it is divided into four different chapters.

In the first chapters, by changing and adding the halogentad sites within the molecular we explore the reactivity of the molecular precursor originally employed to synthesize the pioneer 7-aGNR, by changing (or adding) the halogenated positions within its aromatic skeleton, what results in the effective formation of cGNRs instead of aGNRs on different coinage metallic substrates. Followed by a detailed study of the transfer of the innate chirality of these precusors along the whole synthetic process, resuting into the steroselective synthesis of pro-chiral GNRs. Finally we characterize in detail the electronic structure of cGNRs, observing a semiconducting character with no edge states in the narrow nanoribbons that developes into a metallic character with colse-to-Fermi edge states in the wider cGNRs.

# Resumen

Esta tesis expone un estudio detallado sobre la síntesis en superficie de nanotiras de grafeno (en inglés 'Graphene Nanoribbons', GNRs) y la posterior caracterización de su estructura electrónica, principalmente empleando como técnica analítica, microscopía y espectroscopía de barrido de efecto túnel de baja temperatura (en inglés 'Low temperature-Scanning Tunnneling Microscopy/Spectrosocopy', LT-STM/STS) en condiciones de ultra alto vacío (en inglés 'Ultra High Vacuum', UHV). Para la obtención de los resutados detallados en esta tesis, se han empleado dos equipos de microscopía independientes, ambos ubicados en San Sebastián (Guipúzcoa). En primer lugar, 'Milano', un microscopio ensamblado a partir de elementos de distintios equipos y ubicado en el centro de investigación cooperativo 'CIC nanoGUNE'. En segundo lugar, 'Apollo', un equipo comercial Sigma-Omicron y situado en el instituto de investigación 'Centro de Física de Materiales' (CFM). Paralelamente al uso de estos microscopios, distintas técnicas de análisis de superficies, en concreto, espectroscopía de fotoemisión de rayos x (en ingles 'X-ray Photoemission Spectroscopy', XPS) y de ángulo resuelto (en inglés 'Angle-Resolved Photoemission Spectroscopy'), han complementado el estudio de las distintas reacciones de química de superficie que dan pie a la formación de las nanotiras de grafeno, así como el posterior estudio de sus propiedades electrónicas.

El trabajo realizado durante esta tesis se enmarca dentro del campo cientiífico conocido como 'nanociencia', definiendose esta como la rama de la ciencia centrada en el estudio de los fenómenos físico-químicos que se suceden en sistemas cuyas propiedades están gobernadas por las dimensiones que las definen, comprendiendose estas entre 1 y 100 nanometros.[1] Por impedimentos tecnológicos, este campo científico ha permanecido inexplorado experimentalmente hasta que recientes progresos en el desarollo de instrumentos analíticos y métodos de producción han permitido el acceso al estudio de fenómenos que ocurren a escala nanométrica con la precisión suficiente como para poder comprender la naturaleza de dichos fenómenos. De hecho, el desarrollo del STM en 1981 de la mano de los científicos Binning y Rohrer en los laboratorios IBM en Zürich (Suiza),[2,3] hecho por el cual recibieron el premio Nobel en física en 1986, impulsó considerablemente el acceso experimental al 'mundo nanométrico' debido a la capacidad resolutiva espacial que dicho instrumento otorga, capacidad que alcanza una resolución expresable en ángstroms.

Un material que ilustra magnificamente esta nueva revolución en la ciencia es el grafeno. En su concepción teórica ideal, el grafeno se define como un material bidimensional compuesto única y exclusivamente por una capa de átomos de carbono con una hibridación de tipo sp$^2$ situados, por lo tanto, en el mismo plano geométrico.[4] Durante años, la visión de este material no sobrepasó su mera concepción teórica debido a que su creación y estabilidad se creían imposibles dentro de los límites de la naturaleza tal y como la conocemos en nuestro planeta, sirviendo pues exclusivamente como material abstracto objeto a investigación meramente teórico y/o simulada. Sin embargo, la realización de este material a principios del siglo XXI mediante exfoliación micromecánica de grafito de la mano de lso científicos Andre Geim y Konstantin Novoselov,[5] hazaña por la cual recibieron el premio Nobel de física en 2010, revolucionó el mundo de los materiales nanométricos. La razón de tal revolución reside en las propiedades potencialmente explotables del grafeno, muchas demonstradas hoy en día experiemntalmente, siendo el material más resistente y duro en términos mecánicos,[6] presen-

tando la mayor conductividad eléctrica[4] y térmica[7] conocidas hasta la fecha y siendo capaz de albergar, catalizar o impedir reacciones químicas de diversa índole.

Sin embargo el grafeno como tal presenta una considerable limitación para su aplicación directa en dispositivos electrónicos: la falta de una brecha energética en las bandas electrónicas que definen su carácter electronico, es decir, la separación energética entre su banda de valencia y su banda de conducción. Esta separación dicta si, a la hora de conduicir corrientes eléctricas, un material se comporta como aislante, semimetal, semiconductor o aislante. Los componentes lógicos de un circuito programado son en su mayoría materiales semiconductores por lo que, al hallarse las bandas de valencia y conducción del grafeno solapadas, este posee un carácter metálico. Una solución muy prometedora a la hora de crear una separación energética en el grafeno consiste en reducir una de sus dimensiones a escala nanométrica, pasando de esta manera de tener forma de lámina a presentar una forma de tira a escala nanométrica. De ahí el nombre de 'nanotiras de grafeno'. El confinamiento de los electrones ($\leq 10$ nm) debido a la reducción de una de las dimensiones del grafeno 'abre' una brecha energética en las GNRs que les otorga un carácter semiconductor, tal y como esta demostrado teórica y experimentalmente.

Existen diversos parámetros que definen las propiedades de las nanotiras de grafeno, siendo el primordial la dirección cristalográfica de alta-simetría del grafeno a lo largo de la cual crecen y que, a su vez, determina el tipo de borde que predomina en la estructura. Estas direcciones se denominan como 'armchair' y 'zigzag', en inglés, respectivamente. Derivadas de distintas combinaciones lineales de estas direcciones, surgen otras direcciones de menor simetría denominadas 'quirales'. Tal y como establece los cálculos y simulaciones teóricos, las GNRs que presentan bordes de tipo 'armchair' presentan un carácter semiconductor el cual puede regularse a través de la anchura de la nanotira. El mismo tipo de cálculos establece de la misma manera que las GNRs que presentan bordes de tipo 'zigzag', son metálicas y pueden albergar estados electrónicos localizados en dichos bordes y con un acoplamiento de tipo ferromagnético a lo largo del mismo borde y de tipo antiferromagnético entre ambos bordes longitudinales. Por derivado, las GNRs quirales, las cuales presentan una combinación periódica de ambos tipos de borde, pueden presentar ambas cualidades características de los bordes tanto de tipo 'armchair' como de tipo 'zigzag'.

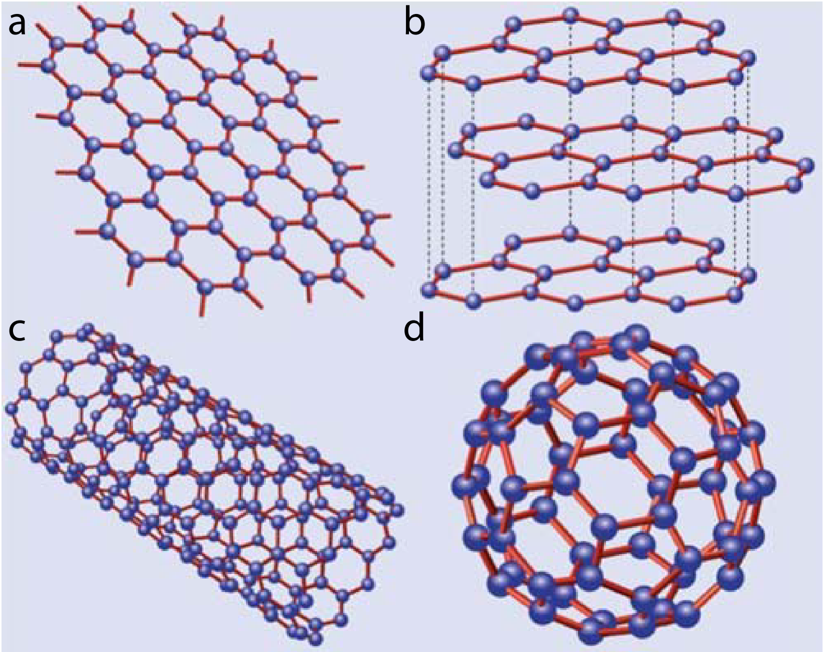

**Figure 1: Modelos del grafeno y sus principales materiales derivados. (a)** Grafeno, **(b)** grafito, **(c)** nanotubos, **(d)** fulerenos. Adaptado de ref.[8]

La formación de estas nanomateriales se realiza mediante estrategias sintéticas de química de superficie ya que, debido a la gran sensibilidad que presentan las GNRs a la alteración de sus propiedades electricas innatas ante cualquier mínimo defecto estructural,[9,10] es la única metodología que permite, junto con ciertas metodologías de química convencional, la obtención de GNRs con precisión atómica, es decir, donde no falta ningúno de los átomos que conforma la nanoestructura. Sin embargo, ante las ténicas de química convencional, las de superficie presentan la ventaja de permitir la caracterización de las propiedades eléctricas de las GNRs tras su síntesis con instrumentos que presentan una resolución energética y espacial como los STMs. La estrategia de síntesis en superficie por excelencia fue desarrollada y publicada en el año 2010 por el grupo de investigación del profesor Roman Fasel en el centro de investigación EMPA (Zürich) en colaboración con el grupo del profesor Klaus Müllen, del instituto Max Planck de investigación en polímeros (en Mainz, Alemania).[11] Mediante este método, gracias a la actividad catalítica de las superficies metálicas (normalmente oro, plata y/o cobre) sobre los cuales se suceden las reacciones sintéticas, las nano-tiras se forman a partir de precursores moleculares aromáticos que previamente se han depositado sobre dichas superficies. Las reacciones que formane ste proceso son dos: el acoplamiento de Ullmann[12] y la ciclodeshidrogenación,[13] y ambas se producen aportando energía térmica en el caso de las reacciones empleadas en esta tesis. Una vez la moléculas se hallan depositadas en la superficie metálica, primeramente se induce el acoplamiento de Ullmann en el cual los enlaces simples carbono-halógeno de los precursores se rompen para formar un nuevo enlace carbono-carbono que une las moléculas individuales en polímeros que normalmente presentan una dimensionalidad lineal debido a la posición de los grupos halógenos en los precursores. La mayor parte de estos polímeros no son planos ya que adoptan cierta conformación tridimensional para minimizar la repulsión estérica causada por los átomos de hidrógeno que se encuentran unidos covalentemente a los átomos de carbono limítrofes. Son precisamete estos enlaces carbono-hidrógeno los que se escinden seguidamente en la ciclodeshidrogenación para formar nanotiras de grafeno, estructuras que en la mayoría de los casos alcanzan su planaridad en este segunda etapa.

El manuscrito de esta tesis está estructurado en tres partes. La primera parte, la cual abarca hasta el capítulo tres, describe el marco científico en el que se cimientan los objetivos y la motivación de los resultados descritos en este trabajo. Las siguientes partes de esta tesis, comprendidas entre los capítulos cuatro y nueve, exponen los resultados y observaciones de especial interés científico logrados en la síntesis con precisión atómica de distintas nanotiras

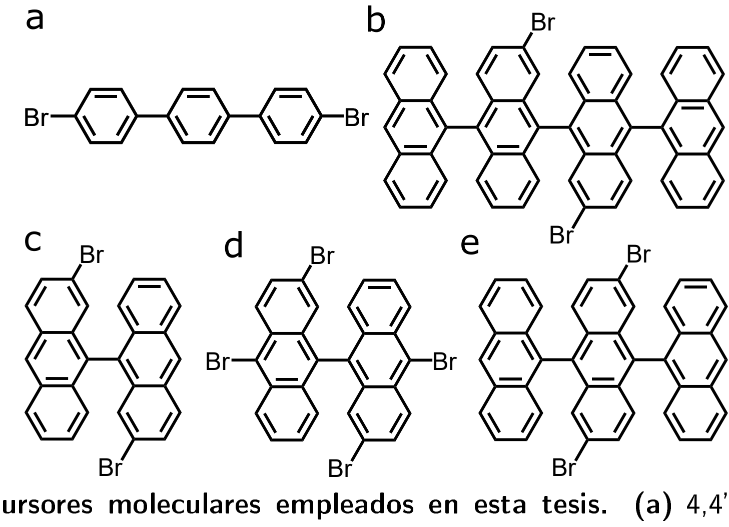

**Figure 2: Precursores moleculares empleados en esta tesis.** **(a)** 4,4”-dibromo-1,1’:4’,1”-terphenyl (DBTP), **(b)** 2”,3’-dibromo-9,9’:10”,9”-quateranthracene (DBQA), **(c)** 2,2’-dibromo-9,9’-binthracene, **(d)** 2,2’,10,10’-tetrabromo-9,9’-bianthracene and **(e)** 2,6’-dibromo-9,9’:10,9”-teranrthracene.

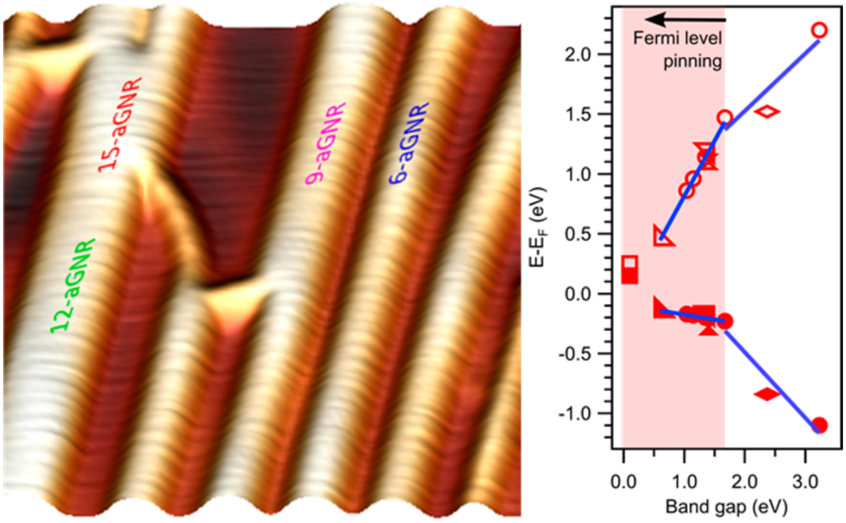

**Figure 3: Esquema descriptivo de parte de los resultados obtenidos con las nanotiras de grafeno de tipo armchair. (Izquierda)** Imagen STM tridimensional donde se aprecian segmentos estructuralmente perfectos a nivel atómico de todas las anchuras de aGNRs estudiadas en este trabajo. **(Derecha)** Gráfica donde se aprecia los resultados espectróscopicos de las bandas de valencia y conducción de las nanotiras de tipo armchair así como el valor de energía a partir del cual se da el escenario de 'Fermi-level pinning'.

de grafeno y en la caracterización de su estructura electrónica en las distintas superficies metálicas empleadas en los experimentos. Estos resultados se dividen en dos partes, centrándose primeramente en las GNRs de tipo 'sillón' (o en inglés, 'armchair') y seguidamente en las GNRs de tipo quiral (o en inglés, 'chiral'), siendo en esta última parte en la cual se ha dedicado más esfuerzo y, por lo tanto, la más extensa de la tesis.

La figura 2 muestra los modelos esquemáticos de los distintos precursores moleculares empleados en este tesis. Siguiendo el orden de los capítulos tal y como se desarrolllan en este trabajo, en primer lugar se ha utilizado el precursor molecular 4,4"-dibromo-1,1':4',1"-terphenyl (DBTP) (figura 2.a) para la síntesis de GNRs de tipo 'armchair' (aGNRs) sobre la superficie de oro (111). Sobre esta superficie, las moléculas de DBTP forman cadenas lineales de poli-*para*-fenileno (en inglés, 'PPP nanowires') mediante el acoplamiento de Ullmann para formar aGNRs de distinta anchura mediante la fusión lateral de las tiras PPP, dependiendo la anchura final de las aGNRs del número de tiras PPP que se fusionana en cada caso. En la figura 3.a podemos apreciar un imagen STM donde se distinguen aGNRs pertenecientes a la familia *3p* con una anchura que varía desde las seis hasta las quince líneas diméricas ($N_A$). La síntesis de estas estructuras con precisión atómica, nos ha permitido caracterizar su estructura electrónica medainte STS, observando como presentan un carácter semiconductor el cual se escala inversamente proporcional a su anchura, tal y como establecía anteriormente la literatura científica tanto a nivel teórico[14,15] como a nivel experimental.[16]

Sin embargo, esta síntesis de aGNRs pertenecientes carece de un control sobre el producto final debido a que la fusión lateral de tiras PPP es un proceso 'aleatorio' dado que, mediante esta metodología y sobre este substrato, no se puede controlar el número de nanotiras PPP que se fusionan en cada caso. Para otorgar selectividad a este proceso, hemos realizado la misma reacción sintética sobre la superficie escalonada de oro (322) tal y como se ilustra en el capítulo 5. Esta superficie, presenta una serie de terrazas supericiales ordenadas y con la misma anchura. Es precisamente esta anchura la que limita la fusión lateral de las tiras PPP limitando el proceso a la formación selectiva de 6-aGNRs. Esto resulta en una muestra ordenada a nivel macroscóopico donde la mayoría de los 6-aGNRs están orientados en una dirección determinada, permitiendo la caracterización de su estructura electrónica mediante ARPES, para cada una de las etapas sintéticas.

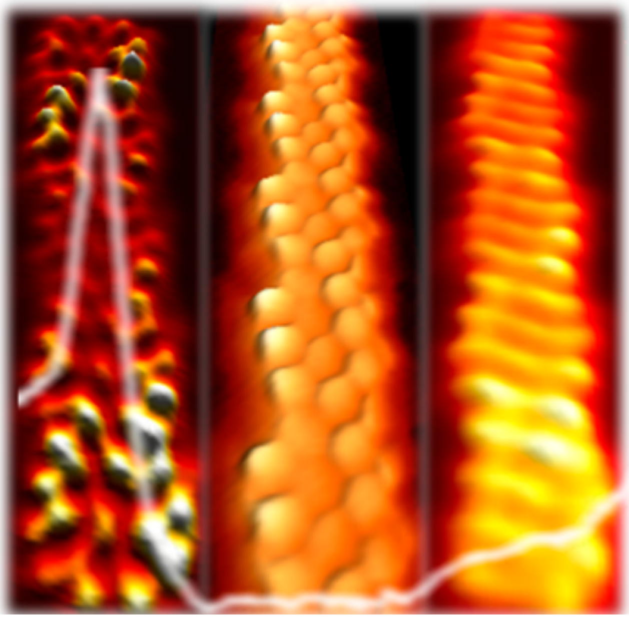

Figure 4: **Descripicón esquemática de la estructura electrónica de las nanotiras de grafeno de tipo quiral de anchura pequeña.**

En el siguiente capítulo seis, mediante el empleo del precursor molecular que se muestra en la figura 2.c, hemos sintetizado GNRs de tipo quiral en distintas superficies de Au(111), Ag(111) y Cu(111), resultando efectiva la síntesis en todos ellos. Esta eficacia reside en la reactividad preferente de los precusores en sus posiciones halogenadas, las cuales son distintas en comparación con el precursor molecular empleado originalmente para sintetizar 7-aGNRs.[11] Comparando ambos precursores, aquel que forma nao-tiras de tipo 'armchair' y aquel que forma GNRs de tipo quiral, y con el fin de evaluar que la reactividad de ambas posiciones halogenadas en el mismo precursor, hemos empleado la molécula que se muestra en la figura 2.d sobre la superficie Au(111). Los resultados demuestran, tal y como explica en el capítulo siete, como el proceso sintético resulta en el mismo tipo de nanotira que mediante el empleo del precursor dibrominado de la figura 2.a debido a una mayor actividad catalítica del sustrato metálico sobre las posiciones halogenadas del precursor que dan pie a la formación de GNRs quirales.

Sin embargo, este proceso esconde más puntos de interés ya que atendiendo a la quiralidad de los productos, las nanotiras pueden presentar dos tipos de pro-quiralidad. Para evaluar la estereoselectividad de este proceso, la mezcla racémica de precursores DBBA utilizada anteriormente se trata para poder aislar mayoritariamente los dos distintos enantiomeros. Mediante el uso por separado de cada enantiómero, hemos comprobado que esta reacción posee una gran esteroselectividad ya que durante todo el proceso sintético la quiralidad innata de cada enantiómero es transmitida a lo largo de la reacción para formar mayoritariamente un solo tipo de nanotira pro-quiral.

La eficacia sintética nos ha permitido caracterizar la estructura electrónica de las nanotiras quirales mediante STS. Este tipo de estructuras prseentan una brecha energética de $\sim$ 670 meV, demonstrando así su carácter semiconductor. Sin embargo, en nuestro estudio no observamos la presencia de estados de borde en este tipo de nano-tiras quirales. Debido a que la teoría estipula que este tipo de GNRs deben presentar una anchura mínima para que puedan albergar dichos estado de borde, hemos utilizado precursores moleculares que contiene más grupos antracenos (ver figura 2.b,e) de manera que obtenemos el mismo tipo de nanotira quiral pero con una anchura creciente. La caracterización de la estructura electrónica de estas tiras más anchas muestra la presencia de estados de borde cercanos al nivel de Fermi de nuestro sistema.

# Contents

**Abstract** **v**

**Resumen** **vii**

**List of Figures** **xix**

**I Introduction** **1**

**1 Scientific context and Motivation** **3**

1.1 Nanoscience and Nanotechnology . . . . . . . . . . 4

1.2 Materials of the future: Graphene . . . . . . . . . . 5

1.3 Opening a gap in graphene: graphene nanoribbons . . . . . . . . . . 6

1.4 Manufacturing GNRs: top-down and bottom-up strategies . . . . . . . . . . 7

1.5 Tuning graphene nanoribbons' band gap . . . . . . . . . . 9

1.5.1 Substrate influence on graphene nanoribbons' bandgap . . . . . . . . . . 12

1.6 On-surface synthesis as chemistry testing workbench . . . . . . . . . . 12

**2 Experimental Techniques** **13**

2.1 Scanning Tunneling Microsocopy . . . . . . . . . . 14

2.1.1 Tunneling Theory . . . . . . . . . . 15

2.1.2 Scanning Tunneling Spectroscopy . . . . . . . . . . 17

2.1.3 Bond-resolved imaging resolution by tip functionalization . . . . . . . . . . 19

2.1.4 Common methodology to functionalize tips in this thesis . . . . . . . . . . 21

2.1.5 Scanning Tunneling Microscopes employed in this thesis . . . . . . . . . . 21

2.2 Photoemission spectroscopy . . . . . . . . . . 26

2.2.1 Photoelectric effect and three step model . . . . . . . . . . 26

2.2.2 X-Ray Photoemission Spectrocopy (XPS) . . . . . . . . . . 27

2.2.3 Angle-Resolved PhotoEmission Spectrocopy (ARPES) . . . . . . . . . . 28

**3 Graphene Nanoribbons' Electronic Structure** **29**

3.1 Graphene's electronic structure . . . . . . . . . . 30

3.2 Armchair graphene nanoribbons . . . . . . . . . . 32

3.3 Zigzag Graphene Nanoribbons . . . . . . . . . . 34

3.4 Chiral Graphene Nanoribbons . . . . . . . . . . 35

3.4.1 cGNRs width dependence on the emergence of edge states . . . . . . . . . . 37

II Armchair Graphene Nanoribbons 39

4 Width-dependent band gap and Fermi level pinning in aGNRs 41
4.1 Synthesis of varying-width aGNRs from PPP lateral fusion . . . . . . . . . . . 42
4.2 Electronic structure: width-dependent band gap . . . . . . . . . . . . . . . . . . 43
4.3 Fermi-level pinning of valence band . . . . . . . . . . . . . . . . . . . . . . . . 48
4.4 Conclusions . . . . . . . . . . . . . . . . . . . . . . . . . . . . . . . . . . . . 50

5 Selective synthesis of armchair graphene nanoribbons on vicinal surfaces 51
5.1 Au(322) substrate as synthetic template . . . . . . . . . . . . . . . . . . . . . 52
5.2 6-aGNR electronic structure characterization . . . . . . . . . . . . . . . . . . 54
5.3 Conclusions . . . . . . . . . . . . . . . . . . . . . . . . . . . . . . . . . . . . 59

III Chiral Graphene Nanoribbons 61

6 Substrate-independent growth of chiral graphene nanoribbons 63
6.1 Synthesis of (3,1)-chGNRs on Au(111) and Ag(111) . . . . . . . . . . . . . . . 64
6.2 Growth characterization by temperature-dependent XPS . . . . . . . . . . . . 66
6.3 Covalent or metal-organic? : Linear periodicity analysis . . . . . . . . . . . . 68
6.4 GNRs' length dependence on reactions temperature . . . . . . . . . . . . . . . 69
6.5 Synthesis of (3,1)-chGNRs on Cu(111) . . . . . . . . . . . . . . . . . . . . . . 71
6.6 Conclusions . . . . . . . . . . . . . . . . . . . . . . . . . . . . . . . . . . . . 72

7 Halogen activation hierarchy during surface-promoted Ullmann coupling 73
7.1 Growth of GNRs from TBBA precursor . . . . . . . . . . . . . . . . . . . . . . 74
7.2 XPS characterization of carbon-halogen scission . . . . . . . . . . . . . . . . . 76
7.3 DFT-calculated adsorption of TBBA on Au(111) . . . . . . . . . . . . . . . . . 77
7.4 Conclusions . . . . . . . . . . . . . . . . . . . . . . . . . . . . . . . . . . . . 80

8 Transferring molecular chirality through multi-step reactions 81
8.1 Introduction to molecular chirality on surfaces . . . . . . . . . . . . . . . . . . 82
8.2 Global overview of the chirality transfer process . . . . . . . . . . . . . . . . . 83
8.3 Synthesis of chiral bianthryl polymers . . . . . . . . . . . . . . . . . . . . . . 84
8.4 Synthesis of prochiral graphene nanoribbons . . . . . . . . . . . . . . . . . . . 86
8.5 Conclusions . . . . . . . . . . . . . . . . . . . . . . . . . . . . . . . . . . . . 90

9 Electronic structure of chiral graphene nanoribbons 91
9.1 Semiconducting band gap of narrow chGNRs . . . . . . . . . . . . . . . . . . . 92
9.2 Valence band dispersion analysis by Fourier Transform-STS . . . . . . . . . . 94
9.3 Characterization of valence band by ARPES . . . . . . . . . . . . . . . . . . . 95
9.4 Growth of varying-width (3,1)-chiral GNRs on Au(111) . . . . . . . . . . . . . 97
9.5 Width-dependent electronic structure transition . . . . . . . . . . . . . . . . . 98
9.6 Conclusions . . . . . . . . . . . . . . . . . . . . . . . . . . . . . . . . . . . . 99

Conclusions and Outlook 101

References 126

**List of publications derived from this thesis** iii

**Other publications** v

**Acknowlegdements** vii

# List of Figures

1 Grafeno y principales materiales derivados . . . viii
2 Precursores moleculares empleados en esta tesis . . . ix
3 Esquema descriptivo de resultados con aGNRs . . . x
4 Esquema descriptivo de resultados con cGNRs . . . xi

1.1 Richard Feynman and Moore's Law . . . 4
1.2 Graphene allotropes . . . 5
1.3 Graphene's crystallographic orientations . . . 6
1.4 Top-down and bottom-up nanostructures manufacturing strategies . . . 7
1.5 Connecting functionalized molecular precursors . . . 8
1.6 On-surface bottom-up synthesis of atomically precise GNRs . . . 8
1.7 Graphene nanoribbons' structural parameters . . . 9
1.8 Graphene nanoribbons' edge orientations . . . 10
1.9 Graphene nanoribbons' intrinsic doping examples . . . 11
1.10 Molecule-metallic adsorbate interaction as a function of the length . . . 11

2.1 Common STM desing and imaging methods . . . 14
2.2 Wavefunction tunneling thorugh a 1D squared potential barrier. . . . 16
2.3 Voltage polarity dependence of probed sample states . . . 17
2.4 Lock-in amplifier working principle . . . 18
2.5 Examples of different bond-resolved imaging techniques . . . 19
2.6 Hapala's probe-particle (PP) model . . . 20
2.7 Tip functionalization with CO molecules . . . 22
2.8 'Milano' STM photograph . . . 22
2.9 Milano's LT-STM 'Beetle' head photograph . . . 23
2.10 'Apollo' LT-STM photograph . . . 23
2.11 'Apollo's LT-STM 'single-tube' head photograp . . . 24
2.12 Electron mean free path in solids . . . 26
2.13 Photoelectric effect and three step model . . . 27
2.14 Geometry of an ARPES experiment . . . 28

3.1 Graphene's lattice and electronic band structure . . . 30
3.2 Brillouin zone for aGNRs and zGNRs . . . 33
3.3 aGNRs' bandgap dependence on the width . . . 34
3.4 Edge states formation energies for chGNRs with different chiral angle and width 37

4.1 Synthesis of 3p-aGNRs from DBTP precursor . . . 42
4.2 Electronic structure of PPP nanowires . . . 43

4.3 Electronic structure of 3p-aGNRs . . . . . . . . . . . . . . . . . . . . . . . 44
4.4 Second valence band (VB+1) of 3p-aGNRs . . . . . . . . . . . . . . . . . . 45
4.5 Average 3p-aGNRs bands' energy values . . . . . . . . . . . . . . . . . . . 46
4.6 DFT calculated 3p-aGNRs electronic structure . . . . . . . . . . . . . . . . 46
4.7 DFT computational setup for 6 and 12-aGNRs on Au(111) . . . . . . . . . . . 47
4.8 Fermi level pinning scenarios . . . . . . . . . . . . . . . . . . . . . . . . . 49
4.9 Summary of GNRs' VB and CB onsets . . . . . . . . . . . . . . . . . . . . . 50

5.1 Growth comparison of 3p-aGNRs on Au(111) and Au(332) . . . . . . . . . . . 52
5.2 Synthetic steps of 6-aGNR growth on Au(322) . . . . . . . . . . . . . . . . . 53
5.3 ARPES signal of 6-aGNR growth steps on Au(322) . . . . . . . . . . . . . . . 54
5.4 Work function measurements of Au(111) and Au(322) surfaces . . . . . . . . 56
5.5 Constant-current dI/dV spectra of PPP nanowires and 6-aGNRs . . . . . . . 56
5.6 Spectroscopic characterization of 6-aGNR's electronic structure on Au(322) . 57
5.7 DFT-calculated VB and CB orbital decay towards vacuum . . . . . . . . . . . 58
5.8 Tilted structure of 6-aGNRs . . . . . . . . . . . . . . . . . . . . . . . . . . 58

6.1 Substrate-dependent chemical pathways of DBBA precursor . . . . . . . . . . 64
6.2 Growth of (3,1)-chGNRs on Au(111) and Ag(111) . . . . . . . . . . . . . . . 65
6.3 Temperature-dependent XPS monitoring of chGNRs growth from DBBA precursor . . . . . . . . . . . . . . . . . . . . . . . . . . . . . . . . . . . . . 67
6.4 DFT relaxed structures and periodicites of possible products . . . . . . . . . 68
6.5 Length distribution of GNRs grown on Au(111) . . . . . . . . . . . . . . . . 70
6.6 (3,1)-chGNRs growth on Cu(111) . . . . . . . . . . . . . . . . . . . . . . . 71

7.1 Possible synthetic routes fro TBBA precursor . . . . . . . . . . . . . . . . . 74
7.2 Polymers from TBBA precursor . . . . . . . . . . . . . . . . . . . . . . . . 75
7.3 chGNRs from TBBA precursor . . . . . . . . . . . . . . . . . . . . . . . . . 75
7.4 Photoemission spectra of precursor TBBA . . . . . . . . . . . . . . . . . . . 76
7.5 DFT simulated adsorption of TBBA on Au(111) . . . . . . . . . . . . . . . . 77
7.6 Optimum TBBA conformation in gas phase . . . . . . . . . . . . . . . . . . 78
7.7 Non-reacted TBBA molecules deposited on Au(111) . . . . . . . . . . . . . . 78
7.8 chGNRs from DBBA and TBBA precursors . . . . . . . . . . . . . . . . . . . 79

8.1 Schematic model of the global chirality transfer process . . . . . . . . . . . . 83
8.2 Schematic model of the steric hindrance between DBBA radical enantiomers . 84
8.3 Synthesis of chiral polymers from enantiomer P . . . . . . . . . . . . . . . . 84
8.4 Alternative identification of polymers' absolute chirality . . . . . . . . . . . 85
8.5 Herringbone distortion due to adsorbate-substrate interaction . . . . . . . . . 85
8.6 Epitaxial growth of prochiral GNRs on Au(111) . . . . . . . . . . . . . . . . 86
8.7 Bond-resolved prochiral ribbons in all their orientations on Au(111) . . . . . . 87
8.8 Preferential nucleation of chGNRs on fcc regions . . . . . . . . . . . . . . . 88
8.9 Interspacing between chGNRs . . . . . . . . . . . . . . . . . . . . . . . . . 89

9.1 Electronic structure characterization of (3,1)-chGNRs . . . . . . . . . . . . . 92
9.2 Constant-current maps of (3,1)-chGNRs . . . . . . . . . . . . . . . . . . . . 93
9.3 Valence band energy-dependent LDOS modulation . . . . . . . . . . . . . . 93

9.4 (3,1)-chGNR's valence band dispersion by FT-STS . . . . . . . . . . . . . . . . 94
9.5 Full energy and momentum VB dispersion by FT-STS . . . . . . . . . . . . . . 95
9.6 ARPES characterization of VB on Au(322) . . . . . . . . . . . . . . . . . . . . . 96
9.7 Growth of (3,1)-chGNRs with different widths . . . . . . . . . . . . . . . . . . . . 97
9.8 Atomic and electronic structure of (3,1)-chGNRs with varying-width . . . . . 98

# Part I

# Introduction

The first part of this thesis aims to describe the backgorund underlying the different experimental results shown in later sections. For this reason, this part is divided in three chapters. To begin with, we describe the scientific frame and most relevant achievements in the field defining the context, and hence the motivation, of the work presented here. Secondly, a brief introduction to the different experimental equipments employed in htis thesis is provided together with aspecific description of the main equipments used. Lastly, we descibe the electronic properties of graphene and graphene nanoribbons from a theoretical point of view.

# Chapter 1

# Scientific context and Motivation

In this first chapter, we briefly review the historical background giving birth to what we currently term as nanoscience and nanotechnology. Then we introduce one of the ioconic materials representing this new age of science, i.e. graphene, which this thesis is based on, these are, graphene nanoribbons. Next, we describe the different manufacturing strategies of nanostructures employed in recent years, giving a detalied description of those particularly used for synthesizing graphene nanoribbons with atomic precission. Aftet that, we describe graphene nanoribbons parameters relevant for the understanding of their structure-properties relation. Finally, we briefly talk on the relvance of surface assited reactions in the study of new synthetic chemical paths.

## 1.1 Nanoscience and Nanotechnology

In his seminal speech *'There's Plenty of Room at the Bottom'* in 1959 (see Figure 1.1.a), Professor Richard Feynman disclosed his vision of a precise control over single atoms and molecules that would lead to the production of future materials presenting new exciting phenomena, and thus generating a revolution in science and technology.[17] This innovative perspective initiated the emergence of the terms nanoscience and nanotechnology, coined in 1974 by Norio Taniguchi,[1] concerning the study of the peculiar properties of nanoscaled materials featuring sizes from ~1 Å to ~100 nm along one of its dimensions. Shortly after Feynman's speech, Gordon Moore stated in 1965 his famous prediction declaring that the number of transistros in a integrated circuit will double every two years, and so the computing power of the different electronic devices integrating those circuits will experience the same prospering trend.[18] This forecast became thereafter the flagship of a technology revolution. Since then, transistor size scaled down from 10 $\mu$m to ~10 nm,[19] giving rise to the creation of increasignly sophisticated machines, from the first home computers in the 1970s to today's smartphones in the high-speed internet society. However after 50 years of succesful Moore's Law (see Figure 1.1.b), it slowed down after the 28 nm node and seems to be reaching its limit since barriers either technical (as the inherent electrical leakage and resistance) and/or economical (as the manufacturing cost) increase drastically below transistor sizes of 10 nm.[20,21] Moreover, in such reduced devices, electrical currents start to experience quantum effects, like undesired electron tunneling between the channel region and the gate, that may drastically alter their proper functioning.

One the currently pursued approaches towards further miniaturization keep on pushing the current Silicon-based technology miniaturization forward by expanding the two-dimensional integrated circuits into three dimensional structures, thus allowing transistors cramming within an extra dimension.[22] A different option beyond Silicon relies on the use nanostructures made up from a combination of few (or even single) atoms and/or molecules equivalently featuring transistor-like behaviour, in line with Feynman's vision. This latter solution is termed as *'Molecular Electronics'*.[23–25] The idea of incorporating atoms and molecules into electronic circuits is considered to begin upon Aviram and Ratner's theoretical research *'Molecular Rectifiers'*,[26] pointing out that a rationally designed aromatic molecule combining donor/acceptor units and brigded by sigma bonds could resemble the functionality of its macroscopic counterpart. This conception gave rise to an emerging field focused on the synthesis and study of materials structured at the nanoscale and presenting new structural, chemical and physical quantum phenomena steming from its reduced dimensionality.

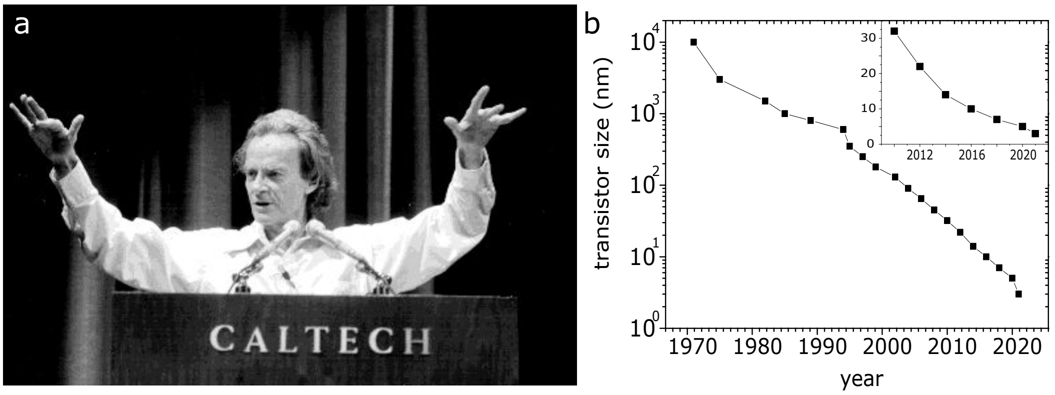

**Figure 1.1:** **(a)** Richard Feynman at Caltech giving his famous lecture entitled *'There's Plenty of Room at the Bottom'* and **(b)** transistor size reduction as a function of time, illustrating Moore's Law. The inset shows the same data than in (b) over the last 10 years..

## 1.2 Materials of the future: Graphene

One example of these revolutionary nanoscaled materials is graphene. Graphene is defined as one-atom-thick monolayer of carbon atoms packed into a two-dimensional honeycomb lattice. These carbon atoms present a sp$^2$ configuration characteristic of aromatic molecules where in-plane $\pi$-like orbitals host the conduction electrons. Therefore, with no real boundaries, graphene can be considered as an infinite aromatic molecule. Graphene represents the essential structural component of other carbon allotropes with different dimensionality such as graphite, carbon nanotubes and/or fullerenes (see Figure 1.2).

More than seventy years ago, first theoretical studies on this material aimed to understand the electronic properties of its three dimensional allotrope graphite.[27–29] Being a strictly two-dimensional crystal, graphene was presumed to be thermodynamically unstable in a 'real environment',[30] so described as an 'academic material' for fundamental studies in condensed matter physics. After scientists theorized about graphene for years, all of a sudden it came into reality when graphene flakes were unexpectedly obtained by micromechanical cleavage of bulk graphite,[31] by the scientists Andre Geim and Konstantin Novoselov, awarded with the Nobel Prize in Physics in 2010. Being the thinnest, lightest and strongest material known to date,[6] with the highest electron[4] and thermal conductivity,[7] and nearly transparent,[32] its wide-ranged potential applications early fascinated the scientific community.[5] However, a relevant drawback of graphene is the lack of an electrical bandgap that considerably limits its implementation into electronic devices needing large current on/off ratios.

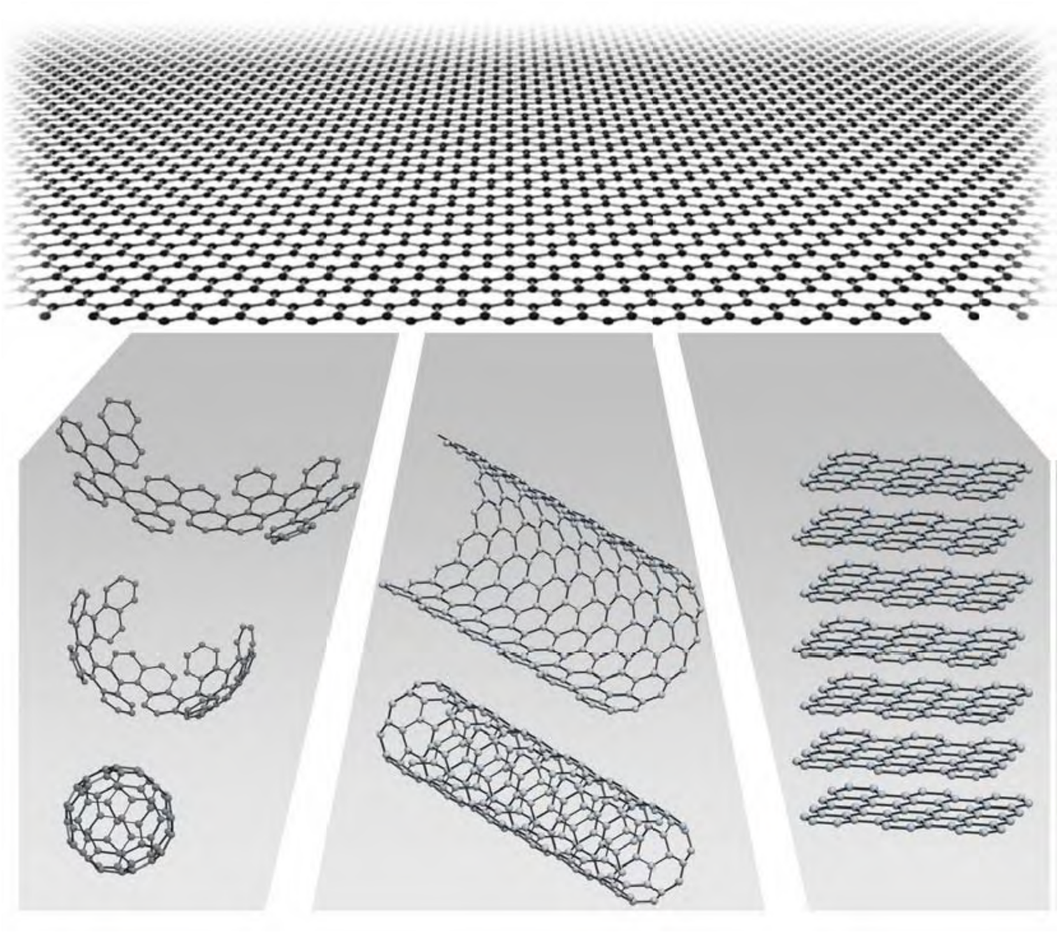

**Figure 1.2: Graphene allotropes.** Representation of **(top)** graphene and **(bottom)** some of its common allotropes: from left to rigth, fullerenes, carbon nanotubes, and graphite. Adapted from ref.[5]

## 1.3 Opening a gap in graphene: graphene nanoribbons

Bandgaps of $\geq$ 0.4 eV are required for digital-logic applications at room-temperature.[33] Different alternatives can potentially create a bandgap in graphene.[34] As a way of example, structural strain could solve this problem,[35–37] however the strain required for opening a gap is extremely high and basicaly not reasonably feasible. In addition, gaps of ~0.7 - 1.0 eV are obtained via doping or functionalization either with atoms or molecules,[38–47] albeit the chemical procces inevitablily leads to a drastic reduction of the mobility. Nevertheless, one promising way to induce a bandgap in graphene is the electronic confinement.[48] This alternative relies on reducing one of its dimensions below ~10 nm thus being now a one-dimensional structure, commonly referred as graphene nanoribbons (GNRs). GNRs hold many of the fascinating properties of graphene but, in addition, the confinement of electrons due to their nanometer width and the presence of finite edges opens a bandgap and provide these ribbons with new electronic properties.

Primarily, we can classify GNRs depending on their edge orientation. In accordance with graphene's high-symmetry directions, these orientations are zigzag and armchair directions (see Figure 1.3, red and blue vectors). Consequently, those ribbons growing along the former(latter) orientation are termed as zigzag(armchair) GNRs. Alternatively, a combination of zigzag and armchair directions result into different low-symmetry crystallographic orientations which can define a new family of GNRs. These low simmetry-orientations are characterized by a chiral angle $\theta$ (see Figure 1.3, purple range), as the ribbons that they define. The edge structure is the main parameter defining the expected properties for each ribbon. From a general theoretical point of view, on the one hand, zigzag GNRs (zGNRs) are gapless and can host spin-polarized electrons tightly localized at their edges,[14,15,49–54] with an (anti)ferromagnetic coupling along the (opposite)same longitudinal edges.[55] On the other hand, armchair GNRs (aGNRs) have a semiconductor character which can be modulated by tuning the width of the ribbon, and do not present edge localized states.[14,15,49,56–58] Finally, chiral GNRs (chGNRs) can potentially show both the characteristic properties of armchair and zigzag GNRs, i.e. a semiconductor electronic character and spin-polarized edge states.[59–63] Due to these exotic features, GNRs hold great interest for many different applications, ranging from capacitors,[64] batteries,[64] gas sensors,[65] photodetectors,,[66] transistors,[33] thermoelectric devices,[67,68] or integrated circuits.[69]

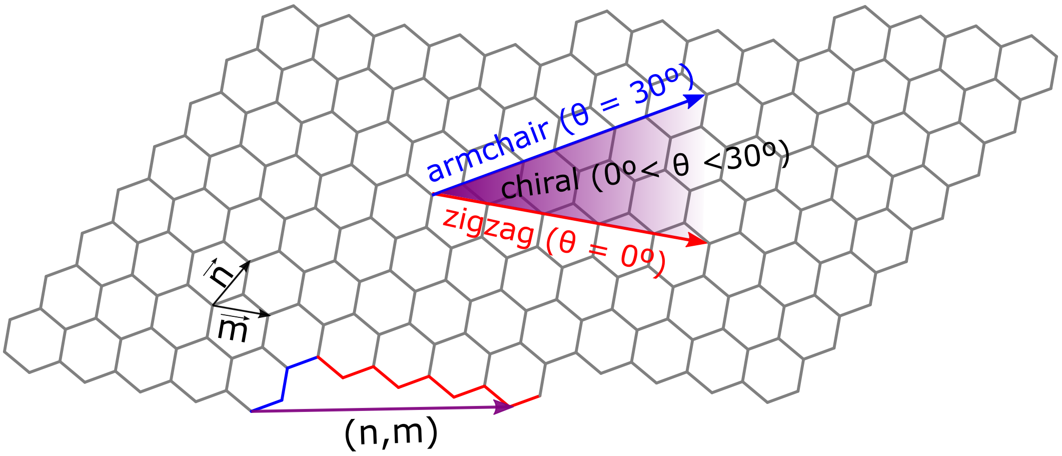

**Figure 1.3: Graphene's high-symmetry crystallographic orientations:** (red) zigzag and (blue) armchair. (Purple) range of chiral low-symmetry crystallographic orientations. The chiral vector exemplified in this figure (in purple) corresponds to the chiral vector (m = 4, n = 1), therefore the ribbon resulting from that edge orientation would be the (4,1) chiral GNR.

## 1.4 Manufacturing GNRs: top-down and bottom-up strategies

The production of precise nanostructured materials is a technological challenge. The two main strategies for patterning surfaces and devices down to the nanoscale in a controlled and repeatable manner are the top-down and bottom-up methodologies[74,75] (see Figure 1.4). On the one hand, the top-down strategy is based on the formation of structures from bigger source materials, with fabrication methods such as lithography, masked etching, writing, thin film deposition, stamping, etc., to pattern nanoscaled structures with an acurracy of $\leq$100 nm.[76] This apporach is commonly used, for example, to create integrated circuits from bare Silicon wafers. On the other hand, the bottom-up approach seeks to create structures by the interconnection of smaller entities which, at the nanoscale, are mainly molecules and/or atoms.[77] The controlled arrangement of such small components rely on the basic chemical interactions between them, from weak Van der Waals forces, to the stronger cohesion energies given in covalent, metalic or ionic bonds.

Both approaches have been used for the production of graphene nanoribbons. Nevertheless, the final structural result greatly differs depending on the employed methodology. To begin with, the top-down strategies involve different lithographic methods,[78–83] carbon nanotubes unzipping,[84–88] graphene sheets sonochemical-cutting[89] and etching approaches.[90–98] Unfortunately, given the extremely sensitivity of GNRs' properties to the minimum structural defect,[9,10,99,100] all these top-down approaches do not attain the appropiate synthetic accuracy to obtain the smooth-edged, defect-free ribbons required to access the pristine electronic structure of these nanomaterials. The different bottom-up methodologies providing GNRs involve techniques like wet chemistry,[101–103] sonochemically-cutted graphene sheets,[89] and chemical vapor deposition[104–109] among others, but similarly these techniques failed to attain a reproducible synthesis of defect-free GNRs featuring widths smaller than 10 nm, as required for inducing a semiconducting bandgap.[110]

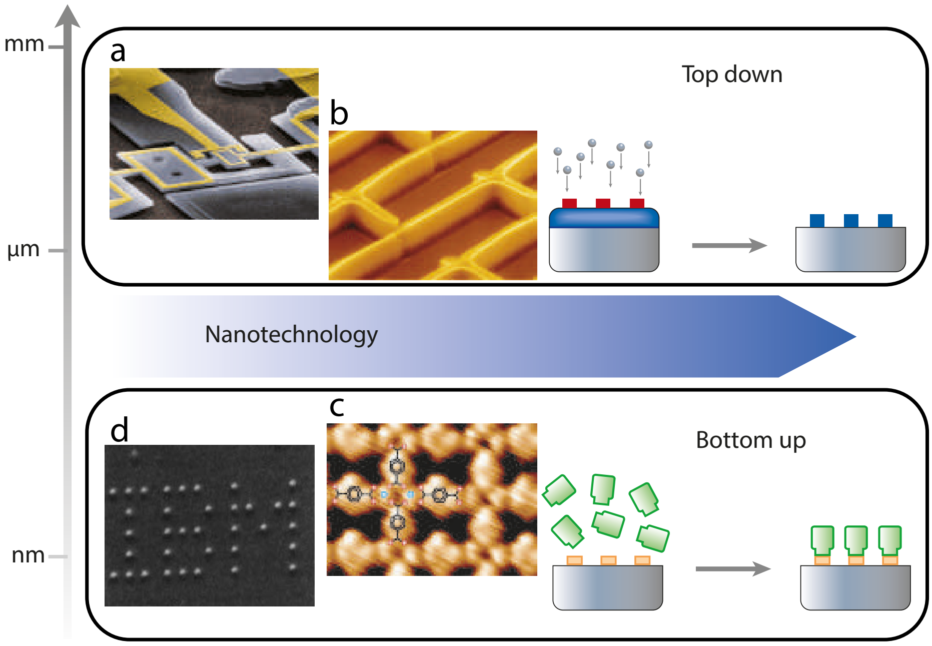

**Figure 1.4: Top-down and bottom-up nanostructures manufacturing strategies. (a)** Nanomechanical electrometer obtained by electron-beam lithography,[70] **(b)** patterned films of carbon nanotubes obtained by microcontact printing and catalytic growth,[71] **(c)** regular metal-organic nanoporous network integrating iron atoms and functional molecules,[72] and **(d)**Xenon atoms forming the word 'IBM' positioned with the tip of a scanning tunnelling microscopes.[73] Figure adapted from ref.[74]

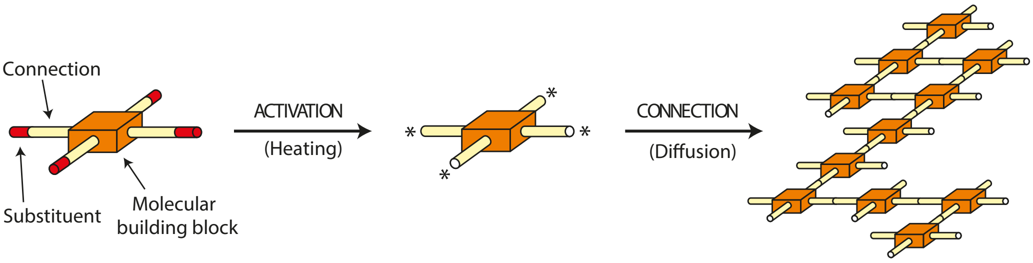
Connection
Substituent
Molecular building block
ACTIVATION
(Heating)
CONNECTION
(Diffusion)
*

**Figure 1.5: Schematic representation of the methodology for connecting functionalized molecular precursors.** Taken from ref.[111]

Nevertheless this goal was achieved in 2010 by the group of Prof. R. Fasel who, based on previous works reporting the controlled linking of molecular precursor[111] (Figure 1.5) and the formation of aromatic rings from $\pi$-conjugated molecules,[112,113] developed an on-surface chemical methodology yielding atomically-precise GNRs with the appropiate dimensions.[11] Figure 1.6.a depicts the overall process. After depositing the molecular precursors onto a catalytic metallic substrate, this approach involves two synthetic steps triggered by thermal annealing. Firstly, brominated aromatic molecules undergo dehalogenation and the formation of new carbon-carbon covalent bonds at the dehalogenated positions, hence forming non-planar linear polymers (Figure 1.6.b). This reaction is known as Ullmann coupling,[12,114] and it is assisted by the catalytic effect of the substrate (being Au(111) and Ag(111) in this particular example).[11] Secondly, cyclodehydrogenation is induced at higher temperatures. In this synthetic step, the internal carbon-hydrogen bonds are broken and new carbon-carbon are formed resulting into planar GNRs (Figure 1.6.c,d).

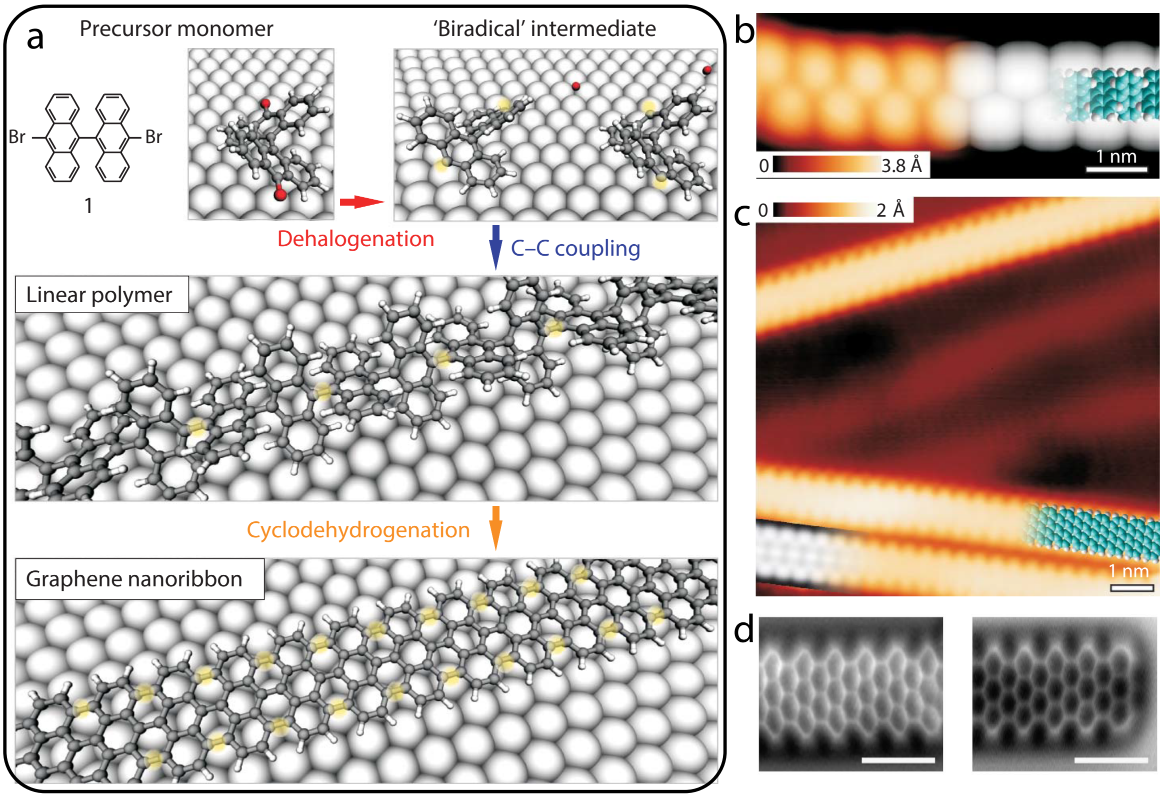
a
Precursor monomer
'Biradical' intermediate
Br
Br
1
Dehalogenation
C–C coupling
Linear polymer
Cyclodehydrogenation
Graphene nanoribbon
b
0
3.8 Å
1 nm
c
0
2 Å
1 nm
d

**Figure 1.6: On-surface bottom-up synthesis of atomically precise 7-aGNRs. (a)** Schematic representation of the whole synthetic process. STM images of **(b)** the polymer and **(c)** final 7-aGNRs resulting from precursor 1 in (a). **(d)** Bond-resolved nc-AFM images of the 7-aGNR. Images in (a-c) are taken from ref.[11] Images in (d) are taken from ref.[115]

## 1.5 Tuning graphene nanoribbons' band gap

Beyond the primary classification imposed by the edge orientation (section 1.3), there are more parameters tuning GNRs' properties such as the width, the edge structure, the doping, as well as the length and longitudinal termination[124] (see Figure 1.7). This fact remarks the versatile, strong structure-property relation present in these nanostructures. To begin with, as will be shown in chapter 4 and 9 of this manusript, the width can modulate or rule the band structure predicted for each kind of ribbon.[14–16,59,62,125] The common convention employed to describe GNRs' width, with respect to their edge orientation, is given by the number of carbon dimer lines ($N_A$) for aGNRs, and the number of carbon zigzag lines ($N_Z$) in the case of zGNRs, as shown in Figure 1.8. There is no specific settled notation to describe particularly the width of cGNRs. The different ratio between armchair- and zigzag-like edges that can give rise to the formation of cGNRs of disparate chiral orientations. Intuitively, the width of those cGNRs formed by a majority of armchair or zigzag-like edges can be accurately defined by the notation employed for the kind of edge which is present in a major proportion (with respect to its counterpart) in its periodic chiral edge orientation. That is, the width of cGNRs which present a major proportion of armchair-like edges are easily described by the notation employed for aGNRs and *vice versa*. Nevertheless, cGNRs with a major proportion of zigzag-like edges are the common synthetic objectives since those are the kind of cGNRs which can hold, from a theoretical point of view, the spin-polarized states related to the zigzag-like edges.[49] So, the width notation employed for zGNRs is the one commonly applied to cGNRs, as done with the cGNRs studied here.

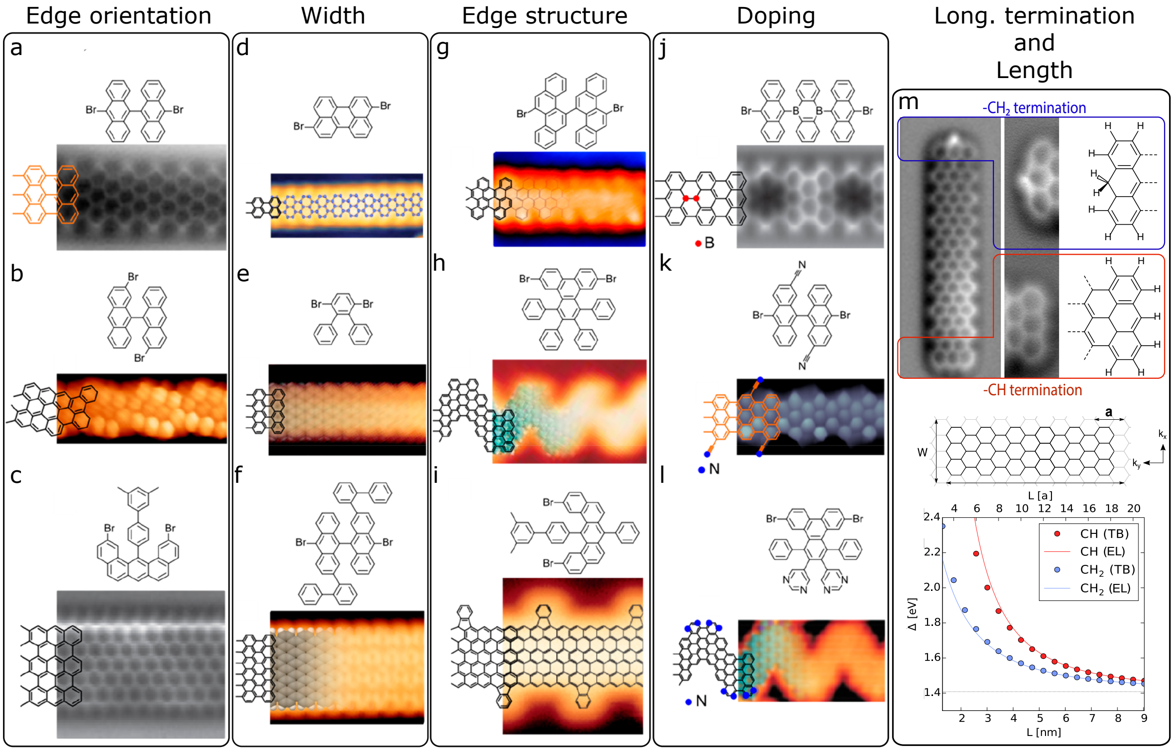

**Figure 1.7: Classification of graphene nanoribbons' structural parameters.** GNRs classified by **(a-c)** edge orientation, **(d-f)** width, **(g-i)** edge structure,**(j-l)** doping, and **(m)** longitudinal termination and length. Figure adapted from ref.[116] including (a) ref.,[115] (c,i) ref.,[117] (d) ref.,[118] (e) ref.,[119] (f) ref.,[16] (g) ref.,[120] (h) ref.,[11] (j) ref.,[121] (k) ref.,[122] (l) ref.[123] and (m) ref.[124]

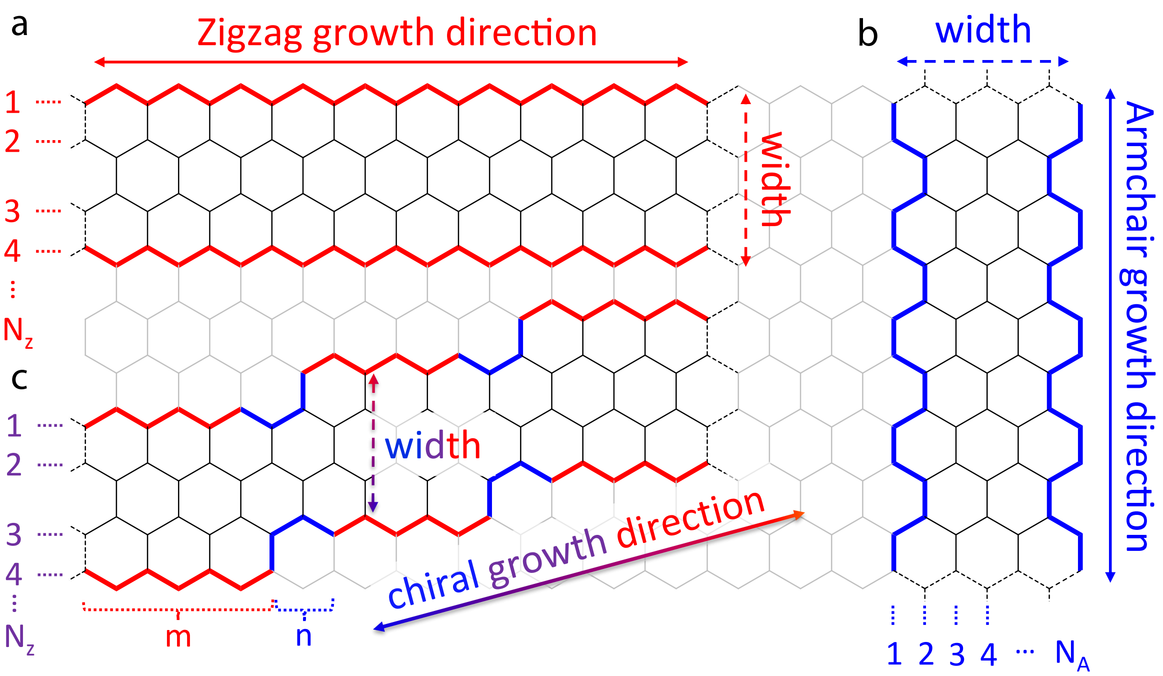

**Figure 1.8: Classification of graphene nanoribbons by edge orientation.** GNRs growing in the **(a)** zigzag, **(b)**armchair and **(c)** chiral orientation.

Despite some works describe the width of GNRs with different edge structure,[126,127] yet there is no general formalized notation for them. In the case of GNRs functionalized with peripherical functional groups, their width is described as their non-doped analogues. Using bottom-up on-surface synthetic methodologies (section 1.4), GNRs width can be precisely tuned by the designed of a suitable molecular precursor,[128] or alternatively by the lateral fusion of previously formed GNRs.[125,129–138]

GNRs' edge structure is defined by the periodic combination of armchair- and zigzag-like edges characterizing ribbons which do not grow along a single crystallographic orientation.

Changes in the edge structure as displayed in the examples of figure 1.7 require a case-by-case study and description, as they lack a systematic variation Regarding this parameter, we highlight here the extensive work reported on the synthesis and electronic structure characterization of chevron graphene nanoribbons (cGNRs), both on single pristine,[11,140–142] or different edge-structured[126,143] cGNRs, as well as on heterojunctions.[123,144–148]

While the bandgap value of GNRs can be controlled in terms of width by the smart pre-design of molecular precursors, the alignemnt of GNRs frontier orbitals with respect to Fermi level of a metal electrode is equally relevant for the development of GNRs-based devices such as field-effect transistors.[?,139,149] Such a shifting of GNRs bands can be attained either by extrinsic doping, i.e. the co-deposition of doping agents,[150] or by intrinsic doping methodologies.[151] GNRs intrinsic doping involves the alteration of their pristine structure either by the substituion of carbon atoms forming the ribbon skeleton by akin atoms (termed here as 'internal doping')(see Figure 1.9.b), or by adding chemical functional groups to the longitudinal edges of the ribbons (termed here as 'external doping' or 'functionalization'). In the case of internal doping, the range of atoms suitable for being embedded in GNRs skeletons at the carbon atom positions is very limited taking into account that these atoms must have a similar atomic size and orbital configuration (Figure 1.9.a). Apart from inducing a band shifting, some works reported on the creation of new frontier bands.[152–155] Lastly, as recently observed,[124] the length can have an relevant influence on GNRs bandgap when they are shorter than a threhold length at which bandgap values converge.

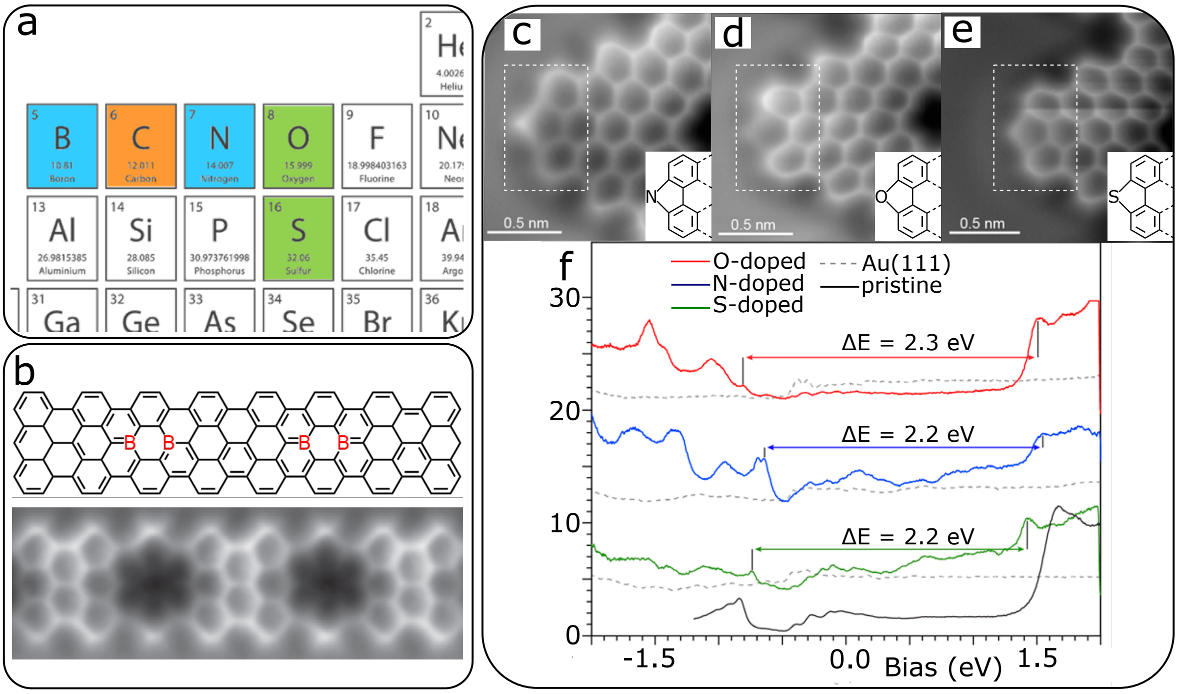

**Figure 1.9: Graphene nanoribbons' intrinsic doping examples. (a)** Chemical elements suitable for substitute carbon atoms (in orange) either inside and at the edges of the carbon skeleton (in blue), or just at the edges (in green) **(b)** (Top) Schematic model of boron-doped 7-aGNR and (bottom) corresponding nc-AFM image of the ribbon. Adapted from ref.[121] **(c-e)** nc-AFM images of (c) nitrogen-, (d) oxygen-, and (e) sulfur-doped chGNRs whit schematic models (inlets) corresponding to the structure inside the white dashed rectangles. **(f)** dI/dV spectra of examples shown in (c-e) where the band shifting exerted by the doping effect is clearly evident in comparison with the pristine ch-GNR spectrum (in black). Data in (c-f) adapted from ref.[139]

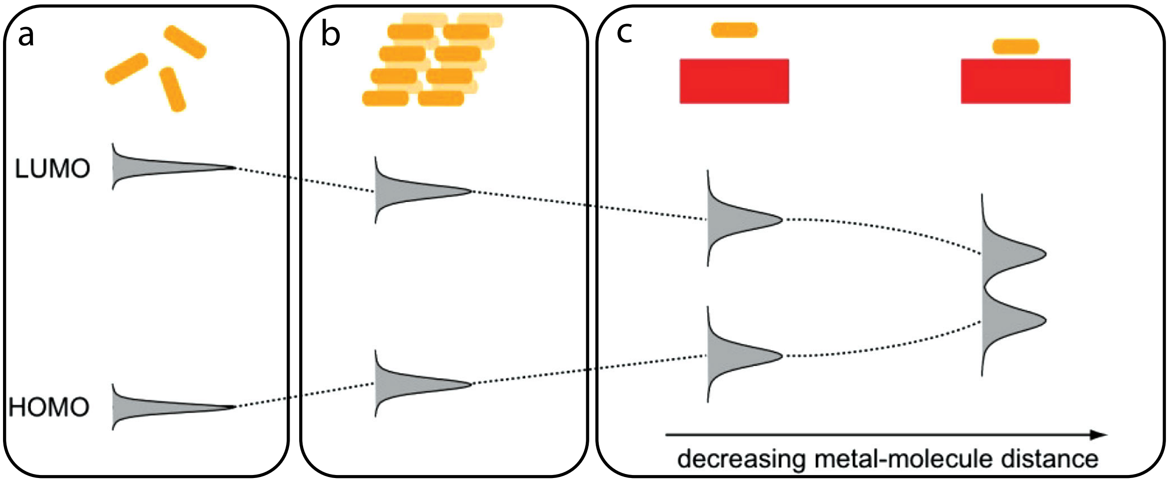

**Figure 1.10: Molecule-metallic adsorbate interaction as a function of the length (a)** Molecules in gas phase, **(b)** in a molecular solid**(c)** and adsorbed on a metal substrate. Copied from ref.[156]

### 1.5.1 Substrate influence on graphene nanoribbons' bandgap

Most of experiments involving the electronic structure characterization of GNRs have been performed on a metallic substrate, since their catalytic effect is required for the synhtesis of these structures (see section 1.4). Once the GNRs are formed, the interaction of their orbitals with the electron reservoir of the metallic substrate have a considerable impact on GNRs electronic structure. This interaction is stronger if the adsorbates are chemisorpted instead of phisysorpted. In the former, the creation of new bonds leads to an electron transfer between adsorbate and substrate, while the latter involves a polarization of both adsorbate and surface. This weaker physisorption scenario, commonly dominated by VdW forces have a considerable influence on the adsorbates' electronic structure.

This screening, known from induced charge redistributions depends on the polarizability of the surroundings of the molecule, resulting in the reduction of the bandgap. In turn, the broadening of the frontier molecular bands increases as the hybridization of its sorrounding, as illustrated in Figure 1.10.[156] Therefore, the strength of these effects decay from metallic, to semiconducting, until insulating surfaces as well as with increasing molecule-substrate distance. The substrates employed are coinage metals (Au, Ag and Cu).

## 1.6 On-surface synthesis as chemistry testing workbench

On-surface synthesis (OSS) has become nowadays an emerging field making use of solid surfaces as substrates for the formation of different advanced nanostructures thorugh the study of surface-mediated chemical reactions.[157–161] Most of current on-surface experiments are based on the use of molecular precursor as building blocks for the production of the desired products. Therefore according to the fabrication methodologies classification explained in section 1.4, OSS belongs to the 'bottom-up' manufacturing techniques and, according to the sort of given catalytic processes, OSS rely within the heterogeneus catalysis field.

Although first succesful surface-assisted synthetic reactions date from the end of past 20th century ,[162,163] the seminal work of Grill. and coworkers in 2010,[111] where they reported on the controlled covalent linking of different porphyrines by the smart pre-desing of the halogentad positions within these molecular precursors which rules the dimensionality of the products formed, supposed a strong impulse to this synthetic field. In fact, due to the structural weakness of self-assembled materials, the current scope in OSS focuses on the creation of covalently bonded structures, thus presenting the mechanical resistance required for the subsequent implementation of these nanostructured entities into future generation devices.[164]

OSS offers some advantages not present in conventional wet chemistry, as the reduction of the reaction barrier energy required for provoking the desired reaction,[161,165,166] which is commmonly provided by thermal heating, thus reducing or avoiding the formation of undesired byproducts or the degradation or decomposition of the original or intermediate reactants. In this regard, we highlight the insteresting progress observed reccently in photo-induced on-surface synthesis,[167] which due to the nature of the energy provided (light), reduce considerably the temperature reached by the system during the synthetic proccess. Moreover, given the natural dimensionality of the commonly planar substrates employed in OSS, it allows for the formation of two-dimensional networks hardly obtained by other means. In adittion, OSS allows sample characterization using sofisticated surface analysis techniques with spatial resolution with angstroms accuracy such us STM.

# Chapter 2

# Experimental Techniques

This chapter provides a general description of the different analytical techniques employed in this thesis. The study of the growth and the electronic structure of the different nanostructures is mostly performed with a scanning tunneling microscope (STM). In the first section we describe the working principle of this technique and its different funcionalities such as scanning tunneling spectroscopy and bond-resolved imaging by tip functionalization, together with a schematic description of the sample preparation and the specific equipment(s) employed. In the last section, we explain the fundamentals of the complementary surface-sensitive techniques used complementary in this thesis, namely, X-ray photoemission spectroscopy (XPS) and angle-resolved photoemission spectroscopy (ARPES).

## 2.1 Scanning Tunneling Microsocopy

Scanning tunneling microscopy represents the first kind of scanning probe microscopes, a branch of microscopy which uses a physical probe to scan solid surfaces.[168] The development of STM technology by Gerd Binnig and Heinrich Rohrer in 1981[2] at IBM Zürich (Switzerland) established a new course in the field of surface science, providing unprecedented resolution in real space to resolve topographic features of flat surfaces down to the atomic scale. Shortly after, Binning and Rohrer obtained the first STM images of the well-known 7x7 surface reconstruction of the Si(111) surface,[169] receiving in 1986 the Nobel Prize in Physics for their outstanding contribution to science. Modern STM instruments can operate at temperatures ranging from a few miliKelvins[170] to more than 500K[171,172] and in different ambient such as air,[173] liquids[174] and or even electrochemical cells,[175] making the STM a key imperative instrument in surface science laboratory.

The working principle of STM is based on the quantum tunneling effect where electrons, contrary to classical physics, have a certain probability to overcome a potential barrier, this is, to 'tunnel'. In UHV conditions, the vacuum gap between tip and sample represents this potential barrier. Quantum tunneling is physically attained by approaching a very sharp metallic tip (typically made of tungsten or platinum-iridium alloy) towards a conductive surface while applying a DC voltage bias between both. Before tip and sample come into direct contact, electron wave functions overlap, therefore allowing quantum tunneling at distances of ∼ 1 nm and with current intensities within the nano-ampere range.

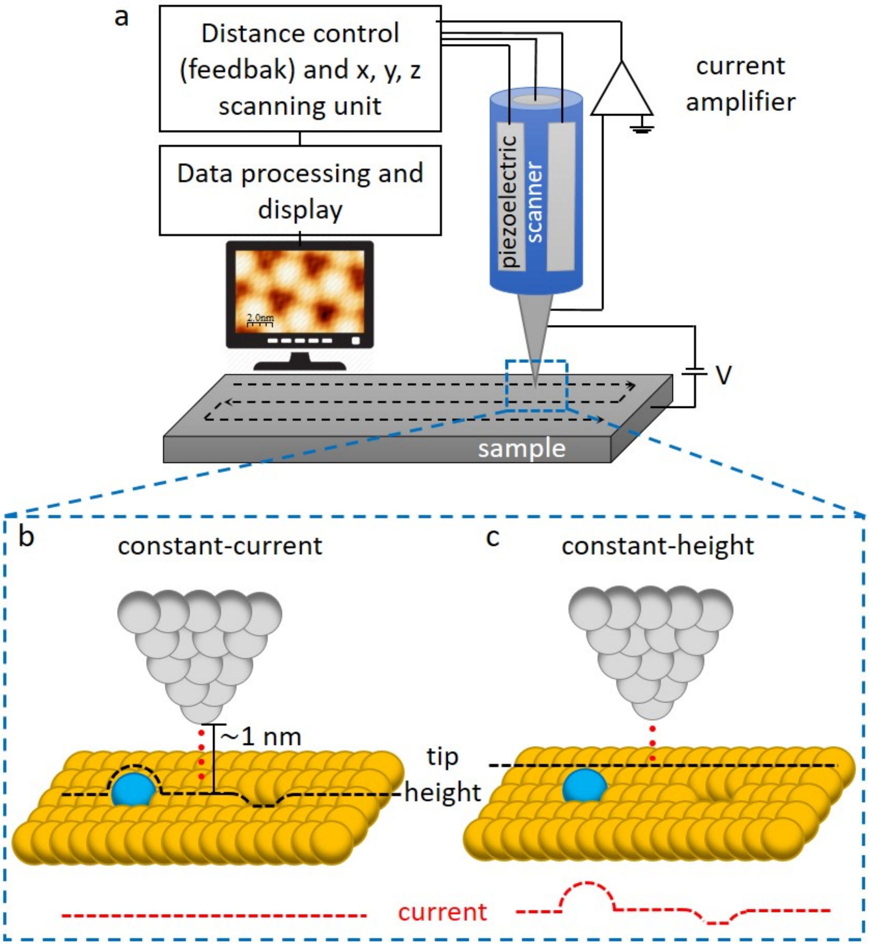

**Figure 2.1: Common STM desing and imaging methods.** Schematic models of a) a common STM design, b) constant-current and c) constant-height imaging modes.

Figure 2.1.a illustrates a typical STM design. In the common imaging mode, i.e. constant current mode (Figure 2.1.b), both voltage bias and tunneling current determine a certain sample-tip distance (or tip height $z$). Once the tip starts to scan the surface, a computer-controlled feedback mechanism adjusts constantly this distance by approaching or retracting the tip so that the tunneling current remains constant. Thus, STM images are three-dimensional images generated by registering the tip height as a function of the tip position on the sample (xy plane). Making use of a series of piezoelectric transducers attached to the scanner (the component holding the tip), the tip height is regulated with pico-meter sensitivity. This precise control is possible due to the exponential relation between the tunneling current intensity and tip-sample distance, as explained in the next subsection 2.1.1.

In addition, complementary constant-height imaging mode (Figure 2.1.c) can be done by disabling the feedback loop system. In this way, the tip scans the surface at a fixed voltage and tip-sample distance, and the local current intensity variations create the corresponding image. This imaging method, is often preferred for mapping the spectroscopic signal because but requires flat surface areas and a fine scanning plane adjustment to keep the tip height constant. Moreover, this method is used to resolve the internal structure of aromatic molecules with CO-functionalized tips as explained later in this chapter.

### 2.1.1 Tunneling Theory

To provide a basic description of the tunneling effect, we consider a non-relativistic single electron (without spin) interacting with a squared potential barrier in a one-dimensional space as depicted in Figure 2.2, considering that the free particle impinges on the barrier from the left. In classical physics, the system is described as:

$$\frac{p^2}{2m_e} + U_0 = E \tag{2.1}$$

where $U_0$ represents the potential barrier energy, and $p$, $m_e$ and $E$ the electron momentum, mass and energy, respectively. In the classical interpretation, if $E > U_0$ the electron will overcome the potential barrier having a non-zero momentum and, if $E < U_0$, the electron will not pass the potential barrier and it will be totally reflected. Nevertheless in quantum mechanics, when $E < U_0$ the electron has a finite probability to 'tunnel' through the potential barrier due to the quantum wavelike nature of particles. Thus the state of an electron is defined by a wavefunction that, for a particle with zero potential energy moving to the left in the $x$ axis, satisfies the one-dimensional time-independent Schrödinger equation:

$$-\frac{\hbar}{2m_e}\frac{\partial^2}{\partial x^2}\psi(x) = E\psi(x) \tag{2.2}$$

In equation 2.2, the term at the left represents the particle kinetic energy where $\hbar$ is the reduced Planck constant. The wavefunction $\psi(x)$ satisfying this equation is:

$$\psi_i(x) = A_i e^{-\kappa_i x}\ (with\, i = I, II, III) \tag{2.3}$$

where $A$ is the wavefunction amplitude and $\kappa_i$ is the wavevector in each region defined as:

$$\kappa_{I,III} = \sqrt{\frac{2m_e(E)}{\hbar^2}}\ and\, \kappa_{II} = \sqrt{\frac{2m_e(U_0 - E)}{\hbar^2}} \tag{2.4}$$

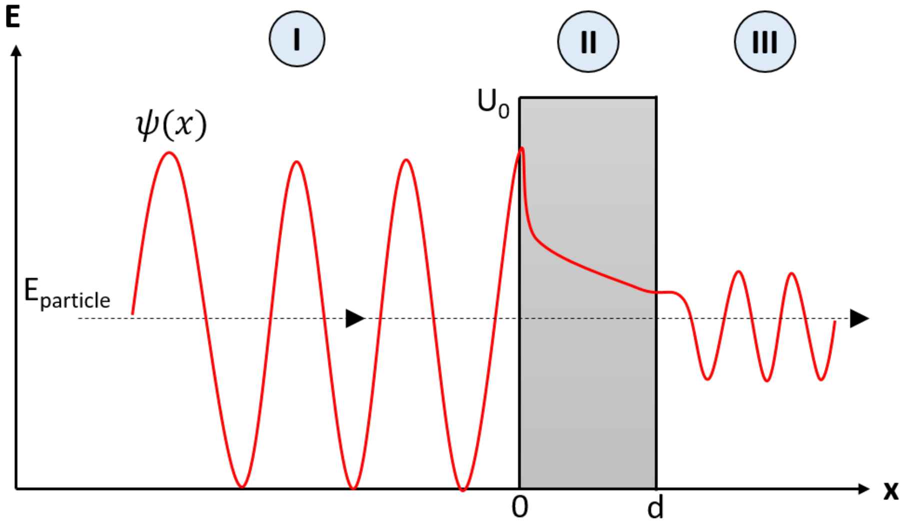

**Figure 2.2: Schematic one-dimensional model of wavefunction tunneling through a squared potential barrier.** Regions I, II and III correspond to the unidimensional space where the incident, tunneling and transmited wavefunction is represented. Reflected wavefunctions are suppressed in this scheme for an easier understanding of the main concepts inviolved in the tunneling effect.

Now it is worthy to mention that $|\psi_i^2(x)|$ is the probability density, and it is proportional to the probability of finding the particle in the $x + \partial x$ region. Then for $x > d$, the probability density of the transmitted wave (region III) with respect to that of the incident wave (region I) is proportional to the probability of electrons tunneling through the potential barrier, so-called *transmission coefficient* $T$:

$$T = \frac{|\psi(d)^2|}{|\psi(0)^2|} \propto e^{-2\kappa d} \tag{2.5}$$

Beyond this one dimensional model for a single electron system, the tunneling current is a complex process where many electrons are involved. In an attempt to model it, Bardeen established an early theory applied to the tunneling current of an STM,[176,177] taking into account the following assumptions:

i. Electron-electron correlations can be ignored.
ii. Tip and sample occupation probabilities are independent of each other and constant, despite of the tunneling process.
iii. Tip and sample are each electrochemically stable.

Based on Bardeen's considerations, Tersoff and Hamann developed a simplified model of an STM tunneling junction with a spherical tip in the limit of zero bias and zero temperature,[178,179] simplified in the following expression:

$$I_t = \propto \int_{E_F}^{E_F+eV} \rho_t(E_F)\rho_s(E_F - eV)T(E, eV, d)\partial E \tag{2.6}$$

Therefore, the tunneling current $I_t$ is proportional to the number of tip and sample electrons (density of states $\rho$) in the energy window $E_F + eV$, i.e. the number of electrons participating in the current, and their probability to tunnel $T$ (Equation 2.5). Importantly, this equation determines that the STM is not sensitive to the surface shape but to its electron density $\rho$ at each point, that is, its local density of states (LDOS). The voltage bias polarity, commonly applied on the sample, is a crucial aspect as it determines the relative energy alignment of tip and sample Fermi levels and so, which sample states participates in the tunneling current (see Figure 2.3). On the one hand, if $E_{F,tip} > E_F$,sample, electrons will tunnel from the tip to the unoccupied states of the sample. On the other hand, if $E_{F,tip} < E_{F,sample}$, electrons will tunnel from the occupied states of the sample to the tip. In the absence of voltage bias $eV$, the Fermi level of both tip and sample would be energetically aligned, resulting in no net electrical current flow.

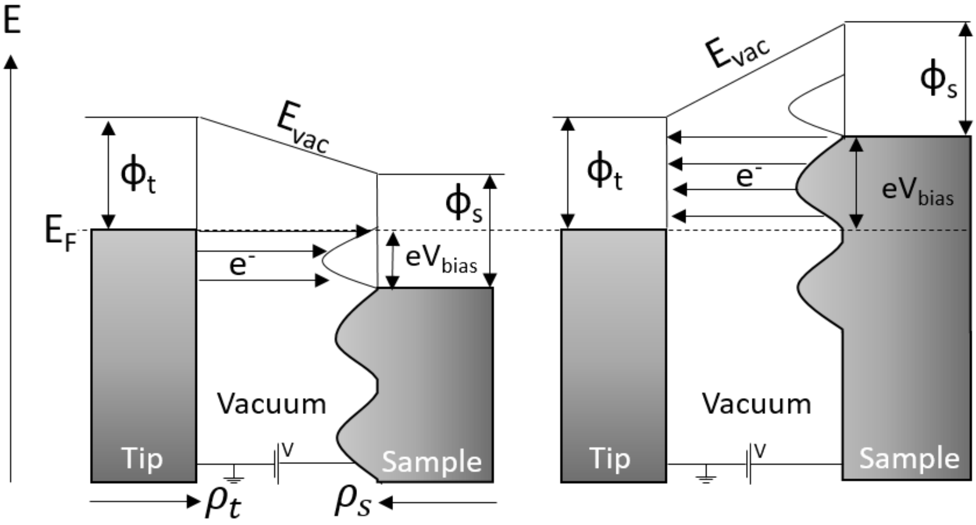

**Figure 2.3: Model illustrating the dependence of the probed sample states on the voltage polarity, being the voltage applied on the sample.**

### 2.1.2 Scanning Tunneling Spectroscopy

As stated in equation 2.6, the tunneling current depends on the applied bias voltage $eV$, the tunnelign current intesity $I_T$ (directly related to the transmission coefficient $T$), the tip-sample distance $d$ and the Fermi level energy of the system $E_F$. Scanning Tunneling Spectroscopy (STS) quantifies the relation between two of these parameters by keeping constant the third one. Therefore, we can establish three different modes to perform STS. However, hereinafter the discussion is focused on the spectroscopic procedure used in this thesis, that is, I-V curves. Within this method, the feedback loop is disabled and the current intensity is quantified as the voltage bias is swept at a fixed sample-distance, which is determined by the starting values of current intensity and voltage (known as set point parameters). Thus, the changes in the slope of the so measured differential conductance (dI/dV) gives information about the LDOS of the sample. This relation is justified by differentiating equation 2.6 with respect to the voltage, as follows:

$$
\begin{aligned}
\frac{dI}{dV} \propto\ & \rho_t(E_F)\,\rho_s(E_F+eV)\,T(E_F+eV,E_F,d)+\\
& +\rho_t(E_F-eV)\,\rho_s(E_F)\,T(E_F+eV,E_F,d)+\\
& +\int_{E_F}^{E_F+eV}\rho_t(E_F-eV)\,\rho_s(E)\,\frac{\partial T(e,eV,d)}{\partial V}+\\
& +\int_{E_F}^{E_F+eV}\rho_s(E)\,\frac{\partial\rho_t(E-eV)}{\partial V}\,T(E,eV,d)\,\partial E
\end{aligned}
\tag{2.7}
$$

Then, assuming that the density of states of the tip $\rho_t$ and the transmission coefficient $T$ are constant, we can simplify equation 2.7 as:

$$\frac{dI}{dV} \propto \rho_t(E_F)\,\rho_s(E_F+eV)T(E_F+eV,E_F,d)+ \\ +\rho_t(E_F-eV)\,\rho_s(E_F)\,T(E_F+eV,E_F,d) \tag{2.8}$$

Taking into account that in the first (second) term dominates at positive (negative) bias, we can assume that measuring the differential conductance (dI/dV) is proportional to the sample density of states $\rho_s$ at a given voltage bias $eV$.

The acquisition of the (dI/dV) signal is commonly obscured by the presence of a noisy environment. For this reason, a lock-in amplifier assists in the spectroscopic measurements with a phase-sensitive detection method. This method is based on adding a reference signal with a certain frequency and phase to the input signal, so that the lock-in instrument discern this reference from the noise in the output (see Figure 2.4).

Particularly in STS, the DC tunneling voltage $V_T$ is modulated by a small sinusoidal AC voltage of the form $V_{mod}\,\sin(\omega t)$. Thus, the modulated tunneling current $I_T$ can be described as a Taylor series:

$$I_T(V_T+V_{mod}\sin(\omega t)) \sim \\ \sim I(V_T)\frac{\partial I(V_T)}{\partial V}V_{mod}\sin(\omega t)+ \\ +\frac{1}{2}\frac{\partial^2 I(V_T)}{\partial V^2}V_{mod}^2\sin^2(\omega t)+... \tag{2.9}$$

The amplitude of the first harmonic frequency gives a proportional magnitude to that of the differential conductance signal. In addition, the amplitude of the second harmonic allows to probe vibrational spectroscopy[180] and and spin-flip dynamics[181] in single molecules by means of inelastic electron tunneling spectroscopy (IETS).

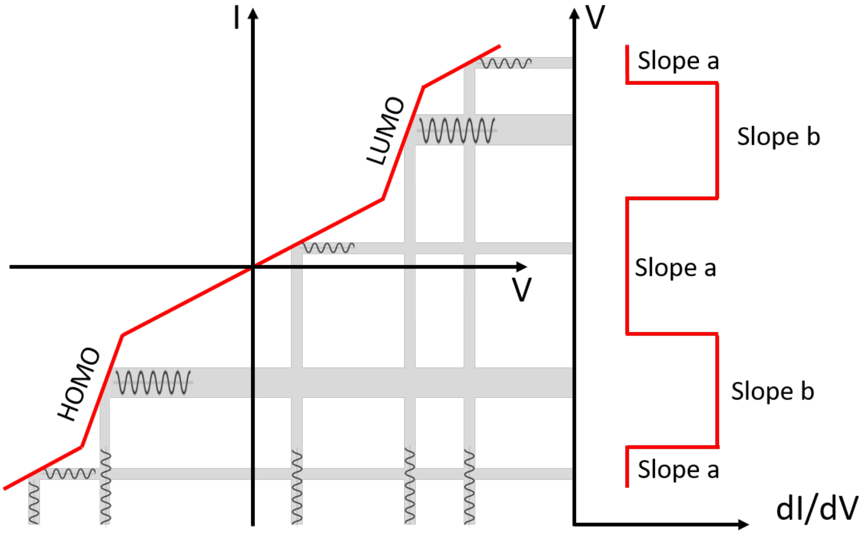

**Figure 2.4:** Schematic representation a lock-in amplifier working principle.

### 2.1.3 Bond-resolved imaging resolution by tip functionalization

Despite the powerful imaging resolution of SPM techniques, molecules on surfaces were commonly seen as featureless objects, and accessing their internal chemical structure remained elusive for many years. This limitation arises from the convolution between the molecule shape and LDOS near the Fermi level in common STM imaging, while deeper chemical structure information hides in lower-energy orbitals. Nowadays, this drawback is easily overcome by recent-developed imaging techniques based on the functionalization of the SPM probes apex with small atoms or molecules that significantly enhance the detected signal. In 2008, Temirov and coworkers reported an unprecedented sub-molecular resolution with a STM tip (Figure 2.5.a). Followed shortly after by Gross and coworkers, who reproduced this approach by means of non-contact AFM (nc-AFM) (Figure 2.5.b).[183] Some years later, Ho's group reported on very similar constrast via IETS-STM (Figure 2.5.c).[184] Lastly, the group of prof. Michael F. Crommie obtained bond-resolved contrast by means of STS,[144] employing a similar methodology to Temirov's but, in this latter example, the signal measured stem from the capacitance channel of the lock-in amplifier.

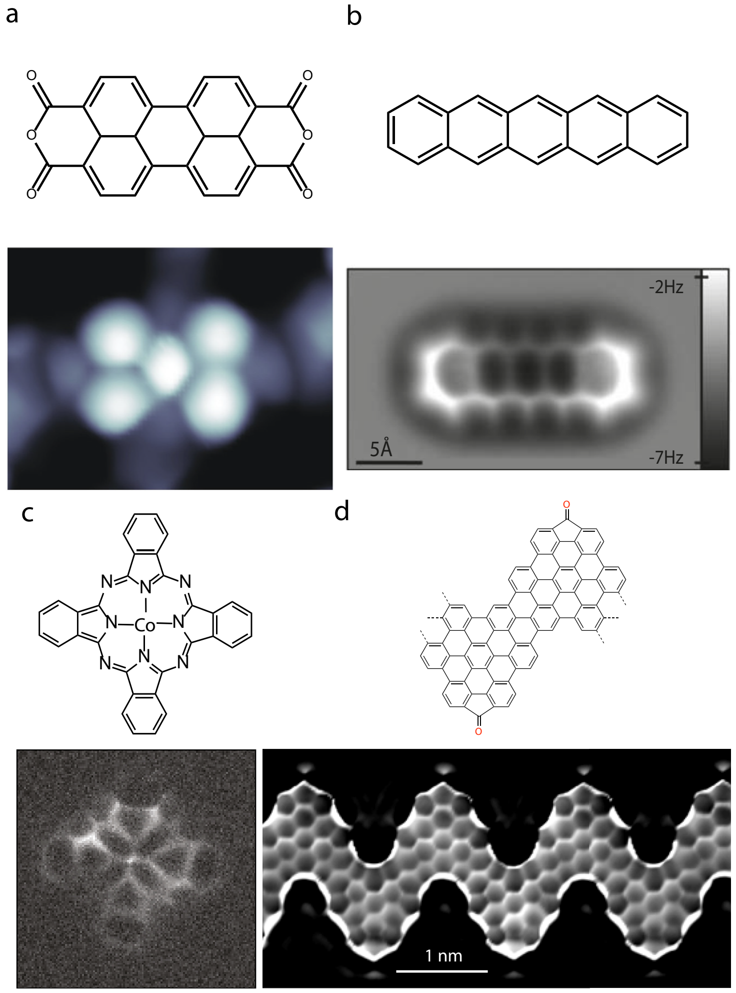

**Figure 2.5: Examples of different bond-resolved imaging techniques. (Top)** Molecular models and **(bottom)** corresponding bond-resolved images obtained by **(a)** STHM image of PTCDA (3,4,9,10-perylenetetracarboxylic-dianhydride) molecule with a $D_2$-terminated tip, from ref.[182] ; **(b)** nc-AFM image of a pentacene molecule with a CO-functionalized qPlus sensor, form ref.[183] ; **(c)** IETS-STM image of a cobalt phthalocyanine with a CO-decorated tip from ref.[184] and **(d)** STS map of oxygen-doped chevron GNR from ref.[144] In all the examples, the images were acquired in constant-height scanning mode.

In the case of the bond-resolved resolution attained by STM, the metallic tip was functionalized with a $H_2$ (or $D_2$) molecule below its condensation temperature, so-called Scanning Tunneling Hydrogen Microscopy (STHM).[182,185] These probes act as an electrical transducer turning the short-range Pauli repulsion into a varying signal of the junction conductance, later replicated with different probing atoms or molecules (CO, Xe, and $CH_4$).[186,187] The enhanced resolution observed in nc-AFM was achieved after picking up a CO molecule with a quartz tuning fork (qPlus sensor).[188–190] Then this sensor, operated in frequency modulation mode, is closely approached to the surface and scanned over a pentacene molecule. In close proximity, the Pauli repulsion modulates the sensor oscillation, providing frequency shift maps that reproduce the bonding structure as shown in Figure 2.5. This achievement initiated relevant progresses not only in the elucidation of the internal structure of molecular adsobates,[191–198] but also in the analysis of on-surface chemical reactions,[192,199–201] in the study of VdW interactions,[202–205] elemental identification by combination with Kelvin Probe Force Microscopy (KFPM) measurements[206] and even the conformational, adsoprtion and bond-order changes of molecules as a function their charge state.[207] Lastly, by means of IETS-STM with a CO-functionalized metallic tip, energy and intesity variations of a hindered translational vibration of the probing molecule, sensitive to the spatially varying potential energy landscale of the adsorbate, are detected though the inelastic electron tunneling channel.

The resemblance of the imaging contrasts achieved in every case underlines the presence of a common mechanism providing this enhanced resolution. The probe-particle (PP) model developed by Hapala et al. (Figure 2.6.a) gives a general explanation considering the lateral force exerted on the tip apex by an interplay between the repulsive Pauli and attractive Van der Waals (VdW) when the probe is brought into close proximity to the surface and low energy voltages (commonly of a few milivolts) are applied for scanning the surface in constant-height mode.[208] In these scanning conditions, the origin of this contrast relies on the predominance of Pauli repulsion over the long-range forces and the abrupted lateral relaxation of the probing molecule when scanning over points of maxima potential energy surface (see Figure 2.6.b,c) However, it has been shown that these sharped relaxation movements of the probing molecule do not only coincide strictly with the spatial location of chemical covalent bonds,[209,210] but also where hydrogen bonds,[211] halogen-halogen bonds,[212] or high electron density areas[213] are expected. These observations evidenced that Hapala's PP model can be improved by including the effect of electrostatic field of the probing molecule.[214–216]

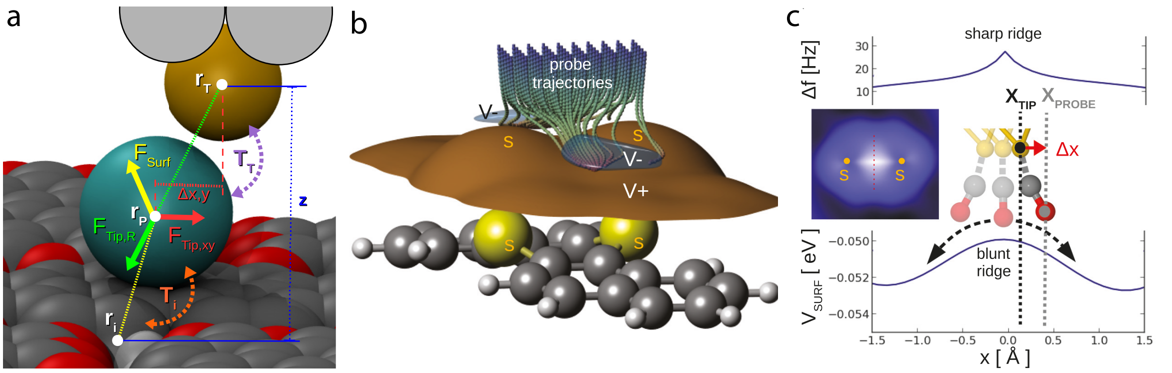

**Figure 2.6: Hapala's probe-particle (PP) model.** **(a)** Schematic representation of the PP model. **(b)** Schematic model of the probe molecule trajectories scanning over a DBTH (dibenzo[a,h]thianthrene) molecule and **(c)** frequency shift (top) and surface potential (bottom) along the central cross section of the molecule depicted in (a). Figures taken from ref.[208]

Overall, the chemical inertness of the probing molecule located at the tip apex is crucial since it drastically reduces the chemical reactivity with respect to the metallic tip (or cantilever) when it is brought in close proximity to the surface and , considering that the probing molecule is the structural softest part of the tip-sample system, the mechanical stress given at close tip-sample distances is mainly released through the lateral relaxation of the ending molecule, therefore neglecting adittional surface relaxation at least for planar adsorbates. In adittion, although the bond-resolved examples considered above are generally limited to temperature conditions of 4K or lower, near the absolute zero, recently some experiments achieved the same enhanced imaging resolution at liquid nitrogen temperature,[217,218] and even at room temperature.[219]

### 2.1.4 Common methodology to functionalize tips in this thesis

Bond-resolved images were acquired with tungsten tips functionalized with a CO molecule. Despite CO molecules can be picked up directly from the common metallic substrate employed in most of the experiments of this thesis, i.e. Au(111), the adsorption energy of this surface, although being relatively low compared with other metallic substrates,[220] yet is high enough to slow down a fast and effective usual tip-functionalization procedure. For this reason, monolayered NaCl islands were formed on Au(111) before dosing the chamber and hence the microscope and the sample with CO gas. Disregarding any kind of unexpected chemical bonding with the substrate, the adsorption of CO molecules on insulating layers like NaCl is known to be less energetic than those of metallic substrates,[221] therefore reducing the attractive forces required from the tip to pick the CO molecule up. To form the monolayered NaCl islands, high-purity powder of the salt were evaporated at 500-580°C from a commercial Knudsen cell onto the gold substrate held at RT. Then, the sample is slightly annealed up to ∼60°C to form flat, large, monolayered NaCl islands with smooth edges. Higher annealing after deposition results into smaller, multilayered islands while deposition with the substrate below RT and no post-annealing results into very small, rough-edged and holed monolayered islands where the CO picking gets more complicated.

Once the adequate NaCl islands are formed, the STM chambers are dosed with high-purity CO gas to pressures of $\sim 10\,\mathrm{E}^{-7}$ mbar, afterwhat the micrsocope shields are open for ≥1 minute. This commonly results in a relatively low surface coverage of CO molecules, suitable to avoid imaging difficulties due to an excess of adsorbates in the surface (or attached to the different nanostructures of interest) yet high enough for easily picking the CO molecules up since they are clearly discernable on top of the NaCl islands (see Figure 2.7.a). The prodecure to functionalize the tip is fairly simple. Scanning over the CO molecules adsorpted on the NaCl with a bias voltage of ∼1.0 eV and a tunneling current of ≥100 pA commonly results into an almost immediate picking up of the molecule, what is clearly obvious at the moment since the resolution instantly changes revealing a characterictic CO shape and the squared lattice of the of NaCl atoms (see Figure 2.7.b, below the blue arrow), evidencing the enhanced resolution from sharper tip.

### 2.1.5 Scanning Tunneling Microscopes employed in this thesis

The results shown in this thesis were mainly obtained by means of low-temperature STM (LT-STM), using two different equipments. Both of them consist of two chambers, i.e. the sample preparation chamber (with sputter gun, mass spectrometer, quartz micro balance (QMB), gas inlet valves and a load-lock chamber) and the microscope chamber (with liq. $N_2$ and $H_2$ cryostates able to reach ∼ 5K and the microscope head); four peumatic dumping legs, a complete UHV vacuum system (with scroll, turbo and ion pumps) and a manipulator. In the following sections, we give a brief description of the peculiarities of each microscope.

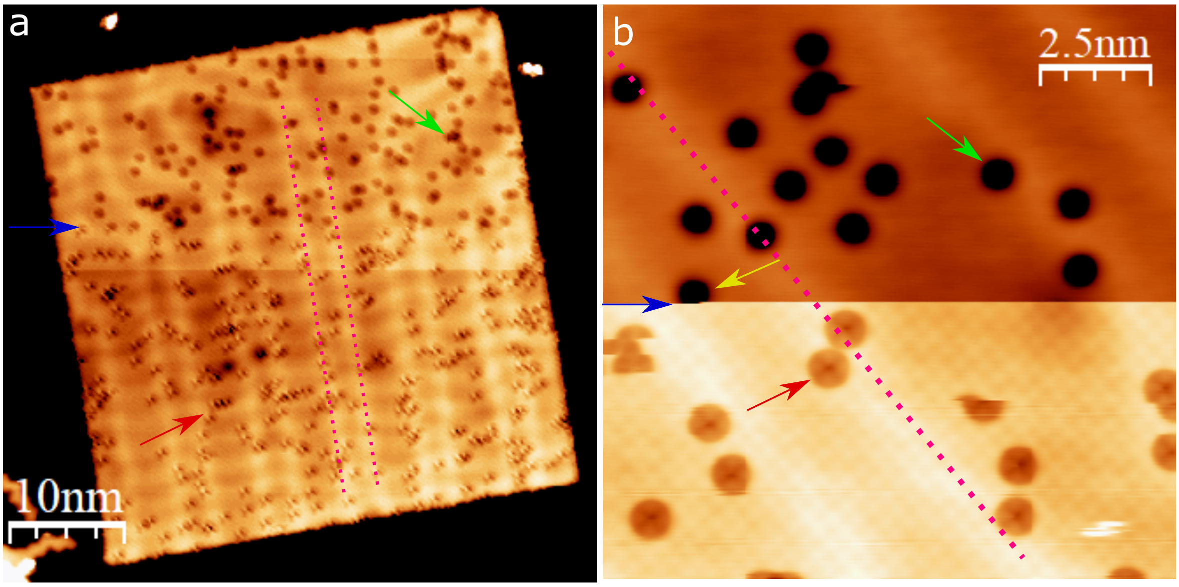

**Figure 2.7: Pickcing CO molecules with the STM tip from NaCl islands on Au(111). (a)** STM topographic image (52.1 nm x 50.8 nm, $V_s$= 0.4 V, $I_t$= 220 pA). **(b)** STM topographic image (12.5 nm$^2$, $V_s$= 1.1 V, $I_t$= 880 pA). It is clearly visible in the images the characteristic CO shape with a metallic tip (green arrows) and with a CO-functionalized tip (red arrows). The change in the constrast resolution (blue arrows) is instantly and clearly noticeable upon picking up a CO molecule with the tip (yellow arrow), as well as the squared lattice of the NaCl atoms in image (b) (below the blue arrow). Au(111) herringbone reconstruction is visible under the NaCl islands (pink pointed line).

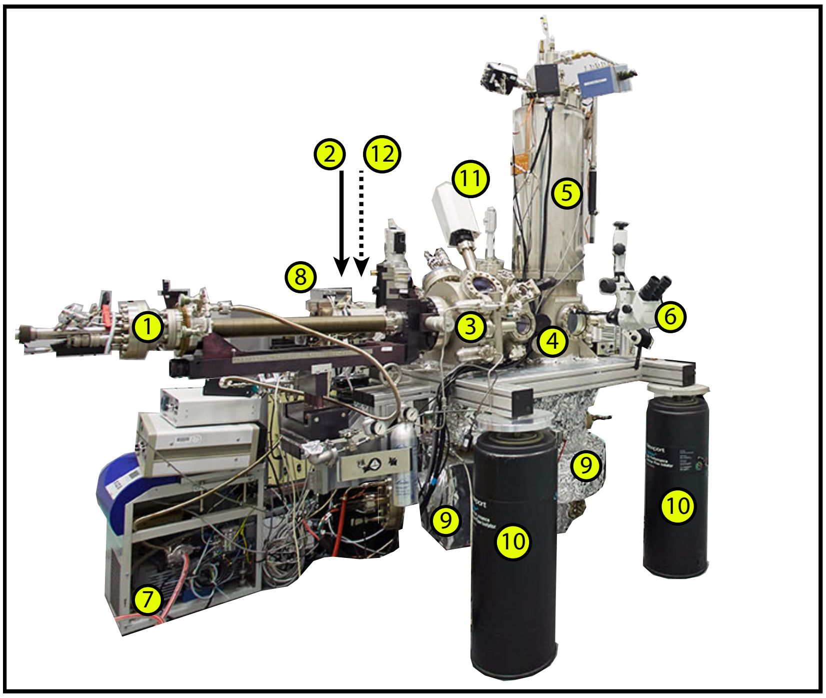

**Figure 2.8: Home-made 'Milano' STM equipment employed in this thesis.** Located at CIC nanoGUNE cooperative research center. Numbered circles correspond to (1) manipulator, (2) load-lock, (3) preparation and (4) microscope chambers; (5) cryostates, (6) optical microscope for placing the sample in the microscope head; (7) scroll, (8) turbo and (9) ion pumps; (10) pneumatic dumping legs, (11) mass spectrometer and (12) molecular evaporators (at the back, not visible from this perspective).

### ‘Milano’ STM

This LT-STM equipment (see Figure 2.8) was designed by Prof. Gerard Meyer and Dr. Sven Zöphel and built by Christian Roth and Dr. Mico Alemany in 2003. The microsocope head design is a Besocke ‘beetle’ type,$^{222}$ as shown in Figure 2.9. Apart from the common dumping system, the micrsocope is placed on top of a ∼35 tonnes concrete block isolated from the whole building by a different pneumatic damping system. The experimental measurements were carried out using a Createc DSP and HV amplifier units, and the spectroscopic measurements were acquired using an external Standford Research SR830 lock-in amplifier. In order to clean the substrates surfaces, sputtering is performed with neon gas in a closed environment once that certain neon pressure is reached.

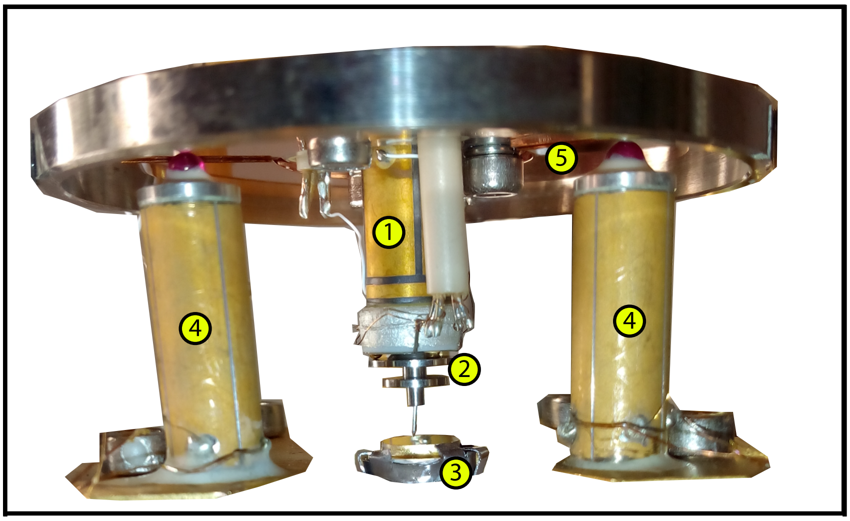

**Figure 2.9: Milano’s LT-STM ‘Beetle’ head photograph.** Numbered circles correspond to (1) piezo scanner, (2) STM tip, (3) Au(111) sample, (4) coarse piezos and (5) ramp.

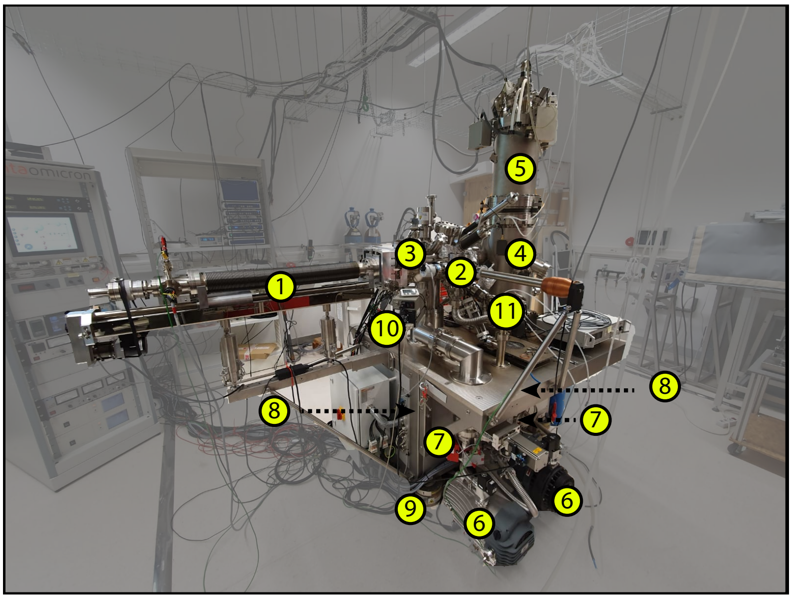

**Figure 2.10: Commercial ‘Apollo’ LT-STM equipment employed in this thesis.** Located at Materials Physics Center research center. Numbered circles correspond to (1) manipulator, (2) load-lock, (3) preparation and (4) microscope chambers; (5) cryostates; (6) scroll, (7) turbo and (8) ion pumps (inside the metallic ; (9) pneumatic dumping legs, (10) mass spectrometer and (11) molecular evaporators.

### ‘Apollo’ STM

‘Apollo’ is a Scienta-Omicron commercial LT-STM installed at the Physics Material Center (see Figure 2.10). The microsocope head design is ‘single-tube’ type.[223] The experimental measurements were carried out using a Nanonis control electronics and its integrated internal lock-in amplifier. In order to clean the substrates surfaces, sputtering is performed with argon gas in a closed environment once that certain neon pressure is reached.

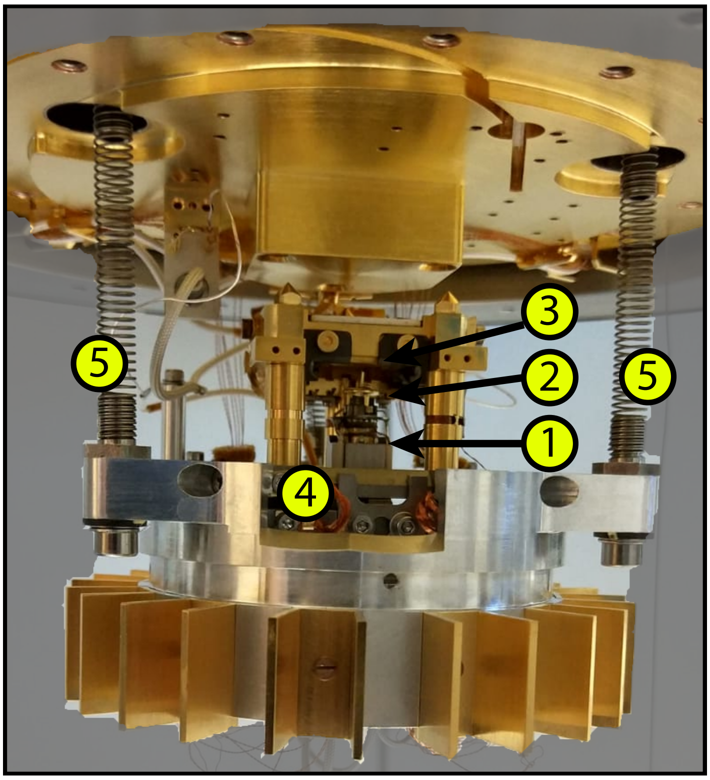

**Figure 2.11: Apollo’s LT-STM ‘single-tube’ head photograph.** Numbered circles correspond to (1) piezo scanner, (2) STM tip, (3) sample holder and (4) coarse scanner and (5) dumping springs.

### Sample preparation and ultra high vacuum conditions

The common sample preparation involves different stages. First of all, the surface of the substrates are cleaned down to the atomic scale by applying different cycles of sputtering and annealing on it. In the former process, a beam of acelerated ions is directed towards the surface so that the first surface layers get ‘bombarded’, removing all the impurities (and lots of metallic atoms of the substrate) fromt he very first layers of the surface. This result into a high irregular surface topography which is flaten afterwards by thermal annealing to temperatures close to the melting point of the metallic or alloyed substrate. One might repeat these cycles several times until reaching a surface cleaness suitable for the experiment.

Simultaneously, molecules are placed in a Knudsen cell which, together with other different structural and electrical components, compose a so-called molecular evaporator. Once the precursors are loaded in the evaporator, this is attached to the preparation chamber and got into UHV vacuum conditions. The Knudsen cell is surrounded by a thin metallic wire and connect to some external electrical connections so one can apply an electrical current through the connection. Therefore, the electrical resistance heat the metallic wire and this heat is transmitted to the molecules and monitored with the help of a temperature diode. As some temperature related mainly with the molecular weigth of the precursor, it start to sublimate (not evaporate, since there is no solvent in UHV conditions). Hence, at this point, a molecular flow composed of sublimated molecules start to travel through the preparation with a certain direction ruled by the relative position of the Kundsen cell hole with respect to the chamber structure. The rate of this molecular flow, this is, the number of molecules (in weigth) por unit of time crossing the inside of the chamber in that direction can be monitored with a quartz microbalance (QMB), which is an instrument sensitive to the mass deposited in a gold rod detector. This rate known, one can control the number of molecules deposited on a certain surface by simply controlling the deposition time. The substrate surface is then oriented to the molecular flow. Once that the desired amount of precursors are placed on top of the surface (or other molecules which previously reached the surface), the sample (precursors and substrate) can be heated by electrical resistance or e-beam heating, and the temperature can be monitored by another temperature diode or (infrared instruments ocassionally). This heating provoke (or not) the different surface-assited reactions as a function of the sample heating.

All the samples considered in this thesis were prepared under ultra high vacuum conditions. These pressure conditions (pressures below $1.0^{-9}$mbar) are obtained through the complementary use vacuum pumps, namely scroll, turbo and ion pumps. These conditions are required since the analysis of surfaces down to the atomic scale are extremely sensitive to the minimum elemental contamination so needing of atomically clean surfaces to avoid the presence of undesired adsorbates or byproducts that could hamper the study of the chemical and physica phenomena observed in an STM experiment.

## 2.2 Photoemission spectroscopy

Photoemission spectroscopy (PES) has been established as one of the most relevant techniques to study the collective behaviour of electrons in solids, liquids or gases, this is, to study the electronic structure of different materials. The first experiments revealing the interaction of light with solids, were performed by Heinrich Hertz, in 1887,[224] and Wilhem Haawachs, in 1888.[225] Based on the use of the photoelectric effect, PES relies on the analysis the electrons emitted by a material upon being irradiated with light, making feasible to understand the fundamental physics laws dominating the behaviour of bound electrons, related to the chemistry of materials and therefore having notable applications in different areas fields such as surface chemistry and materials science.

Some examples of this familiy are X-ray photoemission spectroscopy (XPS) and angle-resolved photoemission spectroscopy (ARPES). The analysis of ejected electrons from the sample offers a way to experimentlly probe the properties of matter. Depending on the ionization surce employed for probing the samples, we can distinguish between X-ray and/or Ultraviolet PES for probing the filled electronic states. In the following sections we will focus on the case where filled bands are probed by means of XPS and ARPES.

### 2.2.1 Photoelectric effect and three step model

The photoelectric effect (see Figure 2.13.a) was initially discovered by Hertz in 1887,[224] and later explained by Einstein,[227] and explains the mechanism by which a metal emits electrons when light shines on it. These emitted electrons are so called photoelectrons. The process can be explained using the three step model shown in Figure 2.13.b in which, firstly, an electron is optically excited, secondly, it travels to the crystal surface. Along its path, electrons may suffer scattering events with other electrons, phonosn, or plasmons and lose their initial energy and momentum information. The distance travelled by an electron before being scattered is refered as the mean free path (see Figure 2.12), and depends on the initial energy of the electrons. The core electrons (valence electrons) have a characteristic kinetic energy values

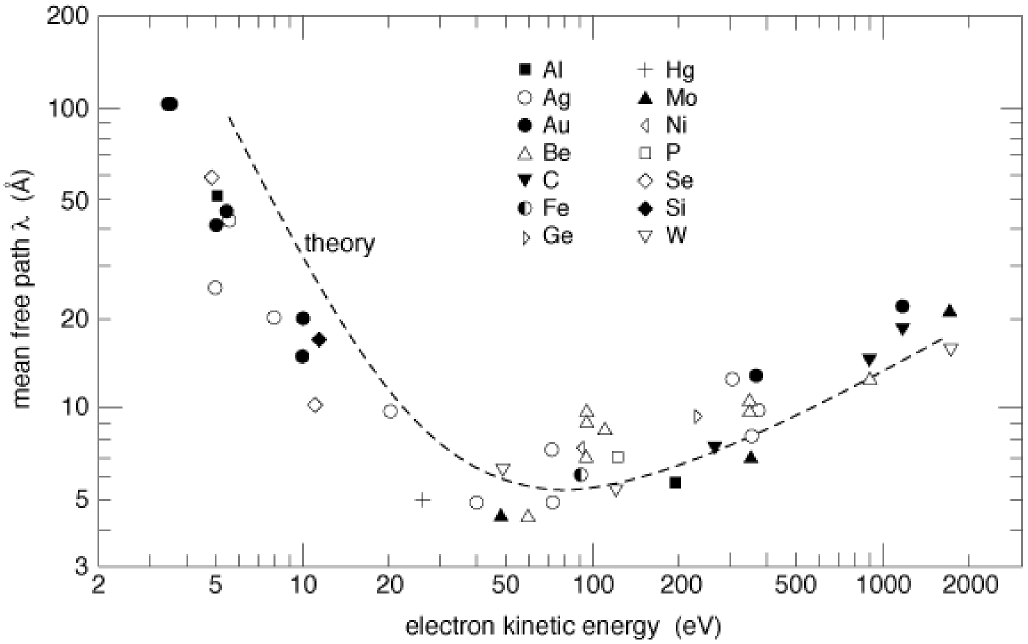

**Figure 2.12: Electron mean free path in solids as a function of the kinetic energy.** The dots are experimental measurements while the dashed curve is the theoretical calculation. Copied from ref.[226]

of ~ 100-500 eV (0 - 50 eV) and a mean free path of ~ 0-10 Å. This, indeed, is why PES is a surface sensitive technique , since the electrons originated in the very first layers have less probability of being scattered and more probabiltiy of reaching the surface. In the last part of the three step model, electrons overcome the surface work function ($\phi$) and are ejected to the vacuum with a certain kineti energy ($E_k$). The kinetic energy of the ejected electrons can be measured with an electron energy analyze, as well as their dependence on the emission angle.

Consequently, from the kinetic energy ($E_k$) of the outgoing electrons and, knowing the Fermi level energy $E_F$ of our system, we can calculate the electron binding energy ($E_b$). Moreover, the momentum of the electrons inside the solid can be determined through the energy of the ejected electrons and the emission angle.

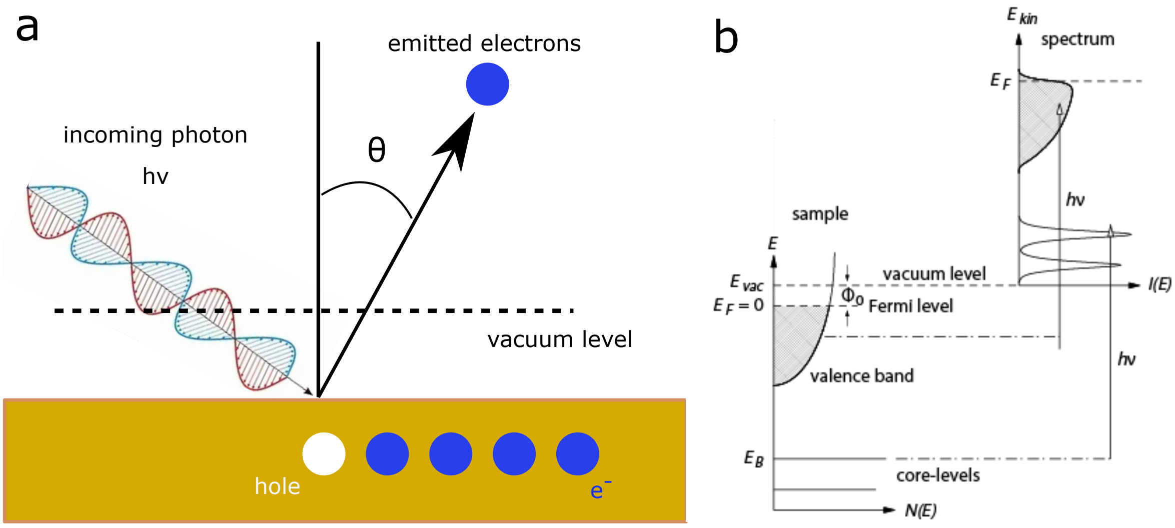

**Figure 2.13: Photoemission models.** **(a)** Photoelectric effect and **(b)** three step model describing the path followed by the photo ejected electron until it scapes from the surface. Copied from ref.[228]

## 2.2.2 X-Ray Photoemission Spectrocopy (XPS)

The photoemission of electrons in CLs is measured with low-energy X-rays sources with typical energies of ~100-1500 eV. The binding energy of CLs represent chemical fingerprints of the elements and accessing these values is what defines the well-known elemental sensitivity of X-ray photoemission spectroscopy (XPS). This technqiue can be used for studying the chemical structure of molecules and in-situ follow chemical reactions. Since the BE of an electron depends on the nucleus potential well, in an XPS spectra, electrons of different atomic elements. Moreover, XPS is also sensitive to the electronic environment around the atom or molecule, revealed again as changes in the measured BE.

### Temperature-dependent X-ray photoemission spectroscopy‘(TD-XPS)

Temperature-dependent X-ray photoemission spectroscop (TD-XPS) is a powerful tool for studying in-situ chemical reactions on surfaces. The experiment is based on tracking the teperature evolution of a certain CL signal, normally elements involved in the chemical reaction. Taking into account that XPS can address the bonding nature of elements and considering that on a chemical reaction, bonds are either formed or destroyed, the CL temperature evolution of certain elements are the fingerprints of chemical reactions.

### 2.2.3 Angle-Resolved PhotoEmission Spectrocopy (ARPES)

The geometry of an ARPES experiment is shown in Figure 2.14. The ionization sources commonly employed are Ultraviolet. ARPES equipments measure the momentum and energy of the electrons in the VBs of a crystal, emitted during the photoelectric proccess, what is possible due to the energy and momentum conservation laws[229] by collecting the photoelectrons with an electron kinetic energy $E_k$ for a given emission angle. Thus, the wave vector momentum $k = p/\hbar$ of the photoelectrons in vacuum is also completely determined: its modulus is given by $k = \sqrt{2mE_K}/\hbar$ and its component parallel ($k_{\|} = k_x + k_y$) and perpendicular ($k_{\perp} = k \ \|$) to the sample surface are obtained in terms of the polar $\vartheta$ and azimuthal $\varphi$ emission angles defined in the experiment.

The $k$ components are defined in terms of the previous parameters by the following equations:

$$k_x = \frac{1}{\hbar}\sqrt{2\,m\,E_k}, sin\vartheta\, cos\,\varphi \tag{2.10}$$

$$k_y = \frac{1}{\hbar}\sqrt{2\,m\,E_k}\, sin\vartheta\, sin\,\varphi \tag{2.11}$$

$$k_z = \frac{1}{\hbar}\sqrt{2\,m\,E_k}\, sin\vartheta \tag{2.12}$$

Thus, although an ARPES equipment needs of ordered sample to get a coherent signal, it represent a striking relevant instrument in a surface science lab since it is capable of measuring the dispersion of electrons in filled bands, a key parameter to define the charge carrier mobility in crystalline materials.

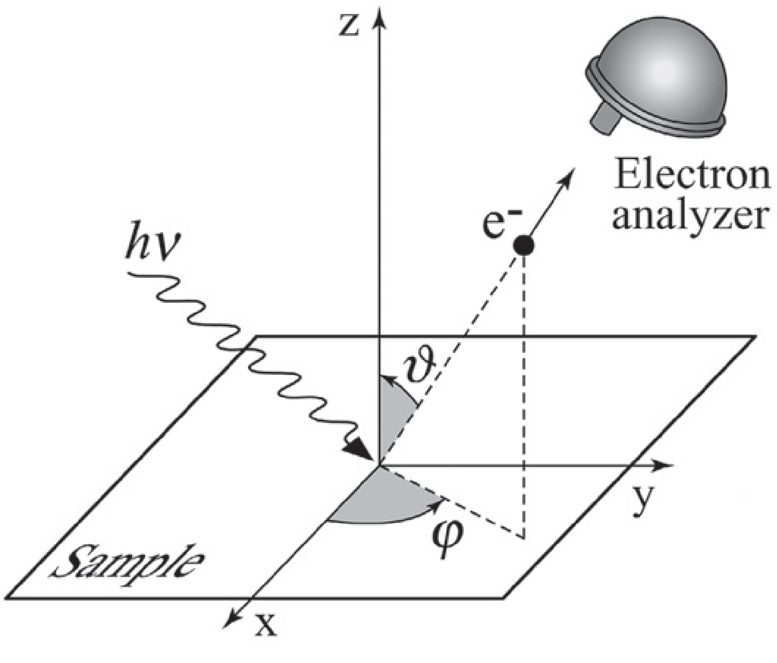

**Figure 2.14: Geometry of an ARPES experiment.** Copied from ref.[229]

# Chapter 3

# Graphene Nanoribbons’ Electronic Structure

Different theoretical approaches have been employed to define the electronic properties of graphene and graphene nanoribbons from a theoretical point of view, from qualitative models like Clar‘s theory,[230] to quantitative ones like density functional theory (DFT) or thight-binding (TB) approaches.[231] In this chapter, with the focus on the TBl approximation and, considering straigth planar GNRs with edges pasivated by hydrogen atoms, we give a detailed explanation of the theoretical conception of these nanostructures.

## 3.1 Graphene's electronic structure

A fundamental knowledge on graphene's electronic structure is a necessary step as it is the basis for understanding the electronic properties of derived allotropes such as graphene nanoribbons. The hexagonal crystallographic structure of graphene can be rationalized as two hexagonal sublattices A and B with a basis of two atoms per unit cell as shown in Figure 3.1.a. This lattice is described by the primitive vectors $\boldsymbol{a_1}$ and $\boldsymbol{a_2}$ as follows:

$$\vec{a_1} = \frac{a}{2}(3, \sqrt{3}) \qquad \vec{a_2} = \frac{a}{2}(3, -\sqrt{3}) \tag{3.1}$$

where $a$ represent the distance between carbon atoms with an approximate value of 1.42 Å.[232] The corresponding Brillouin zone is represented in Figure 3.1b, where the reciprocal vectors $\boldsymbol{a_1^*}$ and $\boldsymbol{a_2^*}$ are given by:

$$\vec{a_1^*} = \frac{2\pi}{3a}(1, \sqrt{3}) \qquad \vec{a_2^*} = \frac{2\pi}{3a}(1, -\sqrt{3}) \tag{3.2}$$

Then, the three nearest-neighbor vectors in real space that defines the translation between the two triangular sublattices are described as:

$$\vec{\delta_1} = \frac{a}{2}(1, \sqrt{3}) \qquad \vec{\delta_2} = \frac{a}{2}(1, -\sqrt{3}) \qquad \vec{\delta_3} = a(-1, 0) \tag{3.3}$$

Graphene electronic structure can be described from either a qualitative, as Clar's theory, or a quantitative, as the tight binding (TB) model, theoretical points of view. For the case of graphene, the TB model represents a simple approach to describe its electronic structure,[27] where the difficulty of the problem relies on finding a optimal representation for a basis of pre-defined orbitals localized at atomic *positions.* We can describe the Hamiltonian matrix element of an orbital $m$ at position $i$ and of an orbital $n$ at position $j$ by the following expression:

$$H_{im,j} = \langle \phi_{im} | \hat{H} | \phi_{jn} \rangle = \langle \phi_{im} | -\hbar^2 \nabla^2 / 2m + V(\mathbf{r}) | \phi_{jn} \rangle \tag{3.4}$$

Each carbon atom has a delocalized $\pi$-electron, therefore we can describe each carbon atom by a single $2p_z$ orbital. Moreover, considering just the interaction between nearest neighbors carbon atoms as a first aproximation, we can drop the $m, n$ indexes and set the $\hat{H}_{i,i}$ as a constant shift of energy, since it is identical for all positions. The hopping integral $H_{i,j} =: -t$

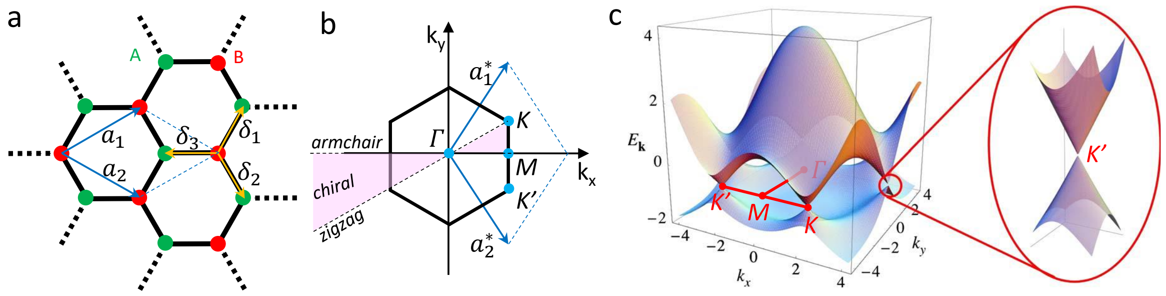

**Figure 3.1: (a)** Lattice structure of graphene including its primitive $a_i$ (blue arrows) and translation $\delta_i$ vectors (yellow arrows). **(b)** Corresponding Brillouin zone in the reciprocal lattice including reciprocal vectors $a_i{}^*$ (blue arrows). **(c)** Electronic band structure calculated using an orthogonal tight-binding model and considering only nearest neighbor atom interactions. The inset depict the conical energy band dispersion of one Dirac point near the Fermi energy (adapted from[8]).

between two neighboring $i, j$ positions is the only non-zero matrix element. Finally, $t$ is commonly considered as a parameter adjusted to fit the resulting band structure when compared with experimental results[233] or ab-initio calculations,[234] with common values between 2.5 and 3.0 eV.[235]

Hence, in second quantization, the corresponding Hamiltonian is described by the following equation:

$$\hat{H} = -t \sum_{\langle ij \rangle} \hat{c}_j^\dagger \hat{c}_i + \hat{c}_i^\dagger \hat{c}_j \tag{3.5}$$

being $\hat{c}_j^\dagger \hat{c}_i$ are the electron creation and annihilation operators at positions $i$ and $j$.
The generalized eigenvalues for solving the TB model are:

$$Hv = \varepsilon S v \tag{3.6}$$

$$S_{ij} = \langle \phi_i | \phi_j \rangle \tag{3.7}$$

for the eigenenergies $\epsilon_\alpha$ with the following corresponding eigenvectors:

$$\psi_\alpha(\mathbf{r}) = \sum_j \upsilon_\alpha \phi_j(\mathbf{r}) \tag{3.8}$$

Nevertheless, the overlap $S_{ij}$ between $2p_z$ orbitals is found to be <0.1 in graphene,[236] and so it can be neglected, then being $t$ as the only parameter in the model.
Using an orthogonal tight-binding model considering that any electron can hop to both sublattices, we obtain graphene's band structure (Figure 3.1c) where energy bands have the following form:

$$\begin{gathered} E_\pm(\boldsymbol{k} = \pm t\sqrt{3 + f(\boldsymbol{k})} - t' f(\boldsymbol{k}) \\ f(\boldsymbol{k}) = 2\cos\left(\sqrt{3}k_y a\right) + 4\cos\left(\frac{\sqrt{3}}{2}k_y a\right)\cos\left(\frac{3}{2}k_x a\right) \end{gathered} \tag{3.9}$$

being $\boldsymbol{k}$ the electron wavevector and $t\,(t')$ the (next) nearest neighbor hopping terms with an approximated value of 2.8 eV[8] and 0.1 eV,[90] respectively. The plus sign refers to the upper ($\pi$) and the lower ($\pi^*$) bands, as explained hereafter.

Carbon atoms in graphene display an $sp^2$ hybridization where each atom locate three strongly-bound electrons in the $\sigma$-bonds and one electron in a $p_z$-like orbital creating an extended conjugated $\pi$-band of delocalized electrons. This $\pi$-band constitutes the valence band below Fermi energy (Figure 3.1c), while the conduction band above Fermi energy stems from the non-occupied $\pi^*$-bands. Both bands converge at the high symmetry points $K$ and $K'$ (Figure 3.1c inset). The positions of these points in momentum space are given by:

$$K = (\frac{2\pi}{3a}, \frac{2\pi}{3\sqrt{3}a}) \qquad K' = (\frac{2\pi}{3a}, -\frac{2\pi}{3\sqrt{3}a}) \tag{3.10}$$

Expanding the full band structure from Equation 3.4 close to $\boldsymbol{K}$ (and $\boldsymbol{K'}$), as $\boldsymbol{k} = \boldsymbol{K} + \boldsymbol{q}$, being $|\boldsymbol{q}| \ll |\boldsymbol{K}|$, we obtain the dispersion at these points:

$$E_\pm(\boldsymbol{q}) \approx \upsilon_F |\boldsymbol{q}| + O[(\frac{q}{K})^2] \tag{3.11}$$

being $q$ the momentum measured relatively to the $K$ and $K'$ points and $\upsilon_F$ the Fermi velocity. A relevant consequence from the former equation is that the Fermi velocity $\upsilon_F$ is independent of the carrier mass or momentum, thus we can consider graphene electrons as massless Dirac fermions and hence, $K$ and $K'$ points are so-called Dirac points.

Graphene nanoribbons' electronic properties stem from those of graphene. Yet, as commented in chapter 1 (section 1.3), the width confinement and the presence of finite edges may lead to pretty different properties of the states near the Fermi level in a narrow graphene sheet.[50,237] In the following sections, considering planar straight ribbons with edges passivated by hydrogen atoms and no structural defects, we describe the properties of GNRs according to their edge orientation from a theoretical point of view.

## 3.2 Armchair graphene nanoribbons

In the case of aGNRs, the band structure can be calculated considering the boundary conditions imposed by the edges. As depicted in Figure 1.8 (section 1.5), aGNRs width is defined by the carbon dimer lines $N_A$, where each of the carbon atoms on these dimer lines belong to the two different sublattices $A$ and $B$ of graphene. At $N = 0$ and $N = N + 1$, missing carbon atoms are replaced by hydrogen atoms. Here, we consider the unit cell size $a = 1$ as a matter of simplicity, and an infinite ribbon along its growing axis. Therefore, the electronic wavefunctions of each sublattice can be described as the following general form:

$$\psi_{m,A} = Ae^{ik_\perp m} + Be^{-ik_\perp m} \tag{3.12}$$

$$\psi_{m,B} = Ce^{ik_\perp m} + De^{-ik_\perp m} \tag{3.13}$$

being $m, A(B)$ the $m^th$ position in the $A(B)$ sublattice, $k_\perp$ the wavenumber in the perpendicular direction to the ribbon growing axis, and $A, B, C, D$ arbitatry coefficients. Since the carbon rows are missing for $N = 0$ and $N = N + 1$ in both sublattices, we can stablish the next boundary conditions:

$$\psi_{0,A} = \psi_{0,B} = \psi_{N+1,A} = \psi_{N+1,B} = 0 \tag{3.14}$$

what leads to:

$$\psi_{0,A} = A + B = 0 \Rightarrow A = -B \tag{3.15}$$

$$\psi_{N+1,A} = Ae^{ik_\perp N+1} + Be^{-ik_\perp N+1} = 0 \quad if \quad \eta = e^{ik_\perp (N+1)} \Rightarrow A\eta = -B\eta^-1 \tag{3.16}$$

From the previous equations we can extract the following relation:

$$\eta^2 = 1 = e^{2ik_\perp (N+1)} \tag{3.17}$$

leadingto the discrete $k_\perp$ condition:

$$k_\perp = \frac{r}{N+1}\pi \quad for \quad r = 1, 2, ..., N \tag{3.18}$$

what, defining the unit cell size $a = 1$, can be redefined as:

$$k_\perp = \frac{2\pi}{a/\sqrt{3}} \frac{r}{N+1} \quad for \quad r = 1, 2, ..., N \tag{3.19}$$

This relation describes the possible electron momenta across the graphene nanoribbon. aGNRs band structure result from a set of discrete equidistant planes cutting the reciprocal space of graphene in certain $k_\perp$ directions as shown in Figure 3.2 (continuous lines). For this reason, whenever $N = 3p+2$ (being $p$ and integer number), the resulting aGNR will present a gapless band structure because their corresponding plane cuts pass across graphene's Dirac points.

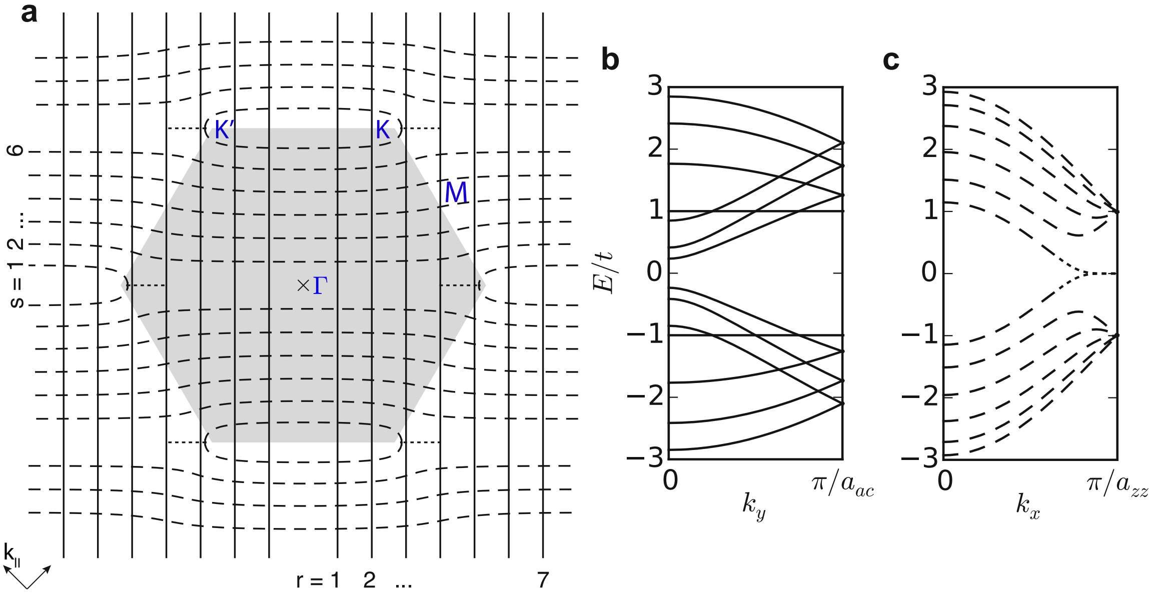

**Figure 3.2: Brillouin zone for aGNRs and zGNRs. (a)** Brillouin zone of graphene with cutting lines for 7-aGNR (continuous lines) and 6-zGNR (dasehd lines). **(b,c)** Band structures for (b) 7-aGNR and (c) 6-zGNR, plotted in their respective first Brollouin zones. Copied from ref.[231]

aGNRs' band structure can be also define from the analytical solution of the eigenenergies by solving the first neighbor TB Hamiltonian:[237]

$$E_s = \sqrt{1 + 2\epsilon_p cos(\frac{k_\parallel}{2}) + \epsilon_p^2} \tag{3.20}$$

being $s = 1$ and $s = -1$, the corresponding conductance and valence bands, respectively, and $\epsilon_p = 2\,cos\,k_\perp$. $E_s = 0$ at $k_\perp$ whenever $N = 3p + 2$, providing the aGNRs with a semimetallic band structure. We can infer from Figure 3.2b,c as well that aGNRs' bandgap is defined by the cutting plane closest to the $K_+$ points. Therefore, an increasing ribbon's width will make the bandgp decrease, as Equation 3.19 stablishes. In adittion, these bandgaps can be defined from a TB approximation as follows:[14]

$$E^{TB}_{g,3p} = t[4cos\frac{p\pi}{3p+1} - 2] \tag{3.21}$$

$$E^{TB}_{g,3p+1} = t[2 - 4cos\frac{(p+1)\pi}{3p+2}] \tag{3.22}$$

$$E^{TB}_{g,3p+2} = 0 \tag{3.23}$$

As clearly shown in Figure 3.3, for $\sigma = 0.12$, aGNRs band structures splits into three families with different bandgap-width scaling rules. We note here that the local density approximation (LDA) simplifies the exchange-correlation potential, which plays a relevant role in nanostructures due to the stronger electron-electron correlations, and hence the resulting bandgap values are smaller than those obtained experimentally. Nevertheless, when using Green's Wavefunctions (GW), based on many-body perturbation theory, calculations provide more precise results with respect to experimental values. Finally, first principles calculations of free-standing GNRs yield larger bandgap values than experimental resutls because the surface screening is not considered.[133, 141, 238]

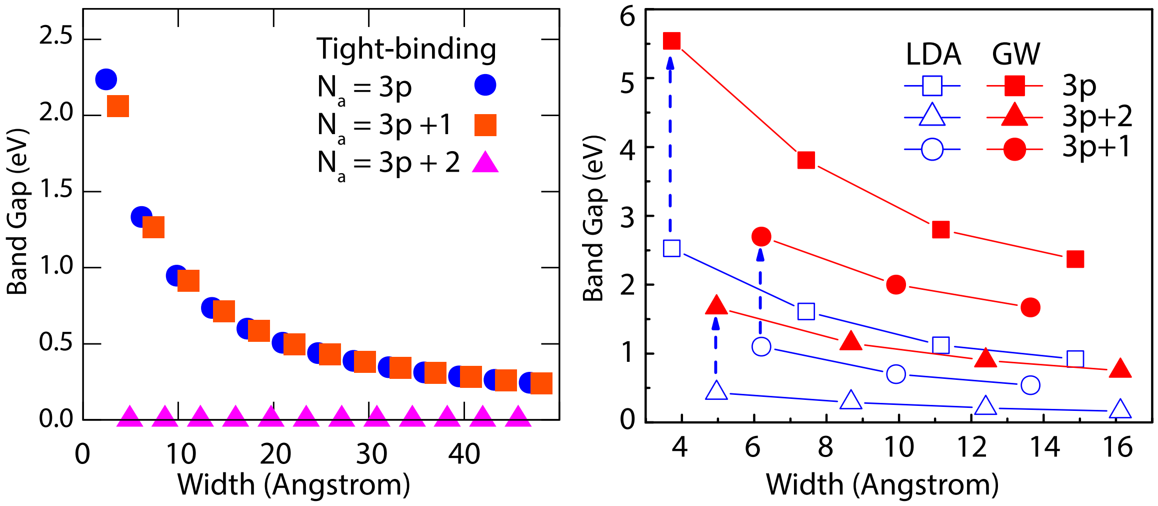

**Figure 3.3: aGNRs' bandgap dependence on the width** from **(a)** tight-binding (TB), **(b,c)** and first-principles calculations including (b) local-density approximation (LDA) and (c) Green's Wavefunctions (GW).The three different aGNRs families ($N = 3p$, $N = 3p + 1$ and $N = 3p + 2$) are represented by different symbols and colors. Adapted from ref.[14,15]

## 3.3 Zigzag Graphene Nanoribbons

In the case of zGNRs' electronic structure, the scenario is not that simple. As seen in Figure 3.1a, hydrogen atoms at the edges are located at the two different graphene's sublattices $A$ and $B$. Seting a GNR unit cell as $a = 1$, the boundary conditions for the generic wavefunctions are the following:

$$\psi_{m,A} = Ae^{ik_\perp m} + Be^{-ik_\perp m} \tag{3.24}$$

$$\psi_{m,B} = Ce^{ik_\perp m} + De^{-ik_\perp m} \tag{3.25}$$

Due to the particular arrangement of the hydrogen atoms in graphene's sublattice in zGNRs, $\psi_{0,B} = \psi_{N+1,A} = 0$, and therefore:

$$\psi_{0,B} = C + D \Rightarrow C = -D \tag{3.26}$$

$$\psi_{N+1,A} = Ae^{ik_\perp(N+1)} + Be^{-ik_\perp(N+1)} = 0 \quad if \quad \eta = e^{ik_\perp(N+1)} \Rightarrow A\eta = -B\eta^{-1} \tag{3.27}$$

Therefore, we can not extract discrete values of $k_\perp$ from the boundary conditions, as in the case of aGNRs. Nevertheless, we can stablish the following condition:

$$sin[k_\perp N] + g_k sin[k_\perp(N+1)] = 0 \quad with \quad g_k = 2cos(k_\parallel/2) \tag{3.28}$$

implying that in this case, $k_\perp$ depends on the nanoribbon width and the wavenumber along the zGNR growth axis $k_\parallel$, which causes $k_\perp$ cuts on graphene's BZ not to be straight but curved lines as shown in Figure 3.2.a. Therefore, in contrast to aGNRs, zGNRs bands are degenerated at $k_\parallel = \pi$ due to the two-dimensional projection of graphene's band structure. However, valence and conduction bands are also degenerated beyond some critical value of $k_\parallel$, termed as $k_c$, and defined as follows:

$$k_c = \pm 2\, arccos\left(\frac{1}{2 + 2/N}\right) \tag{3.29}$$

Valence and conduction bands join at $k_c$ values between $0 < k_\parallel < 4\pi/3$ (or $0 < k_\parallel < \pi$, if we consider band folding), denoted as $K$ and $K'$ in Figure 3.1b,c and Figure 3.2. These two values

($K_Lc$ and $K_Rc$) define a region where valence and conduction bands evolve into localized states because in these regions of the reciprocal space, the band structure does not cut graphene's BZ and therefore, two states emerge since the valence and conduction bands can no longer be defined as $k_\perp$ solutions of Equation 3.29. These new states are strongly localized at the longitudinal zigzag-like edges of the ribbon for $k_c < k_\| < \pi$,[49,237] and their wavefunctions have only amplitude in one of the two graphene's sublattices of the zGNR structure. The origin of these edge states relies on the two $k_\perp$ imaginary solution for Equation 3.29 at $k_\perp = 0$ and $k_\perp = \pi$, defined in some particular graphene's BZ regions as:

$$k_\perp = \begin{cases} \pi \pm i\,\zeta, & k_{Lc} < |k_\|| < \pi \\ 0 \pm i\,\zeta, & \pi < |k_\|| < k_{Rc} \end{cases} \tag{3.30}$$

leading to to wavefunctions for the egde states decaying to the inner sites of the zGNR structure.[49,237] These edge states present a strong DOS located at Fermi level what explains their magnetic polarization. We can understand this phenomena considering the nature of the edge states, with amplitude in only one of graphene's sublattices and a very small electron-phonon cuopling.[239] Even small electron correlations due to the sharp edge states' DOS give rise to magnetic moments, particularly strong along the longitudinal edges of zGRNs and fastly deacying into the center of the structure.[49,237] Furthermore, since the magnetic moments associated with the edge state acummulate in one particular sublattice and the total magnetization of the ribbon is zero, these magnetic moments hold an ferromagnetic order along the same zigzag edges yet an antiferromagnetic order considering opposite zigzag edges. As a result, the edge states are considered to be spin-polarized and their magnetic interaction opens a small bandgap between them.

## 3.4 Chiral Graphene Nanoribbons

As commented in previous sections, cGNRs can represent an even more interesting sort of graphene nanoribbon since they can potentially host both of the characteristic predcited properties of aGNRs and zGNRs. In addition, they present an extra tunable parameter, this is, their chiral angle $\theta$. As previously explained in section 1.3, we can use the vectors $\vec{m}$ and $\vec{n}$ (see Figure 1.3) to stablish a general convention to describe the edge orientation of GNRs by defining a vector $\vec{R}$ as follows:

$$\vec{R} = a\vec{m} + b\vec{n} \tag{3.31}$$

where $a$ and $b$ are real numbers. As well, using the same vectors, we can define the chiral angle $\theta$ as:

$$\theta = arctan\Big(\frac{\sqrt{3}m - n}{\sqrt{3}m + n}\Big) \tag{3.32}$$

Both the chiral angle $\theta$ and the chiral vector $\vec{R}$ define a ratio $r_{zig}$ given by the proportion of zigzag sites $N_z$ over the total number of edges sites $N_{TOT}$ as follows:

$$r_{zig} = \frac{N_z}{N_{TOT}} \tag{3.33}$$

Using a simple single-orbital nearest-neighbour (NN) TB model for the network formed by the electrons in $\pi$-orbitals, we can build the following hamiltonian to study the electronic structure of chGNRs:[62]

$$H = -t \sum_{\langle i,j \rangle} (a_i^{\dagger} b_j) + H.c.) \tag{3.34}$$

being $\langle i, j \rangle$ the sites $i$ and $j$ in the NN lattice, $a_i^{\dagger}$ ($a_i$) the create (annihilate) operators on sites of sublattice $A$ as $b_j^{\dagger}$ ($b_j$) is the create (annihilate) operators on sublattice $B$, and $t$ the hopping integral with an approxiamted value of 2.8 eV.[62] Here, we neglect the effect of the edge deformation becasue we focus on GNRs lying on surfaces. The TB Hamiltonian can be described as a sum of Bloch-like wavefunctions, considering the periodicity of along the axis of cGNRs as follows:

$$\phi(\vec{k}, \vec{r}) = \frac{1}{\sqrt{N}} \sum_{\vec{T}_m} e^{i\vec{k}(\vec{T}m+\vec{D}i)} \phi(\vec{r} - \vec{T}_m - \vec{D}_i) \tag{3.35}$$

being $\vec{T}$ the translation vector, $N$ the total number of primitive cells, $\phi(\vec{r})$ the $\pi$ orbital perpendicular to the plane, and $\vec{k}$ the moments in the one-dimensional BZ. The crystalline wave-function can be expressed as a linear combination of Bloch sums:

$$\Psi(\vec{k}, \vec{r}) = \sum_i A_i(\vec{k})\, \phi_i(\vec{k}, \vec{r}) \tag{3.36}$$

where $A_i(\vec{k})$ are the expansion coefficients. Based on the basis set $\phi_i$, the NN electronic Hamiltonian can be rewritten as follows:

$$H(\vec{k}) = t \begin{pmatrix} 0 & b & 0 & 0 & 0 & \ldots \\ b^* & 0 & c^* & 0 & 0 & \ldots \\ 0 & c & 0 & a & 0 & \ldots \\ 0 & 0 & a^* & 0 & c^* & \ldots \\ 0 & 0 & 0 & c & 0 & \ldots \\ \ldots & \ldots & \ldots & \ldots & \ldots & \ldots \end{pmatrix}_{10N} \tag{3.37}$$

where:

$$a = e^{ika\, cos((2\pi/3)-\alpha)} \tag{3.38}$$

$$b = e^{ika\, cos((2\pi/3)+\alpha)} \tag{3.39}$$

$$c = e^{ika\, cos(\alpha)} \tag{3.40}$$

Diagonalising the Hamiltonian in Equation 3.38 leads to the energy band structures and the expansion coefficients of the crystalline wave-function for the chGNRs.

### 3.4.1 cGNRs width dependence on the emergence of edge states

The presence of a majority of zigzag-like edges defining the periodic chiral-like edges of cGNRs is not the unique requisite related exclusively to the ribbon for observing the edge states in chGNRs from a theoretical point of view. They must present a certain width upon which the edge states emerges, as depicted in Figure 3.4, where $n_z$ represent the ratio of zigzag- over armchair-like edges in forming the chGNRs, and $n_w$ represent the ribbons' width.[63] This width dependence might arise from the electron correlations between the electronic states located at each longitudinal edge. All things considered, this theoretical scenario depicts how the magnetic moment of the edge states possibly present in chGNRs can be ruled the particular width of the nanoribbon as well as by its chiral angle.

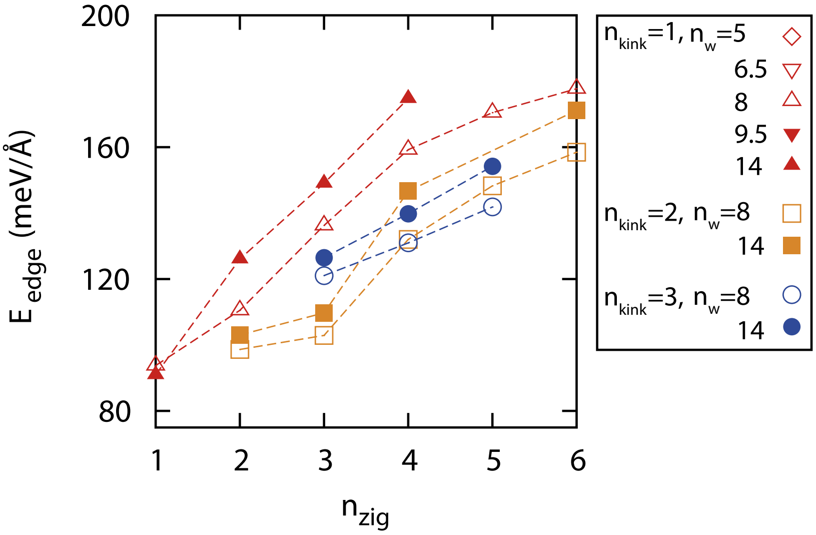

**Figure 3.4: Edge states formation energies for chGNRs with different chiral angle and width** $n_{zig}$ represents the number of zigzag- over the armchair-like edges defining the chiral edge in every case. $n_{kink}$ represents the number of carbon atoms in the armchair-like edges connecting the zigzag-like edges, and $n_w$ represents the chGNRs width as defined in ref.[63] Graph coppied from ref.[63]

# Part II

# Armchair Graphene Nanoribbons

The bottom-up methodology based on the use of molecular precursors as building blocks developed by Cai and coworkers in 2010 resulted in the synthesis of the first armchair graphene nanoribbon with atomic precision, i.e. 7-aGNR.[11] This pioneering example quickly became a reference system for the production of a large variety of different aGNRs, being the type of GNR most extensively synthesized to date.[128, 130, 131, 138, 240] Calculations reveal that aGNRs can be classified into three different subfamilies depending on the number of dimer lines $p$ across their width *(3p, 3p+1*, or *3p+2)*, their band gaps being inversely proportional to the width within each of those families.[14, 15, 241] The reported band gap values of the various aGNRs synthesized to date confirm this picture with scattered points along the predictions for each of the GNR families.[16, 118, 119, 129, 133, 134, 242, 243]

The second part of this thesis focuses on the synthesis and characterization of the electronic properties of the *3p*-aGNR family on gold surfaces. To begin with, we study the growth of different aGNRs from the lateral fusion of poly-*para*-phenylene (PPP) nanowires on the flat Au(111) surface and how their semiconducting band gap is modulated by their width. Secondly, we improve the selectivity of the same synthetic reaction by the use of the vicinal surface Au(322) as template to limit the resulting products into one single type of aGNR.

# Chapter 4

# Width-dependent band gap and Fermi level pinning in aGNRs

Besides the characterization of their fundamental electronic properties, the increasing pool of available GNRs with well-defined structures has allowed the correlation of those electronic properties with their performance when integrated into devices like field-effect transistors.[33,244–252] Interestingly, the device performance is strongly dominated by contact effects, in particular, by the Schottky barrier at the GNR-contact interface. As opposed to studies of other GNR properties like their band gaps, systematic studies of the energy level alignment between GNRs and common contact materials are still limited in spite of their determining role in the ultimate response of GNR-based devices.

In this chapter, we provide a systematic study of the band gap and energy level alignment of GNRs focused on the *3p* family, addressing from the smallest possible aGNR (3-aGNR) to its four immediately following sister structures (6-, 9-, 12-, and 15-aGNRs). Moreover, we amend our understanding of the interface energetics between GNRs and gold, in particular, Au(111) surface. Our results reveal, in addition to the width-dependent band gap, the onset of Fermi level pinning for widths $\geq 6$ dimer lines. This work is published in ref.[125]

## 4.1 Synthesis of varying-width aGNRs from PPP lateral fusion

We use 4,4-dibromo-*para*-terphenyl (DBTP) as a molecular precursor to synthesize the structures described here. Figure 4.1.a summarizes the stepwise synthesis of aGNRs starting from the precursor. A submonolayer of DBTP is initially deposited on a Au(111) single crystal held at room temperature. After annealing above 250°C, the precursor undergoes UC[12] yielding PPP nanowires. Figure 4.1.b shows a STM image of a representative sample. As previously reported,[131] these nanowires are highly aligned, separated by arrays of bromine atoms between them (see Figure 4.2.a), and present impressive lengths of up to 200 nm. PPP has been occasionally termed as a 3-aGNR and would thus fit into the family of 3p-aGNRs. However, as previously concluded from near-edge X-ray absorption fine structure (NEXAFS) measurements, it displays a nonplanar structure on Au.[253] Mapping the DOS at the onset of VB and CB, clearly reveals a modulated intensity that mirrors an alternating tilt of subsequent phenyl rings (see Figure 4.2.b,d). The non-planarity of gold-supported PPP is also confirmed by DFT calculations even when using functionals that incorporate the vdW interaction, although reduced with respect to that in gas-phase PPP. As discussed later, this non-planar structure leads to a substantial difference in the electronic properties of the polymer with respect to the rest of the wider (and planar) 3p-aGNRs.

Above 430°C, PPP nanowires merge sideways through dehydrogenation,[253] forming aGNRs of different width, as shown in Figure 4.1.c. This synthetic step relies on random diffusion effects imposed by the high temperature and results in an interconnected network of nanoribbons of different widths. There is a significant number of curved aGNRs, but most of them preserve the preceding nanowire's straight orientation. The final nanoribbon width depends on the number of nanowires getting fused. Discretized by the intrinsic width of PPP nanowires (3-aGNR), we find 6-, 9-, 12-, and 15-aGNRs are formed from the fusion of two, three, four, and five nanowires, respectively. Having them all next to each other on the same Au(111) surface reveals itself as an excellent testbed to measure and compare their respective electronic properties.

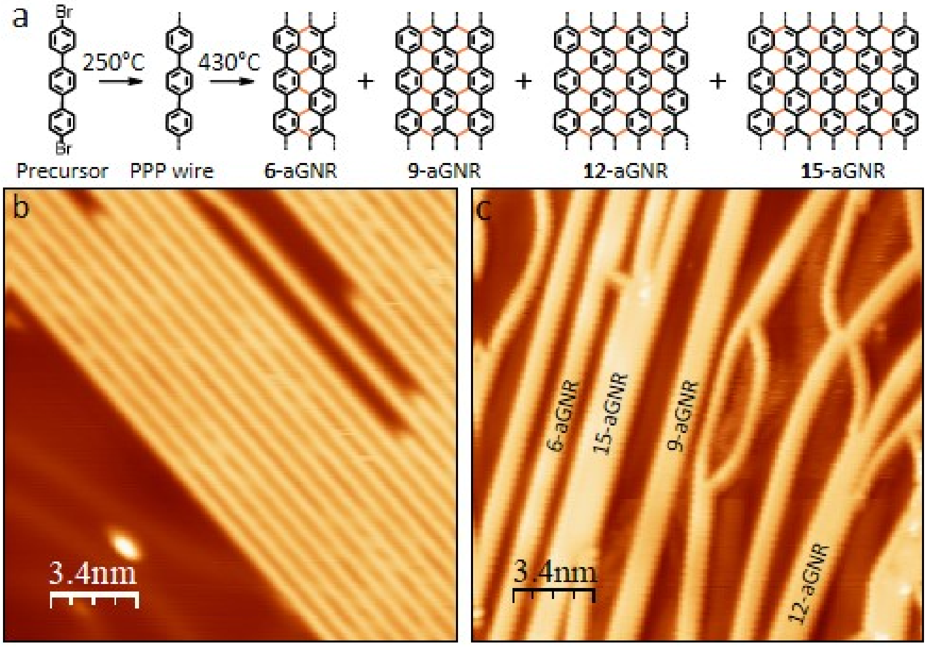

**Figure 4.1: (a) Schematic synthesis from DBTP molecular precursor on Au(111).** STM topography images of **(b)** PPP nanowires (24.6 $nm^2$, $I_t$ = 0.22 nA, $V_s$ = 1.0 V) and **(c)** a-GNRs (24.6 $nm^2$, $I_t$ = 0.22 nA, $V_s$ = -1.7 V), where text inlets indicate the different widths of aGNRs

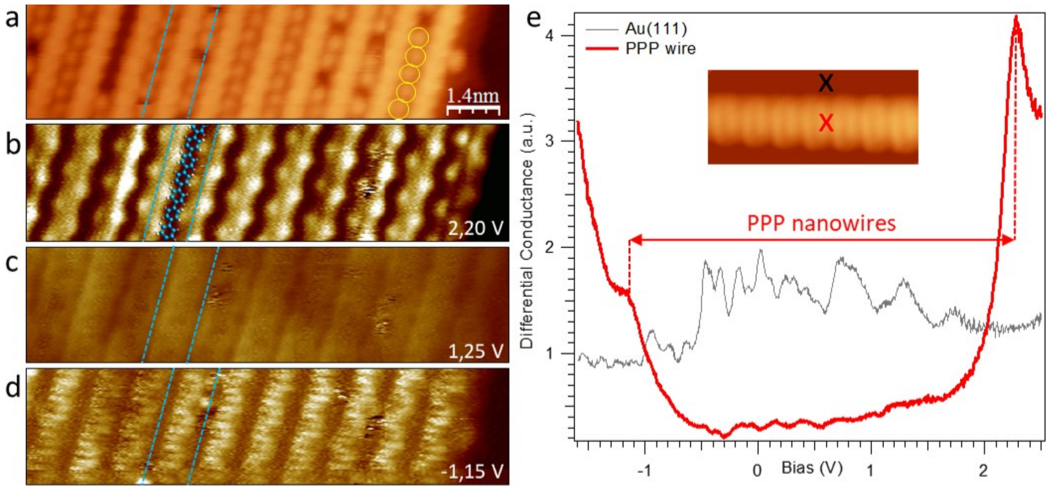

**Figure 4.2: Electronic structure of PPP nanowires. (a)** STM image (12.3 nm x 2.9 nm; $V_s$ = -1.1 V; $I_t$ = 0.60 nA). Bromine atoms between PPP nanowires are indicated with yellow circles. **(b-d)** Constant-current dI/dV maps (12.3 nm x 2.9 nm; $I_t$ = 0.60 nA) on PPP nanowires at (b) valence band edge ($V_s$= 2.20 V), where simulated representation of PPP wire is included as visual guide; **(c)** within the band gap ($V_s$ = 1.25 V), and **(d)** at conduction band edge ($V_s$ = - 1.15 V). Blue dashed lines are included for an easier appreciation of single nanowire features. **(e)** Spectra taken on PPP nanowires (in red) where Au(111) signal (in black) is added to every spectrum as background reference (open-feed-back parameters: $V_s$ = -1.60 V; $I_t$ = 0.54 nA; $_{rms}$ = 18 mV). Crosses in inset topographic image indicate the positions where spectra were recorded.

## 4.2 Electronic structure: width-dependent band gap

The aGNRs' electronic properties have been characterized by STS, measuring both dI/dV point spectra and constant-current dI/dV maps at various sample bias voltages (Figure 4.3). The dI/dV point spectra were taken over the sides (where the measured GNR signal is highest[242,243,254]) of straight GNRs' segments, featuring a well-defined width and defect-free structure over substantial lengths. While segments of 6- and 9-aGNRs easily exceed tens of nanometers, the wider the ribbons, the shorter the average segments are. To avoid notable band gap variations from finite length effects, spectra are only taken into account from segments longer than 4 nm (i.e. ∼9 unit cells). While the convergence behaviour of the GNR band gap with its length depends on a series of aspects such as the ribbon's own polarizability and thus on its particular structure, for the GNRs studied here, the probed electronic properties at these lengths can be considered to be close to those of an infinite ribbon.[255,256] Figure 4.3.a displays representative STS spectra for ribbons with different widths, together with background spectra of the bare Au(111) surface nearby, as a reference.

All STS spectra show a clear conductance rise at positive bias, attributed to the onset of the conduction band. The position of these bands is observed at different energies as a function of the ribbons' width: the wider the ribbon, the closer to $E_F$ its CB is. Thus, the onsets range from 0.86 eV, for the wider 15-aGNR, to 1.47 eV for the narrower 6-aGNR. Regarding the filled states ($V_s < 0$), the first nanoribbon-related feature in the spectra is detected at bias values close to -0.2 eV for all measured widths. We associate it with the corresponding onset of the aGNRs' valence band. A more detailed analysis reveals that the VB onset follows a similar, although less pronounced, width-related trend as the one observed in the conduction band case. The valence bands are slightly closer to $E_F$ as the GNRs become wider, ranging from -0.17 to -0.23 eV. The detection of the VB onset is particularly difficult on Au(111) since the surface state signal overlaps with the 3p-aGNRs spectroscopic features. Additionally, the density of states of the VB of 3p-AGNRs decays particularly fast along the

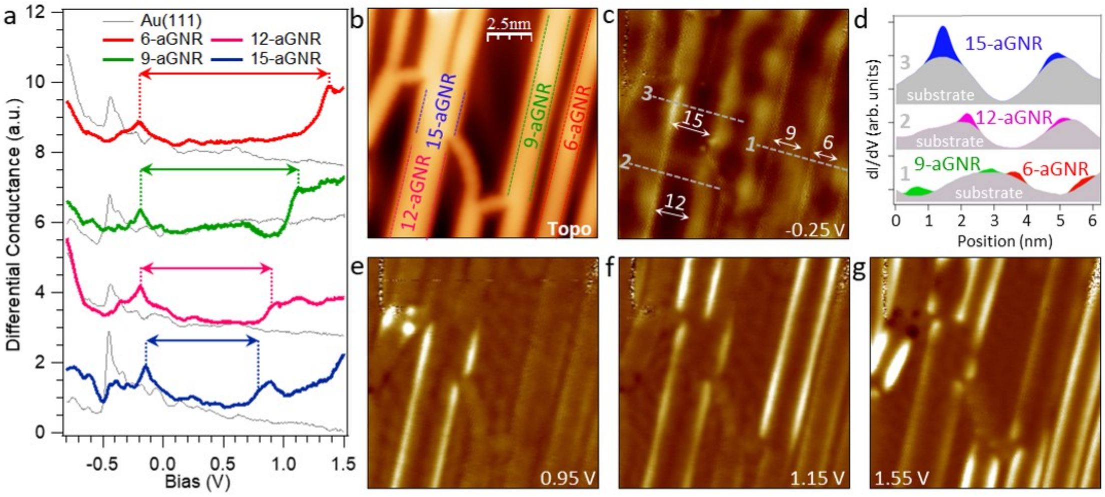

**Figure 4.3: (a) Electronic structure of 3p-aGNRs. (a)** Spectra on 6-aGNR (red), 9-aGNR (green), 12-aGNR (pink), 15-aGNR (blue), and Au(111) signal (grey) as background reference (open-feedback parameters: $V_s$ = 1.55 V, $I_t$ = 1.4-10 nA; $V_{rms}$ = 10 mV). **(b)** STM topography image (12.4 nm$^2$; $V_s$ = -1.1 V; $I_t$ = 0.61 nA). **(c)** Conductance map near the valence band onset ($V_s$ = -0.25 V), with white arrows as a guide for the eye to the intensity along each aGNR edge. **(d)** Profiles across the conductance map in (c), highlighting the contribution from the VB of differently wide GNRs on top of the dominating Au(111) surface state contribution. Conductance maps near the conduction band onsets for **(e)** 15-aGNRs and 12-aGNRs ($V_s$ = 0.95 V), **(f)** 9-aGNR ($V_s$ = 1.15 V), and **(g)** 6- aGNR ($V_s$ = 1.55 V). Differences in the reference spectra relate to different tips and positions. The comparable intensity in 12- and 15-aGNRs' edges in image (d) probably relates to the limited length of the 15-aGNR segment. Its reduced length causes an increased band gap and thus leads to an upshift in the energy of the conduction band onset. Size and set point for all images are 12.4 nm$^2$ and $I_t$ = 0.61 nA, respectively.

direction perpendicular to the GNR plane.[119, 243] Both of these reasons severely complicate its detection by STS. Nevertheless, our analysis of both VB and CB is in excellent agreement with the recently reported electronic structure and energy level alignment of 9-aGNRs synthesized selectively on Au(111).[119]

The conclusions derived above from our dI/dV point spectra are supported by dI/dV maps obtained at different biases (Figure 4.3.c-g). When probing the empty states ($V_s > 0$), there is an energy threshold at which an increased conductance starts becoming visible along the sides of the ribbons, first for the wider ribbons (Figure 4.3.e) and as the energy increases also for 9-aGNRs (Figure 4.3.f) and 6-aGNRs (Figure 4.3.g). Such intensity in conductance maps is related to the LDOS of aGNR bands,[16, 243] and the threshold energies at which the increased conductance sets in are in agreement with the width-dependent band onsets determined from the point spectra. In the case of the filled states ($V_s < 0$), conductance maps at -0.25 V reveal the strong intensity of the scattered surface state. Superimposed to it, we observe a weak but recognizable intensity distributed along the edges of every nanoribbon (Figure 4.3.c) further highlighted in the profiles displayed in Figure 4.3.d. This agrees with the VB onsets being at similar energies for all GNRs, as observed in the spectra (Figure 4.3.a). Besides the frontier bands, our spectroscopy measurements reveal an additional nanoribbon-related signal at higher negative bias (Figure 4.4). We associate it with the second valence band (VB+1), which is easier to be probed by the tip of the STM than is the VB. Its slower decay away from the nanoribbon plane explains,[119, 243] together with the absence of the Au(111) surface state at these energies, its stronger and more easily measurable signal. For a clear visualization of the overall data, Table 4.1 summarizes the energies of all band onsets averaged over several measurements on different aGNRs, as well as the associated band gaps.

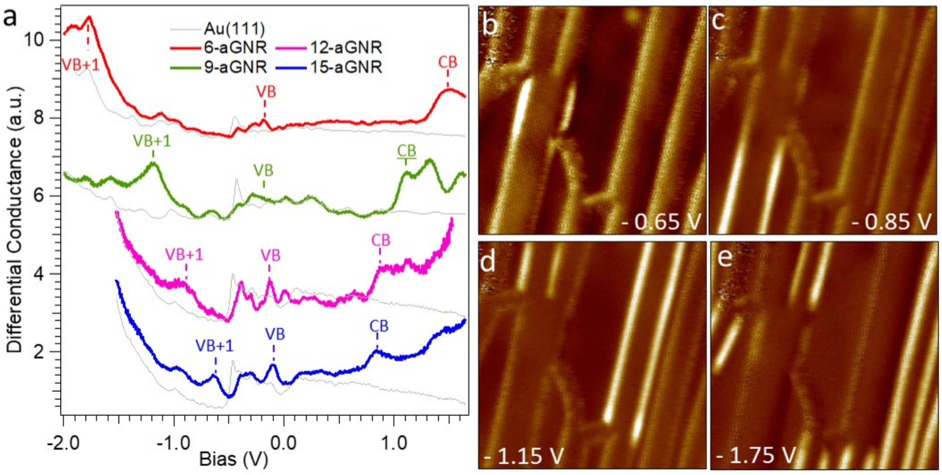

**Figure 4.4: 3p-aGNRs' second valence band (VB+1) spectroscopic characterization. (a)** Spectra taken on 6-aGNR (in red), 9-aGNR (in green), 12-aGNR (in pink) and 15-aGNR (in blue) where Au(111) signal (in grey) is added to every spectrum as background reference (open-feed-back parameters: $V_s$= -1.0 V; $I_t$ = 0.5-10 nA; modulation voltage $V_{rms}$ = 10-12 mV). **(b-e)** Constant-current conductance maps (12.4 nm$^2$; $I_t$ = 0.60 nA) at the onsets of the second valence band (VB+1) on (b) 15-aGNR ($V_s$ = -0.65V), (c) 12-aGNR ($V_s$ = -0.85V), (d) 9-aGNR ($V_s$ = -1.15 V) and (e) 6-aGNR ($V_s$ = -1.75 V).

**Table 4.1:** Average *3p*-aGNR VB+1, VB, CB and band gap values

| Structure | VB+1 (eV) | VB (eV) | CB (eV) | Band gap (eV) |
|---|---|---|---|---|
| 6-aGNR | -1.73 ± 0.04 | -0.23 ± 0.08 | -1.47 ± 0.05 | -1.69 ± 0.10 |
| 9-aGNR | -1.17 ± 0.06 | -0.20 ± 0.05 | -1.14 ± 0.05 | -1.35 ± 0.07 |
| 12-aGNR | -0.84 ± 0.04 | -0.18 ± 0.04 | -0.96 ± 0.04 | -1.13 ± 0.05 |
| 15-aGNR | -0.66 ± 0.09 | -0.17 ± 0.03 | -0.86 ± 0.03 | -1.03 ± 0.04 |

The average band gaps obtained for the differently wide aGNRs are displayed in Figure 4.5, where PPP nanowires (analyzed in Figure 4.2) are included for comparison as 3-aGNRs. The values fit into the predicted range for gold-supported nanoribbons of similar widths,[241] and their smooth evolution is also in line with predictions.[14,241] However, 3-aGNRs clearly stick out of the smoothly varying trend of a monotonously decreasing band gap with incremental width within the *3p*-aGNR family. The reason behind this is that, in addition to the larger band gap associated with its narrower width, it is the only nonplanar structure. As a result, the degree of conjugation is reduced,[257] causing an anomalous band gap increase for this particular structure different from the wider graphene nanoribbons. Figure 4.5 also displays the average onset energies of valence and conduction band for the differently wide aGNRs. It becomes immediately clear that GNRs display an overall p-type alignment on Au(111) and that for 6- and wider aGNRs, as the band gap decreases, the CB onset approaches the $E_F$ much faster than the VB.

Both of these effects are indeed reproduced by DFT calculations of gold-supported graphene nanoribbons from 3 (PPP wires) to 12 dimer lines. Figure 4.6 displays the band structure of the various systems, where the diameter of blue symbols is proportional to the weight of each state on the carbon atoms and thus on the GNRs. Next to the band structures, the figure displays the DOS projected onto GNR's carbon atoms. In line with our experimental observations, wider ribbons show a clear p-type alignment with the Au(111) substrate. After a notable upshift of the valence band from 3-aGNR to 6-aGNRs, the VB onset appears close to the $E_F$ at a position fairly independent of the ribbon width. It shifts by only ~0.16 eV when going from 6- aGNRs to 12-aGNRs, to be compared with an about 3 times larger shift of the CB for the same widths.

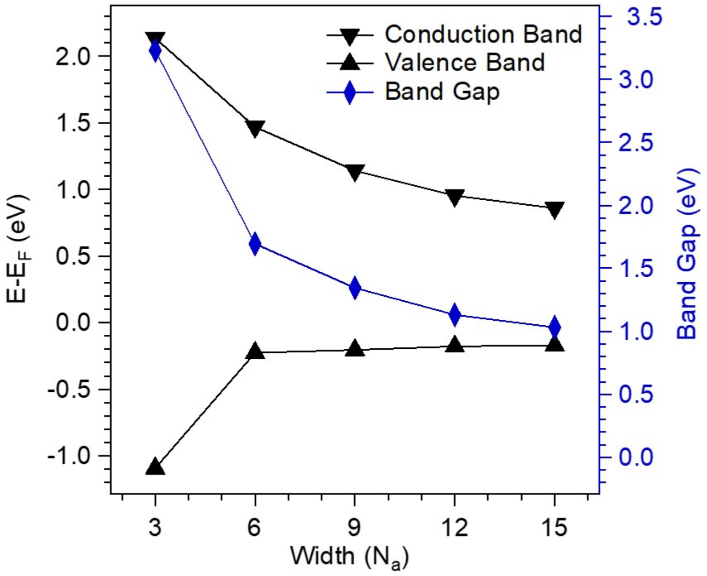

**Figure 4.5: Average 3p-aGNRs bands' energy values.** (Left scale, black lines) Valence and conduction bands and (right scale, blue line) the resulting band gaps.

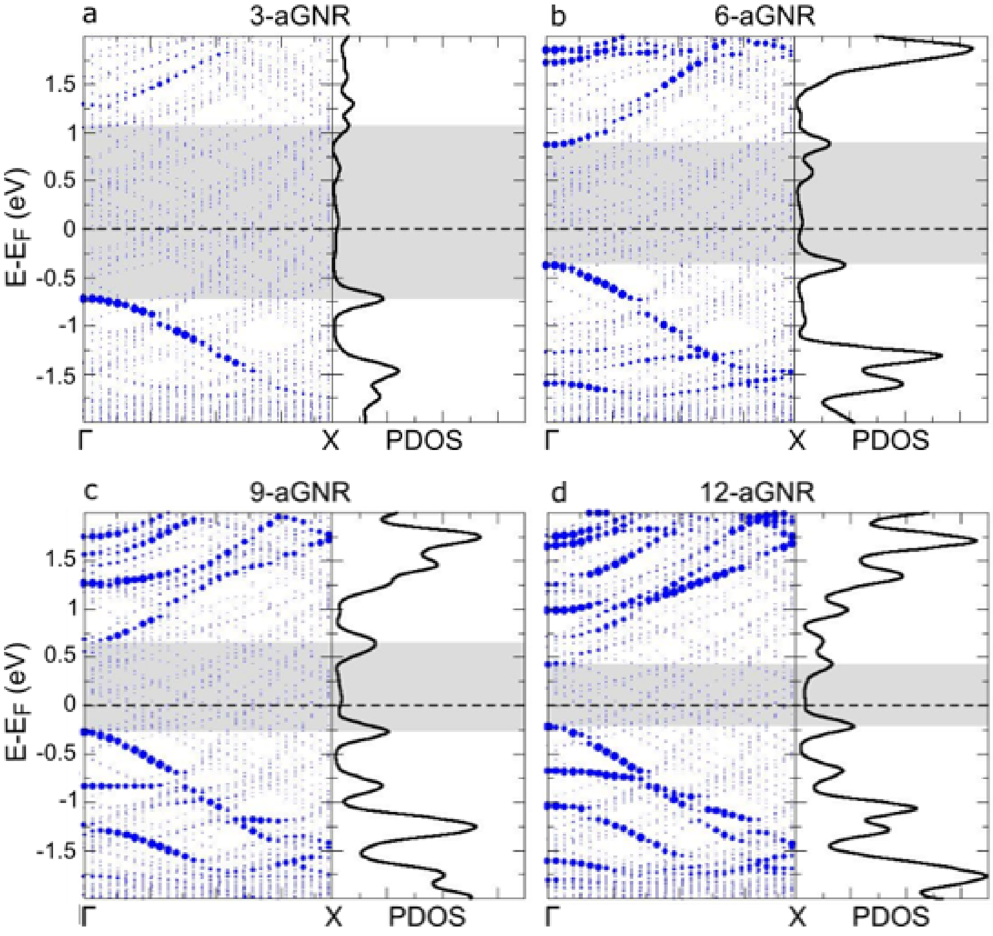

**Figure 4.6: DFT calculated band structure for 3, 6, 9, ad 12-aGNRs. (left)** Band structure and **(right)** projected density of states for **(a)** 3-aGNRs, **(b)** 6-aGNRs, **(c)** 9-aGNRs, and **(d)** 12-aGNRs. The diameter of the blue circles denotes the density of states projected onto the GNR's carbon atoms. The shadowed areas indicate the respective band gaps.

Experimentally, the p-type alignment of GNRs seems reasonable due to the p-type doping observed for gold-supported graphene,[258–262] which stems from the much larger work function of gold as compared to that of graphene. However, calculations have shown the understanding of this alignment not to be trivial as it depends on the dipole layer formed at the metal-graphene interface and displays a marked dependence on the details of the graphene-substrate interaction and the associated adsorption distance.[263–265] GNRs have a weak interaction with the Au(111) surface, dominated by vdW forces. As a weakly interacting semiconducting adsorbate approaches a metal surface, the substrate's intrinsic surface dipole is modified by an amount $\Delta$ as a result of a variety of processes that include, among others, the surface's electron cloud redistribution arising from Pauli repulsion with the adsorbate (commonly termed as "pillow effect") or intrinsic adsorbate's dipole moments.[266] In the case of aGNRs on Au(111), only the former process is relevant, giving rise to an effective reduction of the substrate work function. Indeed, for extended graphene on Au(111), the effect is such that, although at the equilibrium adsorption height ($\sim$3.3 Å) p-doping is predicted by first-principles calculations, for only slightly smaller distances ($<$ 3.2 Å), n-doping is obtained instead.[263,264] Therefore, the strong p-type alignment observed here for the aGNRs is not necessarily obvious. Particularly intriguing is the observation, in agreement with experiment, of very asymmetric shifts of the VB and CB onsets in the DFT calculations. Although the VB approaches the Fermi level as the GNRs become wider, in our calculations, it remains below the Fermi level without indications of a partial charge transfer to the substrate. In the absence of charge transfer, one would expect a rather symmetric closing of the gap. Thus, the observed behavior requires a width-dependent alignment of the aGNR levels with respect to those of Au(111). At this point, it is worth noting that the dependence of the ribbon's polarizability on its width has been recently proposed as instrumental to understand the width dependence of the band gap of adsorbed GNRs.[241] However, in contrast to our experimental observations, this effect should affect both the VB and CB in a comparable way.

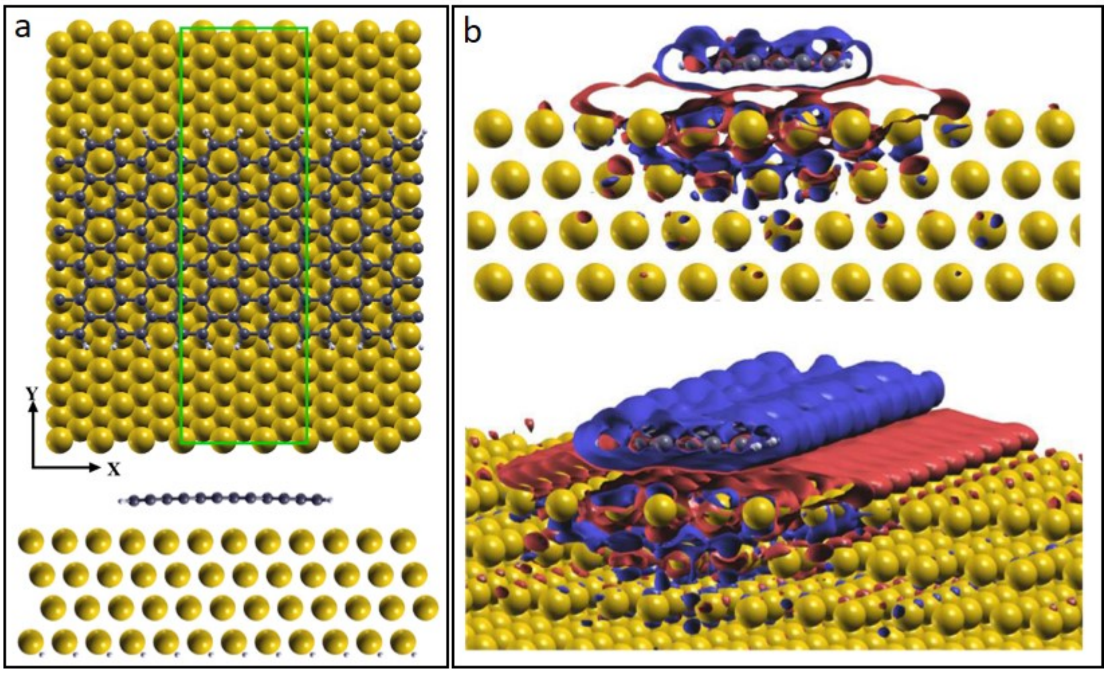

**Figure 4.7: DFT computational setup examples used for calculations of figure 4.6 (a)** Top and side view of 12-aGNRs on Au(111) slab with a lateral unit cell as indicated by the green rectangle. The ribbon is periodic along the x direction. **(b)** Front and side view of iso-surface (5 x $10^{-4}$ electrons/bohr$^3$) of the computed induced charge upon adsorption for a 6-aGNR on Au(111). Red(blue) surfaces correspond to electron accumulation(depletion).

Figure 4.7 shows the relaxed geometry for a 12-aGNR and the distribution of the induced charge upon adsorption for a 6-aGNR on Au(111), respectively. The computed equilibrium adsorption height of the central portion of the ribbon is in the range of 3.23-3.34 Å (larger for wider ribbons). The limit for extended graphene is 3.34 Å, in good agreement with previous calculations.[263] Figure 4.7.b shows how the electron charge accumulated in the surface (in red) as a result of the "pillow effect" extends beyond the region covered by carbon, piling up along the edges. This is most probably favored by the positive partial charge on the hydrogen atoms along the GNR edges. Thus, we find that the charge distribution is noticeably affected by the finite width of the ribbons. This characteristic distribution of the induced charge produces a width-dependent decrease of the interface dipole $\Delta$, favoring a stronger p-type alignment the narrower is the GNR. This effect partially compensates the downshift of the VB as the GNRs become narrower while increases the upshift of the CB. Therefore, it can explain the asymmetric level movement observed in the DFT calculations and, as a consequence, be a key ingredient to understand also our experimental results. However, this effect smoothly scales inversely proportional to the GNR width, while the experiment evidences a relatively sharp transition from a rapidly varying valence band alignment at widths below 6-aGNRs to an almost unchanged valence band as the width increases (see Figure 4.5). In fact, as will be shown below, the transition seems to relate directly to the GNR's band gap, which is no longer inversely proportional to the width if different families of armchair GNRs or even differently oriented GNRs are considered. Thus, in addition to the width-dependent interface dipole, other band-gap-dependent effects must be responsible for our observations.

## 4.3 Fermi-level pinning of valence band

A sharp transition from having a varying onset energy in frontier bands to having them quasi-unchanged (close to the Fermi energy) is typically termed as Fermi level pinning.[267,268] It is a well-known phenomenon observed at metal-semiconductor interfaces when one of the semiconductor's bands gets close in energy to the substrate's Fermi level, typically due to particularly high or low work functions (Figure 4.8a). Observing a transition from a non-Fermi level pinning behavior to the pinning usually requires the work function to be changed and thereby the interface chemistry. Instead, in this particular study on Fermi level pinning, the same phenomenology is observed while keeping the interface chemistry almost unchanged, the only varying parameter being the GNR's width and thus its associated band gap (Figure 4.8b).

The typically proposed explanation for Fermi level pinning is as follows. In the current case of an unchanged substrate and a decreasing adsorbate's band gap, valence and conduction band onsets plotted vs the band gap would be expected to symmetrically approach the midgap value with a slope S = 0.5 (Figure 4.8b). However, as one of the bands (e.g., valence band in Figure 4.8b) gets close to the Fermi level, further band gap reductions create a compensating dipole moment $\sigma$ to refrain the band from crossing the Fermi level. Although not confirmed by our calculations, whether due to the inability of current semilocal functionals to describe the energies of the electronic levels with sufficient accuracy for the free-standing ribbons and adequately incorporate correlation effects upon adsorption, or to slight deviations in the calculated adsorption distances that can substantially alter the interface energetics,[263] this is typically assumed to occur through partial charge transfer into metal-induced gap states.[156,267,268] As a result, the non-pinned band (conduction band in 4.8b) now supports a shift equal to the full band gap decrease (S = 1), while the alignment of the pinned band remains unchanged (S = 0). By preventing the semiconductors' bands from crossing the Fermi level, the interfacial charge transfer is reduced. It is therefore commonly observed with physisorbed materials because its absence would imply substantial charge transfers and consequently a chemisorption scenario.[269] Fermi poinning is thus exactly what we could expect from the interaction of graphene nanoribbons with an inert surface like Au(111).

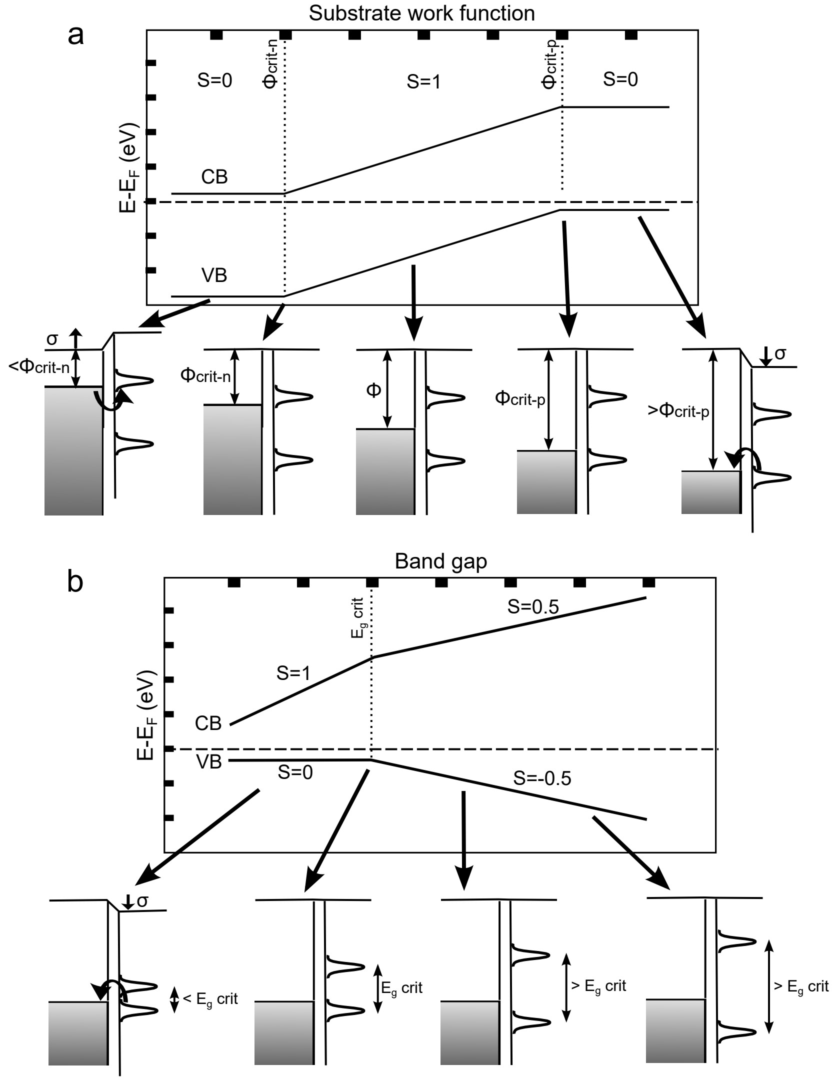

**Figure 4.8: Energy level alignment schematic models of substrate and adsorbate frontier bands. (a)** Bands' evolution for a varying substrate work function. Analyzing the slope S of the energy level alignment vs. substrate work function, the scenario changes from vacuum level pinning (S = 1) to Fermi level pinning (S = 0) of adsorbate bands at critically high and low work functions, respectively. **(b)** Bands evolution for a varying adsorbate band gap. As the band gap is reduced, the adsorbate bands onsets move towards the midgap value with a slope S = 0.5. As one of the bands gets close enough to substrate's Fermi level, the band (valence band in this case) gets pinned and henceforth the non-pinned band fully supports the gap reduction, shifting with a slope of S=1.

Indeed, we observe a striking agreement between the model Fermi level pinning behavior of band onset vs band gap (Figure 4.9) and the experimentally observed values from this work, together with results from other Au(111)-supported GNRs reported elsewhere, like 13-aGNR,[254] 9-aGNRS,[119] 7-aGNR,[242,243] and even (3,1) chiral GNRs[270] as shown latter in chapter 9. As displayed in 4.6, for band gaps above the critical value of ∼1.7 eV, valence and conduction bands shift symmetrically around their midgap value with a slope close to S = 0.5. However, as the band gap gets below that threshold value, the valence band remains almost constant (S = -0.09 ± 0.04) while the conduction band supports almost the full band decrease by shifting with a slope of S = 0.92 ± 0.05. Several GNRs have been characterized previously on an even less interacting substrate, namely, on Au(111) with an intercalated Si layer.[133]

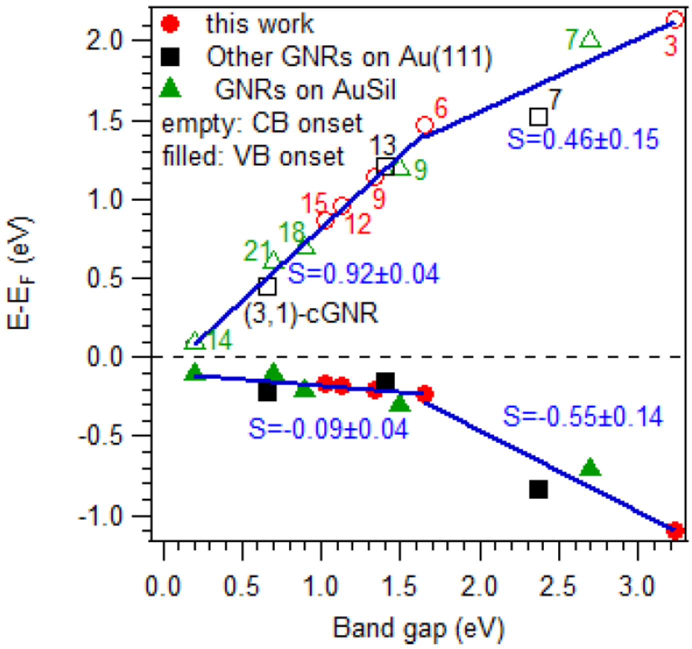

**Figure 4.9:** Valence and conduction band onsets of GNRs studied in this work and in other reports of Au(111)-supported ribbons vs their respective band gap (width given by the numbers next to the symbols). Data of GNRs on an even less interactive substrate as is a Si intercalated layer on Au(111) are also added for comparison.

On the Si-intercalated Au(111) surface, the GNRs display a slightly larger band gap due to the reduced substrate screening. However, not only does the band alignment similarly fit into our proposed Fermi level pinning picture, as expected from such weakly interacting surface, but it actually displays strikingly similar energies (Figure 4.9). Fermi level pinning energies of molecular adsorbates' orbitals may vary substantially from system to system, which is normally associated with the different density of states hosted by the frontier orbitals and how far in energy the tails of the frontier bands' density of states extend into the gap. In general, typical values remain below 0.4 eV away from the Fermi level,[266,271] which coincides with our observations.

## 4.4 Conclusions

In conclusion, in this chapter we report spectroscopic evidence of the width-dependent band gap predicted for armchair graphene nanoribbons and the associated energy level alignment. Starting with the synthesis of PPP wires (3-aGNRs), subsequent annealing drives their lateral fusion into 6-, 9-, 12-, or 15-aGNRs depending on the number of involved PPP chains. That is, the first five members of 3p-aGNR family are obtained on the same surface, on which both valence and conduction bands are probed by means of STS. We observe a continuously decreasing band gap as the GNRs structures get wider. Most importantly, Fermi level pinning of the valence band is found on Au(111) for 6 or more dimer lines wide aGNRs, in qualitative agreement with DFT calculations. Results known from other GNRs equally fit the pinning phenomenon proposed here, whenever their bandgap is below ~1.7 eV. This has important implications on the energy level alignment across GNR/metal interfaces, which may in turn be crucial for future GNR-based devices displaying similar interfaces at charge collection electrodes.

# Chapter 5

# Selective synthesis of armchair graphene nanoribbons on vicinal surfaces

The development of selective synthetic strategies represents a key objective for the integration of GNRs in future devices. Most of the known examples attain this selectivity by the rational pre-design of molecular precursors, guiding its reactivity through well-known, controlled pathways that end in the formation of the sought GNR.[128,272,273] An alternative route toward atomically precise GNR structures has been the lateral fusion of GNRs through cyclodehydrogenation.[129,131–134,136,138] An example of this alternative option is shown in the previous chapter, where armchair graphene nanoribbons of varying width are synthesized through the lateral fusion of poly-para-phenylene (PPP) nanowires on Au(111). Due to the flat topography of this surface, the lateral fusion of PPP nanowires results in a random synthetic process, hence lacking a precise selectivity over the final structure. Inspired by previous substrate-guided 'on-surface synthesis' (OSS) examples,[165] in this chapter we show how GNR synthesis can be guided by an adequately nanotemplated substrate instead of by the traditionally designed reactants. Still using a bottom-up approach to guarantee the atomic precision, based on the fusion of neighboring molecular structures, we switch from reactant to substrate engineering in the GNR design. That is, the selectivity in the synthesis process now is triggered and guided by the nanotemplating effect of an adequate substrate. These results are published in ref.[274]

## 5.1 Au(322) substrate as synthetic template

This selectivity is attained using the same molecular precursor 4,4"-dibromo-*para*-terphenyl (DBTP) on a different gold surface, namely Au(322). Figure 5.1 depicts the different scenario found on both gold surfaces after depositing the precursor at RT and inducing firstly, their polymerization of the precursor into PPP nanowires at 180 °C, subsequently followed by cyclodehydrogenation at 380 °C that results in the formation of *3p*-aGNRs (see Figure 4.1 in previos chapter). Contrary to the smooth topography of Au(111), the Au(322) surface is characterized by uniaxially aligned and regularly spaced terraces, whose steps run along the $[10\bar{1}]$ direction.[275] In addition to the natural templating effect of the steps,[140,276,277] the favored PPP nanowires growth direction along the $[10\bar{1}]$ crystallographic orientation coincides with that of the terraces, thus strongly promoting the uniaxial growth of PPP parallel to the substrate steps.[131]

The terraces of Au(322) are characterized by an average width of ∼12 Å,[275,278] which can fit side-by-side two PPP chains at most. This was initially expected to drive a selective pairwise fusion of PPP, and the result indeed shows the desired selectivity, displaying 6-aGNR as the only product (Figure 5.1.b). It should be noted, however, that the average length of defect free 6-aGNRs is relatively short, namely in the order of 6 nm, typically terminated by 6-aGNR/PPP junctions (including, e.g., the shortest possible PPP segments arising from a missing phenyl ring in 6-aGNRs). Nevertheless, this length is sufficient for the GNRs to readily display electronic properties close to those of their infinite analogues.[256] In essence, making use of reactions that can form a variety of different products, it is the appropriate substrate that imposes synthetic selectivity of 6-aGNR and at the same time their unique azimuthal alignment.

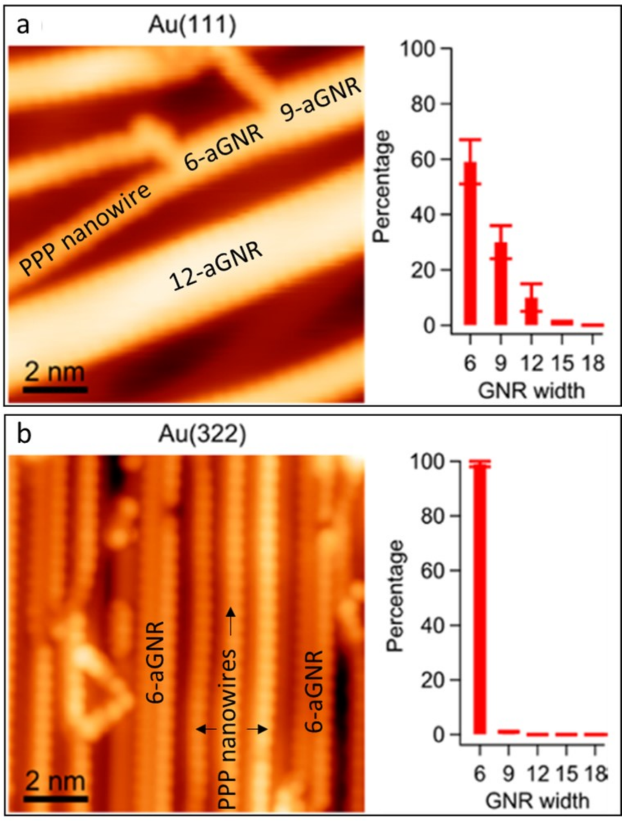

**Figure 5.1: Bottom-up synthesis of 3p-aGNRs from DBTP precursor on Au(111) and Au(322).** Constant-current STM images **(a)** on Au(111) (10 x 10 $nm^2$, $V_s$= -1.0 V; $I_t$ = 50 pA) and **(b)** on Au(322) (10 x 10 $nm^2$, $V_s$= -1.5 V; $I_t$ = 500 pA) where histograms show the percentage of PPP consumed for the formation of aGNRs in each case.

However, as displayed in Figure 5.2, looking at the sample at different stages of the reaction, the process is found to be more complicated than anticipated. Upon DBTP deposition, the periodic Au(322) terraces (Figure 5.2.a) act as expected, driving the self-assembly of the pristine molecules into a highly ordered structure with all molecules uniaxially aligned parallel to the steps and with two side-by-side rows of molecules fitting each terrace (Figure 5.2.b). Five lobes can be clearly distinguished along each DBTP molecule in the STM images, the two outer ones corresponding to the Br atoms and the three inner ones to the three phenyl rings. Upon polymerization, the STM imaging reveals the most surprising changes. Polymerized structures with periodic lobes corresponding to the phenyl-units along the PPP are clearly recognized, separated by rows of round objects that correspond to Br atoms (brown dots in Figure 5.2.c).[125, 131, 253, 279, 280] However, the underlying surface appears completely reconstructed, hosting the alternating rows of PPP and Br on much wider and irregular terraces. This reconstruction is associated with the strong interaction of the halogen atoms with the stepped Au substrate,[281] but will not be discussed further, as it is beyond the scope of this chapter. At first sight, this fact may be expected to hinder the templating effect of the Au(322) surface. However, as bromine desorbs upon further annealing, the Au(322) periodicity is recovered, and the substrate templating effect sets in, resulting in the selective production of 6-aGNRs only accompanied by unreacted PPP (Figure 5.2.d).

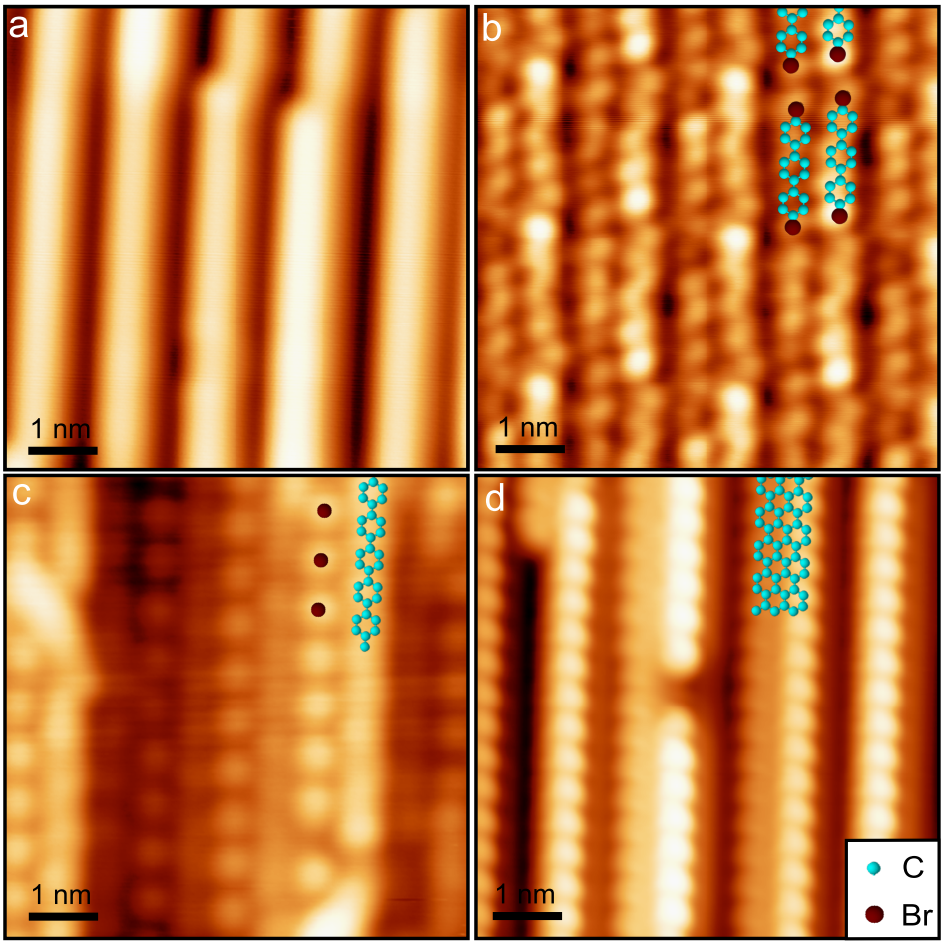

**Figure 5.2: Different growth stages of 6-aGNRs from DBTP precursor on Au(322).** Constant-current STM images (6 x 6 nm$^2$) of **(a)** clean Au(322) surface ($V_s$ = -5.0 mV; $I_t$ = 2.0 nA), **(b)** after DBTP deposition ($V_s$ = 25.0 mV; $I_t$= 74.0 pA), **(c)** after Ullmann polymerization ($V_s$ = 86 mV; $I_t$ = 29 pA), and **d)** after 6-aGNR formation through cyclodehydrogenation of neighboring PPP chains ($V_s$ = 1.5 V; $I_t$ = 516 pA). Molecular models are overlaid on part of the images as a guide to the eye.

## 5.2 6-aGNR electronic structure characterization

From a characterization point of view, the resulting uniaxially aligned products have the virtue of allowing the use of laterally averaging techniques like angle-resolved photoemission without losing the momentum resolution. Thus, we have used ARPES to monitor the valence band structure of the vicinal sample at different stages of the GNR synthesis process. Figure 5.3 displays the electron dispersion along the terraces for the substrate before and after deposition of the reactant, as well as after subsequent annealing treatments. From comparison to the clean Au(322) reference (Figure 5.3.a), the as-deposited DBTP is observed to produce distinct intensity at an energy of -1.78 ± 0.05 eV (Figure 5.3.b). This signal is associated with its highest occupied molecular orbital (HOMO), which exhibits a flat band due to the electron's confinement within the relatively small molecule.[279,282]

After Ullmann polymerization, the band structure changes substantially with the appearance of a strongly dispersive band with the apex at $E = 1.09 \pm 0.05$ eV and $k_{||} = 1.43$ Å$^{-1}$ (Figure 5.3.c). The dispersive behavior now stems from the electron delocalization along the $\pi$-conjugated PPP chain.[279,282] Because the band gap of a conjugated polymer scales approximately with a $1/N$ relation,[257,283] $N$ being the number of conjugated electrons, the increased conjugation length when going from a precursor with three conjugated rings to a polymer with tens of them is equally responsible for the reduction of the adsorbates' band gap. As a consequence, the frontier bands' onsets approach the $E_F$, as observed in the ~0.7 eV upshift in energy of the valence band onset with respect to DBTP's HOMO.

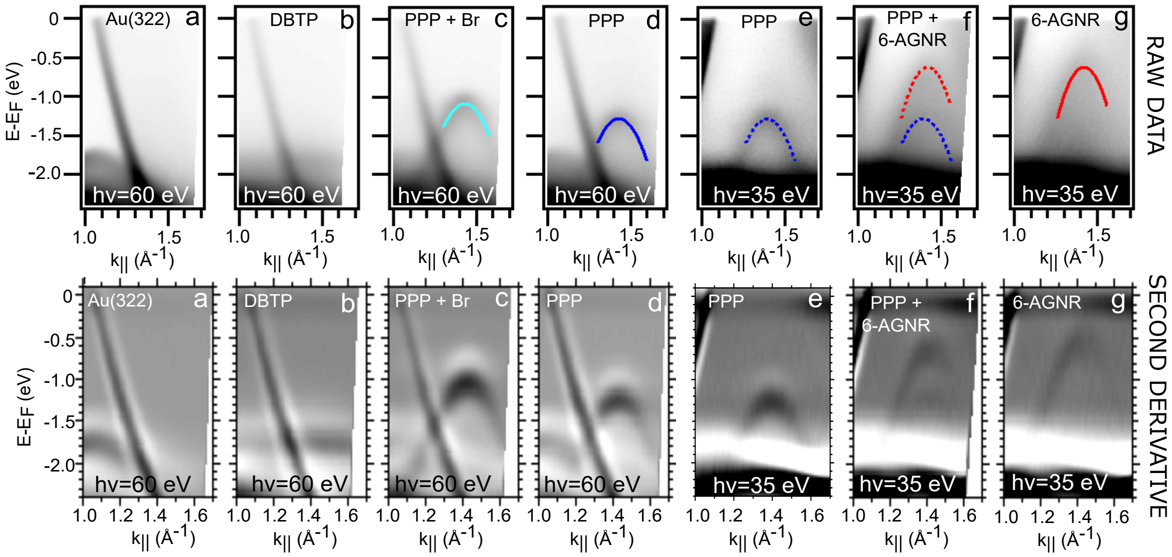

**Figure 5.3: Angle-resolved photoemission signal, displaying the dispersion parallel to the step direction, at different stages of the reaction process** (integration along $k_\perp$ from 0.2 to 0.4 Å$^{-1}$) **(a)** Reference spectrum for the bare Au(322) substrate, **(b)** after DBTP deposition, **(c)** after Ullmann polymerization into PPP, **(d,e)** after Br desorption, **(f)** after partial fusion of PPP into 6-aGNRs, and **(g)** after a maximized transformation of PPP into 6-aGNRs. All correspond to different samples heated to increasingly high temperatures, starting from a DBTP covered sample after molecular deposition onto a substrate held at RT. The photon energy used is 60 eV for panels (a-d) and 35 eV for panels (e-g) to enhance the signal of the existing organic bands. **(Top)** Raw data with parabolic fittings used to extract band onset and effective mas. The dotted profiles in panels (e) and (f) are not fitted, but included as a superposition of the profiles in (d) and (g) **(Bottom)** second derivative processing of the spectral functions for optimum visualization.

Annealing at higher T (∼320 °C) triggers the desorption of Br[131,283–285] and the associated change in work function[284,285] lowers the band onset to E = -1.29 ± 0.03 eV (Figure 5.3.d,e) while keeping the effective mass unchanged. The latter may be expected from the absence of chemical changes on the PPP, but it also underlines the limited effect of the intercalated Br chains on the polymers, other than altering the supporting substrate and its associated work function. Annealing to even higher temperature (T > 380 °C) triggers the lateral fusion of PPP chains.[125,131] In the initial stages, one can observe the coexistence of the PPP band together with an additional band at higher energy that we associate with the newly formed 6-aGNRs (Figure 5.3f). At higher temperature, the PPP band practically disappears at the expense of the new band (Figure 5.3.g) with an effective mass of $m^* = 0.15 \pm 0.02\, m_e$. Other experimental parameters being unchanged, the photoemission signal associated with PPP is proportional to its surface coverage, thus suggesting a transformation of most PPP into 6-aGNRs. It is worth noting that such a high yield has not been achieved in our STM experiments, which always revealed substantial amounts of unreacted PPP (Figure 5.1 and Figure 5.2). Presumably this relates to the different heating rates in the preparation chambers for the ARPES and STM experiments, with a potentially strong impact on the kinetics of this complicated reaction that involves not only the molecular adsorbates, but also important substrate reconstructions.

The VB onset of 6-aGNRs appears at the same momentum as that of PPP, but its energy shifts upward by ∼0.6 eV to -0.65 ± 0.08 eV. The common momentum of the VB maxima at 1.43 $Å^{-1}$ is associated with a periodicity of 4.39 Å, in turn related to the adsorbate's unit cell, the interphenyl spacing in PPP and the coincident armchair periodicity of 6-aGNR. Corresponding to the center of the second Brillouin zone, 1.43 $Å^{-1}$ also coincides with the reciprocal space area where the reactant's and all products' photoemission intensity is seen best, since the band's spectral weight distribution is known to correlate with the Fourier transform of the orbitals, and the HOMO orbitals of the various structures studied are all modulated according to the armchair periodicity.[279,286,287] Thus, since the maximum ARPES intensity along the direction of its long molecular axis is expected around $k$ values of ∼1.45 $Å^{-1}$, the reciprocal space region depicted in Figure 5.2 allows an excellent comparison of the electronic properties of the different adsorbate systems.

PPP, being arguably considered a 3-aGNR, belongs to the same *3p* family as 6-aGNR.[14,125,241] Because within each aGNR family the band gap decreases monotonously with increasing width,[14,125,241] the observed upward shift in energy of the VB onset relates again to a decreasing band gap (which brings both valence and conduction band (CB) onsets closer to the Fermi level) when changing from PPP to 6-aGNR. This change in band gap is shown on Au(111) in the previous chapter 4.[125] However, because the stepped structure of Au(322) substantially lowers its work function as compared to that of flat Au(111), a notable discrepancy in the energy level alignment is expected. As extracted from measurements of the cut-off energy of photoemitted electrons from either surface (Figure 5.4), the work function changes by 0.25 eV. Thus, by STS we have now accessed the band gap and energy level alignment of PPP and 6-aGNRs directly on Au(322) (Figure 5.5).The VB onsets measured by STS appear at E = -1.34 ± 0.06 eV and E = -0.79 ± 0.06 eV for PPP and 6-aGNRs, respectively. Meanwhile, the measured band gaps amount to 3.05 ± 0.13 eV and 1.88 ± 0.09 eV. If we compare the STS values on Au(111) (see Table 4.1 in previous chapter 4) with the STS (ARPES) values on Au(322), the offset between the measured VB onsets amounts to 0.25 ± 0.08 eV (0.2 ± 0.06 eV) for PPP and to 0.56 ± 0.1 eV (0.42 ± 0.11 eV) for 6-aGNRs. For PPP the offset equals the 0.25 eV change in work function between the two surfaces (Figure 5.4) thus closely following an ideal vacuum level pinning scenario.[156] For 6-aGNRs, the slightly larger offset qualitatively still fits the work function change, but is around 0.2 eV larger. This minor increase may arise from additional differences in the interface chemistry, like, e.g., an enhanced GNR-substrate hybridization.[156,288] As will be shown later, there is experimental evidence hinting at such enhanced hybridization.

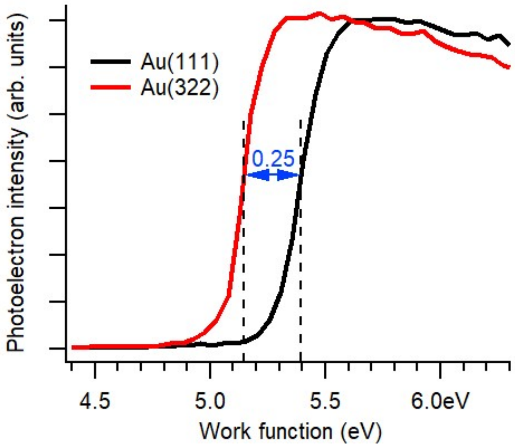

**Figure 5.4: Work function measurements of Au(111) and Au(322) surfaces.** Photoemission spectra were taken with the sample biased at -9 V and the absolute work function value was extracted from $\Phi = h\nu - E_F - E_{cuttoff}$, where $E_F$ and $E_{cutoff}$ have been taken from the corresponding maxima in derivated spectra. Spectra in the figure have been subsequently shifted to fit the cut off energy to the extracted work function values.

We now focus and deepen the characterization of 6-aGNRs, whose selective synthesis by substrate templating is the key point of this work. Its band gap (Eg = 1.88 ± 0.09 eV) is in excellent agreement with previous state-of-the-art calculation based on many-body perturbation theory (in particular the GW approximation) and the addition of substrate screening through a classical image charge model.[241] Beyond the energy determination, we have characterized the spatial distribution of valence and conduction band orbitals: experimentally wit conductance maps at the corresponding onset energies an theoretically with DFT calculations. These are all summarize in Figure 5.6, along with the associated constant current image and STS spectrum.

The simulated conductance images at the energies of valence (Figure 5.6.d) and conduction band (Figure 5.6.e) of freestanding 6-aGNRs are evaluated at 4 Å above the molecular plane. Doing so, one accounts for the differently rapid decay toward the vacuum (where the STM tip actually probes the states) of the VB and CB orbitals due to their different wave function symmetries.[119,243] The lacking phase cancellation of the CB orbitals at the GNR sides causes these states to extend further into the vacuum along the ribbon's edges (Figure 5.7). By contrast, the oscillating phase along both the transverse and longitudinal GNR directions of the VB states' wave functions causes a faster but more homogeneous decay of the

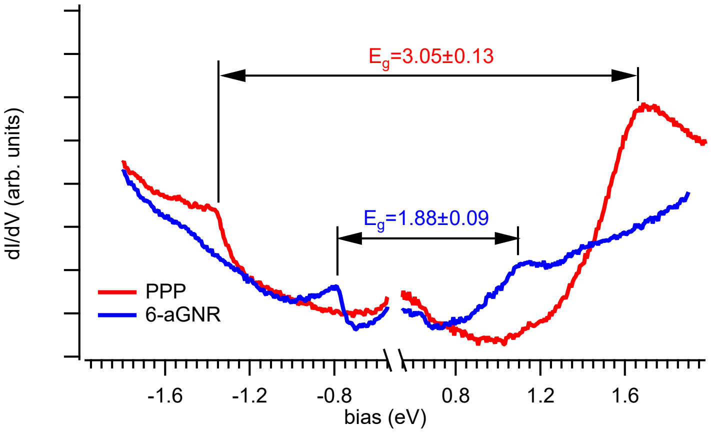

**Figure 5.5: Constant current dI/dV spectra of PPP and 6-aGNRs on Au(322)** ($I_t$ = 430 pA), revealing their correspondingly different band gaps and band onset energies.

LDOS toward the vacuum (Figure 5.7).[119,243] As displayed in Figure 5.6.c,d, taking these effects into account by simulating the conductance maps at 4 Å above the carbon backbone, a good agreement is obtained with the experimental measurements. In addition to complementary constant-height dI/dV spectra displaying no increased conductance anywhere around $E_F$ (Figure 5.6.b, such good agreement allows the unambiguous assignment of the observed onsets in Figure 5.6.a to VB and CB, since the nodal structure and wave function symmetry of the VB-1 and CB+1 are completely different. That is, due to the arguments described above, the VB-1 would be observed strongest along the GNR sides, while the CB+1 would display two nodal planes along the ribbon axis (Figure 5.7). The calculations, however, do not reproduce the additional superstructure with twice the armchair unit cell period that is clearly resolved in the experimental images. The superstructure is particularly visible along one of the sides of the GNR, and the reason for it is found in the underlying substrate, not included in our calculations.

Armchair graphene nanoribbons aligned along the compact $[10\bar{1}]$ direction are commensurate with every second unit cell.[125,131] On flat Au(111), the molecule-substrate interaction is so weak that STM and STS measurements show no signature of such commensuration in the nanoribbon's signal.[125,131] However, a different scenario appears as GNRs interact with under-coordinated (and thus more reactive) Au atoms like those at the step edges. Under these circumstances the interactions of Au with GNR and the associated hybridization is stronger, translating into an evident fingerprint of the commensuration in the ribbon's electronic density of states. The fact that this commensuration fingerprint is more visible along one of the GNR's sides (top GNR side in Figure 5.6.c) relates to the position of the step edges. Careful image analysis reveals that the GNRs are tilted across two neighboring terraces with the substrate step off-center, that is, closer to one of the two GNR sides (Figure 5.8). As a consequence, this particular side will hybridize more strongly with the substrate and thus show a more pronounced imprint of it in the imaging of the GNR orbitals.

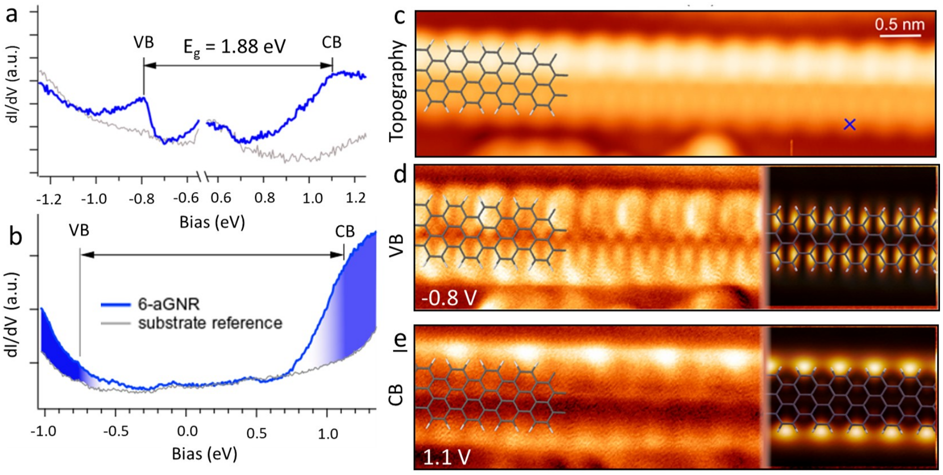

**Figure 5.6: Spectroscopic characterization of 6-aGNR's electronic structure on Au(322).** **(a)** Constant-current ($I_t$ = 430 pA) and **(b)** constant-height dI/dV point spectra on a 6-aGNR (in blue), revealing the valence and conduction band onsets. Au(322) spectrum (in grey) is included as reference.**(c)** Constant-current STM image of a 6-aGNR and the associated dI/dV maps at the energies of the **(d)** valence band onset ($I_t$ = 1.05 nA, $V_s$ = -0.8 V) and **(e)** conduction band onset ($I_t$ = 1.05 nA, $V_s$ = 1.1 V). The simulated dI/dV images for valence and conduction onsets, evaluated at 4 Å above the C backbone, are superimposed on the right side of the experimental conductance images for comparison. The molecular structure of the 6-aGNRs is superimposed on both experimental and simulated dI/dV images as a guide to the eye. A location used for the point spectroscopy on the GNRs (a) is marked by the blue cross in panel b.

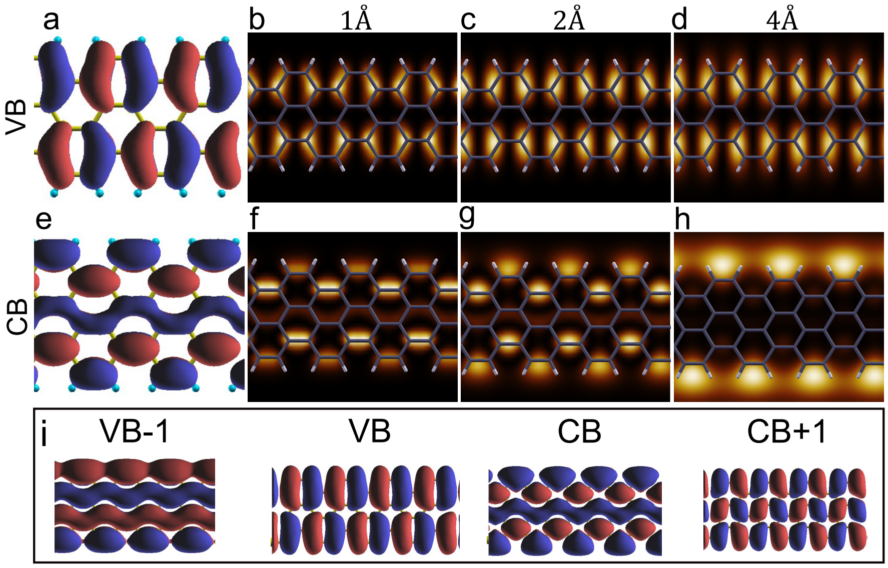

**Figure 5.7: DFT calculations displaying the differently fast orbital decay towards vacuum for VB and CB. (a,e)** Wave functions of the VB and CB, and **b-d** simulated STM images integrating 100 mV around its onset at distances of (b) 1 Å, (c) 2 Å and (d) 4 Å above the carbon backbone. The contrast in simulated STM images is saturated to their maximum range in each of the cases. **(i)** Wave functions for VB-1, and CB+1 are added to those of the VB and CB for comparison of their symmetries, from which the VB-1 is expected to display a similar behavior to the CB, while the CB+1 is expected to behave rather like the VB in terms of their height dependence or the orbital decay toward vacuum.

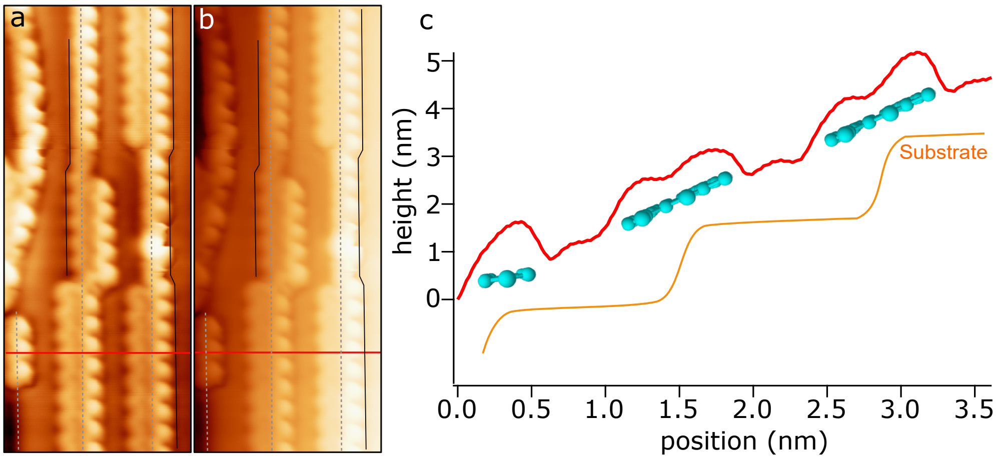

**Figure 5.8: Tilted structure of 6-aGNRs. (a)** Constant-current STM image (with and without a subtracted plane to emphasize the molecular structures or the topography, respectively) marking the step positions (dashed grey lines). Their position with respect to poly-*para*-phenylene chains are extracted from their imaging on incompletely covered steps (e.g. left step, lower area). Position of adsorbate-decorated steps are in turn marked according to areas covered with PPP and its known alignment relative to the steps. The 6-aGNR edges shift (as compared to the alignment of the connected PPP segments, marked with solid black lines) towards the upper (lower) terrace when they fuse with a second PPP wire from the lower (upper) terrace. The result is a tilted 6-aGNR across the steps of Au(322). **(b)** Profile along the marked red line in (a), together with an approximate schematic representation of the substrate, PPP and 6-aGNR structures positions. Constant current imaging parameters: $I_t$ = 102 pA, $V_s$ = -0.92 V.

## 5.3 Conclusions

In conclusion, we prove a new strategy toward the selective synthesis of GNRs, namely the use of substrate templating. Combining a stepped Au(322) surface and DBTP precursors, we report the first selective synthesis of 6-aGNRs. Furthermore, the uniaxial alignment imposed to the products by the substrate has allowed us characterizing the electronic properties of 6-aGNRs by angle resolved photoemission, in addition to density functional theory calculations and scanning tunneling microscopy/ spectroscopy. Thereby, not only the bandgap, but also another important figure of merit in GNRs has been accessed, as is the valence band's effective mass.

# Part III

# Chiral Graphene Nanoribbons

The synthesis of atomically-precise GNRs has fruitfully produced a large variety of armchair and chevron-like ribbons.[11,16,118,122,129–133,139,140,143–145,150,242,289,290] However in comparison, known examples of zigzag and chiral GNRs are really limited. The scarce examples of zGNRs[117,153,255] can be explained by the higher reactivity of their edges, which may show a pronounced interaction with the substrate thus hampering an effective on-surface growth. As well, chGNRs are largely unexplored to date, although they represent an interesting type of GNRs since different calculations state that their electronic structure can display both the width-modulated semiconducting band gap of aGNRs and the localized edge states of zGNRs.[49,59–63] The few examples found in literarute just report on their synthesis,[201,291–294] but do not address their innate electronic structure.

The third part of this thesis aims to explore chGNRs. In the forecoming chapters, we firstly focus on key synthetic aspects such as the impact of the halogenated positions within the molecular precursor and its innate chirality on the synthesis of chGNRs. Lastly, we study their electronic structure and how it can be modulated from a semiconducting to a metallic behaviour, giving rise to the emergence of localized edge states.

# Chapter 6

# Substrate-independent growth of chiral graphene nanoribbons

The result of the bottom-up methodology employed by Cai and coworkers in 2010 afforded the synthesis of the first armchair graphene nanoribbon with atomic precision, i.e. 7-aGNR, on Au(111) and Ag(111)by the use of 10,10'-dibromo-9,9'-bianthracene (DBBA) molecular precursor.[11] Surprisingly, the use of the same precursor on Cu(111) resulted in the formation of (3,1)-chGNRs.[291,295] This result was subject to debate since the polymerization does not involve the carbon atoms attached to bromines.[296–298] However, the debate was settled by unambiguous high-resolution imaging of the resulting bonding structure.[201] In fact, the same (3,1)-chGNRs were obtained from the dichlorinated and non-halogenated version of DBBA precursor,[201,292] underlining how the higher catalytic activity of Cu(111) favores the C-H activation at C2(2') positions over the carbon-halogen scission at C10(10') positions, indicating that the surface-assisted dehydrogenative coupling outweigh the Ullmann-like route observed for dibrominated precursors on Au(111). These examples evidence the delicate balance between carbon-halogen and surface-assisted C-H activation, dictated by the specific halogen and substrate employed in every case.[299] Moreover, as recently observed on the intermediate reactive surface Ag(111), the use of the dichlorinated precursor resulted in the formation of both 7-aGNRs and (3,1)-chGNRs,[294] showing how the ratio between these two can be tuned by the reaction parameters (i.e. the sample annealing slope) and the presence of co-adsorbed species. Additionaly, the precursor shape and so their adsorption configuration, can have a determining impact on the reaction pathway.[292] All these different synthetic scenarios highlight a complex interplay between the halogen-carbon scission energy, the substrate catalytic effect, the precursor geometry, the reaction kinetics, and the influence of different species.

Nevertheless, these observations inspired the results of this chapter in which we exchange the halogenated position in the pionneer DBBA precursor to test its impact in the formation of GNRs in different metallic surfaces. This has been shown to work independently of the used substrate, as proven with growth studies on Au(111) and Ag(111). A similar study on Cu(111) is out of the scope of this chapter due to the readily proven growth of (3,1)-GNRs from precursor 1 (and even from non-halogenated precursors) on that substrate.[201,292] However, also on Cu(111), we show how changing the halogen functionalization site, and thereby changing the polymerization mechanism from a selective C-H bond activation to Ullmann coupling, is still a significant advancement by greatly increasing the resultant GNR length. These results are published in ref.[284]

## 6.1 Synthesis of (3,1)-chGNRs on Au(111) and Ag(111)

In particular, the bromine atoms in positions 10,10' of precursor 1 (Figure 6.1.a) are shifted to positions 2,2' in precursor 2 (Figure 6.1.b) , which are the positions selectively activated on Cu(111) and through which the polymerization preceding the (3,1)-chGNR formation takes place. Starting from precursor 2, the reaction pathway associated with the surface-supported synthesis of (3,1)-GNRs is closely related to the well-known transformation of precursor 1 into 7-AGNRs.[11] That is, in a first step, the molecules polymerize by Ullmann coupling into polymer 2. This polymer is a highly non-planar molecular structure in which the steric hindrance between the hydrogen atoms in neighboring anthracene units drives their alternating tilting. As a consequence, the polymer's imaging by STM displays a sequence of protruding features that we associate with the up pointing ends of the anthracene units (Figure 6.1.b). This correspondence is highlighted by yellow circles in the wireframe chemical structure and in the STM image. In a following reaction step, CDH sets in and polymer 2 transforms into the planar (3,1)-chGNR structure, as can be directly discerned in the high-resolution STM images in Figure 6.1.b.

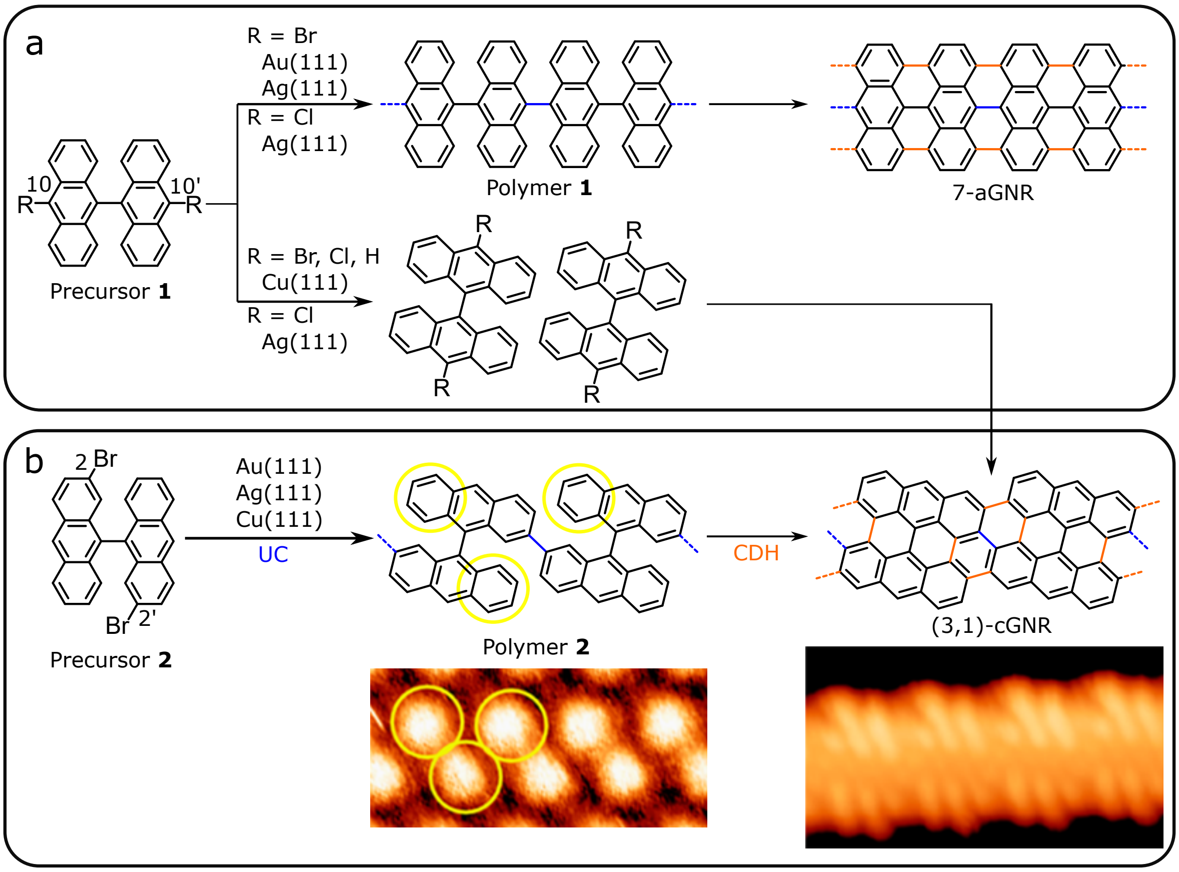

**Figure 6.1:** **(a)** Schemes of the chemical reactions of precursor 1 on various metallic surfaces. On Au(111) and Ag(111), it affords armchair GNRs. On Cu(111), it affords chiral (3,1)-GNRs. **(b)** Our work (highlighted with the red line) reports the transformation of reactant 2 into chiral GNRs independently of the substrate [Au(111), Ag(111), and Cu(111)]. Associated STM images are shown for poly-2 after initial polymerization by Ullmann coupling (5.6 nm x 2.2 nm, $I_t = 0.09$ nA,$V_s = 1.5$ V), as well as for the final (3,1)-GNR after cyclodehydrogenation (5.6 nm x 2.2 nm,$I_t$ = 0.2 nA, $V_s$ = -650 mV), both on Au(111). Steric hindrance causes poly-2 to be nonplanar. The high parts (circled in yellow) are correspondingly marked in the polymer's wireframe structure above.

Figure 6.2 summarizes, as observed by STM, the growth process of (3,1)-chGNRs on top of Au(111) and Ag(111). On either substrate, the images correspond to the same sample at different stages of its growth: after deposition of precursor 2 on substrates held at room temperature, after being annealed to 150°C, and after being annealed to 205 °C.

We first focus on Au(111) (Figure 6.2, top). After room temperature deposition, the molecules aggregate into islands of linear structures formed by a zig-zag arrangement of protrusions comparable to those expected from polymer 2 (Figure 6.1a,b). Upon annealing to 150 °C, we observe clear changes in the sample's topology. It is difficult to discern changes in the STM contrast within the linear structures. The periodicity along the chains on Au(111) changes from 8.6 ± 0.6 Å at RT to 8.3 ± 0.6 Å at 150 °fC. Thus, in spite of their difference, the clear overlap of the error margins doesn't allow concluding structural changes from

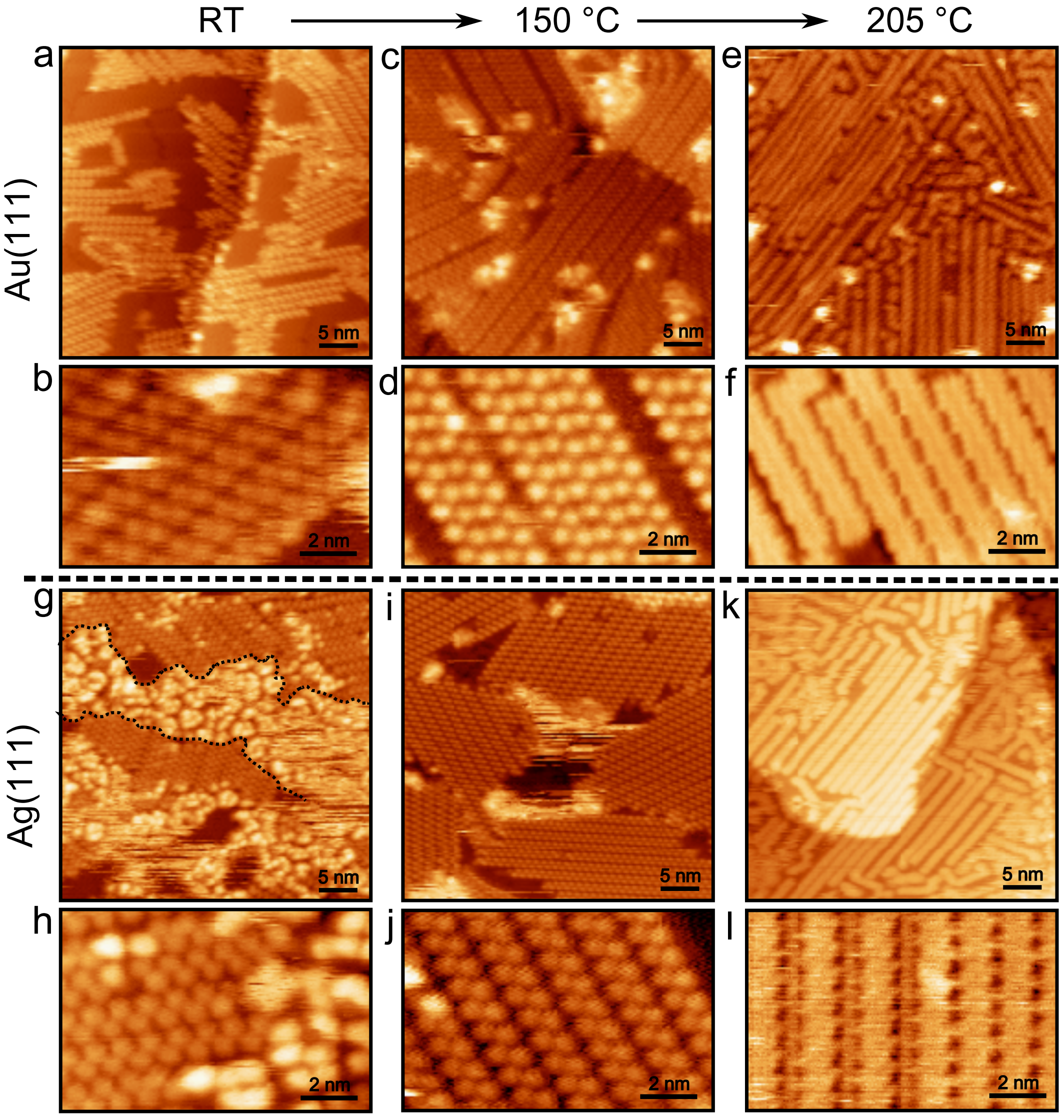

**Figure 6.2: Growth of (3,1)-chGNRs from precursor 1 on (top) Au(111) and (bottom) Ag(111). (a-f)** Large-scale (36 nm x 36 nm) and smaller-scale (10 nm x 6.5 nm) STM images on Au(111) and **(g-l)** Ag(111) of the same samples at different growth stages: **(a,b,g,h)** after deposition on substrates held at RT, **(c,d,i,j)**and after being annealed to 150°C, and **(e,f,k,l)** to 205°C. STM imaging parameters are (a) $I_t$ = 0.086 nA, $V_s$ = 1.4 V; (b) $I_t$ = 0.086 nA, $V_s$ = 1.5 V; (c) $I_t$ = 0.16 nA, $V_s$ = 1.76 V; (d) $I_t$ = 0.16 nA, $V_s$ = 1.76 V; (e) $I_t$ = 0.16 nA, $V_s$ = 0.47 V; (f) $I_t$ = 1.29 nA, $V_s$ = -0.13 V; (g) $I_t$ = 0.09 nA, $V_s$ = 1.5 V; (h) $I_t$ = 0.06 nA, $V_s$ = -2.02 V; (i) $I_t$ = 0.36 nA, $V_s$ = 1.76 V; (j) $I_t$ = 0.36 nA, $V_s$ = -1.6 V; (k) $I_t$ = 0.42 nA, $V_s$ = 1.07 V; and (l) $I_t$ = 0.19 nA, $V_s$ = -0.13 V.

these measurements. Instead, we infer chemical changes from RT to 150 °C from the rest of morphological changes in combination with the determining XPS analysis (shown in the next section). After annealing at 150 °C, the overall length of the chains substantially increases and the spacing between them (perpendicular to the structure's long axis) becomes less regular and decreases the minimum distance (Figure 6.2.c,d). Annealing to 205 °C brings about more notorious changes, displaying arrays of planar structures clearly recognizable from the edge topology as (3,1)-GNRs (Figure 6.2.e,f).

In the case of Ag(111), two distinct sections are observed after molecular deposition at room temperature. On the one hand, we find regions of ordered, linear structures packed side by side (Figure 6.2.g). The linear structures are imaged again as zig-zagging protrusions (Figure 6.2.h). Instead, other regions display a disordered arrangement of adsorbates with increased mobility and a much larger apparent height ($\pm$ 2.7 Å vs $\pm$ 1.8 Å). The areal ratio between these two different sections is approximately 1:1 (Figure 6.2.h). Annealing to 150 °C brings about the growth of the ordered, linear structures at the expense of the disappearing disordered regions (Figure 6.2.i,j). As opposed to the findings on Au(111), on Ag(111), the arrangement within the ordered arrays of linear structures remains unchanged after this annealing. Annealing the sample to 205 °C triggers the cyclodehydrogenation and thereby the ultimate formation of (3,1)-GNRs (Figure 6.2.k,l).

## 6.2 Growth characterization by temperature-dependent XPS

Complementary information on the chemical transformation process is obtained from core-level XPS measurements. As in the STM experiment, molecules were deposited on Au(111) and Ag(111) substrates held at room temperature. The samples were then annealed stepwise while their Br 3p and C 1s core-level spectra were monitored. The data are summarized in Figure 6.3.

On Au(111), the molecules remain intact upon deposition at room temperature and only start showing chemical changes for substrate temperatures of around 125 °C. As the temperature increases above that threshold, the most evident change in the core-level spectra is a pronounced shift of the Br 3p peaks to ∼2 eV lower binding energies. This effect is well-known from other studies on Ullmann coupling of different precursors and relates to the dehalogenation process and the new chemical environment as Br detaches from the organic molecule and binds to the metallic surface.[131,283,300] Concomitantly, the C 1s peak displays a smaller shift (∼0.3 eV) to lower binding energies. Similar C 1s shifts have also been observed in previous studies on Ullmann coupling with different precursors an surfaces, for which a variety of explanations have been given: (i) bond formation between the carbon atoms hosting the generated radicals and the substrate atoms or adatoms,[283,300] (ii) a change in the supramolecular assembly prior to dehalogenation that brings about changes in the interaction with the substrate,[131] or (iii) a change of work function caused by the chemisorption of Br to the substrate.[283] We discard the first because on Au the formation of organometallic compounds is disfavored and the molecules are known to polymerize as the radicals are formed.[157,301] We also discard the second because we observe the C 1s and Br 3p shifts simultaneously in a correlated way. Thus, we ascribe the observed C 1s shift to the change of work function generated by the metal-bound Br atoms. Besides, this is further supported by the changes observed in the core levels as the temperature is increased further: as Br desorption starts to set in, the C 1s level shifts in the opposite direction, toward higher binding energy. A similar shift on closely related systems has also been ascribed to different reaction processes like the transformation from an organometallic to a polymer phase[300,302] or cyclodehydrogenation.[283] In addition to the chemical change, these reactions also cause an alteration in the molecule-substrate distance that may, in turn, additionally affect the core hole screening effects and thereby the core-level spectra. However, we can again discard these justifications for our system because we know the polymerization and cyclodehydrogenation to occur at

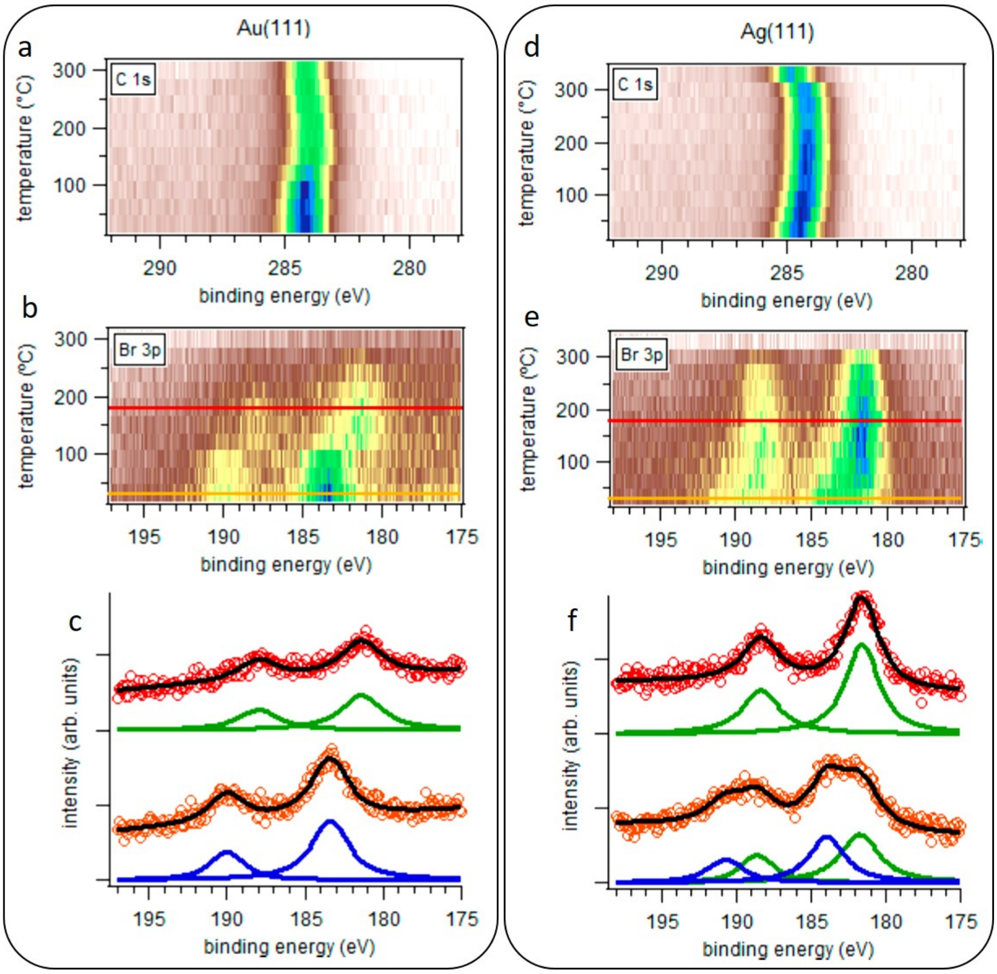

**Figure 6.3: Temperature-dependent XPS monitoring of chGNRs growth from DBBA precursor2.** Photoemission spectra of the C 1s core levels of precursor 2 deposited on **(a)** Au(111) and **(d)** Ag(111) held at room temperature and their evolution as a function of sample annealing temperature. **(b,e)** Similar measurements of the Br 3p core levels. **(c,f)** Br 3p spectra, together with their associated fits (blue and green lines correspond to organic and metal-bound Br components, respectively), of two representative temperatures marked with the colored lines in (b) and (e), respectively. The spectra are shifted along the intensity axis for better comparison.

lower temperatures. Altogether, XPS on Au(111) thus shows that the structures observed on Au(111) at room temperature are a non-covalent self-assembled supramolecular arrangement, polymerizing only upon annealing above 125 °C, in line with the overall sample topology changes observed by STM at 150 °C and described above.

On Ag(111), the molecules are readily partially dehalogenated upon deposition at room temperature. This is clearly observed in the Br 3p core-level spectra, which shows the coexistence of organic and metal-linked Br atoms in a 1:1 ratio. As the temperature is increased, the metal-bound Br increases at the expense of the organic Br. From the correlation with the STM observations, we can readily ascribe the pristine precursors to the disordered structures found at room temperature and the dehalogenated molecules to be the building blocks forming the ordered structures. As in Au(111), the dehalogenation brings about a minor shift to lower binding energy in the C 1s spectrum, which shifts back again as the Br is desorbed at higher temperatures. Again, we ascribe the dominating effect behind the C 1s shifts to the changes in work function as Br binds or leaves the metal surface. However, spectroscopy-wise, this leaves the question open as to what is the nature of the linear, ordered structures formed by the dehalogenated precursors. Do those radical species link covalently or via metal-organic coordination, as is commonly the case on Ag at temperatures below ~ 150 °C. In the absence of clear spectroscopic fingerprints, the answer will be given based on periodicity analysis along the one-dimensional structures, organometallic structures typically having significantly larger periodicities than polymers.[301,303,304]

## 6.3 Covalent or metal-organic? : Linear periodicity analysis

DFT calculations for freestanding structures predict periodicities of 9.52 Å for the metal-organic chain (Figure 6.4.c), 8.21 Å for the polymer (Figure 6.4.b), and 8.96 Å for the flat (3,1)-GNR (Figure 6.4.a), the latter in good agreement with the value of 8.89 Å that results from assuming an undisturbed graphene lattice for the GNR. Our STM measurements reveal the periodicity of the GNRs to be 9.0 ± 0.8 Å, excellently fitting the calculations. For the nonplanar structures, we observe the same periodicity at room temperature and after annealing to 150 °C, with an average value of 8.2 ± 0.7 Å. The value is similar to that of poly-2 on Au(111) (8.3 ± 0.6 Å) and in excellent agreement with a polymeric phase, with the error margins remaining clearly below the metal-organic periodicity (Figure 6.4.d). Thus, in spite of the flexibility associated with the nonplanarity of polymer 2 and the metal-organic chain, which may introduce minor uncertainties in the calculated periodicities, the results still allow us to conclude that the polymer is directly formed after dehalogenation.

As only reported with a few other systems,[305] we thus observe a covalent polymer formation readily at room temperature instead of the metal-organic intermediates reported with most precursors linking through Ullmann coupling on Ag(111) and Cu(111).[157,283,301,302] The reason behind this may be sought in the different coordination geometry imposed by the nonplanar precursors, readily known to be a critical aspect in the coupling pathway followed by this family of aromatic precursors.[292] As observed in most previous Ullmann coupling studies on Ag surfaces, Ag atoms present linear coordination geometry,[157,301,302] while the anthracene units hosting the generated radicals upon dehalogenation of precursor 2 display a strong tilt with respect to the substrate plane due to the steric congestion within the or-

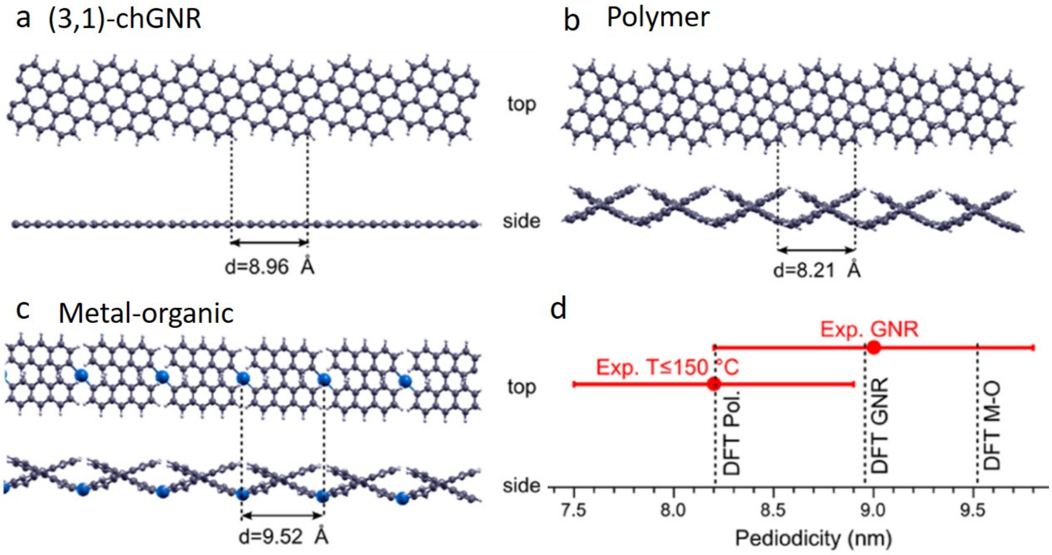

**Figure 6.4:** Relaxed structures for (a) free-standing (3,1)-GNRs, (b) poly-2, and (c) metal-organic chains. (d) Comparison of the periodicities of the calculated structures with those measured experimentally for the GNRs and for the nonplanar structure on Ag(111). The latter fits the polymer period, and its error margin (shown as the standard deviation) is well below the periodicity of the metal-organic chain.

ganic backbone (Figure 6.4.c). Under these circumstances, and based on our experimental observations, we conclude that the metal-organic intermediate is not sufficiently stable and the reaction directly proceeds toward the polymeric phase.

## 6.4 GNRs' length dependence on reactions temperature

As noted above, at 205 °C, the GNRs are fully cyclodehydrogenated on both Ag(111) and Au(111). Similarly, low cyclodehydrogenation temperatures (177 °C) are reported for precursor 1 on Ag(111),[129] but higher temperatures, similar to those required on Au(111), are needed to really form GNRs (377 °C).[11,129] On Cu(111), the required temperature for fully cyclodehydrogenated GNRs to be formed is 250 °C.[201,297] Most remarkably, precursor 2 renders fully dehydrogenated GNRs at significantly lower temperatures than precursor 1 even on the low reactivity Au(111) surface. This surprisingly large change relates to the substantially altered strain in the two polymer structures since sterically induced strain is known to weaken the involved C-H bonds and thereby lower the cyclodehydrogenation barriers.[306,307] In polymer 1, the anthracene units are linked covalently along their short axis by a bond that allows free rotational movement with respect to their neighbors. This freedom results in alternatively tilted anthracene units along the polymer backbone so as to minimize the steric hindrance from opposing H atoms. Instead, the anthracene units within polymer 2 are linked covalently to their neighbors both along their long and short axes. Thus, although the anthracene units still display the same alternative tilt to reduce the steric hindrance, the covalent bonds along the long anthracene's axes limit the structure's rotational freedom, resulting in a substantially strained geometry. It is this strain opposing the anthracene's tilting which favors the planarization of the structure and thus reduces the cyclodehydrogenation temperature threshold regardless of the substrate.

Both on Ag(111) and Au(111), the cyclodehydrogenation threshold is between 150 °C, at which no cyclodehydrogenation is observed, and 205 °C, at which the whole sample has readily become fully planar (Figure 6.2). On Ag(111), where polymerization readily starts at room temperature, there is still a substantial temperature gap before the onset of cyclodehydrogenation. However, on Au(111), the threshold temperatures for polymerization (∼125 °C) and cyclodehydrogenation are in close proximity. This may have an impact on the growth process and the resulting GNRs since liberated H in the cyclodehydrogenation process could quench the available radicals and terminate the polymerization. To shed light on this issue, we have increased the number of sampling temperatures, figuring the cyclodehydrogenation onset on Au(111) to be below 175 °C, at which most of the sample has readily become a planar GNR but some of the polymer units still remain unreacted (inset in Figure 6.5) A systematic GNR length analysis of samples as a function of the substrate temperature upon reactant deposition is shown in Figure 6.5, with all samples having coverages of around 0.8 ML. For temperatures below the cyclodehydrogenation threshold, a second annealing step to 205 °C was applied to the sample for GNR formation before performing the length analysis.

Representative distributions for selected temperatures are shown in Figure 6.5a, making immediately obvious that high temperatures narrow the distribution significantly and prevent formation of long GNRs. Because of the asymmetric length distribution, we take the median length as a representative value and plot it versus substrate temperature upon first deposition (Figure 6.5b). We observe an important drop in the length with increasing temperature once the cyclodehydrogenation threshold is passed. Under this scenario, radical step growth and cyclodehydrogenation take place simultaneously. Thus, radical quenching by liberated H atoms competes with the radical stepgrowth polymerization. Deposition on Au held at room temperature and subsequent annealing to cyclodehodrogenation temperatures suffers from the same effect because the precursors on the surface remain intact at room temperature, and bothpolymerization and cyclodehydrogenation occur during the same subsequent annealing process. However, the length-limiting effect is less pronounced, among other reasons, due to the finite heating rate. Longest GNRs are obtained at substrate temperatures that first activate polymerization, only to form the GNRs in a subsequent annealing process. Under these circumstances, GNRs in excess of 30 nm can be easily obtained, well beyond the longest (3,1)-GNRs obtained from 1 on Cu(111).[295] Moreover, additional studies to maximize GNR lengths by optimizing surface coverages or heating rates may bring about even further improvements in the future.

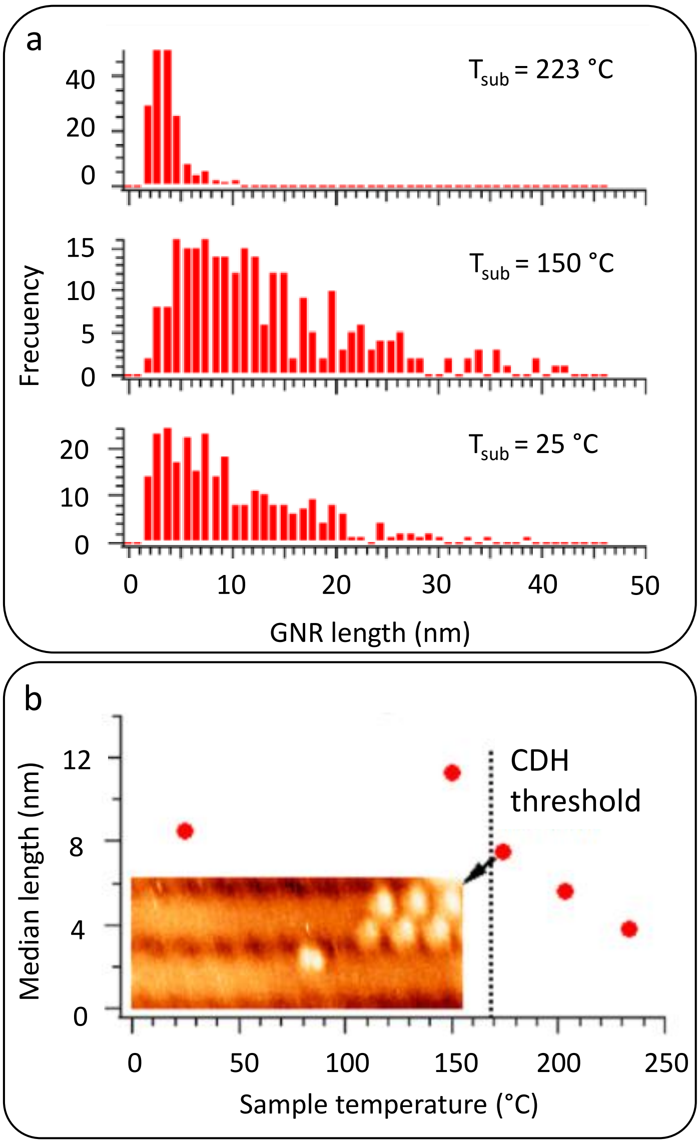

**Figure 6.5: (a) Length distribution of GNRs grown on Au(111)**, at coverages close to the full monolayer, for different substrate temperatures upon first deposition. For temperatures below the cyclodehydrogenation threshold (T < 174 °C), a second annealing step to 205 °C was applied to the sample for GNR formation by cyclodehydrogenation. **(b)** Median length for each substrate temperature. The inset depicts an STM image (7.4 nm x 2.9 nm, $I_t$ = 0.16 nA, $V_s$ = 0.47 V) of a sample deposited at 174 °C, revealing a mostly, but not yet fully, cyclodehydrogenated structure. This value has been thus taken as the cyclodehydrogenation threshold temperature.

## 6.5 Synthesis of (3,1)-chGNRs on Cu(111)

Lastly, we have confirmed the suitability of this molecular precursor to form longer (3,1)-GNRs than precursor 1 also on Cu(111). This is shown in Figure 6.6 and underlines the great advancement provided by this new GNR precursor. In addition to the (3,1)-GNR formation, a concomitant etching of triangular holes into the remaining uncovered Cu(111) surface is observed, lined along their sides by Br atoms (Figure 6.6.a). A detailed study and description of this process, however, is beyond the scope of this paper. We also want to note that the GNR length analysis of this sample on Cu(111) (Figure 6.6.c) should not be compared with that on Au(111) (Figure 6.6) because the growth was performed in a different chamber with different coverage and a different heating rate, two parameters that may play an important role in the length distribution. However, most importantly, we want to remark that, different from what occurs with precursor 1 on Cu(111), the precursor 2 allows on the one hand to grow chiral GNRs on different materials not relying on specific and strong molecule-substrate interactions. On the other hand, on all surfaces studied, it forms long GNRs that easily exceed several tens of nanometers, a great advantage for their implementation in actual device structures.

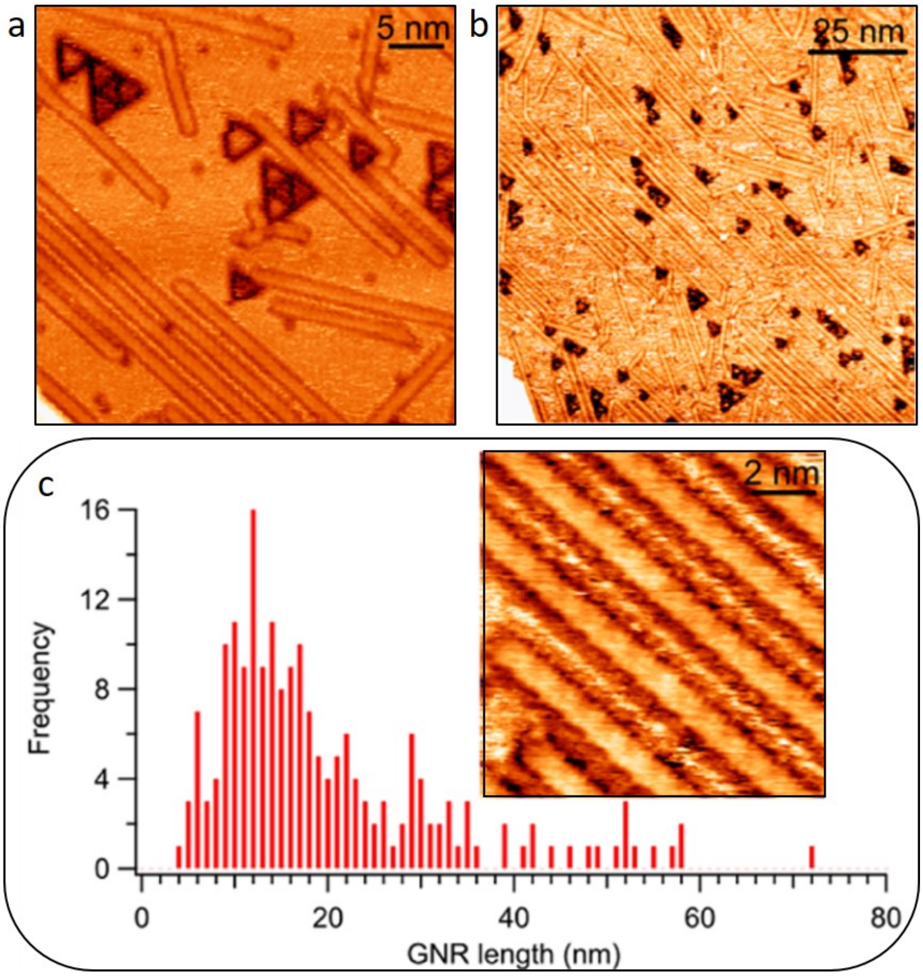

**Figure 6.6: (3,1)-chGNRs growth on Cu(111). (a,b)** Constant-current STM images (a) (36 x 36 nm$^2$ , $I_t$= 0.58 nA, $V_s$= -400 mV) and (b) (100 x 100 nm$^2$ , $I_t$= 0.05 nA,$V_s$= -200 mV). **(c)** GNR length distribution as obtained from large-scale images as in (b), showing a significant portion of GNRs to be longer than 40-50 nm and the average and median length values well above those of GNRs grown from precursor 1 on Cu(111). The inset depicts a 10 x 10 nm$^2$ close-up view of the GNRs ($I_t$= 1.0 nA, $V_s$= -150 mV).

## 6.6 Conclusions

In conclusion, inspired by the previously reported system-specific growth of (3,1)-GNRs on Cu(111) from precursor 1, we have designed an alternative precursor 2 that renders the same (3,1)-GNRs but now independently of the substrate material. This has been proven on Au(111), Ag(111), and Cu(111), revealing additional advantages of the use of this monomer in the growth of selective and atomically precise GNRs, as is the substantially increased length of the resultant GNRs and the low processing temperature required for their formation. Furthermore, the growth process has been followed in detail combining corelevel spectroscopy, scanning tunneling microscopy, and density functional theory calculations, providing a clear correlation between the spectroscopic fingerprints and the different reaction processes, as well as revealing the unusual absence of a metastable metal-organic intermediate preceding the covalent polymerization in the Ullmann coupling process on Ag(111).

# Chapter 7

# Halogen activation hierarchy during surface-promoted Ullmann coupling

In the previous chapter we show how the smart pre-design of the halogenated position in the molecular precursor can result in the controlable synthesis of the desired graphene nanoribbons on different metallic surfaces. Since the first coupling mechanism between monomers involves the cleavage of carbon-halogen bonds, those halogenated positions rule the formation of the final graphene nanoribbons after cyclodehydrogenation. This fact highligths the remarkable relevance and versatility of Ullmann coupling in the controlled synthesis of carbon-carbon covalent bonds, and therefore in the formation of complex one- and two-dimensional structures.[12,111,162,308] A step beyond the controlled synthesis of C-C covalent bonds resides in the development of hierarchical synthetic processes, this is, controlled sequences of reactions which promote the correct step-by-step connection of molecules in the formation of complex molecular structures. With Ullmann coupling, this hierarchy can be achieved by functionalizing the carbon backbone with different halogens, since each of them features different energy barriers for the scission of its carbon-halogen bond.[146,290,309–314] Thus, if an energy gradient is provided to the sample (e.g. common thermal annealing), we can control the order in carbon-halogen bonds scission and promote a controlled multi-step coupling of the precursors.

In this chapter we show how, even when using the same halogens, a selective activation of specific C-Br bonds can be obtained depending on their location within the same aromatic precursor. Our combined STM, XPS measurements and DFT simulations reveal that this site-selectivity is driven by the substrate and the X shape conformation of the precursor. At the preferred adsorption configuration of the precursor, the halogens display different distances to the metal surface, which leads to a strongly modulated catalytic effect of the substrate for each C-Br bond.

## 7.1 Growth of GNRs from TBBA precursor

The precursor employed in this case is 2,2',10,10'-tetrabromo-9,9'-bianthracene (TBBA, Figure 7.1.a). In the previous chapter we commented on the reactivity of similiar dibrominated precursor with halogens atoms either located at 2(2') or 10(10') positions. The former renders chGNRs on Au(111), Ag(111) and Cu(111) (Figure 7.1.c,e). The latter forms aGNRs on Au(111) and Ag(111) (Figure 7.1.b,d), and chGNRs on Cu(111), where the coupling selectivity given by the halogen excision is overruled by the higher catalytic effect of the susbtrate. It remains unclear which would be the dominant route on a less catalytic substrate using a precursor with haloge atoms at both 2(2') and 10(10') positions. Here, we employ TBBA precursors (Figure 7.1.a) on Au(111) in an attempt to specifically address this interplay.

After TBBA deposition, UC is thermally-induced at ~450 K and TBBA precursors form bianthrylene polymers. Figure 7.2 shows different scale STM images of this phase. As observed also with either type of DBBA reactants, the polymers appear aggregated into islands, indicating the presence of attractive intermolecular forces. These polymers are seen as a series of zigzagging lobes corresponding to the up-pointing termini of anthracene subunits. The latter arrange in an alternatingly tilted non-planar configuration to minimize the steric hindrance exerted by the neighbouring hydrogen atoms. Because this zigzag-display is shared by both armchair and chiral GNRs,[11,284] an unambiguous determination of the polymer structure is not straightforward at this point.

Figure 7.2 also reveals the presence of a disordered network surrounding the polymeric islands and spreading over the remaining Au(111) surface. A closer look reveals that this web consists of single circular adsorbates arranged either in line or in a zigzag manner (Figure 7.2.d,e). Similar networks have been observed for submonolayer coverages of halogens on Au(111),[315,316] as well as with other GNR precursors with a large stoichiometric halogen ratio,[311] which leads us to the conclusion that these adsorbates are bromine atoms. This kind of networks has not been observed in polymers formed from similar di-brominated precursors because the halogens are preferentially placed underneath the up-pointing anthracene ends, "hidden" from the scanning probe.[317] The observed Br network is thus assigned to the additional Br atoms as we change from dibrominated to tetrabrominated reactants, which can no longer be incorporated below the polymers. This finding underlines that both 2,2' as well as 10,10' positions are dehalogenated at this stage.

After polymerization, intramolecular CDH is induced by annealing the sample to higher temperatures, thereby turning the polymers into planar GNRs. At this point it is easy to identify from the lateral edge morphology that the resulting product is exclusively (3,1)-

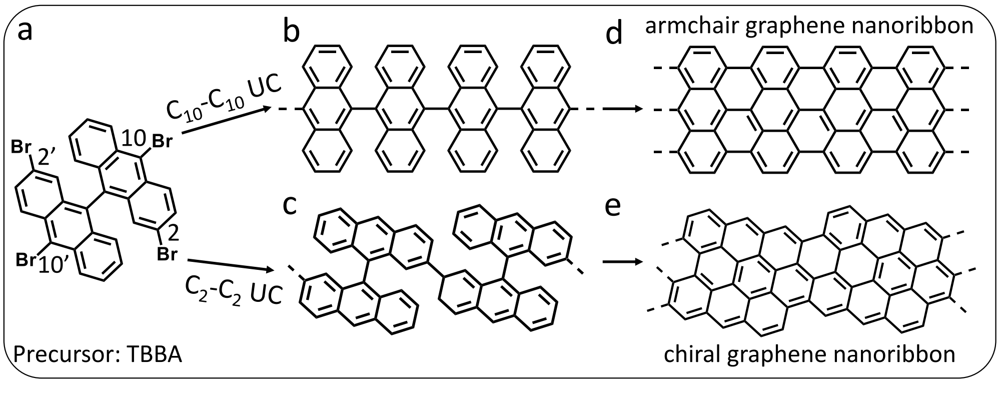

**Figure 7.1: Possible synthetic routes expected from (a) TBBA precursor. (b)** Debromination and $C_{10}$-$C_{10}$ UCfollowed by CDH leads to **(d)** aGNRs formation. **(c)** Debromination and $C_2$-$C_2$ UC leads to **(e)** chiral GNRs formation. Note that primed position *x'* is chemically equivalent to the corresponding unprimed position *x* and either would yield the same GNR.

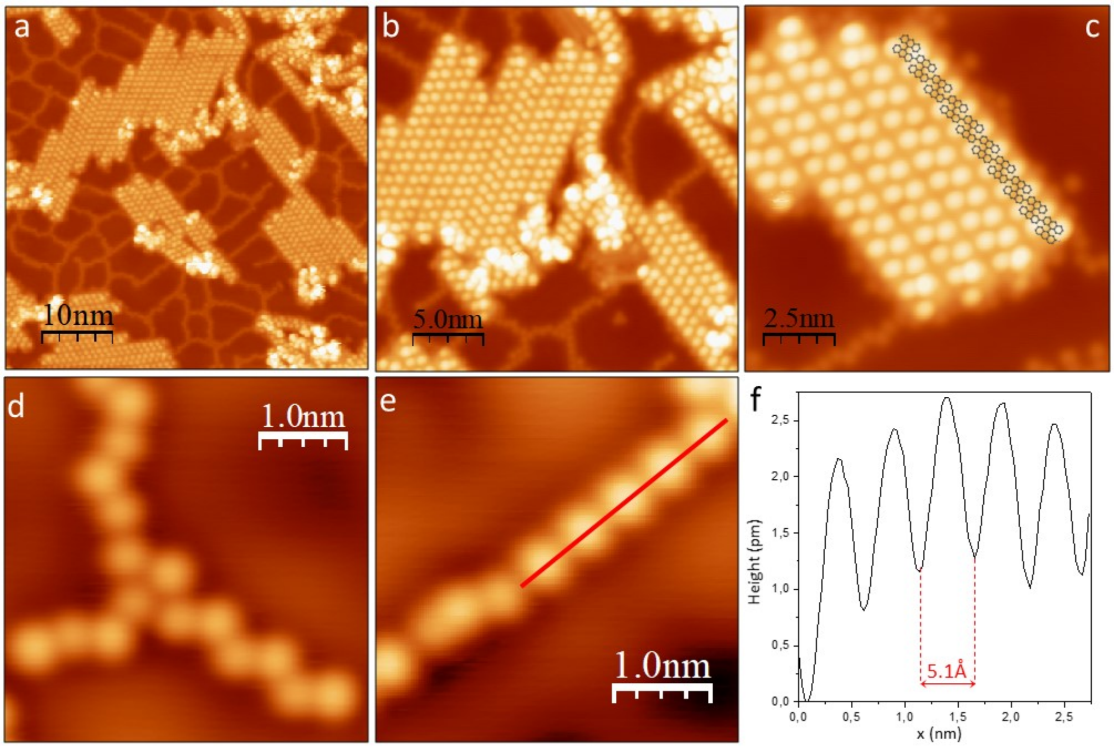

**Figure 7.2: Polymers from TBBA precursor (a-c)** STM images of polymeric phase. (a) 50 nm$^2$ ($V_s$= 1.4 V, $I_t$= 140 pA). (b) 25 nm$^2$ ($V_s$= 1.4 V, $I_t$= 140 pA). (c) 12.5 nm$^2$ ($V_s$= 1.5 V, $I_t$= 1.0 nA) with superimposed wireframe model where only the carbon skeleton is shown. **(d,e)** STM images ($V_s$= 65 mV, $I_t$= 250 pA) showing bromine atoms arranged (d) in zigzag and (e) in line. **(f)** Line profile corresponding to the red line in (e)

chGNRs (Figure 7.3). This implies a dramatically favored UC via the 2,2' positions between the debrominated precursors, which is a surprising result given the well-known preferred reactivity of acenes at their central ring positions.[318–321] Ullmann coupling itself being a multistep reaction, the observed preference may arise from any of the different steps. Reactant diffusion can be discarded because it would affect both halogen positions alike. A difference in the barriers associated to the bond formation between two nearby carbon radicals is also unlikely, since they are typically much lower than the barriers associated with the homolytic cleavage of the C-Br bonds.[322] Thus, the homolytic cleavage seems to be the determining step.

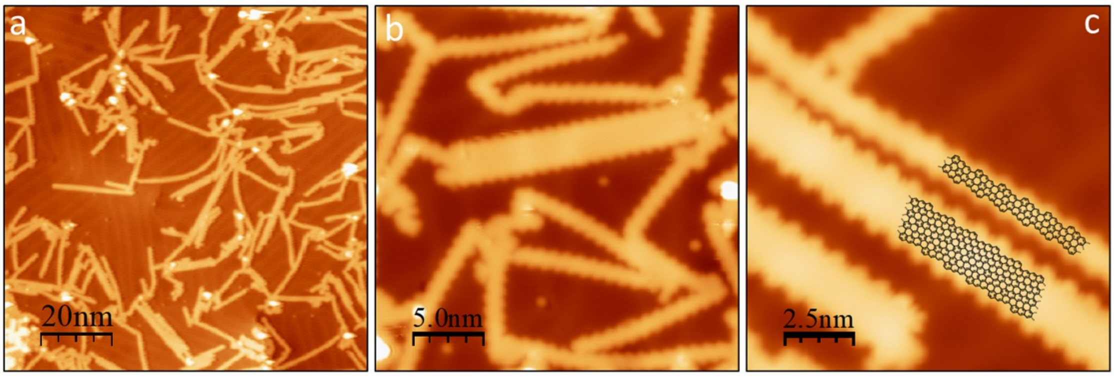

**Figure 7.3: GNRs resulting from TBBA precursor. (a)** 100 nm$^2$ ($V_s$= 1.1 V, $I_t$= 80 pA). **(b)** 25 nm$^2$ ($V_s$= 1.0 V, $I_t$= 120 pA). **(c)** 12.5 nm$^2$ ($V_s$= 50 mV, $I_t$= 0.5 nA) with superimposed wireframe models showing only the carbon backbone.

## 7.2 XPS characterization of carbon-halogen scission

We have indeed proved the sequential Br activation by temperature-dependent XPS measurements. Figure 7.4.a depicts the evolution of Br 3d core level spectra in the temperature range displaying the changes. At low temperatures, the spectra evidence two different sets of Br 3d doublets (marked with green red arrows, respectively), each associated with one of the different Br pairs. As the temperature is raised, the doublet at higher binding energies dissappears first (green arrows), with a relatively sharp transition temperature around 525 K. We thus associate this Br 3d doublet to the Br at 2,2' positions (green arrows). Subsequently, the second doublet also fades (red arrows), although with a smoother temperature dependence. Concomitant with the dissappearance of those two core level doublets, a new one appears at more than 2 eV lower binding energies, associated with the atomic Br adsorbed on the metal surface (blue arrows). Its intensity profile (Figure 7.4.b) as a function of the temperature (at ∼68.9 eV, see the vertical dashed blue line), reveals two distinct increases that correlate with the activation temperatures of each of the 'organic Br pairs', marked respectively with green and red horizontal lines as a guide to the eye. Finally, at around 615 K the Br 3d core level intensity dissappears, evidencing the Br desorption from the surface. Because Br desorbs preferentially as HBr,[317,323] this desorption temperature can be associated with the cyclodehydrogenation temperature, at which H becomes available for Br atoms to combine with and desorb. Although the threshold temperature values extracted from the XPS and STM analyses differ, this may relate to the different chambers and temperature mesurement methods (pyrometer vs. thermocouple, respectively). However, most importantly their combination unambiguously reveals a stepwise activation of the different Br species within the reactant.

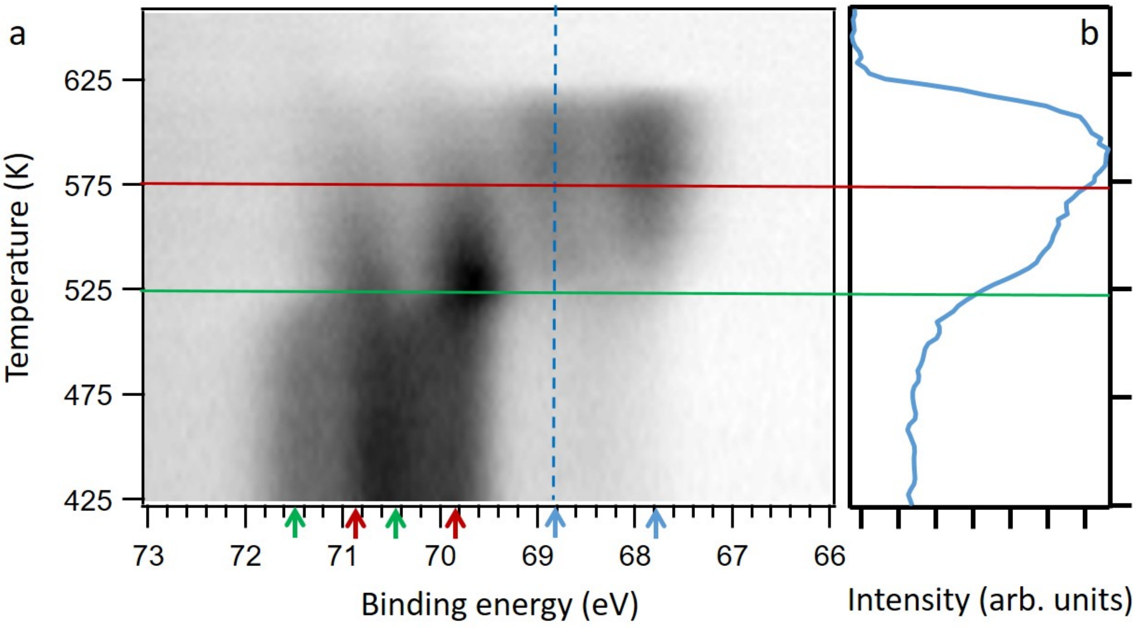

**Figure 7.4: Photoemission spectra of precursor TBBA. (a)** Photoemission spectra of the Br 3d core levels of precursor TBBA and their evolution as a function of sample annealing. **(b)** intensity profile at ∼68.9 eV (vertical dashed blue line) reveals the two distinct intensity increases with temperature.

## 7.3 DFT-calculated adsorption of TBBA on Au(111)

For a better understanding of the experimental findings we performed DFT calculations on this system. We studied the homolytic cleavage of C-Br bonds in TBBA and dibromoanthracene (DBA) molecules in the gas phase and found that the 10,10' positions exhibit a slightly higher reactivity (i.e., a lower C-Br dissociation binding energy) than the 2,2' positions with a marginal difference of 1.1 kcal/mol for both molecules, suggesting that having an additional neighboring DBA subunit (as in TBBA) has a negligible impact on the dissociation binding energy of C-Br bonds (i.e., DBA and the more sterically congested TBBA have almost identical C-Br dissociation binding energies). The preference for 2,2' positions for TBBA on Au(111) surface must thus have a different origin.

To address a possible influence of the substrate, we investigate the relative stability of two adsorption configurations in which the C2-Br can be either oriented towards (Figure 7.5.a) or away from (Figure 7.5.b) the surface. Both configurations show a dihedral angle between the anthracene subunits of ∼127°, consistent with the relatively low energy cost (∼5 kcal/mol) needed to distort from the 90°optimum angle calculated for TBBA molecule in gas phase (Figure 7.6). We find that the adsorption geometry with $C_2$-Br pointing towards the surface is 0.387 eV more favorable, making it the dominant configuration on Au(111). Although as deposited molecules are difficult to image experimentally and display notable polymorphism and disorder, the best recognizable structure indeed fits an assembly of molecules with the $C_2$-Br pointing down (Figure 7.7). Interestingly, in this conformation bromine atoms located at positions 2 and 2' are closer to the surface by ∼0.27 Å than those at positions 10 and 10' (Figure 7.5). A difference that may be further enhanced as the temperature increases, taking into account the vibrational modes of the respective C-Br bonds (with the $C_2$-Br bonds pointing towards the surface more than C10-Br). As the homolytic cleavage of the C-Br bonds can be catalyzed by metallic substrates,[322] we associate this proximity to the substrate with an enhanced catalytic effect on the $C_2$-Br bonds, which in turn promotes the polymerization along the 2,2' rather than along the 10,10' positions.

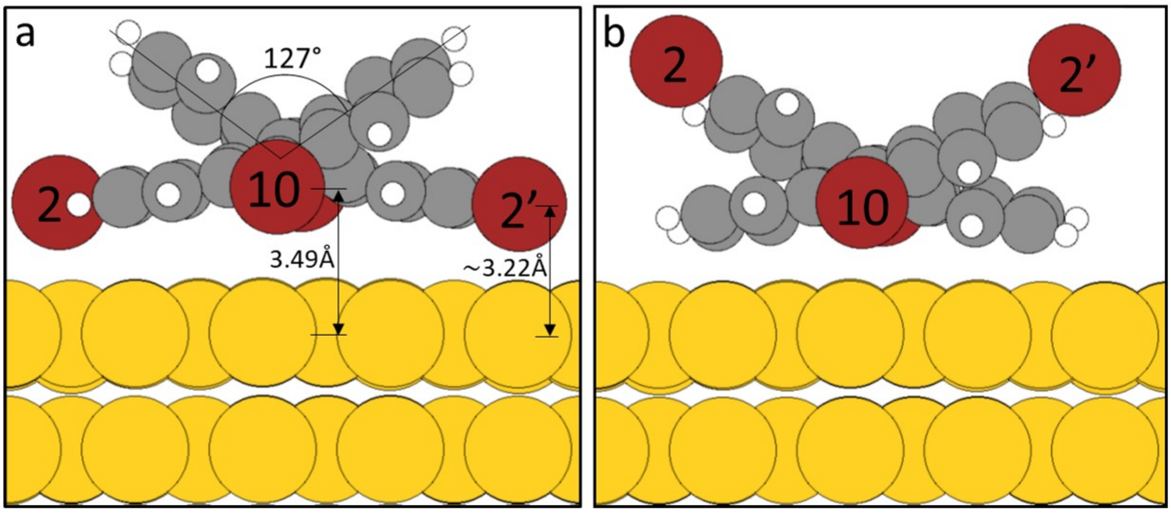

**Figure 7.5: Simulated models for the adsorption of TBBA precursor on Au(111).** Adsorption configuration with C2-Br pointing **(a)** towards or **(b)** away from the surface. The yellow, gray, red, and white spheres represent the Au, C, Br, and H atoms, respectively.

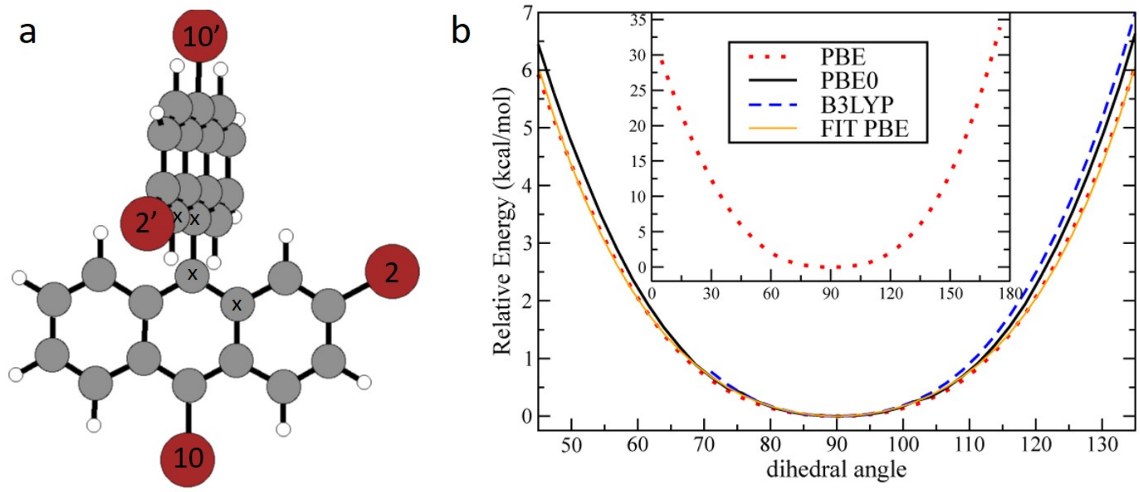

**Figure 7.6: Optimum TBBA conformation in gas phase. (a)** Relaxed structure of gas-phase TBBA calculated at the PBE-D3/def2-TZVP level. The bromine positions (2, 2', 10, and 10') are indicated. This global minimum conformation features a dihedral angle (defined by the 'x' symbols, 0°means eclipsing Br atoms at 2 and 2' positions) of 90°, that is, the two anthracene subunits are perpendicular. The gray, red, and white spheres represent the C, Br, and H atoms, respectively. **(b)** Calculated energy profile for the rotation around the single C-C bond connecting the anthracene subunits of TBBA in gas phase.

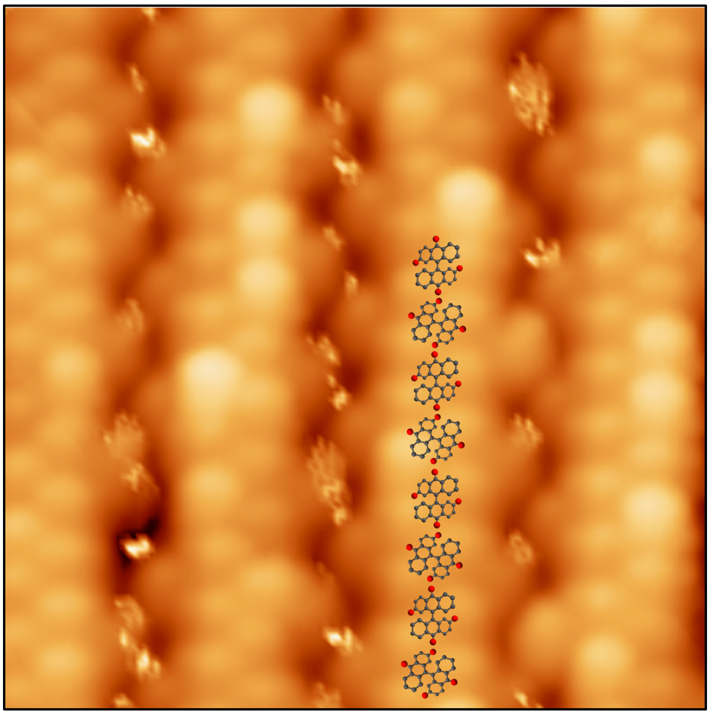

**Figure 7.7: Non-reacted TBBA molecules deposited on Au(111) tentative model of this particular ordered structure**. The molecules display alternating orientation and the structure is presumably stabilized by halogen bonding of the Br atoms along the molecular rows. Only the Br atoms at 10,10' positions and facing out of the molecular rows are observed (every second molecule along the rows), the rest being hidden from the scanning probe by the neighboring up-pointing anthracene units

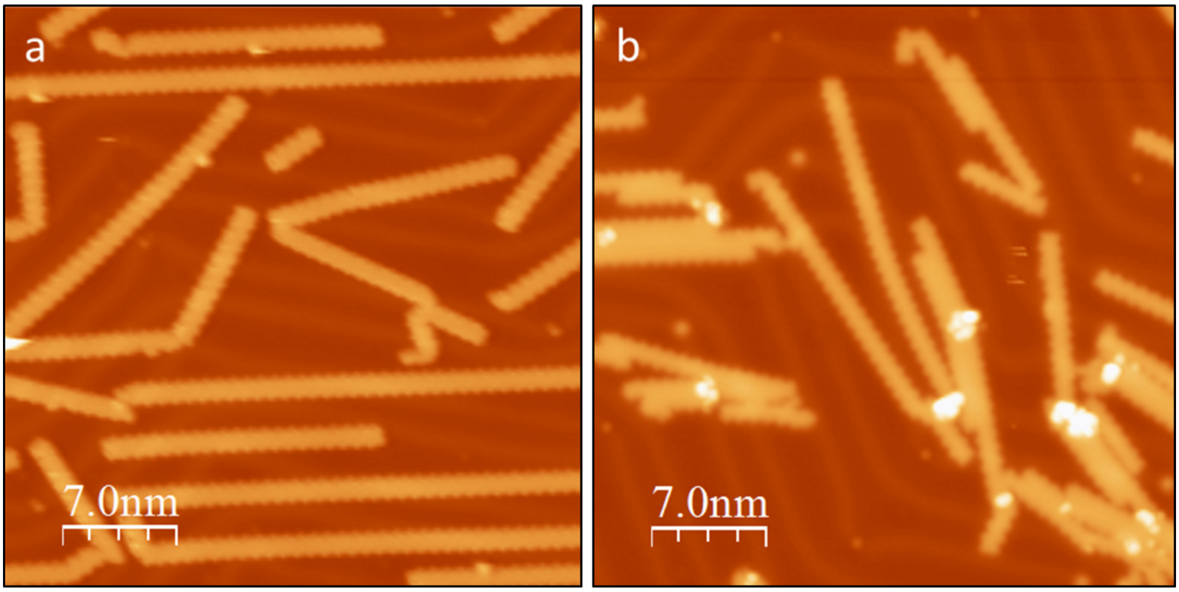

**Figure 7.8: chGNRs from DBBA and TBBA precursors.** Comparative images of samples obtained with **(a)** 2,2'-DBBA after annealing to 590 K ($V_s$= 0.8 V , $I_t$= 20 pA ) and with **(b)** TBBA after annealing to only 530 K ($V_s$= 0.8 V , $I_t$= 50 pA )

Lastly, it is important to note that the chiral ribbons display a variety of widths, which in turn indicates a lateral fusion of the polymers. Although the cyclodehydrogenative fusion of GNRs has been reported earlier and would lead to similar results,[125,129,131–134,274,324] in this particular case it can be discarded. The reason for this is that while samples prepared from 2,2'-DBBA reveal no lateral fusion of the chiral ribbons after annealing to temperatures of 590 K (Figure 7.8.a), starting from TBBA at a similar coverage we observe wider, fused GNRs readily at 530 K (Figure 7.8.b). The additional halogenation thus appears to be an efficient way to increase the chiral ribbons' widths (with its associated impact on their electronic properties[272]) with only mild annealing treatments.

Knowing that 530 K is not sufficient to drive the lateral cyclodehydrogenative fusion, the presence of radicals must be involved. It seems unlikely that GNRs would display radicals at the 10,10' positions because they would most probably be immediately saturated by the hydrogen released in intramolecular CDH. We can thus conclude that the lateral fusion must occur in the polymeric phase, when the polymers may still be displaying the radicals at the 10,10' positions and following the alternative coupling direction outlined in Figure 7.1.b. The fact that most ribbons are only one-monomer wide implies that this lateral coupling is not very effective. This may be ascribed to two different factors that may both contribute, presumably playing together. One is the chiral nature of reactants and polymers, which only allows UC between molecules with the same chirality. The deposited reactants being a racemic mixture, there is a 50% chance for two neighboring polymers to display the same chirality and thereby allow for lateral UC. In addition, the steric hindrance between the up-pointing anthryl units of neighboring polymers sharing the same chirality may interfere and further limit their coupling.

## 7.4 Conclusions

In conclusion, we have evaluated the reactivity of multiple C-Br bonds located at different positions within the same aromatic precursor and observed how the relative distance of the halogens with respect to the substrate results in the selective activation at C2 sites due to the closer proximity to the catalyst. This favored reactivity promotes one of the possible reaction pathways and limits the product formation to chiral GNRs. Particularly interesting is the fact that substrate-favored debromination at C2 position overrules the well-known preferred reactivity of acenes at the central rings (C10 positions in the case of DBBA precursor). Our results underscore the critical influence of the catalytic substrate on surface-assisted Ullmann coupling. We also demonstrate the use of surface adsorption to design new synthetic strategies that redirect the innate reactivity of aromatic molecules. Specifically, surface adsorption can afford new hierarchical synthetic routes even when carbon atoms are functionalized with the same halogen atoms.

# Chapter 8

# Transferring molecular chirality through multi-step reactions

So far in this part, we studied the reactivity of different brominated bianthracene precursors focusing on the type of graphene nanoribbons formed at the end of the synthetic process. However, we did not consider an intrinsic feature of these molecular precursors, that is, their chirality and how it can be transferred to the resulting graphene nanoribbons. Indeed this is a relevant issue since, although the fine management of chiral processes on solid surfaces has progressed over the years, yet still faces the need for the controlled and enantioselective production of advanced chiral materials. Therefore in this chapter, we use enantiomerically enriched molecular precursors and study the transmission of their innate chirality throughout a multistep on-surface reaction. Making use of bond-resolved scanning tunneling microscopy, the absolute chirality of the various species synthesized here is unambiguously determined at the single molecule level. We demonstrate all variants of chirality transfer within one system as it undergoes a sequence of surface supported chemical reactions: from chiral reactants to chiral polymers, and from the latter to prochiral endproducts.

## 8.1 Introduction to molecular chirality on surfaces

Chirality (or handedness when referring to molecules), the property of an object of being non-superimposable onto its own mirror image, is ubiquitous in nature. The relevance of this concept, discovered by Louis Pasteur and his groundbreaking work on tartaric acid crystals in the middle of the 19th century,[325] is well-known long ago in several branches of science.[326] For example, most biological molecules (such as proteins, enzymes, carbohydrates, etc.) present a certain chirality, essential for their proper function. Stereoselective reactions are also often used in chemistry in order to arrive at specific enantiomeric products. These reactions indeed draw great interest among the pharmaceutical industry since the effectiveness of most medical active components depend on the particular chiral arrangement of their chemical components, whereas using a different chiral configuration of the same drug may result in serious and undesired side effects,[327] as was observed during the infamous Thalidomide disaster in the 1950s.[328]

As the scientific community realized the relevance of understanding and controlling chirality in daily processes, enantioselective synthesis eminently emerged as an important field in academic and industrial chemistry. In this context, solid surfaces appeared as a good candidate for the development of heterogeneous enantioselective catalytic processes.[329] With time, chirality became a topic of interest within the field of surface science, profiting from the application of new analytical techniques. One such example is scanning probe microscopy, which allows the identification of an adsorbate's absolute chirality readily at the single molecule level,[330] in contrast to the much more complex conventional methods, which require the analyte's crystallization (in turn needing relatively large quantities) and subsequent X-ray diffraction analysis. The earliest on-surface experiments addressing chirality in ultra-high vacuum conditions arrived at the end of the last century, reporting on the formation of chiral nanostructures (molecular domains, clusters and/or single molecules) after the deposition of molecular racemates on different two-dimensional surfaces, analyzed by means of low-energy electron diffraction,[331,332] scanning tunneling microscopy[330,333–335] and atomic force microscopy.[336,337] These pioneering works revealed the presence of additional intriguing aspects of chirality on surfaces to be addressed at the nanoscale, such as prochirality. Prochiral molecules, having a mirror plane symmetry parallel to their carbon backbone, are defined as non-chiral (or achiral) molecules that can become chiral in a single step. This step can be achieved, for instance, by adding a two-dimensional surface at one side of the mirror plane i.e. enantiofacial adsorption. Then the system, formed by adsorbate and surface, becomes a three-dimensional object and superposition between molecules adsorbed on different enantiotopic faces is only possible by reflection with a mirror plane perpendicular to the surface. That is, chirality can also arise from achiral molecules upon surface adsorption by mirror-symmetry breaking[338] or by packing into chiral supramolecular lattices.[339] These aspects of chirality on surfaces are extensively reviewed.[340–346]

Nevertheless, a key aspect of chirality at the nanoscale only scarcely explored to date is the transmission of absolute chirality through on-surface reactions, from chiral molecular adsorbates to the resulting covalent products. Pioneering work from Grim et al. reported on the conservation of adsorption-induced chirality from self-assembled domains of diacetylene molecules to homochiral polymeric lattices,[163] as did Zhang et al. in a recent work using alkylated benzenes.[347] Focusing on intrinsic molecular chirality (rather than adsorption-induced), particularly noteworthy reports include the use of helical aromatic molecules (so called helicenes) to study the selective formation of helical diastereoisomers[348–350] or the transmission of the helicene derivative's inherent chirality to planar nanographenes through a sequence of single-molecule reactions.[351]

## 8.2 Global overview of the chirality transfer process

The global chirality transfer process is sketched in Figure 8.1. We use chiral 2,2'-dibromo-9,9'-bianthracene (DBBA) enantiomers as molecular precursors on Au(111) surface. The absolute chirality of these enantiomers is described by the common notation employed for atropisomers, i.e. stereoisomers that originate from hindered rotation about a single bond. As shown in previous chapters, using this precursor racemate, we reported on the growth of graphene nanoribbons on Cu(111), Ag(111) and Au(111),[270,284] observing in every case how the steric hindrance exerted between different enantiomers drives the Ullmann coupling process in such a way that essenstially monomers presenting the same chirality link and thus participate in the polymer formation (sketched in Figure 8.2). Here, the precursors are first separated according to their chirality in an approximate 98:2 enantiomeric ratio, with a different rotation of polarized light for each enantiomer (indicated in Figure 8.1, bottom labels). Thus, our studies are performed with reactants of selected chirality. We start depositing enantioenriched reactants and then study how the inherent handedness of the precursors evolves through the different reactions performed on the substrate.

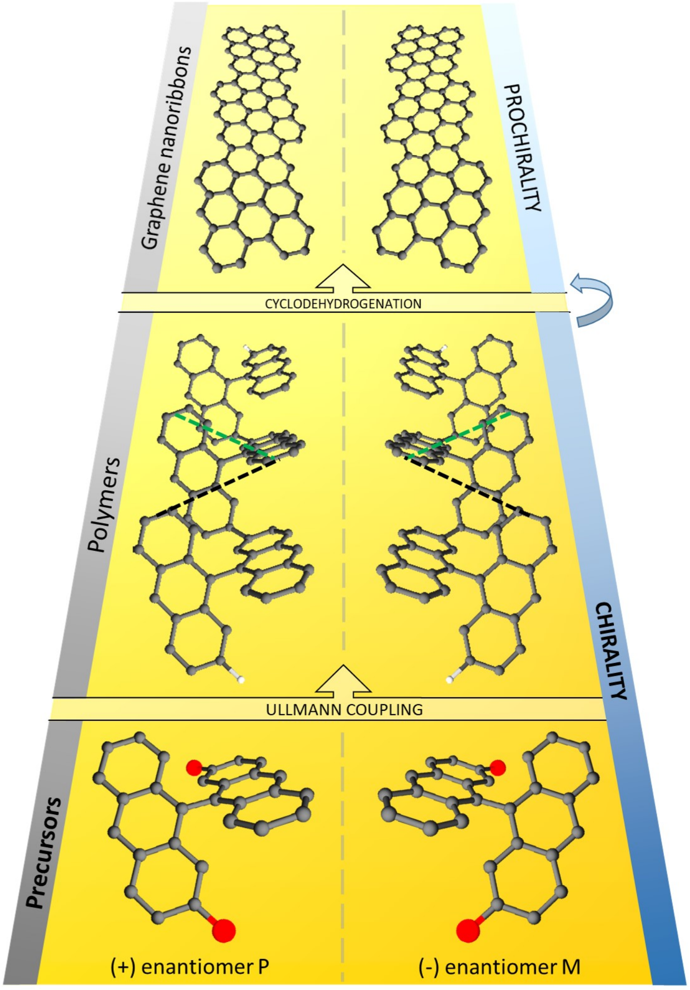

**Figure 8.1: Scheme of the different reactions described in this chapter. (Bottom)** Non-reacted chiral precursors. **(Middle)** chiral polymers. **(Top)** Pro-chiral planar graphene nanoribbons. Carbon(bromine) atoms are represented in grey(red). For clarity, just the terminal hydrogen atoms (in white) in polymers are represented. The non-equivalent distances between up-pointing anthracene ends in the polymer structure are marked in green and black, respectively.

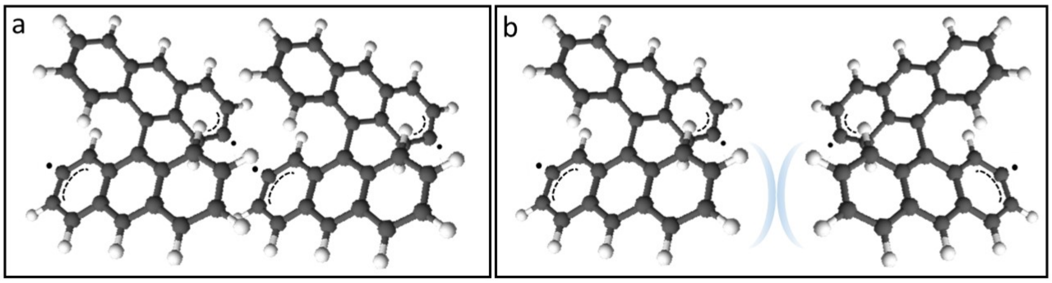

**Figure 8.2:** 3D models illustrating the **(a)** low and **(b)** high steric hindrance secenarios during the coupling of DBBA radical enantiomers. Carbon, bromine and hydrogen atoms are represented in grey, red and white colors respectively.

## 8.3 Synthesis of chiral bianthryl polymers

After precursor deposition, UC is thermally induced,[12] and enantiomers fuse into polymers.[284] Figure 8.3a shows a representative image of the system after polymerization of enantioenriched P-DBBA, where polymers appear aggregated into islands. The reactant's chirality is transferred to the polymer, which displays a non-planar structure in which the steric hindrance between hydrogen atoms leads to an alternating tilting of adjacent anthracene units. Imaged with a scanning tunneling microscope, the result is a zig-zag chain of round features corresponding to the upwards-pointing ends of the anthracenes. The slightly asymmetric intramolecular distances between these features ($d_1$ and $d_2$ in Figure 8.3.b,c) can also be discerned and is associated to each polymeric enantiomer (see Figure 8.1), allowing for the identification of their absolute chirality. In addition, in the absence of undesired species and/or defects, the absolute handedness of these structures can be identified or cross-checked also by analyzing their longitudinal ends, whose oblique orientation depends on the polymer chirality (Figure 8.4). This unambiguous chirality determination thus allows us to quantify the enantiomeric ratio, as shown in Figure 8.3.d, revealing a large enantiomeric excess of P-polymers.

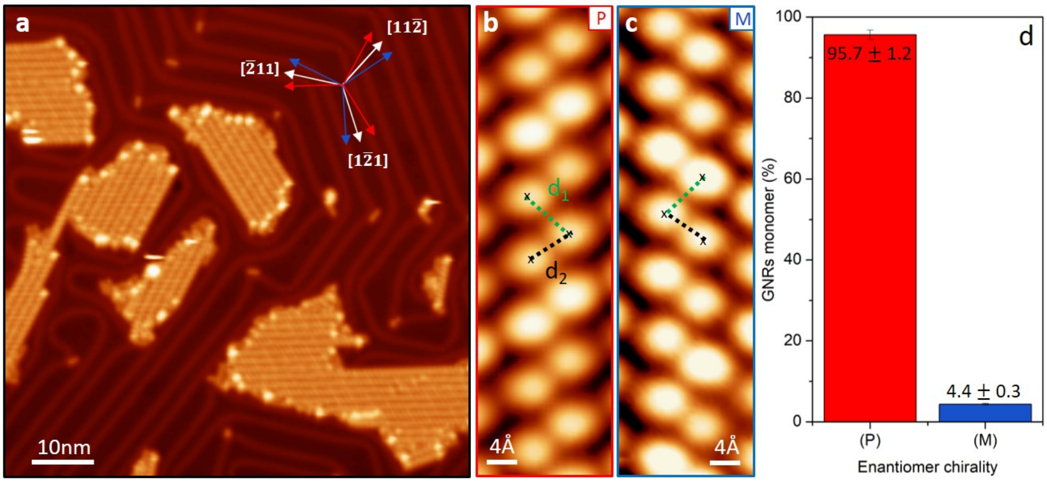

**Figure 8.3: Polymeric phase. (a)** Representative overview of the sample ($V_s$= 1.0 V, $I_t$= 32 pA) after polymerization of enantioenriched P-DBBA, with inset indicating the three growth orientations of each enantiomeric polymer (red and blue arrows) with respect to Au(111) crystallographic directions (white arrows). (tbfb) STM images of chiral polymer P ($V_s$= 0.5 V, $I_t$= 10 pA) and **(c)** chiral polymer M ($V_s$= 0.5 V, $I_t$= 50 pA) where dashed lines represent the different discernible intramolecular distances *d1* and *d2*. **(d)** Percentage of monomers chirality found in polymers after polymerization of enantioenriched P-DBBA.

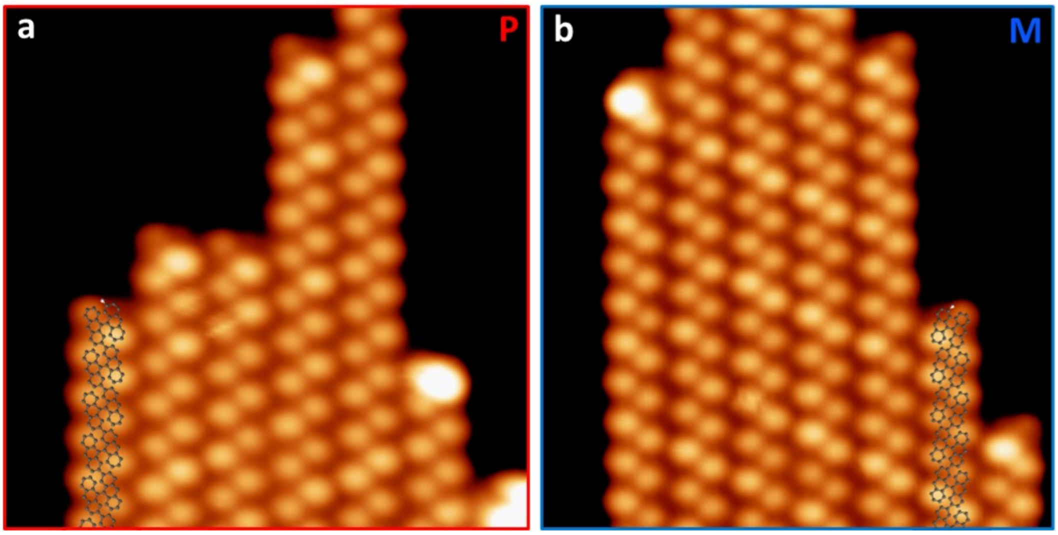

**Figure 8.4: Identification of polymers' absolute chirality by checking their longitudinal end orientation.** Examples ($V_s$= 0.5 V, $I_t$= 50 pA) of a) chiral polymers P and b) chiral polymers M with superimposed models where, for an easier visualization, just terminal hydrogen atoms (in white) are represented.

As marked with the arrows in Figure 8.3.a, substrate-adsorbate interactions steer the growth of each enantiomer into three orientations with respect to the Au(111) crystallographic directions, holding a mirror-symmetry relation that demonstrates their chiral nature. Interestingly, this growth preference is altered for single polymers or islands of small size when enantioenriched reactants are used (Figure 8.5), or even for larger islands when polymers of opposite chirality aggregate together. Moreover we notice that, independently of island dimensions, the surface reconstruction is lifted below the polymers and the soliton lines modified so as to surround the islands. This effect is attributed to the strong interaction of halogen atoms with the surface, as previously reported for similar systems.[274,281,352] Although not visible by STM except along the sides of the islands, it is known from XPS that halogens are still present on the surface, presumably in between the non-planar polymers[317] (which thus “hide” them from the scanning probe) and responsible, in analogy to other hydrocarbon polymers,[280,282] for the attractive interpolymer interactions driving the island formation.

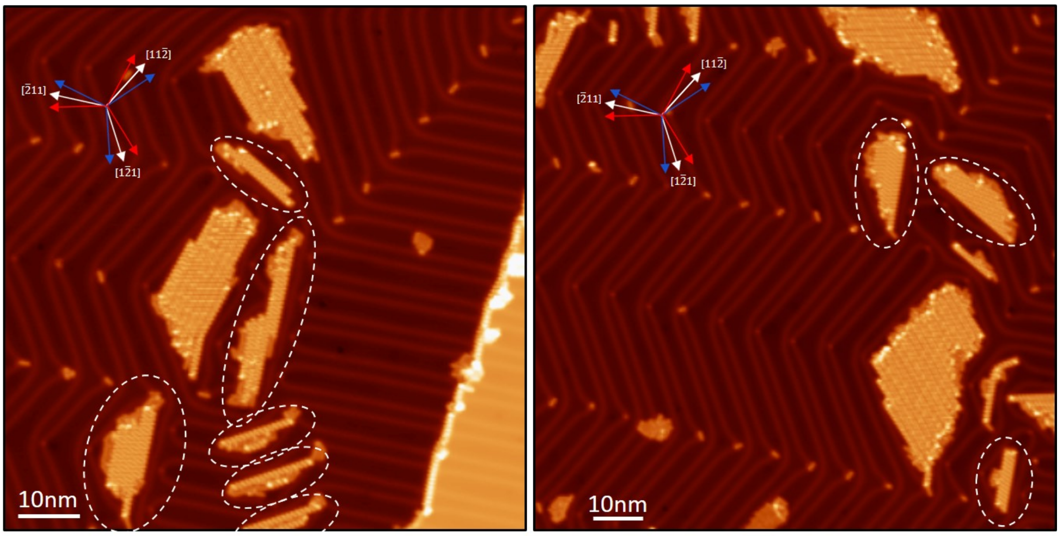

**Figure 8.5:** STM images ($V_s$= 1.0 V, $I_t$= 32 pA) showing examples of polymers P islands out of main growth orientations (circled in white dashed lines).

## 8.4 Synthesis of prochiral graphene nanoribbons

Higher temperature annealing triggers cyclodehydrogenation on polymers, transforming them into planar prochiral GNRs.[284] These ribbons are commonly termed as chiral GNRs in literature (as in other chapters of this thesis) due to the chiral vector (or chiral angle) with respect to graphene high-symmetry directions, that defines their edge topology.[88] However, being adsorpted on a two-dimensional surface makes them prochiral structures, as we refer to them hererin. Although not technically correct, for the sake of simplicity we maintain the same nomenclature of 'P' and 'M' when referring to each ribbon prochirality. Each prochiral ribbon's axis is deviated ~14 degress from the $[11\bar{2}]$ (and equivalent) substrate directions. Figure 8.6 shows a representative overview of the samples obtained from enantioenriched P-DBBA (Figure 8.6.a) and enantioenriched M-DBBA (Figure 8.6.b), respectively. As for the preceding chiral polymers, the adsorbate-substrate interactions drive an epitaxial alignment along three well-defined orientations for ribbons of each prochirality. The associated epitaxial model extracted from high-resolution images is displayed in Figure 8.6.c showing commensuration at every second unit cell of the chiral ribbons.

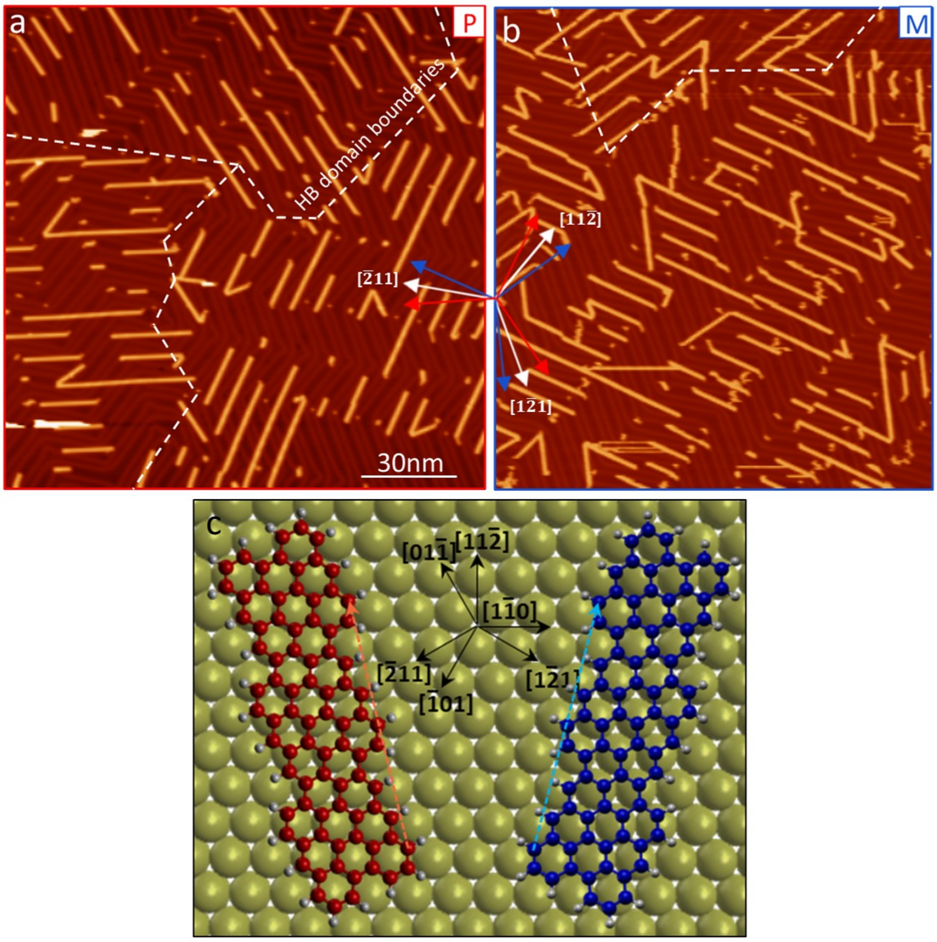

**Figure 8.6: Epitaxial growth of prochiral GNRs on Au(111).** Representative topographic overview of the GNRs ($V_s$= 0.5 V, $I_t$= 40 pA) obatined from **(a)** enantioenriched P-DBBA and **(b)** enantioenriched M-DBBA, with an inset indicating the three growth orientations of each prochirality (red and blue arrows) with respect to Au(111) crystallographic directions (white and black arrows). **(c)** Epitaxial relation exemplified with three-monomer-long GNRs on Au(111). Prochiral GNRs P and M are represented in red and blue colors, respectively. Blue/orange dashed arrows depict the commensuration every two unit cells. The translational adsorption site in the model is arbitrary because the particular adsorption position could not be unambiguously extracted from the experimental images.

By functionalizing the metallic STM tip with a CO molecule we can gain sub-molecular resolution[353] and discern the internal aromatic structure of every adsorbate-substrate configuration (Figure 8.7.a-h). Such unambiguous determination of the prochirality again allows the quantification of the enantiomeric ratio for the GNRs formed from enantioenriched P-DBBA, revealing an enantiomeric excess of P (Figure 8.7.g) that matches, within the error margins, the ratio previously observed for the polymers . In the same way, making use of enantioenriched M-reactants we observe a numerically comparable enantiomeric excess, this time of prochiral M-GNRs (Figure 8.7.j). In this frame, it is important to remark that a random adsorption process of prochiral molecules on achiral surfaces cannot favor a particular prochirality. However, it is the use of an enantiomeric excess of chiral reactants, in combination with chirality transfer across the reactions, which has allowed us obtaining unbalanced prochiral adsorbates.[351]

At this point we compare and analyze the evolution of the enantiomeric ratios at each stage across the complex multistep reaction process. The HPLC analysis of reactants rendered a P:M enantiomeric ratio of 98:2, while STM analysis rendered 95.7 ± 1.2 : 4.4 ± 0.3 for the P-polymers, 93.4 ± 2.1 : 6.6 ± 0.6 for P-GNRs and 98.8 ± 2.2 : 0.2 ± 0.1 for M-GNRs. Although the enantiomeric excess seems to be slightly change across subsequent stages, the changes remain almost within the error margins, making this differences almost negligible. In contrast, what can be unambiguously confirmed is that the reactant's chirality can be

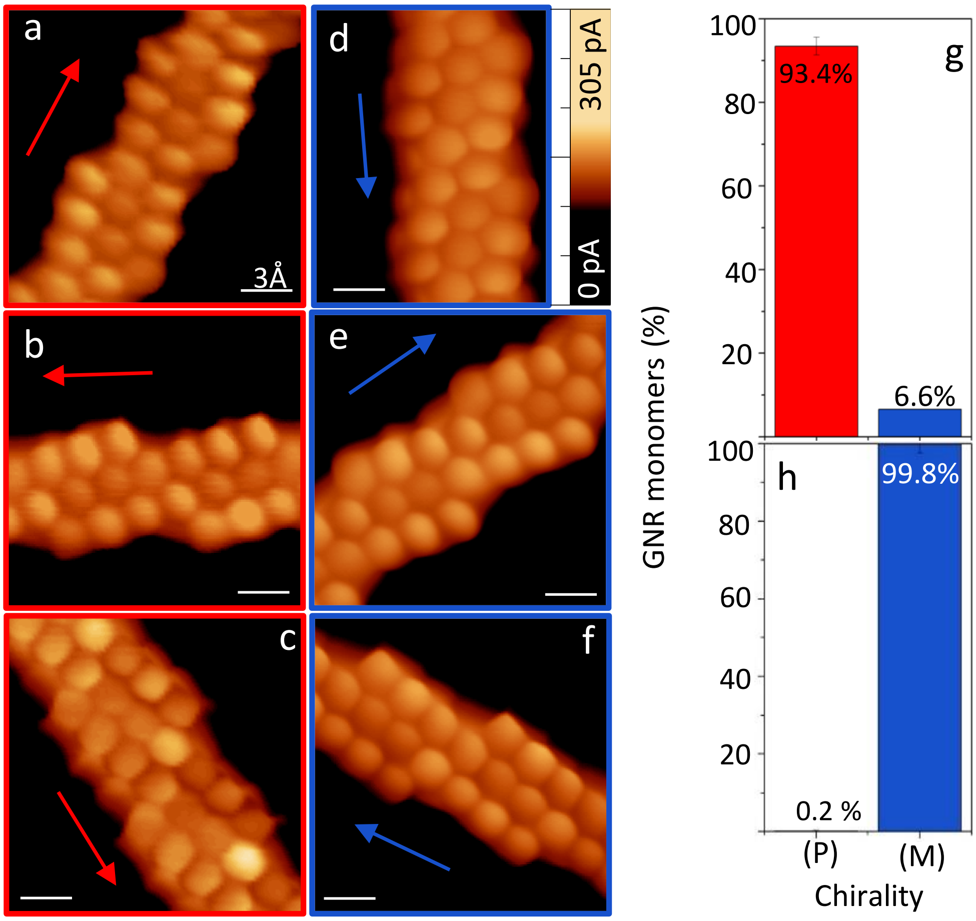

**Figure 8.7: Bond-resolved prochiral ribbons in all their orientations on Au(111).** **a-f**Constant-height current maps ($V_s$= 2 mV, $I_t$= 50 pA) with a CO-terminated tip showing each prochiral GNRs in their three growth orientations on Au(111). Scale bars all correspond to 3 Å. **(h,i)** Enantiomeric distribution counting the number of monomers forming the GNRs after cyclodehydrogenation of (h) sample of polymers P displayed in Fig. 8.3 and (i) a complementary sample from enatiomer M.

transferred across the various substrate-supported reactions in spite of the increasingly high activation temperatures. The possible mechanisms which could promote chirality inversion at each synthetic step are the following. For single monomers, the energy provided during evaporation at 435 K, and/or as the sample is heated for on-surface polymerization at 415 K could cause anthracene units to exchange their relative position with respect to the central C-C bond linking them. This scenario seems, however, unlikely, since the reactant's chirality in solution is preserved for annealing temperatures up to 515 K, the temperature at which the precursors start to show degradation rather than chirality exchange. Following the same principle, the same anthracene interconversion could happen once monomers have polymerized when annealing toward the CDH temperature (625 K), although in this case it would require a concerted change of all monomers along the whole polymeric chain, which may enhance the energetic barrier even further. Finally, the prochirality of GNRs may be lost if polymers or GNRs 'flip' over on the surface. This process, however, may intuitively show an energy barrier not far from that of desorption, which on the other hand seems unsubstantial for the system and the temperatures employed. Thus, also this chirality exchange mechanism seems unlikely, supporting the experimentally observed chiral transfer across the whole reaction sequence.

Lastly, Figure 8.6.a,b also reveals other important details: (i) the recovery of the Au(111) herringbone reconstruction over the whole surface, (ii) the unidirectional alignment of chiral GNRs within each herringbone reconstruction domain and (iii) a periodic interspacing between the parallel ribbons. The first point relates to the desorption of Br as the temperature is increased.[317,323] Upon desorption, its strong interaction with both the substrate and the adsorbates disappears. The former allows for the reappearance of the herringbone reconstruction, while the latter lowers the intermolecular interactions, no longer driving the adsorbate's agglomeration into islands. These two effects in turn cause the unidirectionality and periodicity of GNRs (in case of enantioenriched samples only), related to a now dominating molecule-substrate interaction in combination with the templating effect of the recovered reconstruction. As previously observed with many other aromatic adsorbates,[354–356] also for GNRs, the slightly higher electron potential in the reconstruction's face-centered-cubic (fcc)

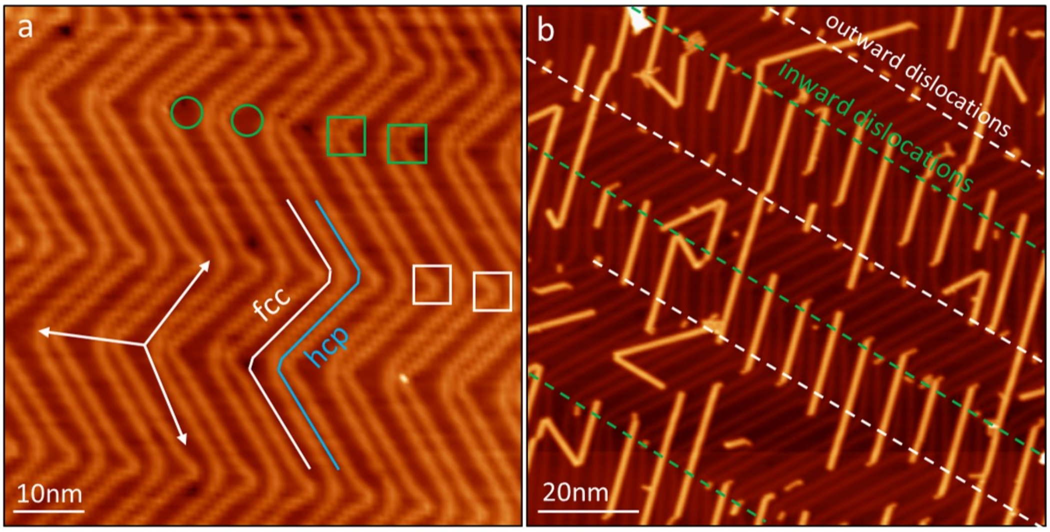

**Figure 8.8:** Preferential nucleation on fcc regions between inward elbow dislocations. a) STM image ($V_s$= 1.0 V, $I_t$= 100 pA) of Au(111) surface reconstruction with indications on some inward/outward elbow dislocations (green/white squares), preferred nucleation sites on fcc regions between inward dislocations (green circles), ffc and hcp regions (white blue lines) and [11-2] and equilavent crystallographic orientations (white arrows). b) STM image ($V_s$= 0.3 V, $I_t$= 30 pA) showing preferential nucleation of pro-chiral ribbons M on inward dislocations (green dashed lines) over outward dislocations (white dashed lines).

regions ( Figure 8.8.a, white lines) with respect to the hexagonal-closed-packing (hcp) regions[357] (Figure 8.8.a, blue lines) cause a favored adsorption on the former.[358,359] These fcc trenches align with the [11$\bar{2}$] and its two equivalent directions (Figure 8.8.a, white arrows), alternating between two of them in each reconstruction domain. In particular, our GNRs adsorb preferentially in the broadest fcc regions (Figure 8.8.a, green circles), corresponding to the herringbone elbows with 'pinch-in' dislocations[358] (Figure 8.8.a, green squares). On the one hand this causes the GNRs to bunch in the pinch-in elbows (Figure 8.8, green deashed lines), leaving most pinch-out elbows empty (Figure 8.8.b, white dasehd lines) at least for low coverage and short ribbons. On the other hand it defines the GNR orientation, since one of the three epitaxially equivalent directions for GNRs of each prochirality maximizes its adsorption length on fcc sections as compared to the other two orientations, which would display more soliton crossing points and hcp adsorption regions. Given the large enantiomeric excess of one chirality, a clearly dominating GNR orientation is observed on each herringbone domain. Coming now to the periodicity of the interspacing, we measure a mean distance of 6.8 ± 0.2 nm independently of GNRs prochirality (Fig. 8.9) or herringbone domain. Taking into account the herringbone reconstruction's periodicity of ~63.4 Å, and the ~14 degrees deviation of the ribbons with respect to the herringbone soliton lines,[270] the reconstruction's periodicity perpendicular to the GNR's orientation direction is ~65.3 Å, in close agreement to the observed GNR spacing.

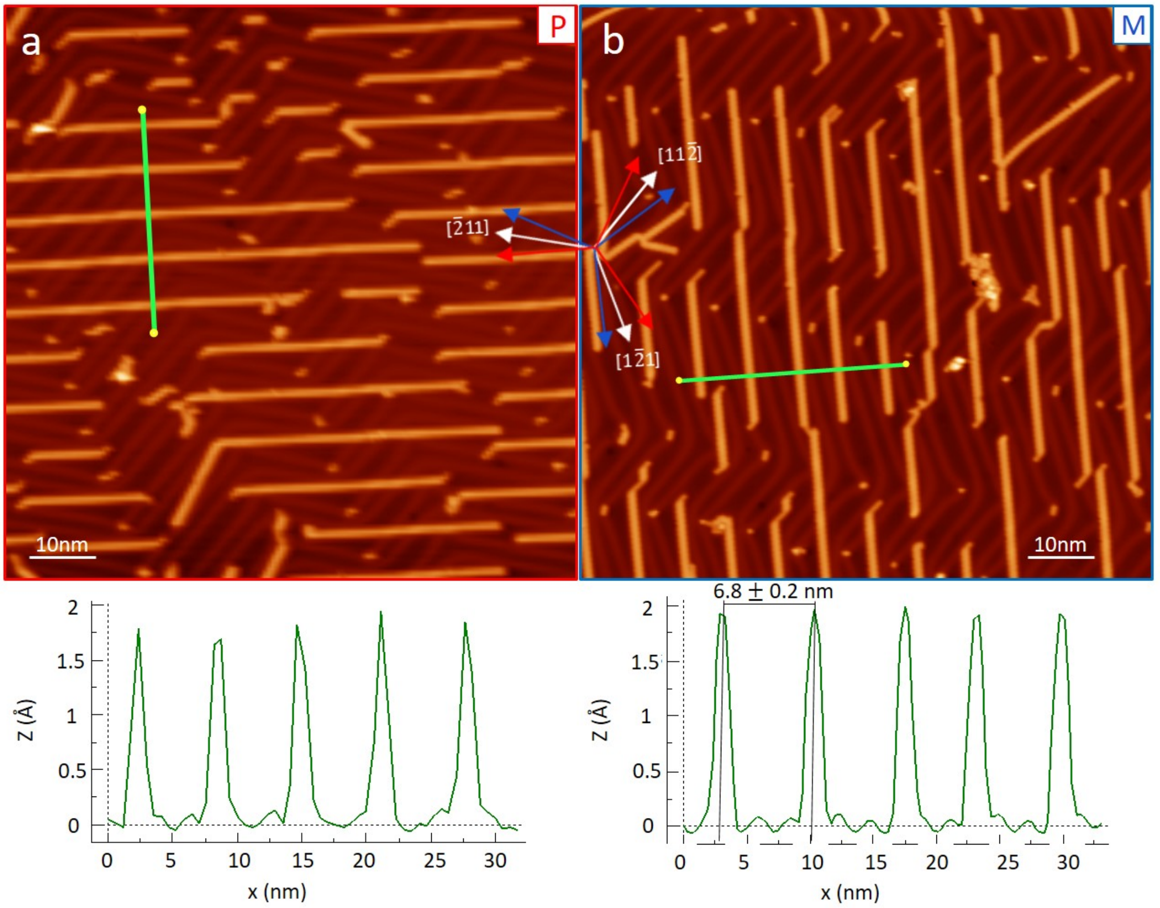

**Figure 8.9:** STM images showing the interspacing of pro-chiral GNRs (left) P and (right) M, where green lines correspond to height profiles located at the bottom of each image.

## 8.5 Conclusions

In conclusion, we have performed a complete transfer of intrinsic molecular chirality from reactants to intermediates and final products. Enantioenriched reactants that present energy barriers high enough to maintain any conformational change were used in order to promote their chirality throughout the different surface-assisted chemical reactions accounted for this chapter. Our results pave the way to exploiting these energy barriers in different polycyclic aromatic hydrocarbons for the stereoselective on-surface synthesis of enantiomerically pure compounds of current interest such as graphene nanoribbons and other *pi*-conjugated molecules, including nanographenes and cyclophanes. The controlled production of these chiral compounds represent a key aspect for the study of physicochemical phenomena directly related to their chiral nature, such as heterogeneous enantioselective catalysis or optical activity, and therefore for the development of forefront devices such as spin filters[360] or circularly polarized light detectors.[361]

# Chapter 9

# Electronic structure of chiral graphene nanoribbons

The previous chapters of this part focused on the growth of chGNRs, studying on different substrates the impact of the halogenated positions in the molecular precursor and their innate chirality in their synthesis. Since most of the examples found in literature report on synthetic aspects of chGNRs, their electronic structure lacks a precise description. Although some spectroscopic measurements were performed on (3,1)-chGNRs on Cu(111),[295] the assessment of important figures of merit like the band gap value or the frontier band's effective masses are still required. Therefore, hereafter we aim to explore the electronic structure of chiral graphene nanoribbons.

In this chapter, we firstly characterize the electronic structure of narrow chGNRs by (Fourier transform-)STS, observing a clear semiconducting behaviour on Au(111). On such a surface, hybridization effects with the substrate are weaker and the ribbon's properties are easier to probe. Next, the use of the vicinal surface Au(322) results in the uniaxilly aligned growth of chGNRs along the substrate terraces, thus enabling the complementary use of averaging techniques such as ARPES to study the occupied band. Lastly, we evaluate the role of cGNRs width in the emergence of zero-energy edges states by the synthesis of cGNRs of different width still preserving the chiral edge orientation. Part of the results shown in thsi chapter are published in ref.[270]

## 9.1 Semiconducting band gap of narrow chGNRs

Figure 9.1a shows chGNRs resulting from five DBBA monomers where the internal bonding structure is resolved with a CO-functionalized tip.[353] The electronic properties of the ribbons are first characterized by STS. Figure 9.1b displays a representative dI/dV point spectrum on a ribbon, together with a reference spectrum on the surrounding substrate. Because tunneling conductance is proportional to the LDOS at the probe position, one can clearly distinguish the onset of the ribbon's valence and conduction bands. From a statistical analysis of several tens of ribbons, we find the band onsets at -0.22 ± 0.05 V and 0.45 ± 0.02 V, respectively. Although the resulting band gap of 0.67 ± 0.06 eV is larger than that obtained from DFT calculations (Figure 9.1c), the understimation of band gaps is a well-known limitation of DFT.[238] However, the constant-height conductance maps at the bands' onset energies (Figure 9.1d,e) show excellent agreement with the calculated wave functions (Figure 9.1f,g) of the frontier states of valence and conduction band at the gamma point (despite being measured with a CO-functionalized tip).[362] This is also confirmed by constant-current conductance maps with a non-functionalized metallic tip (Figure 9.2), where clear GNR-related density of states appears as the energy reaches either band onset, evidencing similar patterns as those in Figure 9.1. Those patterns are clearly different for VB and CB, the latter appearing with a characteristic wavefront structure, while the former displays a more complex sequence of lobes. Both conduction and valence bands display a dispersive behavior as they deviate from $\Gamma$ (Figure 9.1c). A fingerprint of it is found in conductance maps over a wider energy range of the VB, revealing an additional energy-dependent LDOS modulation along the ribbon axis (Figure 9.3a-f).

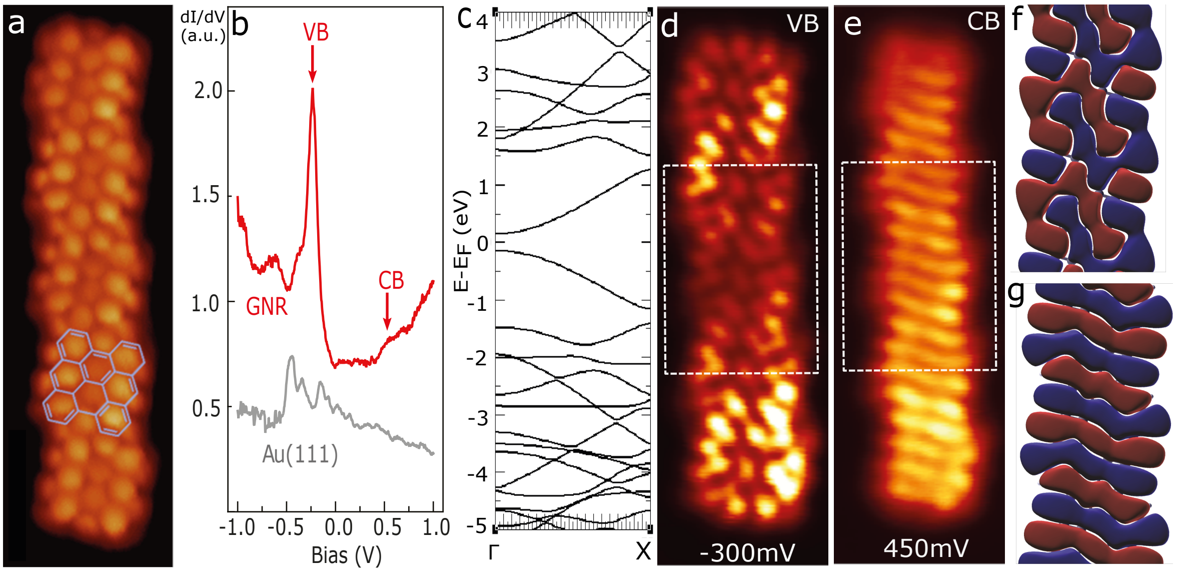

**Figure 9.1: Electronic structure characterization of (3,1)-chGNRs. (a)** Constant-height bond-resolved image ($V_s$= 2 mV, $I_t$= 50 pA) with a CO-terminated tip and a momoner model superimposed. **(b)** Representative dI/dV point spectra with Au(111) signal (in gray) included as background reference (open-feedback parameters: $V_s$= 1.0 V, $I_t$= 0.5 nA, modulation voltage $V_{rms}$ = 0.1 mV). **(c)** DFT calculated band structure. **(d,e)** Constant-height conductance maps (1.7 nm x 5.2 nm; open-feedback parameters: $V_s$= 0.2 V, $I_t$= 0.06 nA, modulation voltage $V_{rms}$ = 1.0 mV) near the VB (-300 mV) and CB (450 mV) onsets. **(f,g)** DFT simulations of the wave functions for states at the onset of VB and CB (at $\Gamma$ point) on an area equivalent to dashed rectangle in panels (d) and (e). Red and blue colors represent isosurfaces of positive and negative wave function amplitudes for an isovalue of 0.015 Å$^{-3/2}$.

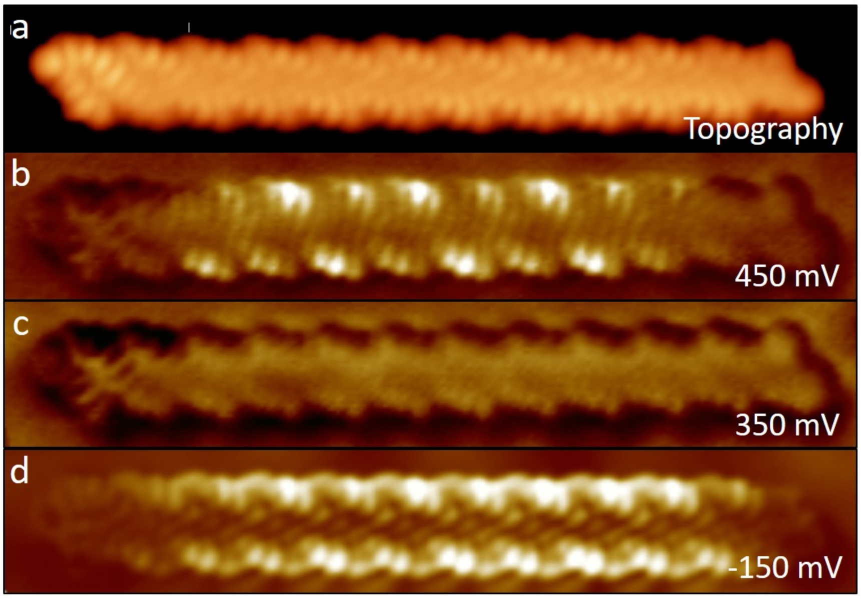
a
Topography
b
450 mV
c
350 mV
d
-150 mV

**Figure 9.2: Constant-current maps of (3,1)-chGNRs.** **(a)** STM topography image (13.1 nm x 3.1 nm; $V_s$= -0.15 V; $I_t$= 1.0 nA) and **(b-d)** STM constant-current dI/dV maps (13.1 nm x 3.1 nm; $I_t$= 1.0 nA) at (b) CB onset, (c) within the band gap and (d) at the VB onset.

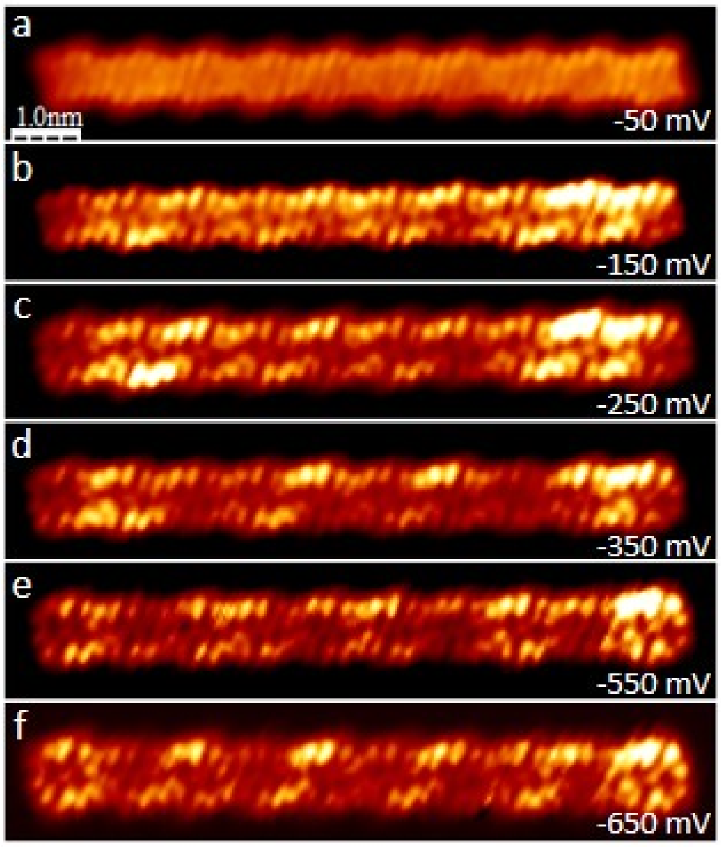
a
1.0nm
-50 mV
b
-150 mV
c
-250 mV
d
-350 mV
e
-550 mV
f
-650 mV

**Figure 9.3: Valence band energy-dependent LDOS modulation.** STM constant-height conductance maps (10.3 nm x 2.0 nm; $I_t$= 30 pA; modulation voltage $V_{rms}$ = 12 mV) **(a)** within the band gap at -50 mV, **(b)** near the VB onset at -150 mV, **(c)** at -250 mV, **(d)** at -350 mV, **(e)** at -550 mV, and **(f)** at -650 mV, exhibiting confined standing waves along the ribbon.

## 9.2 Valence band dispersion analysis by Fourier Transform-STS

To quantify the VB energy-dependent LDOS modulation observed in constant-height maps (Figure 9.3), we measured equidistant point spectra along the edge of a GNR (Figure 9.4a), displayed in Figure 9.4b as a function of its position along the ribbon with a color-coded conductance intensity (z-axis). In addition to the edge periodicity arising from the chGNR structure, another energy-dependent modulation appears. It coincides with that observed in the conductance maps (Figure 9.3), in which the number of nodes increases as the energy departs from the band onset. It relates to the formation of standing waves from electronic states scattered at the nanoribbon edges, thus holding the band's dispersion relation information. This can be better distinguished in Figure 9.4c, which depicts a line-by-line Fourier transform (FT) of Figure 9.4b and thus the dispersion of the probed bands.

The VB is observed dispersing down with an effective mass of -0.34 ± 0.05 $m_0$, as obtained from a parabolic fit to the topmost region of the band (red dashed line in Figure 9.4). In contrast, no dispersion information has been obtained for the CB from the FT-STS analysis. Indeed, the CB is much harder to detect in STS measurements, as can already be guessed from the marked asymmetry in the signal strength of the STS spectrum in Figure 9.1b for valence and conduction bands, respectively. As explained in detail in previous works,[119, 243] the faster a wave function changes its sign along the ribbon axis, the lesser it extends into the vacuum along the GNR normal. This makes it less accessible to STM/STS measurements, where tip-sample distances remain typically above 5 Å. Our wave function calculations of (3,1)-chGNRs in Figure 9.1f,g reveal the CB to change sign along the ribbon axis faster than the VB, thus agreeing with its poorer detection in our spectral measurements.

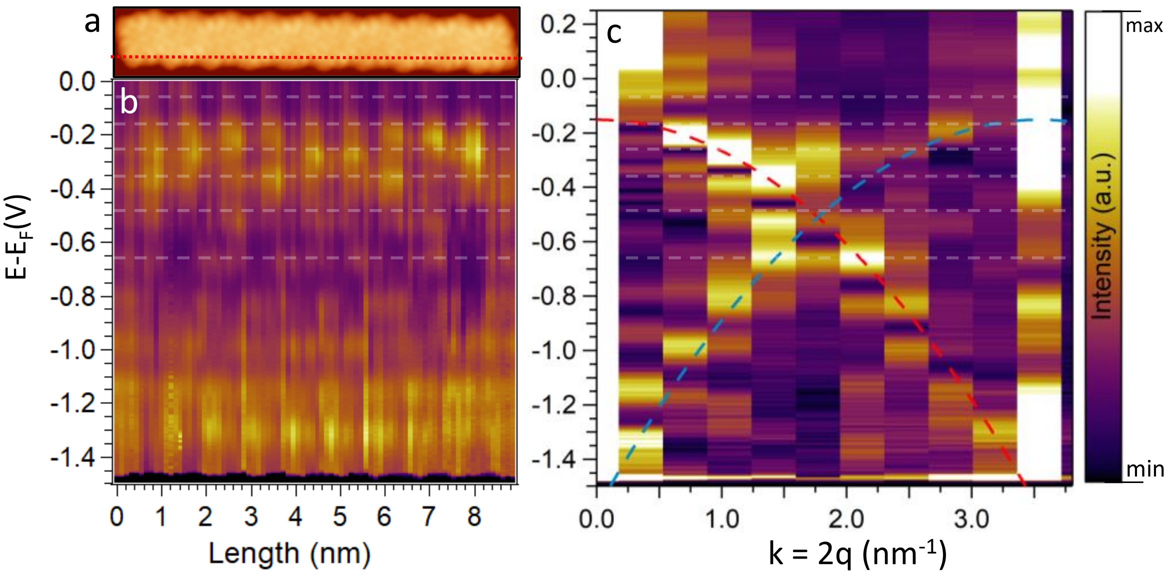

**Figure 9.4: Valence band dispersion by FT-STS. (a)** Constant-current STM image of the same ribbon than in Figure 9.3, showing the path (red dashed line) followed by the equidistant dI/dV spectra. **(b)** Color-coded conductance signal obtained from equidistant dI/dV point spectra (open-feedback parameters: $V_s$= 1.50 V; $I_t$= 0.8 nA; $V_{rms}$= 12 mV) on the ribbon and along the red dashed line displayed in panel g. **(c)** Line-by-line Fourier transform from the stacked spectra in panel (b), showing the two-parameter parabolic fit (red dashed line) used for extracting the effective mass. The additional parabola centered around the Brillouin zone edge is displayed with a green dashed line. Gray horizontal lines corresponding to the voltage biases of maps in Figure 9.3a-f are superimposed in panels (b) and (c) as a guide to the eye.

Interestingly, additional features in the FT-spectral map of the VB are observed, not present in previous works performing a similar analysis on aGNRs.[119,243] A replica of the dispersive band appears shifted by 3.5 nm$^{-1}$ (displayed with a blue dashed line in 9.4c), namely, centered at the Brillouin zone edge, which is defined by the GNR periodicity arising from its chiral edges (periodicity a = 8.97 Å= $\pi/(3.5\ \text{nm}^{-1})$). This band replica and the increased intensity line at the zone edge can be traced back to the additional modulation from the GNR chirality. The imposed periodicity stresses the Bloch wave function character of the electronic states, whose coherent addition resulting from scattering events has been previously shown to lead to exactly those two types of features in FT-STS.[363] The periodicity of these features in reciprocal space can be additionally observed in the line-by-line FT spectra plotted over a wider energy and momentum range displayed in Figure 9.5.

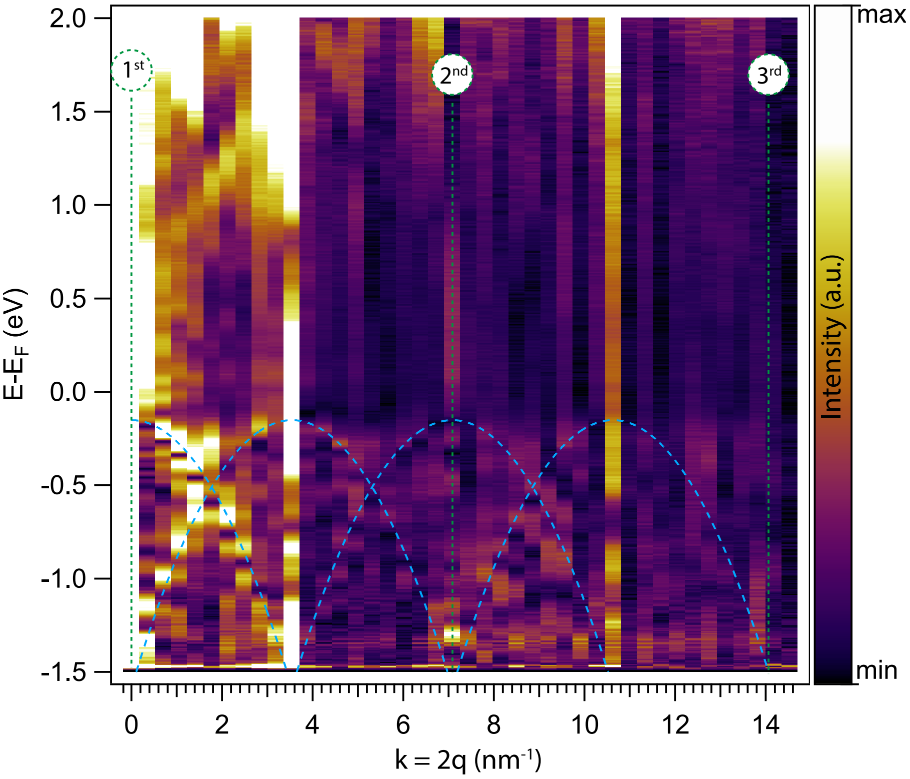

**Figure 9.5: Full energy and momentum VB dispersion by FT-STS.** Line-by-line FT-STS data displayed in Figure 9.4c, depicting the complete energy and momentum range experimentally measured, and showing valence band replica along the momentum space.

## 9.3 Characterization of valence band by ARPES

To compare the VB dispersion properties obtained from FT-STS with results from a more standard approach, we have characterized the (3,1)-chGNRs also by ARPES. Similar comparisons have been performed previously on the VB dispersion of 7-aGNRs[?,140,242,243] and 9-aGNRs.[?,119] Because ARPES is an ensemble-averaging technique, having uniaxially aligned GNRs is a requirement to measure the dispersion along a well-defined direction. The aligned growth of aGNRs has been attempted by using a Au(788) surface as template,[140,242] which features ~4 nm wide (111) terraces periodically separated by steps running along the compact [10-1] direction. However, because the chiral GNRs studied here display a markedly preferred growth orientation at ~16°off from the compact [10$\bar{1}$] (and equivalent) direction (see chapter 8), the Au(788) terraces do not satisfactorily guide an uniaxial growth of the ribbons. Instead, the growth results in low-quality samples with short ribbons oriented partially along the step edges but also along their epitaxially favored directions (Figure 9.6a). The scenario changes when using narrower terraces. The ~1.2 nm wide terraces of Au(322) are wide enough to host a (3,1)-chGNR but narrow enough to largely inhibit molecular coupling along any other orientation than following the terraces. As a result, uniaxially aligned ribbons could be grown on Au(322), as shown in Figure 9.6b,c.

The subsequent ARPES characterization is displayed in Figure 9.6d,e. Whereas no GNR signal is observed in the first Brillouin zone and only a weak shadow in the second, the VB is nicely resolved in the third Brillouin zone. From a parabolic fit to the topmost VB region (red line in Figure 9.6) we extract values of -0.50 ± 0.02 eV and -0.36 ± 0.04 $m_0$ for the band's onset energy and effective mass, respectively. Compared with the results from FT-STS, the effective mass shows agreement within error margins (-0.36 ± 0.04 $m_0$ from ARPES vs -0.34 ± 0.05 $m_0$ from FT-STS), but the band onset is notably lower in energy (i.e., -0.5 ± 0.02 eV from ARPES vs -0.22 ± 0.05 mV from STS). This onset discrepancy, as explained previously in chapter 5 (see Figure 5.4), stems from the different workfunction values of Au(111) and Au(332).

At this point it is interesting to compare the electronic properties of (3,1)-chGNRs and of 7-aGNRs. Both ribbons have comparable widths and result from precursors sharing the same carbon backbone, although polymerizing along different directions. However, the change in edge orientation from armchair to a chiral (3,1) direction brings about dramatic changes in the electronic properties. By way of example, the band gap is reduced from 2.31 ± 0.06 eV in the former[243,364] to 0.67 ± 0.06 eV in the latter, although without evident signatures of the spin-

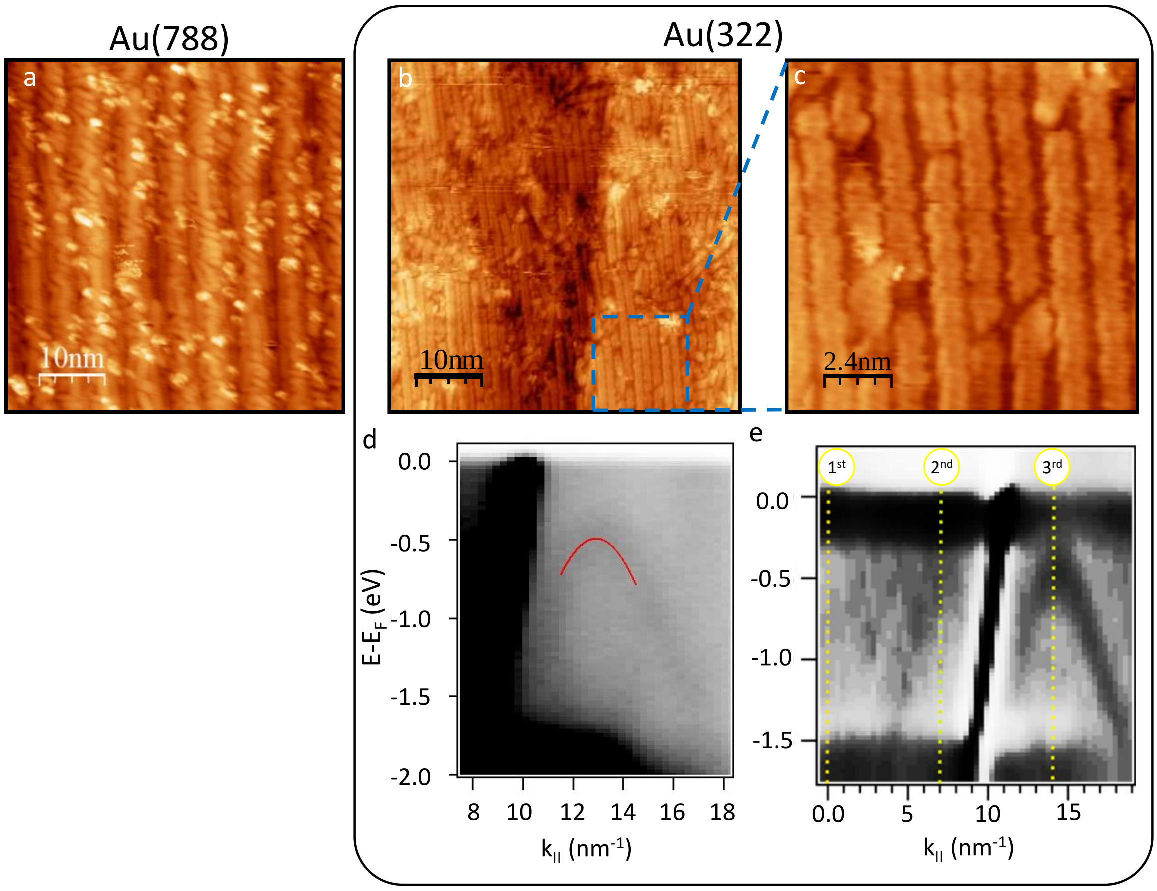

**Figure 9.6: ARPES characterization of VB on Au(322).** **(a-c)** STM images of (3,1)-chGNRs grown (a) on Au(788) (50 x 50 nm, $V_s$= 1.0 V, $I_t$= 50 pA) and (b,c) on (Au(322) (50 x 50 nm, 10 nm x10 nm, $V_s$= -0.2 V, $I_t$= 20 pA). **(d)** Raw signal and **(e)** second derivative of the photoemission intensity reflecting the valence band dispersion.

polarized edge states predicted to appear around the Fermi level in chiral ribbons.[49,61–63] This is presumably due to a too small GNR width and the associated band-gap opening.[49,62,63] According to calculations, a closing of the band gap and the appearance of edge states are predicted to occur either increasing the GNR width or also maintaining a similar GNR width but with chiralities closer to the zigzag direction (as well as for pure zGNRs).[49,62,63] In the next sections we will prove the former.

## 9.4 Growth of varying-width (3,1)-chiral GNRs on Au(111)

To fabricate GNRs with same edge orientation yet of different widths, our collaborators from CIQUS (Santigo de Compostela, Spain) synthesized the three different molecular building blocks shown in Figure 9.7.a-c, namely 2,2’-dibromo-9,9’-bianthracene (DBBA), 2’,6’-dibromo-9,9’:10’,9”-teranthracene (DBTA) and 2”,3’-dibromo-9,9’: 10’,9”:10”,9”’-quateranthracene (DBQA). Each molecular precursor consists on a increasing number of anthracene moieties that enlarge the width of the resulting chGNRs in a controlled way. After independenlty sublimating each precursor onto a clean Au(111) at RT, the precisely selected Br-substitution

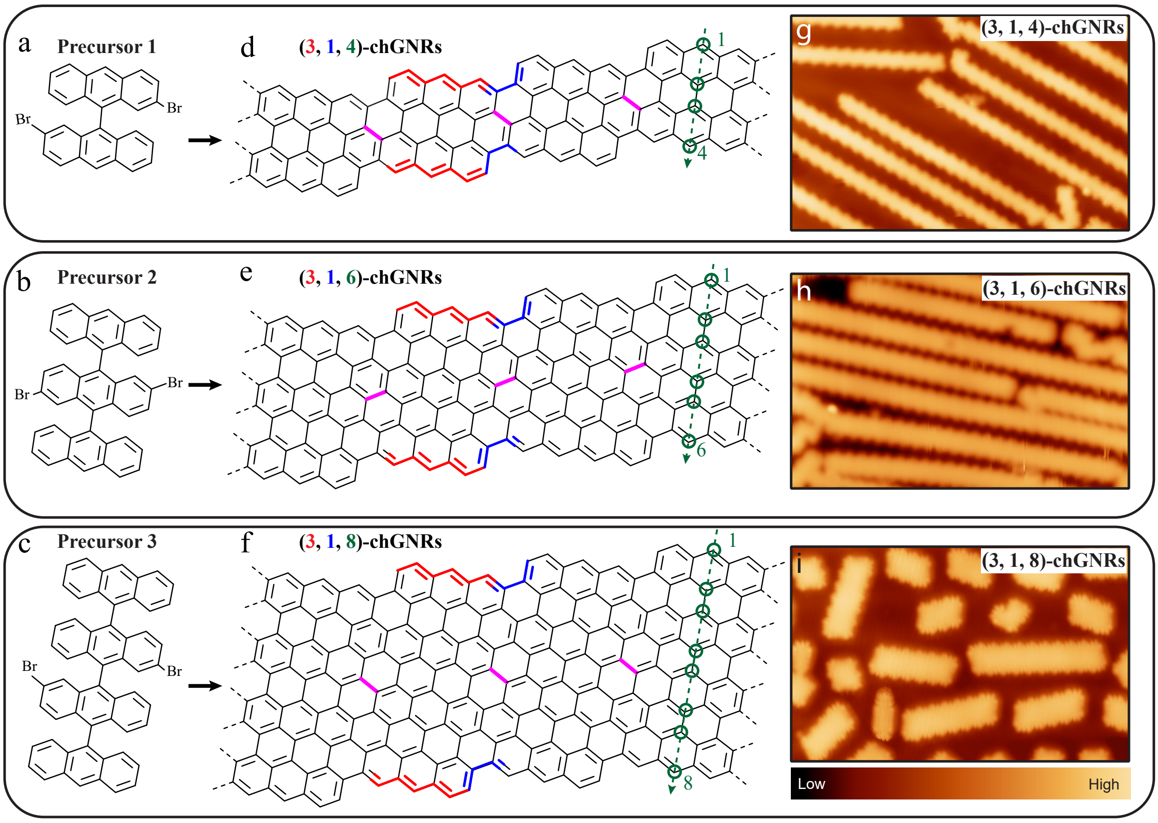

**Figure 9.7: Synthetic strategy and characterization of (3,1)-chGNRs with different widths on Au(111). (a-c)** Model structures of the three molecular precursors (named as Precursor 1, 2 and 3, respectively) and **(d-f)** the resulting varying width (3,1)-chGNRs after the polymerization and CDH. The bonds in pink highlight the bonds formed upon Ullmann coupling. Carbon sites in red(blue) highlight the zigzag(armchair) segments of the GNRs. Carbons atoms highlighted by green circles give a measure of numbers of carbon atoms across the GNRs respectively. According to the zigzag(armchair) segments and the number of carbon atoms across the GNRs, the GNRs are named as (3,1,4)-, (3,1,6)- and (3,1,8)-chGNRs respectively for simplicity. **(g-i)** STM overview images ($V_s$= 1.0 V, $I_t$= 50 pA) of each chGNRs formed on a Au(111) surface. The images share the same scale bar as labeled in (i).

sites in each case ensure a polymerization pathway upon UC (at T ∼ 200°C) that in every case provides, after CDH (at T > 250 °C), GNRs featuring the (3,1) chiral edge orientation. STM images of the resulting structures (Figure 9.7.g-i) show the characteristic straight, planar, saw-like shape of the ribbons confirming the successful synthesis of atomically precise (3,1,w)-chGNR with increasing width (w= 4, 6, 8), where the width is defined by the conventional notation used for describing zGNRs' width in terms of carbon zigzag lines.[117, 255]

## 9.5 Width-dependent electronic structure transition

To confirm the precise atomic structures of the synthesized chGNRs, we acquired constant-height current images using a CO-functionalized tip (Figure 9.8.a-c). The images show that the backbone structures are defect-free and reproduce well the corresponding model structures of Figure 9.7d-f. Since the images were recorded with an applied bias of 2 mV, the current maps show how the frontier molecular bands of the narrow ribbon approach $E_F$ when these structures become wider, as reproduced by the corresponding DFT-calculated band structures

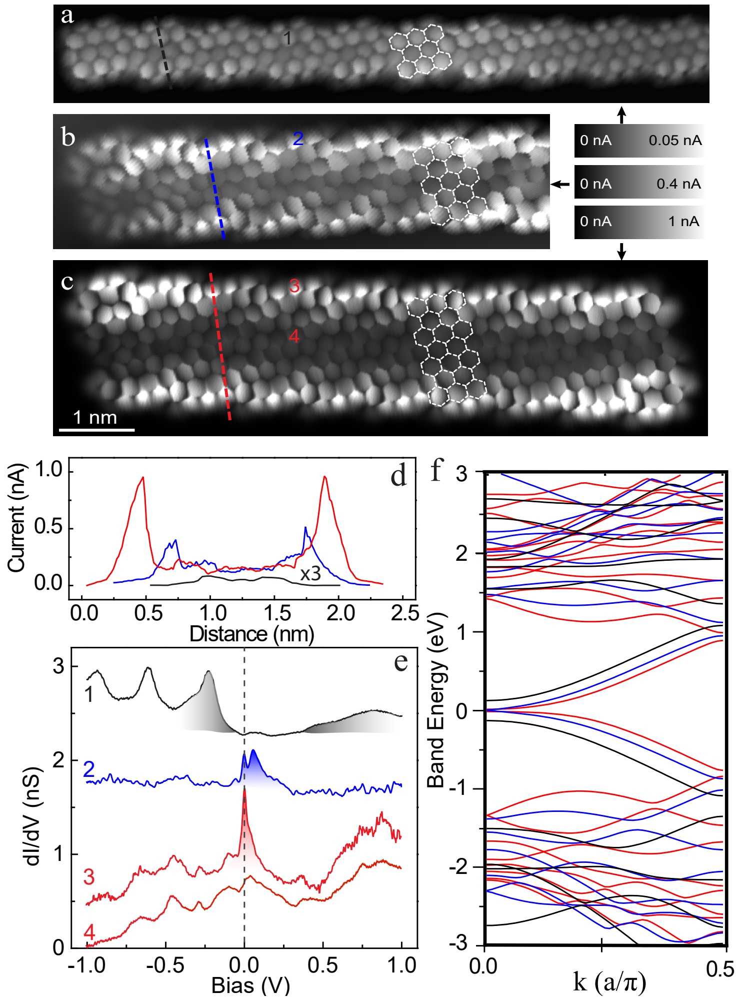

**Figure 9.8: Atomic and electronic structure of (3,1,)-chGNRs with different widths.(a-c)** Constant-height current images ($V_s$= 2 mV) of (3,1)-chGNRs of width (a) w=4, (b) w=6 and (c) w=8, acquired with a CO-terminated tip, with a monomer models (in white) superimposed in each case. All the images share the same scale bar as labeled in (c). **(d)** Line profiles and **(e)** dI/dV point spectra on (3,1,w)-chGNRs as indicated in images (a-c). **(f)** DFT-calculated band structure of (3,1,w)-chGNRs. The black, blue and red color code corresponds to (3,1)-chGNRs data of width w = 4, 6 and 8, respectively.

(Figure 9.8.f). Interestingly, the current intensity on both (3,1,6) and (3,1,8)-chGNRs appears enhanced at the long edges of the structures (Figure 9.8.d compares current profiles across the three structures), while such current increase is absent in (3,1,4) chGNRs. This can be further corroborated by comparing differential conductance spectra (dI/dV) on different sites of the three chGNRs (Figure 9.8.e). In constrat to the clear gap observed in the narrow ribbon (spectrum 1) with a LDOS spread over the whole structure (see Figure 9.1 in previous chapter 9), the spectra measured on the edges of (3,1,6) and (3,1,8) chGNRs show pronounced peaks close to $E_F$ (spectra 2,3), not observed at the center of the ribbons (spectrum 4). The appearance of zero-energy peaks, together with their narrow spatial localization of barely 0.3 nm (i.e. one carbon ring) around the edge,[59] indicates the emergence of edge states on (3,1,6) and (3,1,8)-chGNRs, which are absent on the narrower species. The bands become more populated the wider are the ribbons, as it is reflected by the acute peaks in the dI/dV spectra of Figure 9.8. The presence of zero-energy modes in zigzag and chiral GNRs is the basis for edge magnetism.

## 9.6 Conclusions

In conclusion, we have provided a thorough characterization of the electronic properties of (3,1)-chGNRs on Au(111), which display for the narrower nanoribbons a semiconducting behaviour with its associated band gap. Moreover, the use of adequately stepped surface Au(322) allow us to align the GNRs growth along the substrate terraces. Such ordered samples have been used to characterize the VB dispersion by ARPES and to compare the results with those obtained from FT-STS measurements. We end up with a fully coherent picture of the GNR's band gap (0.67 ± 0.06 eV), effective mass ($\sim$0.35 $m_0$), and energy level alignment (shifting with the substrate work function as in an ideal vacuum level pinning scenario) that will enable a better understanding of their performance in future electronic devices and allow a rational design of heterostructures with complementary GNRs.

To evaluate the role of the cGNRs width in the emergence of edge-states, we fabricate atomically-precise chiral grahene nanoribbons displaying different widths yet preserving the same chiral edge orientation (3,1), using on-surface synthesis strategies. Our spectroscopic analysis reveals an electronic structure transition from a semiconducting character in the narrow ribbons, to a (semi)metallic behaviour in the wider structures. Furthermore, we demonstrate the emergence of zero-energy modes localized at the edges of chiral graphene nanoribbons wider than six zigzag carbon lines. Although spin-polarized STM measurements can track this phases in magnetization maps, the use of wider ribbons and surfaces with lower work-function (e.g. Ag(111)) could be ideal to enhance spin polarization in undoped species. These observations remark the potential use of these systems for the development of spintronics applications.

# Conclusions and Outlook

This thesis deepen into the on-surface synthesis and electronic structure characterization of atomically-precise graphene nanoribbons, in particular, armchair and chiral GNRs. The technique mainly employed is scanning tunneling microscopy/spectroscopy, together with supplementary surface sensitive techniques such as XPS and ARPES. A great majority of the measurements are acquired at low temperature, being most of them taken at $\sim$ 5K by the use of liquid helium. The experimental results are complemented by theoretical simulations or calculations mainly performed by DFT methodologies.

From a synthetic point of view, the experimental observations on aGNRs have scientific relevance since this work shows a new example of an effective synthesis of aGNRs by the lateral fussion of nanowired organic nanostructures. Moreover, depicts an scenario in which this synhtesis can be selective in terms of the resulting ribbon width and main surface orientation by the use of a proper substrate as template, adittionally allowing complementary avering surface techniques like ARPES that confirms the spectroscopic results acquired by means of STM. Regarding the synthetic aspects observed in the study of chGNRs, here we show how the resulting edge structure of the GNRs formed can be precisely controlled by tuning the halogenated positions within the same bianthryl molecular precursors to provide chGNRs instead of aGNRs, and how this proccess yields an unique type of GNR on three different metallic substartes commonly employed in on-surface experiments. Moreover, we evaluate the reactivity of all these halogenated positios present in the same molecule, observing how one particular position is preferably activated due to the particular adsoprtion geometry of the molecule which let this prefered position closer to the catalytic surface and thus exposed to a major catalytic effect than the halogenated positions related to the formation of aGNRs. Furthermore, we analayze the stereochemistry given along the whole synthetic pathway which rules the chirality of the intermediate and final products, observing how the innate chiral configuration of the enantiomeric precursors is conserved and transmitted to the intermediate chiral polymers, until the final pro-chiral GNRs. Finally, we depict a precise scenario to study the influence of chGNRs width on the emergence of edge states by the smart design of a family of molecular precursors which renders three different varying-width chGNRs all presenting the same chirl edge orientation.

Nevertheless these manuscript's results on the characterization of the electronic structure of the synthesized products is particularly fruitful, illustrating in the width-band gap inverse relation of the first four narrowest aGNRs of the $3p$-family, those values within this relation tendency is mainly defined and presenting semiconducting band gap values with the desired range for the manufacuring of many digital-logic electrical components. Moreover, we show how the substrate can have a drastic impact in AGNRs' electronic structure by effects such as Fermi level pinning, relevant for the study of metal-molecule contacts at the atomic level. Regarding cGNRs, we strongly demonstrate that they feature a semiconducting bandgap on Au(111) within the desired semiconducting range and show no presence of edge states until certain width, in which they underego a transtition through a semimetallic, to metallic cGNR with zero-energy modes thightly located at their zigzag-like edges.

All things considered, the amount of results exposed in ths thesis, being most of them published or through journal evaluation process, suppose a considerable step forward in the understanding of the promising and potential role of GNRs in their implementation into post-Silicon electronic devices, as well as it remarks relevant aspects of the on-surface synthesis of graphene-like nanostuctures and the role that the substrate can have on this production methodologies.

# Bibliography

[1] N. Taguchi, *Nanotechnology: Integrated Processing Systems for Ultra-Precision and Ultra-Fine Products.*
Oxford [England]: Oxford science publications, new york: oxford university press ed., 1996.

[2] G. Binnig, H. Rohrer, C. Gerber, and E. Weibel, "Surface Studies by Scanning Tunneling Microscopy," *Physical Review Letters*, vol. 49, pp. 57–61, July 1982.

[3] G. Binnig and H. Rohrer, "SCANNING TUNNELING MICROSCOPY," *Surface Science*, vol. 126, pp. 236–244, 1983.

[4] K. S. Novoselov, A. K. Geim, S. V. Morozov, D. Jiang, M. I. Katsnelson, I. V. Grigorieva, S. V. Dubonos, and A. A. Firsov, "Two-dimensional gas of massless Dirac fermions in graphene," *Nature*, vol. 438, pp. 197–200, Nov. 2005.

[5] A. K. Geim and K. S. Novoselov, "The rise of graphene.," *Nature Materials*, vol. 6, pp. 183–191, 2007.

[6] C. Lee, Xiaoding Wei, Jeffery W. Kysar, and James Home, "Measurement of the Elastic Properties and Intrinsic Strength of Monolayer Graphene," *Science*, vol. 321, pp. 385–388, July 2008.

[7] A. A. Balandin, S. Ghosh, W. Bao, I. Calizo, D. Teweldebrhan, F. Miao, and C. N. Lau, "Superior Thermal Conductivity of Single-Layer Graphene," *Nano Letters*, vol. 8, pp. 902–907, Mar. 2008.

[8] A. H. Castro Neto, F. Guinea, N. M. R. Peres, K. S. Novoselov, and A. K. Geim, "The electronic properties of graphene," *Reviews of Modern Physics*, vol. 81, pp. 109–162, Jan. 2009.

[9] B. Huang, F. Liu, J. Wu, B.-L. Gu, and W. Duan, "Suppression of spin polarization in graphene nanoribbons by edge defects and impurities," *Phys. Rev. B*, vol. 77, p. 153411, Apr. 2008.

[10] D. Querlioz, Y. Apertet, A. Valentin, K. Huet, A. Bournel, S. Galdin-Retailleau, and P. Dollfus, "Suppression of the orientation effects on bandgap in graphene nanoribbons in the presence of edge disorder," *Applied Physics Letters*, vol. 92, p. 042108, Jan. 2008.

[11] J. Cai, P. Ruffieux, R. Jaafar, M. Bieri, T. Braun, S. Blankenburg, M. Muoth, A. P. Seitsonen, M. Saleh, X. Feng, K. Müllen, and R. Fasel, "Atomically precise bottom-up fabrication of graphene nanoribbons.," *Nature*, vol. 466, p. 470, 2010.

[12] F. Ullmann and J. Bielecki, "Ueber Synthesen in der Biphenylrcihe.," *J. Ber. Dtsch. Chem.*, vol. 34, p. 2174, 1901.

[13] Z. Xiao, C. Ma, W. Lu, J. Huang, L. Liang, K. Hong, A.-P. Li, B. G. Sumpter, and J. Bernholc, "Ab initio investigation of the cyclodehydrogenation process for polyanthrylene transformation to graphene nanoribbons," *npj Comput Mater*, vol. 5, p. 91, Dec. 2019.

[14] Y. W. Son, M. L. Cohen, and S. G. Louie, "Energy Gaps in Graphene Nanoribbons.," *Physical Review Letters*, vol. 97, no. 21, p. 216803, 2006.

[15] L. Yang, C.-H. Park, Y.-W. Son, M. L. Cohen, and S. G. Louie, "Quasiparticle Energies and Band Gaps in Graphene Nanoribbons.," *Physical Review Letters*, vol. 99, p. 186801, 2007.

[16] Y.-C. Chen, D. G. de Oteyza, Z. Pedramrazi, C. Chen, F. R. Fischer, and M. F. Crommie, "Tuning the Band Gap of Graphene Nanoribbons Synthesized from Molecular Precursors.," *ACSnano*, vol. 7, no. 7, pp. 6123–6128, 2013.

[17] R. P. Feynamn, "There's plenty of room at the bottom: An invitation to enter a new field of physics," *Resonance*, vol. 16, no. 9, pp. 890–905, 2011.

[18] G. Moore, "Cramming More Components Onto Integrated Circuits," *Proc. IEEE*, vol. 86, pp. 82–85, Jan. 1998.

[19] W. Jeong, S. Maeda, H. Lee, K. Lee, T. Lee, D. Park, B. Kim, J. Do, T. Fukai, D. Kwon, K. Nam, W. Rim, M. Jang, H. Kim, Y. Lee, J. Park, E. Lee, D. Ha, C. Park, H.-J. Cho, S.-M. Jung, and H. Kang, "True 7nm Platform Technology featuring Smallest FinFET and Smallest SRAM cell by EUV, Special Constructs and 3D Generation Single Diffusion Break," in *2018 IEEE Symposium on VLSI Technology*, (Honolulu, HI), pp. 59–60, IEEE, June 2018.

[20] B. Sheu, K. Wilcox, A. M. Keshavarzi, and D. Antoniadis, "EP1: Moore's law challenges below 10nm: Technology, design and economic implications," in *2015 IEEE International Solid-State Circuits Conference - (ISSCC) Digest of Technical Papers*, (San Francisco, CA, USA), pp. 1–1, IEEE, Feb. 2015.

[21] M. Waldrop, "More than Moore," *Nature*, vol. 530, pp. 145–147, 2016.

[22] W. Lu, Y. Lee, J. Murdzek, J. Gertsch, A. Vardi, L. Kong, S. M. George, and J. A. del Alamo, "First Transistor Demonstration of Thermal Atomic Layer Etching: InGaAs FinFETs with sub-5 nm Fin-width Featuring in situ ALE-ALD," in *2018 IEEE International Electron Devices Meeting (IEDM)*, (San Francisco, CA), pp. 39.1.1–39.1.4, IEEE, Dec. 2018.

[23] H. Jeong, D. Kim, D. Xiang, and T. Lee, "High-Yield Functional Molecular Electronic Devices," *ACS Nano*, June 2017.

[24] T. Ogawa, *Molecular Architectonics.*
New York, NY: Springer Berlin Heidelberg, 2017.

[25] X. Guo, *Molecular-Scale Electronics: Current Status and Perspectives.*
New York, NY: Springer Berlin Heidelberg, 2018.

[26] A. Aviram and M. A. Ratrer, "MOLECULAR RECTIFIERS," *Chemical Physics Letters*, vol. 29, no. 2, pp. 277–283, 1974.

[27] P. R. Wallace, "The Band Theory of Graphite," *Physical Review*, vol. 71, no. 9, 1947.

[28] J. W. McClure, "Diamagnetism of Graphite," *Physical Review*, vol. 104, pp. 666–671, Nov. 1956.

[29] J. C. Slonczewski and P. R. Weiss, "Band Structure of Graphite," *Physical Review*, vol. 109, pp. 272–279, Jan. 1958.

[30] N. D. Mermin, "Crystalline Order in Two Dimensions," *Physical Review*, vol. 176, pp. 250–254, Dec. 1968.

[31] K. S. Novoselov, A. K. Geim, S. V. Morozov, D. Jiang, Y. Zhang, S. V. Dubonos, I. V. Grigorieva, and A. A. Firsov, "Electric Field Effect in Atomically Thin Carbon Films.," *Science*, vol. 306, p. 666, 2004.

[32] D. E. Sheehy and J. Schmalian, “Optical transparency of graphene as determined by the fine-structure constant,” *Physical Review B*, vol. 80, Nov. 2009.

[33] F. Schwierz, “Graphene transistors,” *Nature Nanotechnology*, vol. 5, pp. 487–496, July 2010.

[34] A. Celis, M. N. Nair, A. Taleb-Ibrahimi, E. H. Conrad, C. Berger, W. A. de Heer, and A. Tejeda, “Graphene nanoribbons: Fabrication, properties and devices,” *Journal of Physics D: Applied Physics*, vol. 49, p. 143001, Apr. 2016.

[35] V. M. Pereira, A. H. Castro Neto, and N. M. R. Peres, “Tight-binding approach to uniaxial strain in graphene,” *Phys. Rev. B*, vol. 80, p. 045401, July 2009.

[36] N. Levy, S. A. Burke, K. L. Meaker, M. Panlasigui, A. Zettl, F. Guinea, A. H. C. Neto, and M. F. Crommie, “Strain-Induced Pseudo-Magnetic Fields Greater Than 300 Tesla in Graphene Nanobubbles,” *Science*, vol. 329, pp. 544–547, July 2010.

[37] J.-H. Wong, B.-R. Wu, and M.-F. Lin, “Strain Effect on the Electronic Properties of Single Layer and Bilayer Graphene,” *J. Phys. Chem. C*, vol. 116, pp. 8271–8277, Apr. 2012.

[38] R. Balog, B. Jørgensen, L. Nilsson, M. Andersen, E. Rienks, M. Bianchi, M. Fanetti, E. Lægsgaard, A. Baraldi, S. Lizzit, Z. Sljivancanin, F. Besenbacher, B. Hammer, T. G. Pedersen, P. Hofmann, and L. Hornekær, “Bandgap opening in graphene induced by patterned hydrogen adsorption,” *Nature Mater*, vol. 9, pp. 315–319, Apr. 2010.

[39] A. Castellanos-Gomez, M. Wojtaszek, Arramel, N. Tombros, and B. J. van Wees, “Reversible Hydrogenation and Bandgap Opening of Graphene and Graphite Surfaces Probed by Scanning Tunneling Spectroscopy,” *Small*, vol. 8, pp. 1607–1613, May 2012.

[40] Z. Luo, J. Shang, S. Lim, D. Li, Q. Xiong, Z. Shen, J. Lin, and T. Yu, “Modulating the electronic structures of graphene by controllable hydrogenation,” *Appl. Phys. Lett.*, vol. 97, p. 233111, Dec. 2010.

[41] B. R. Matis, J. S. Burgess, F. A. Bulat, A. L. Friedman, B. H. Houston, and J. W. Baldwin, “Surface Doping and Band Gap Tunability in Hydrogenated Graphene,” *ACS Nano*, vol. 6, pp. 17–22, Jan. 2012.

[42] E. Bekyarova, M. E. Itkis, P. Ramesh, C. Berger, M. Sprinkle, W. A. de Heer, and R. C. Haddon, “Chemical Modification of Epitaxial Graphene: Spontaneous Grafting of Aryl Groups,” *J. Am. Chem. Soc.*, vol. 131, pp. 1336–1337, Feb. 2009.

[43] P. A. Denis, “Band gap opening of monolayer and bilayer graphene doped with aluminium, silicon, phosphorus, and sulfur,” *Chemical Physics Letters*, vol. 492, pp. 251–257, June 2010.

[44] P. A. Denis, “Chemical Reactivity and Band-Gap Opening of Graphene Doped with Gallium, Germanium, Arsenic, and Selenium Atoms,” *ChemPhysChem*, vol. 15, pp. 3994–4000, Dec. 2014.

[45] W. Zhang, C.-T. Lin, K.-K. Liu, T. Tite, C.-Y. Su, C.-H. Chang, Y.-H. Lee, C.-W. Chu, K.-H. Wei, J.-L. Kuo, and L.-J. Li, “Opening an Electrical Band Gap of Bilayer Graphene with Molecular Doping,” *ACS Nano*, vol. 5, pp. 7517–7524, Sept. 2011.

[46] R. Lv and M. Terrones, “Towards new graphene materials: Doped graphene sheets and nanoribbons,” *Materials Letters*, vol. 78, pp. 209–218, July 2012.

[47] B. Biel, F. Triozon, X. Blase, and S. Roche, “Chemically Induced Mobility Gaps in Graphene Nanoribbons: A Route for Upscaling Device Performances,” *Nano Lett.*, vol. 9, pp. 2725–2729, July 2009.

[48] C. Berger, Z. Song, T. Li, X. Li, A. Y. Ogbazghi, R. Feng, Z. Dai, A. N. Marchenkov, E. H. Conrad, P. N. First, and W. A. de Heer, "Ultrathin Epitaxial Graphite: 2D Electron Gas Properties and a Route toward Graphene-based Nanoelectronics," *J. Phys. Chem. B*, vol. 108, pp. 19912–19916, Dec. 2004.

[49] K. Nakada, M. Fujita, G. Dresselhaus, and M. S. Dresselhaus, "Edge state in graphene ribbons: Nanometer size effect and edge shape dependence," *Physical Review B*, vol. 54, no. 24, p. 17954, 1996.

[50] K. Wakabayashi, M. Fujita, H. Ajiki, and M. Sigrist, "Electronic and magnetic properties of nanographite ribbons," *Physical Review B*, vol. 59, no. 12, p. 8271, 1999.

[51] T. Hikihara, X. Hu, H.-H. Lin, and C.-Y. Mou, "Ground-state properties of nanographite systems with zigzag edges," *Physical Review B*, vol. 68, July 2003.

[52] D. A. Abanin, P. A. Lee, and L. S. Levitov, "Spin-Filtered Edge States and Quantum Hall Effect in Graphene," *Physical Review Letters*, vol. 96, May 2006.

[53] L. Brey and H. A. Fertig, "Edge states and the quantized Hall effect in graphene," *Physical Review B*, vol. 73, May 2006.

[54] L. Brey and H. A. Fertig, "Electronic states of graphene nanoribbons studied with the Dirac equation," *Physical Review B*, vol. 73, June 2006.

[55] J. Jung and A. H. MacDonald, "Carrier density and magnetism in graphene zigzag nanoribbons," *Phys. Rev. B*, vol. 79, p. 235433, June 2009.

[56] D. Gunlycke and C. T. White, "Tight-binding energy dispersions of armchair-edge graphene nanostrips.," *Physical Review B*, vol. 77, p. 115116, 2008.

[57] H. Raza and E. C. Kan, "Armchair graphene nanoribbons: Electronic structure and electric-field modulation.," *Phys. Rev. B*, vol. 77, p. 245434, 2008.

[58] H. Sevinçli, M. Topsakal, and S. Ciraci, "Superlattice structures of graphene-based armchair nanoribbons.," *Physical Review B*, vol. 78, p. 245402, 2008.

[59] O. V. Yazyev, R. B. Capaz, and S. G. Louie, "Theory of magnetic edge states in chiral graphene nanoribbons.," *Physical Review B*, vol. 84, p. 115406, 2011.

[60] M. Golor, T. C. Lang, and S. Wessel, "Quantum Monte Carlo studies of edge magnetism in chiral graphene nanoribbons," *Physical Review B*, vol. 87, Apr. 2013.

[61] A. R. Carvalho, J. H. Warnes, and C. H. Lewenkopf, "Edge magnetization and local density of states in chiral graphene nanoribbons," *Physical Review B*, vol. 89, June 2014.

[62] Z. Jiang and Y. Song, "Band gap oscillation and novel transport property in ultrathin chiral graphene nanoribbons," *Physica B: Condensed Matter*, vol. 464, pp. 61–67, May 2015.

[63] S. Suda and A. Oshiyama, "Energetics, Electron States, and Magnetization in Nearly Zigzag-Edged Graphene Nano-Ribbons," *Journal of the Physical Society of Japan*, vol. 84, p. 024704, Feb. 2015.

[64] L. Li, A.-R. O. Raji, H. Fei, Y. Yang, E. L. G. Samuel, and J. M. Tour, "Nanocomposite of Polyaniline Nanorods Grown on Graphene Nanoribbons for Highly Capacitive Pseudocapacitors," *ACS Appl. Mater. Interfaces*, vol. 5, pp. 6622–6627, July 2013.

[65] M. Mehdi Pour, A. Lashkov, A. Radocea, X. Liu, T. Sun, A. Lipatov, R. A. Korlacki, M. Shekhirev, N. R. Aluru, J. W. Lyding, V. Sysoev, and A. Sinitskii, "Laterally extended atomically precise graphene nanoribbons with improved electrical conductivity for efficient gas sensing," *Nat Commun*, vol. 8, p. 820, Dec. 2017.

[66] M. Freitag, T. Low, W. Zhu, H. Yan, F. Xia, and P. Avouris, "Photocurrent in graphene harnessed by tunable intrinsic plasmons," *Nat Commun*, vol. 4, p. 1951, Oct. 2013.

[67] F. Mazzamuto, V. Hung Nguyen, Y. Apertet, C. Caër, C. Chassat, J. Saint-Martin, and P. Dollfus, "Enhanced thermoelectric properties in graphene nanoribbons by resonant tunneling of electrons," *Physical Review B*, vol. 83, p. 235426(7), June 2011.

[68] H. Sevinçli, C. Sevik, T. Çağın, and G. Cuniberti, "A bottom-up route to enhance thermoelectric figures of merit in graphene nanoribbons," *Scientific Reports*, vol. 3, Dec. 2013.

[69] J. Kang, D. Sarkar, Y. Khatami, and K. Banerjee, "Proposal for all-graphene monolithic logic circuits," *Applied Physics Letters*, vol. 103, p. 083113, Aug. 2013.

[70] A. N. Cleland and M. L. Roukes, "A nanometre-scale mechanical electrometer," *Nature*, vol. 392, pp. 160–162, Mar. 1998.

[71] H. Kind, J.-M. Bonard, C. Emmenegger, L.-O. Nilsson, K. Hernadi, E. Maillard-Schaller, L. Schlapbach, L. Forró, and K. Kern, "Patterned Films of Nanotubes Using Microcontact Printing of Catalysts," *Advanced Materials*, vol. 11, no. 15, pp. 1285–1289, 1999.

[72] M. A. Lingenfelder, H. Spillmann, A. Dmitriev, S. Stepanow, N. Lin, J. V. Barth, and K. Kern, "Towards Surface-Supported Supramolecular Architectures: Tailored Coordination Assembly of 1,4-Benzenedicarboxylate and Fe on Cu(100)," *Chem. Eur. J.*, vol. 10, pp. 1913–1919, Apr. 2004.

[73] D. M. Eigler and E. K. Schweizer, "Positioning single atoms with a scanning tunnelling microscope," vol. 344, p. 3, 1990.

[74] J. V. Barth, G. Costantini, and K. Kern, "Engineering atomic and molecular nanostructures at surfaces," *Nature*, vol. 437, pp. 671–679, Sept. 2005.

[75] B. D. Gates, Q. Xu, M. Stewart, D. Ryan, C. G. Willson, and G. M. Whitesides, "New Approaches to Nanofabrication: Molding, Printing, and Other Techniques," *Chem. Rev.*, vol. 105, pp. 1171–1196, Apr. 2005.

[76] T. Ito and S. Okazaki, "Pushing the limits of lithography," *Nature*, vol. 406, pp. 1027–1031, Aug. 2000.

[77] V. Balzani, "Nanoscience and nanotechnology: The bottom-up construction of molecular devices and machines," *Pure and Applied Chemistry*, vol. 80, pp. 1631–1650, Jan. 2008.

[78] C. Berger, Z. Song, X. Li, X. Wu, N. Brown, C. Naud, D. Mayou, T. Li, J. Hass, A. N. Marchenkov, E. H. Conrad, P. N. First, and W. A. de Heer, "Electronic Confinement and Coherence in Patterned Epitaxial Graphene," *Science*, vol. 312, pp. 1191–1195, 2006.

[79] Z. Chen, Y.-M. Lin, M. J. Rooks, and P. Avouris, "Graphene nano-ribbon electronics," *Physica E: Low-dimensional Systems and Nanostructures*, vol. 40, pp. 228–232, Dec. 2007.

[80] M. Y. Han, B. Özyilmaz, Y. Zhang, and P. Kim, "Energy Band-Gap Engineering of Graphene Nanoribbons," *Phys. Rev. Lett.*, vol. 98, p. 206805, May 2007.

[81] Jeon, Sang-Chul, Kim, Young-Su, and Lee, Dong-Kyu, "Fabrication of a Graphene Nanoribbon with Electron Beam Lithography Using a XR-1541/PMMA Lift-Off Process," *Transactions on Electrical and Electronic Materials*, vol. 11, pp. 190–193, Aug. 2010.

[82] J. A. Gardener and J. A. Golovchenko, "Ice-assisted electron beam lithography of graphene," *Nanotechnology*, vol. 23, p. 185302, May 2012.

[83] G. Z. Magda, X. Jin, I. Hagymási, P. Vancsó, Z. Osváth, P. Nemes-Incze, C. Hwang, L. P. Biró, and L. Tapasztó, "Room-temperature magnetic order on zigzag edges of narrow graphene nanoribbons," *Nature*, vol. 514, pp. 608–611, Oct. 2014.

[84] L. Jiao, L. Zhang, X. Wang, G. Diankov, and H. Dai, “Narrow graphene nanoribbons from carbon nanotubes.,” *Nature*, vol. 458, pp. 877–880, 2009.

[85] D. V. Kosynkin, A. L. Higginbotham, A. Sinitskii, J. R. Lomeda, A. Dimiev, B. K. Price, and J. M. Tour, “Longitudinal unzipping of carbon nanotubes to form graphene nanoribbons,” *Nature*, vol. 458, pp. 872–876, Apr. 2009.

[86] A. L. Elías, A. R. Botello-Méndez, D. Meneses-Rodríguez, V. Jehová González, D. Ramírez-González, L. Ci, E. Muñoz-Sandoval, P. M. Ajayan, H. Terrones, and M. Terrones, “Longitudinal Cutting of Pure and Doped Carbon Nanotubes to Form Graphitic Nanoribbons Using Metal Clusters as Nanoscalpels,” *Nano Lett.*, vol. 10, pp. 366–372, Feb. 2010.

[87] L. Jiao, X. Wang, G. Diankov, H. Wang, and H. Dai, “Facile synthesis of high-quality graphene nanoribbons,” *Nature Nanotech*, vol. 5, pp. 321–325, May 2010.

[88] C. Tao, L. Jiao, O. V. Yazyev, Y.-C. Chen, J. Feng, X. Zhang, R. B. Capaz, J. M. Tour, A. Zettl, S. G. Louie, H. Dai, and M. F. Crommie, “Spatially resolving edge states of chiral graphene nanoribbons,” *Nature Physics*, vol. 7, pp. 616–620, May 2011.

[89] Z.-S. Wu, W. Ren, L. Gao, B. Liu, J. Zhao, and H.-M. Cheng, “Efficient synthesis of graphene nanoribbons sonochemically cut from graphene sheets,” *Nano Res.*, vol. 3, pp. 16–22, Jan. 2010.

[90] R. S. Deacon, K.-C. Chuang, R. J. Nicholas, K. S. Novoselov, and A. K. Geim, “Cyclotron resonance study of the electron and hole velocity in graphene monolayers,” *Physical Review B*, vol. 76, no. 081406(R), 2007.

[91] L. Ci, Z. Xu, L. Wang, W. Gao, F. Ding, K. F. Kelly, B. I. Yakobson, and P. M. Ajayan, “Controlled nanocutting of graphene,” *Nano Res.*, vol. 1, pp. 116–122, Aug. 2008.

[92] J. Bai, X. Duan, and Y. Huang, “Rational Fabrication of Graphene Nanoribbons Using a Nanowire Etch Mask,” *Nano Lett.*, vol. 9, pp. 2083–2087, May 2009.

[93] L. C. Campos, V. R. Manfrinato, J. D. Sanchez-Yamagishi, J. Kong, and P. Jarillo-Herrero, “Anisotropic Etching and Nanoribbon Formation in Single-Layer Graphene,” *Nano Lett.*, vol. 9, pp. 2600–2604, July 2009.

[94] X. Wang and H. Dai, “Etching and narrowing of graphene from the edges,” *Nature Chem*, vol. 2, pp. 661–665, Aug. 2010.

[95] G. Liu, Y. Wu, Y.-M. Lin, D. B. Farmer, J. A. Ott, J. Bruley, A. Grill, P. Avouris, D. Pfeiffer, A. A. Balandin, and C. Dimitrakopoulos, “Epitaxial Graphene Nanoribbon Array Fabrication Using BCP-Assisted Nanolithography,” *ACS Nano*, vol. 6, pp. 6786–6792, Aug. 2012.

[96] A. Sinitskii and J. M. Tour, “Patterning graphene nanoribbons using copper oxide nanowires,” *Appl. Phys. Lett.*, vol. 100, p. 103106, Mar. 2012.

[97] S. Wu, B. Liu, C. Shen, S. Li, X. Huang, X. Lu, P. Chen, G. Wang, D. Wang, M. Liao, J. Zhang, T. Zhang, S. Wang, W. Yang, R. Yang, D. Shi, K. Watanabe, T. Taniguchi, Y. Yao, W. Wang, and G. Zhang, “Magnetotransport Properties of Graphene Nanoribbons with Zigzag Edges,” *Physical Review Letters*, vol. 120, May 2018.

[98] A. J. Way, E. A. Murray, F. Göltl, V. Saraswat, R. M. Jacobberger, M. Mavrikakis, and M. S. Arnold, “Anisotropic Synthesis of Armchair Graphene Nanoribbon Arrays from Sub-5 nm Seeds at Variable Pitches on Germanium,” *J. Phys. Chem. Lett.*, p. acs.jpclett.9b01079, July 2019.

[99] D. Gunlycke, D. A. Areshkin, and C. T. White, “Semiconducting graphene nanostrips with edge disorder,” *Appl. Phys. Lett.*, vol. 90, p. 142104, Apr. 2007.

[100] C. Stampfer, J. Güttinger, S. Hellmüller, F. Molitor, K. Ensslin, and T. Ihn, "Energy Gaps in Etched Graphene Nanoribbons," *Physical Review Letters*, vol. 102, Feb. 2009.

[101] X. Li, X. Wang, L. Zhang, Sangwon Lee, and H. Dai, "Chemically Derived, Ultrasmooth Graphene Nanoribbon Semiconductors," *Science*, vol. 319, pp. 1226–1229, Feb. 2008.

[102] X. Yang, X. Dou, A. Rouhanipour, L. Zhi, H. J. Räder, and K. Müllen, "Two-Dimensional Graphene Nanoribbons," *J. Am. Chem. Soc.*, vol. 130, pp. 4216–4217, Apr. 2008.

[103] T. H. Vo, M. Shekhirev, D. A. Kunkel, M. D. Morton, E. Berglund, L. Kong, P. M. Wilson, P. A. Dowben, A. Enders, and A. Sinitskii, "Large-scale solution synthesis of narrow graphene nanoribbons," *Nat Commun*, vol. 5, p. 3189, May 2014.

[104] J. Campos-Delgado, J. M. Romo-Herrera, X. Jia, D. A. Cullen, H. Muramatsu, Y. A. Kim, T. Hayashi, Z. Ren, D. J. Smith, Y. Okuno, T. Ohba, H. Kanoh, K. Kaneko, M. Endo, H. Terrones, M. S. Dresselhaus, and M. Terrones, "Bulk Production of a New Form of sp2 Carbon: Crystalline Graphene Nanoribbons," *Nano Lett.*, vol. 8, pp. 2773–2778, Sept. 2008.

[105] X. Jia, M. Hofmann, V. Meunier, B. G. Sumpter, J. Campos-Delgado, J. M. Romo-Herrera, H. Son, Y.-P. Hsieh, A. Reina, J. Kong, M. Terrones, and M. S. Dresselhaus, "Controlled Formation of Sharp Zigzag and Armchair Edges in Graphitic Nanoribbons," *Science*, vol. 323, pp. 1701–1705, Mar. 2009.

[106] I. Martin-Fernandez, D. Wang, and Y. Zhang, "Direct Growth of Graphene Nanoribbons for Large-Scale Device Fabrication," *Nano Letters*, vol. 12, pp. 6175–6179, Dec. 2012.

[107] M. Pan, E. C. Girão, X. Jia, S. Bhaviripudi, Q. Li, J. Kong, V. Meunier, and M. S. Dresselhaus, "Topographic and Spectroscopic Characterization of Electronic Edge States in CVD Grown Graphene Nanoribbons," *Nano Lett.*, vol. 12, pp. 1928–1933, Apr. 2012.

[108] T. Kato and R. Hatakeyama, "Site- and alignment-controlled growth of graphene nanoribbons from nickel nanobars," *Nature Nanotech*, vol. 7, pp. 651–656, Oct. 2012.

[109] A. N. Sokolov, F. L. Yap, N. Liu, K. Kim, L. Ci, O. B. Johnson, H. Wang, M. Vosgueritchian, A. L. Koh, J. Chen, J. Park, and Z. Bao, "Direct growth of aligned graphitic nanoribbons from a DNA template by chemical vapour deposition," *Nat Commun*, vol. 4, p. 2402, Dec. 2013.

[110] V. Barone, O. Hod, and G. E. Scuseria, "Electronic Structure and Stability of Semiconducting Graphene Nanoribbons," *Nano Lett.*, vol. 6, pp. 2748–2754, Dec. 2006.

[111] L. Grill, M. Dyer, L. Lafferentz, M. Persson, M. V. Peters, and S. Hecht, "Nano-architectures by covalent assembly of molecular building blocks," *Nature Nanotechnology*, vol. 2, pp. 687–691, Nov. 2007.

[112] K. T. Rim, M. Siaj, S. Xiao, M. Myers, V. D. Carpentier, L. Liu, C. Su, M. L. Steigerwald, M. S. Hybertsen, P. H. McBreen, G. W. Flynn, and C. Nuckolls, "Forming Aromatic Hemispheres on Transition-Metal Surfaces," *Angew. Chem. Int. Ed.*, vol. 46, pp. 7891–7895, Oct. 2007.

[113] G. Otero, G. Biddau, C. Sánchez-Sánchez, R. Caillard, M. F. López, C. Rogero, F. J. Palomares, N. Cabello, M. A. Basanta, J. Ortega, J. Méndez, A. M. Echavarren, R. Pérez, B. Gómez-Lor, and J. A. Martín-Gago, "Fullerenes from aromatic precursors by surface-catalysed cyclodehydrogenation," *Nature*, vol. 454, pp. 865–868, Aug. 2008.

[114] M. Lackinger, "Surface-assisted Ullmann coupling," *Chemical Communications*, vol. 53, no. 56, pp. 7872–7885, 2017.

[115] J. van der Lit, M. P. Boneschanscher, D. Vanmaekelbergh, M. Ijäs, A. Uppstu, M. Ervasti, A. Harju, P. Liljeroth, and I. Swart, "Suppression of electron–vibron coupling in graphene nanoribbons contacted via a single atom," *Nat Commun*, vol. 4, p. 2023, Oct. 2013.

[116] S. Clair and D. G. de Oteyza, "Controlling a Chemical Coupling Reaction on a Surface: Tools and Strategies for On-Surface Synthesis," *Chem. Rev.*, vol. 119, pp. 4717–4776, Apr. 2019.

[117] P. Ruffieux, S. Wang, B. Yang, C. Sánchez-Sánchez, J. Liu, T. Dienel, L. Talirz, P. Shinde, C. A. Pignedoli, D. Passerone, T. Dumslaff, X. Feng, K. Müllen, and R. Fasel, "On-surface synthesis of graphene nanoribbons with zigzag edge topology.," *Nature*, vol. 531, p. 489, 2016.

[118] A. Kimouche, M. M. Ervasti, R. Drost, S. Halonen, A. Harju, P. M. Joensuu, J. Sainio, and P. Liljeroth, "Ultra-narrow metallic armchair graphene nanoribbons.," *Nature Communications*, vol. 6, p. 10177, 2015.

[119] L. Talirz, H. Söde, T. Dumslaff, S. Wang, J. R. Sanchez-Valencia, J. Liu, P. Shinde, C. A. Pignedoli, L. Liang, V. Meunier, N. C. Plumb, M. Shi, X. Feng, A. Narita, K. Müllen, R. Fasel, and P. Ruffieux, "On-Surface Synthesis and Characterization of 9-Atom Wide Armchair Graphene Nanoribbons.," *ACSnano*, vol. 11, pp. 1380–1388, 2017.

[120] J. Liu, B.-W. Li, Y.-Z. Tan, A. Giannakopoulos, C. Sanchez-Sanchez, D. Beljonne, P. Ruffieux, R. Fasel, X. Feng, and K. Müllen, "Toward Cove-Edged Low Band Gap Graphene Nanoribbons," *J. Am. Chem. Soc.*, vol. 137, pp. 6097–6103, May 2015.

[121] S. Kawai, S. Saito, S. Osumi, S. Yamaguchi, A. S. Foster, P. Spijker, and E. Meyer, "Atomically controlled substitutional boron-doping of graphene nanoribbons.," *Nature Communications*, vol. 6, p. 8098, 2015.

[122] E. Carbonell-Sanromà, P. Brandimarte, R. Balog, M. Corso, S. Kawai, A. Garcia-Lekue, S. Saito, S. Yamaguchi, E. Meyer, D. Sánchez-Portal, and J. I. Pascual, "Quantum Dots Embedded in Graphene Nanoribbons by Chemical Substitution.," *Nano Letters*, vol. 17, pp. 50–56, 2017.

[123] J. Cai, C. A. Pignedoli, L. Talirz, P. Ruffieux, H. Söde, L. Liang, V. Meunier, R. Berger, R. Li, X. Feng, K. Müllen, and R. Fasel, "Graphene nanoribbon heterojunctions.," *Nature Nanotechnology*, vol. 9, p. 896, 2014.

[124] L. Talirz, H. Söde, S. Kawai, P. Ruffieux, E. Meyer, X. Feng, K. Müllen, R. Fasel, C. A. Pignedoli, and D. Passerone, "Band gap of atomically precise graphene nanoribbons as a function of ribbon length and termination," *ChemPhysChem*, p. cphc.201900313, July 2019.

[125] N. Merino-Díez, A. Garcia-Lekue, E. Carbonell-Sanromà, J. Li, M. Corso, L. Colazzo, F. Sedona, D. Sánchez-Portal, J. I. Pascual, and D. G. de Oteyza, "Width-Dependent Band Gap in Armchair Graphene Nanoribbons Reveals Fermi Level Pinning on Au(111)," *ACS Nano*, vol. 11, pp. 11661–11668, Nov. 2017.

[126] E. Costa Girão, L. Liang, E. Cruz-Silva, A. G. S. Filho, and V. Meunier, "Emergence of Atypical Properties in Assembled Graphene Nanoribbons," *Phys. Rev. Lett.*, vol. 107, p. 135501, Sept. 2011.

[127] C. Moreno, M. Vilas-Varela, B. Kretz, A. Garcia-Lekue, M. V. Costache, M. Paradinas, M. Panighel, G. Ceballos, S. O. Valenzuela, D. Peña, and A. Mugarza, "Bottom-up synthesis of multifunctional nanoporous graphene," p. 6, 2018.

[128] L. Talirz, P. Ruffieux, and R. Fasel, "On-Surface Synthesis of Atomically Precise Graphene Nanoribbons.," *Advanced Materials*, 2016.

[129] H. Huang, D. Wei, J. Sun, S. L. Wong, Y. P. Feng, A. H. C. Neto, and A. T. S. Wee, "Spatially Resolved Electronic Structures of Atomically Precise Armchair Graphene Nanoribbons.," *Scientific Reports*, vol. 2, p. 983, 2012.

[130] N. Abdurakhmanova, N. Amsharov, S. Stepanow, M. Jansen, K. Kern, and K. Amsharov, "Synthesis of wide atomically precise graphene nanoribbons from para-oligophenylene based molecular precursor," *Carbon*, vol. 77, pp. 1187–1190, Oct. 2014.

[131] A. Basagni, F. Sedona, C. A. Pignedoli, M. Cattelan, L. Nicolas, M. Casarin, and M. Sambi, "Molecules-Oligomers-Nanowires-Graphene Nanoribbons: A Bottom-Up Stepwise On-Surface Covalent Synthesis Preserving Long-Range Order," *Journal of the American Chemical Society*, vol. 137, pp. 1802–1808, Feb. 2015.

[132] Z. Chen, H. I. Wang, N. Bilbao, J. Teyssandier, T. Prechtl, N. Cavani, A. Tries, R. Biagi, V. De Renzi, X. Feng, M. Kläui, S. De Feyter, M. Bonn, A. Narita, and K. Müllen, "Lateral Fusion of Chemical Vapor Deposited $N = 5$ Armchair Graphene Nanoribbons," *Journal of the American Chemical Society*, vol. 139, pp. 9483–9486, July 2017.

[133] O. Deniz, C. Sánchez-Sánchez, T. Dumslaff, X. Feng, A. Narita, K. Müllen, N. Kharche, V. Meunier, R. Fasel, and P. Ruffieux, "Revealing the Electronic Structure of Silicon Intercalated Armchair Graphene Nanoribbons by Scanning Tunneling Spectroscopy.," *Nano Letters*, vol. 17, pp. 2197–2203, 2017.

[134] C. Ma, L. Liang, Z. Xiao, A. A. Puretzky, K. Hong, W. Lu, V. Meunier, J. Bernholc, and A.-P. Li, "Seamless Staircase Electrical Contact to Semiconducting Graphene Nanoribbons," *Nano Letters*, vol. 17, pp. 6241–6247, Sept. 2017.

[135] S. Song, T. Kojima, T. Nakae, and H. Sakaguchi, "Wide graphene nanoribbons produced by interchain fusion of poly(p-phenylene) via two-zone chemical vapor deposition," *Chem. Commun.*, vol. 53, no. 52, pp. 7034–7036, 2017.

[136] S. Wang, N. Kharche, E. Costa Girão, X. Feng, K. Müllen, V. Meunier, R. Fasel, and P. Ruffieux, "Quantum Dots in Graphene Nanoribbons," *Nano Letters*, vol. 17, pp. 4277–4283, July 2017.

[137] D. Beyer, S. Wang, C. A. Pignedoli, J. Melidonie, B. Yuan, C. Li, J. Wilhelm, P. Ruffieux, R. Berger, K. Müllen, R. Fasel, and X. Feng, "Graphene Nanoribbons Derived from Zigzag Edge-Encased Poly(para -2,9-dibenzo[bc,kl]coronenylene) Polymer Chains," *J. Am. Chem. Soc.*, vol. 141, pp. 2843–2846, Feb. 2019.

[138] K. Sun, P. Ji, J. Zhang, J. Wang, X. Li, X. Xu, H. Zhang, and L. Chi, "On-Surface Synthesis of 8- and 10-Armchair Graphene Nanoribbons," *Small*, p. 1804526, Mar. 2019.

[139] R. A. Durr, D. Haberer, Y.-L. Lee, R. Blackwell, A. M. Kalayjian, T. Marangoni, J. Ihm, S. G. Louie, and F. R. Fischer, "Orbitally Matched Edge-Doping in Graphene Nanoribbons," *Journal of the American Chemical Society*, vol. 140, pp. 807–813, Jan. 2018.

[140] S. Linden, D. Zhong, A. Timmer, N. Aghdassi, J. H. Franke, H. Zhang, X. Feng, K. Müllen, H. Fuchs, L. Chi, and H. Zacharias, "Electronic Structure of Spatially Aligned Graphene Nanoribbons on Au(788)," *Physical Review Letters*, vol. 108, May 2012.

[141] O. Deniz, C. Sanchez Sanchez, R. Jaafar, N. Kharche, L. Liang, V. Meunier, X. Feng, K. Muellen, R. Fasel, and P. Ruffieux, "Electronic characterization of silicon intercalated chevron graphene nanoribbons on Au(111)," *Chemical Communications*, 2018.

[142] V. A. Saroka, H. Abdelsalam, V. A. Demin, D. Grassano, S. A. Kuten, A. L. Pushkarchuk, and O. Pulci, “Absorption in Finite-Length Chevron-Type Graphene Nanoribbons,” *Semiconductors*, vol. 52, pp. 1890–1893, Dec. 2018.

[143] M. Shekhirev, P. Zahl, and A. Sinitskii, “Phenyl Functionalization of Atomically Precise Graphene Nanoribbons for Engineering Inter-ribbon Interactions and Graphene Nanopores,” *ACS Nano*, Aug. 2018.

[144] G. D. Nguyen, H.-Z. Tsai, A. A. Omrani, T. Marangoni, M. Wu, D. J. Rizzo, G. F. Rodgers, R. R. Cloke, R. A. Durr, Y. Sakai, F. Liou, A. S. Aikawa, J. R. Chelikowsky, S. G. Louie, F. R. Fischer, and M. F. Crommie, “Atomically precise graphene nanoribbon heterojunctions from a single molecular precursor,” *Nature Nanotechnology*, Sept. 2017.

[145] D. J. Rizzo, M. Wu, H.-Z. Tsai, T. Marangoni, R. A. Durr, A. A. Omrani, F. Liou, C. Bronner, T. Joshi, G. D. Nguyen, G. F. Rodgers, W.-W. Choi, J. H. Jørgensen, F. R. Fischer, S. G. Louie, and M. F. Crommie, “Length-Dependent Evolution of Type II Heterojunctions in Bottom-Up-Synthesized Graphene Nanoribbons,” *Nano Letters*, p. acs.nanolett.9b00758, Apr. 2019.

[146] C. Bronner, R. A. Durr, D. J. Rizzo, Y.-L. Lee, T. Marangoni, A. M. Kalayjian, H. Rodriguez, W. Zhao, S. G. Louie, F. R. Fischer, and M. F. Crommie, “Hierarchical On-Surface Synthesis of Graphene Nanoribbon Heterojunctions,” *ACS Nano*, vol. 12, pp. 2193–2200, Mar. 2018.

[147] Y. Cao, J. Qi, Y.-F. Zhang, L. Huang, Q. Zheng, X. Lin, Z. Cheng, Y.-Y. Zhang, X. Feng, S. Du, S. T. Pantelides, and H.-J. Gao, “Tuning the morphology of chevron-type graphene nanoribbons by choice of annealing temperature,” *Nano Research*, July 2018.

[148] J. D. Teeter, P. Zahl, M. Mehdi Pour, P. S. Costa, A. Enders, and A. Sinitskii, “On-surface synthesis and spectroscopic characterization of laterally extended chevron graphene nanoribbons,” *ChemPhysChem*, p. cphc.201900445, June 2019.

[149] C. Bronner, S. Stremlau, M. Gille, F. Brauße, A. Haase, S. Hecht, and P. Tegeder, “Aligning the Band Gap of Graphene Nanoribbons by Monomer Doping,” *Angewandte Chemie International Edition*, vol. 52, pp. 4422–4425, Apr. 2013.

[150] B. V. Senkovskiy, A. V. Fedorov, D. Haberer, M. Farjam, K. A. Simonov, A. B. Preobrajenski, N. M?rtensson, N. Atodiresei, V. Caciuc, S. Bl?gel, A. Rosch, N. I. Verbitskiy, M. Hell, D. V. Evtushinsky, R. German, T. Marangoni, P. H. M. van Loosdrecht, F. R. Fischer, and A. Gr?neis, “Semiconductor-to-Metal Transition and Quasiparticle Renormalization in Doped Graphene Nanoribbons,” *Advanced Electronic Materials*, vol. 3, p. 1600490, Apr. 2017.

[151] F. Cervantes-Sodi, G. Csányi, S. Piscanec, and A. C. Ferrari, “Edge-functionalized and substitutionally doped graphene nanoribbons: Electronic and spin properties,” *Phys. Rev. B*, vol. 77, p. 165427, Apr. 2008.

[152] R. R. Cloke, T. Marangoni, G. D. Nguyen, T. Joshi, D. J. Rizzo, C. Bronner, T. Cao, S. G. Louie, M. F. Crommie, and F. R. Fischer, “Site-Specific Substitutional Boron Doping of Semiconducting Armchair Graphene Nanoribbons.,” *J. Am. Chem. Soc.*, vol. 137, pp. 8872–8875, 2015.

[153] P. P. Shinde, O. Gröning, S. Wang, P. Ruffieux, C. A. Pignedoli, R. Fasel, and D. Passerone, “Stability of edge magnetism in functionalized zigzag graphene nanoribbons,” *Carbon*, vol. 124, pp. 123–132, Nov. 2017.

[154] E. Carbonell-Sanromà, A. Garcia-Lekue, M. Corso, G. Vasseur, P. Brandimarte, J. Lobo-Checa, D. G. de Oteyza, J. Li, S. Kawai, S. Saito, S. Yamaguchi, J. E.

Ortega, D. Sánchez-Portal, and J. I. Pascual, “Electronic Properties of Substitutionally Boron-Doped Graphene Nanoribbons on a Au(111) Surface,” *J. Phys. Chem. C*, vol. 122, pp. 16092–16099, July 2018.

[155] Z. Pedramrazi, C. Chen, F. Zhao, T. Cao, G. D. Nguyen, A. A. Omrani, H.-Z. Tsai, R. R. Cloke, T. Marangoni, D. J. Rizzo, T. Joshi, C. Bronner, W.-W. Choi, F. R. Fischer, S. G. Louie, and M. F. Crommie, “Concentration Dependence of Dopant Electronic Structure in Bottom-up Graphene Nanoribbons,” *Nano Letters*, vol. 18, pp. 3550–3556, June 2018.

[156] E. Goiri, P. Borghetti, A. El-Sayed, J. E. Ortega, and D. G. de Oteyza, “Multi-Component Organic Layers on Metal Substrates,” *Advanced Materials*, vol. 28, pp. 1340–1368, Feb. 2016.

[157] L. Dong, P. N. Liu, and N. Lin, “Surface-Activated Coupling Reactions Confined on a Surface,” *Accounts of Chemical Research*, vol. 48, pp. 2765–2774, Oct. 2015.

[158] M. Ammon, T. Sander, and S. Maier, “On-Surface Synthesis of Porous Carbon Nanoribbons from Polymer Chains,” *Journal of the American Chemical Society*, vol. 139, pp. 12976–12984, Sept. 2017.

[159] Q. Shen, H.-Y. Gao, and H. Fuchs, “Frontiers of on-surface synthesis: From principles to applications,” *Nano Today*, vol. 13, pp. 77–96, Apr. 2017.

[160] J. Hu, Z. Liang, K. Shen, H. Sun, Z. Jiang, and F. Song, “Recent Progress in the Fabrication of Low Dimensional Nanostructures via Surface-Assisted Transforming and Coupling,” *Journal of Nanomaterials*, vol. 2017, pp. 1–17, 2017.

[161] D. P. Goronzy, M. Ebrahimi, F. Rosei, Arramel, Y. Fang, S. De Feyter, S. L. Tait, C. Wang, P. H. Beton, A. T. S. Wee, P. S. Weiss, and D. F. Perepichka, “Supramolecular Assemblies on Surfaces: Nanopatterning, Functionality, and Reactivity,” *ACS Nano*, vol. 12, pp. 7445–7481, Aug. 2018.

[162] M. Xi and B. E. Bent, “Mechanisms of the Ullmann coupling reaction in adsorbed monolayers,” *Journal of the American Chemical Society*, vol. 115, pp. 7426–7433, Aug. 1993.

[163] P. C. M. Grim, S. De Feyter, A. Gesquière, P. Vanoppen, M. Rüker, S. Valiyaveettil, G. Moessner, K. Müllen, and F. C. De Schryver, “Submolecularly Resolved Polymerization of Diacetylene Molecules on the Graphite Surface Observed with Scanning Tunneling Microscopy,” *Angewandte Chemie International Edition in English*, vol. 36, pp. 2601–2603, Dec. 1997.

[164] A. Gourdon, “On-Surface Covalent Coupling in Ultrahigh Vacuum,” *Angewandte Chemie International Edition*, vol. 47, pp. 6950–6953, Sept. 2008.

[165] D. Zhong, J.-H. Franke, S. K. Podiyanachari, T. Blomker, H. Zhang, G. Kehr, G. Erker, H. Fuchs, and L. Chi, “Linear Alkane Polymerization on a Gold Surface,” *Science*, vol. 334, pp. 213–216, Oct. 2011.

[166] Q. Fan, C. Wang, Y. Han, J. Zhu, W. Hieringer, J. Kuttner, G. Hilt, and J. M. Gottfried, “Surface-Assisted Organic Synthesis of Hyperbenzene Nanotroughs,” *Angew. Chem. Int. Ed.*, vol. 52, pp. 4668–4672, Apr. 2013.

[167] F. Palmino, C. Loppacher, and F. Chérioux, “Photochemistry Highlights on On-Surface Synthesis,” *ChemPhysChem*, June 2019.

[168] B. Voigtländer, *Scanning Probe Microscopy*.
NanoScience and Technology, Berlin, Heidelberg: Springer Berlin Heidelberg, 2015.

[169] G. Binnig, H. Rohrer, C. Gerber, and E. Weibel, “7x7 Reconstruction on Si(111) Resolved in Real Space,” *Physical Review Letters*, vol. 50, pp. 120–123, Jan. 1983.

[170] M. Assig, M. Etzkorn, A. Enders, W. Stiepany, C. R. Ast, and K. Kern, "A 10 mK scanning tunneling microscope operating in ultra high vacuum and high magnetic fields," *Rev. Sci. Instrum.*, p. 10, 2013.

[171] Z. Klusek, A. Busiakiewicz, P. K. Datta, R. Schmidt, W. Kozlowski, P. Kowalczyk, P. Dabrowski, and W. Olejniczak, "Room and high-temperature scanning tunnelling microscopy and spectroscopy (HT-STM/STS) investigations of surface nanomodifications created on the TiO2(1 1 0) surface," *Surface Science*, p. 8, 2007.

[172] P. Stone, R. A. Bennett, and M. Bowker, "Reactive re-oxidation of reduced TiO2(110) surfaces demonstrated by high temperature STM movies," *New Journal of Physics*, vol. 1, no. 8, p. 13, 1999.

[173] R. L. McCarley and A. J. Bard, "Scanning Tunneling Microscopy Studies of Iodide Adsorption on Au(111): Direct Observation of Adlattice Orientation," *Journal of Physical Chemistry*, vol. 95, pp. 9618–9620, 1999.

[174] B. Drake, R. Sonnenfeld, J. Schneir, and P. K. Hansma, "Scanning tunneling microscopy of processes at liquid-solid interfaces," *Surface Science*, vol. 1-2, no. 1, pp. 92–97, 1987.

[175] K. Itaya and E. Tomita, "Scannning tunneling microsocpe for electrchemistry - A new concept for the in situ scanning tunneling microscope in electrolyte solutions," *Surface Science Letters*, vol. 201, pp. L507–L512, 1988.

[176] J. Bardeen, "Tunnelling from a Many-Particle Point of View," *Physical Review Letters*, vol. 6, pp. 57–59, Jan. 1961.

[177] A. D. Gottlieb and L. Wesoloski, "Bardeen's tunnelling theory as applied to scanning tunnelling microscopy: A technical guide to the traditional interpretation," *Nanotechnology*, vol. 17, pp. R57–R65, Apr. 2006.

[178] J. Tersoff and D. R. Hamann, "Theory and Application for the Scanning Tunneling Microscope," *Physical Review Letters*, vol. 50, pp. 1998–2001, June 1983.

[179] J. Tersoff and D. R. Hamann, "Theory of the scanning tunneling microscope," *Physical Review B*, vol. 31, pp. 805–813, Jan. 1985.

[180] B. C. Stipe, "Single-Molecule Vibrational Spectroscopy and Microscopy," *Science*, vol. 280, pp. 1732–1735, June 1998.

[181] A. J. Heinrich, "Single-Atom Spin-Flip Spectroscopy," *Science*, vol. 306, pp. 466–469, Oct. 2004.

[182] R. Temirov, S. Soubatch, O. Neucheva, A. C. Lassise, and F. S. Tautz, "A novel method achieving ultra-high geometrical resolution in scanning tunnelling microscopy," *New Journal of Physics*, vol. 10, p. 053012, May 2008.

[183] L. Gross, Fabian Mohn, Nikolaj Moll, Peter Liljeroth, and Gerhard Meyer, "The Chemical Structure of a Molecule Resolved by Atomic Force Microscopy," Aug. 2009.

[184] C.-l. Chiang, C. Xu, Z. Han, and W. Ho, "Real-space imaging of molecular structure and chemical bonding by single-molecule inelastic tunneling probe," *Science*, vol. 344, pp. 885–888, May 2014.

[185] C. Weiss, C. Wagner, C. Kleimann, M. Rohlfing, F. S. Tautz, and R. Temirov, "Imaging Pauli Repulsion in Scanning Tunneling Microscopy," *Physical Review Letters*, vol. 105, Aug. 2010.

[186] G. Kichin, C. Weiss, C. Wagner, F. S. Tautz, and R. Temirov, "Single Molecule and Single Atom Sensors for Atomic Resolution Imaging of Chemically Complex Surfaces," *Journal of the American Chemical Society*, vol. 133, pp. 16847–16851, Oct. 2011.

[187] G. Kichin, C. Wagner, F. S. Tautz, and R. Temirov, "Calibrating atomic-scale force sensors installed at the tip apex of a scanning tunneling microscope," *Physical Review B*, vol. 87, Feb. 2013.

[188] F. J. Giessibl, "Atomic resolution on Si(111)-(7x7) by noncontact atomic force microscopy with a force sensor based on a quartz tuning fork," *Applied Physics Letters*, vol. 76, pp. 1470–1472, 2000.

[189] F. J. Giessibl, "Advances in atomic force microscopy," *Rev. Mod. Phys.*, vol. 75, no. 3, p. 35, 2003.

[190] F. J. Giessibl, "Principles and Applications of the qPlus Sensor," in *Noncontact Atomic Force Microscopy: Volume 2* (S. Morita, F. J. Giessibl, and R. Wiesendanger, eds.), pp. 121–142, Berlin, Heidelberg: Springer Berlin Heidelberg, 2009.

[191] L. Gross, F. Mohn, N. Moll, G. Meyer, R. Ebel, W. M. Abdel-Mageed, and M. Jaspars, "Organic structure determination using atomic-resolution scanning probe microscopy," *Nature Chem*, vol. 2, pp. 821–825, Oct. 2010.

[192] N. Pavliček, B. Schuler, S. Collazos, N. Moll, D. Pérez, E. Guitián, G. Meyer, D. Peña, and L. Gross, "On-surface generation and imaging of arynes by atomic force microscopy," *Nature Chem*, vol. 7, pp. 623–628, Aug. 2015.

[193] B. Schuler, G. Meyer, D. Peña, O. C. Mullins, and L. Gross, "Unraveling the Molecular Structures of Asphaltenes by Atomic Force Microscopy," *J. Am. Chem. Soc.*, vol. 137, pp. 9870–9876, Aug. 2015.

[194] S. Wickenburg, J. Lu, J. Lischner, H.-Z. Tsai, A. A. Omrani, A. Riss, C. Karrasch, A. Bradley, H. S. Jung, R. Khajeh, D. Wong, K. Watanabe, T. Taniguchi, A. Zettl, A. C. Neto, S. G. Louie, and M. F. Crommie, "Tuning charge and correlation effects for a single molecule on a graphene device," *Nat Commun*, vol. 7, p. 13553, Dec. 2016.

[195] N. Pavliček, A. Mistry, Z. Majzik, N. Moll, G. Meyer, D. J. Fox, and L. Gross, "Synthesis and characterization of triangulene," *Nature Nanotechnology*, vol. 12, pp. 308–311, Feb. 2017.

[196] S. Kawai, K. Takahashi, S. Ito, R. Pawlak, T. Meier, P. Spijker, F. F. Canova, J. Tracey, K. Nozaki, A. S. Foster, and E. Meyer, "Competing Annulene and Radialene Structures in a Single Anti-Aromatic Molecule Studied by High-Resolution Atomic Force Microscopy," *ACS Nano*, July 2017.

[197] N. Pavliček, Z. Majzik, S. Collazos, G. Meyer, D. Pérez, E. Guitián, D. Peña, and L. Gross, "Generation and Characterization of a meta-Aryne on Cu and NaCl Surfaces," *ACS Nano*, vol. 11, pp. 10768–10773, Nov. 2017.

[198] M. Commodo, K. Kaiser, G. De Falco, P. Minutolo, F. Schulz, A. D'Anna, and L. Gross, "On the early stages of soot formation: Molecular structure elucidation by high-resolution atomic force microscopy," *Combustion and Flame*, vol. 205, pp. 154–164, July 2019.

[199] D. G. de Oteyza, P. Gorman, Y.-C. Chen, S. Wickenburg, A. Riss, D. J. Mowbray, G. Etkin, Z. Pedramrazi, H.-Z. Tsai, A. Rubio, and M. F. Crommie, "Direct Imaging of Covalent Bond Structure in Single-Molecule Chemical Reactions," *Science*, vol. 340, pp. 1431–1434, June 2013.

[200] A. Riss, A. P. Paz, S. Wickenburg, H.-Z. Tsai, D. G. De Oteyza, A. J. Bradley, M. M. Ugeda, P. Gorman, H. S. Jung, M. F. Crommie, A. Rubio, and F. R. Fischer, "Imaging single-molecule reaction intermediates stabilized by surface dissipation and entropy," *Nature Chemistry*, vol. 8, pp. 678–683, May 2016.

[201] C. Sánchez-Sánchez, T. Dienel, O. Deniz, P. Ruffieux, R. Berger, X. Feng, K. Müllen, and R. Fasel, “Purely Armchair or Partially Chiral: Noncontact Atomic Force Microscopy Characterization of Dibromo-Bianthryl-Based Graphene Nanoribbons Grown on Cu(111),” *ACS Nano*, vol. 10, pp. 8006–8011, Aug. 2016.

[202] Z. Sun, M. P. Boneschanscher, I. Swart, D. Vanmaekelbergh, and P. Liljeroth, “Quantitative Atomic Force Microscopy with Carbon Monoxide Terminated Tips,” *Phys. Rev. Lett.*, vol. 106, p. 046104, Jan. 2011.

[203] M. Corso, M. Ondráček, C. Lotze, P. Hapala, K. J. Franke, P. Jelínek, and J. I. Pascual, “Charge Redistribution and Transport in Molecular Contacts,” *Phys. Rev. Lett.*, vol. 115, p. 136101, Sept. 2015.

[204] S. Kawai, A. S. Foster, T. Björkman, S. Nowakowska, J. Björk, F. F. Canova, L. H. Gade, T. A. Jung, and E. Meyer, “Van der Waals interactions and the limits of isolated atom models at interfaces,” *Nat Commun*, vol. 7, p. 11559, Sept. 2016.

[205] A. Riss, “Mechanistic Insights into Surface-Supported Chemical Reactions,” in *On-Surface Synthesis II* (D. G. de Oteyza and C. Rogero, eds.), pp. 1–17, Cham: Springer International Publishing, 2018.

[206] F. Schulz, J. Ritala, O. Krejčí, A. P. Seitsonen, A. S. Foster, and P. Liljeroth, “Elemental Identification by Combining Atomic Force Microscopy and Kelvin Probe Force Microscopy,” *ACS Nano*, vol. 12, pp. 5274–5283, June 2018.

[207] S. Fatayer, F. Albrecht, Y. Zhang, D. Urbonas, D. Peña, N. Moll, and L. Gross, “Molecular structure elucidation with charge-state control,” *Science*, vol. 365, no. 142-145, p. 5, 2019.

[208] P. Hapala, G. Kichin, C. Wagner, F. S. Tautz, R. Temirov, and P. Jelínek, “Mechanism of high-resolution STM/AFM imaging with functionalized tips,” *Physical Review B*, vol. 90, Aug. 2014.

[209] S. K. Hämäläinen, N. van der Heijden, J. van der Lit, S. den Hartog, P. Liljeroth, and I. Swart, “Intermolecular Contrast in Atomic Force Microscopy Images without Intermolecular Bonds,” *Phys. Rev. Lett.*, vol. 113, p. 186102, Oct. 2014.

[210] C.-S. Guo, X. Xin, M. A. Van Hove, X. Ren, and Y. Zhao, “Origin of the Contrast Interpreted as Intermolecular and Intramolecular Bonds in Atomic Force Microscopy Images,” *J. Phys. Chem. C*, vol. 119, pp. 14195–14200, June 2015.

[211] J. Zhang, P. Chen, B. Yuan, W. Ji, Z. Cheng, and X. Qiu, “Real-Space Identification of Intermolecular Bonding with Atomic Force Microscopy,” *Science*, vol. 342, pp. 611–614, Nov. 2013.

[212] S. Kawai, A. Sadeghi, F. Xu, L. Peng, A. Orita, J. Otera, S. Goedecker, and E. Meyer, “Extended Halogen Bonding between Fully Fluorinated Aromatic Molecules,” *ACS Nano*, vol. 9, pp. 2574–2583, Mar. 2015.

[213] N. Pavliček, C. Herranz-Lancho, B. Fleury, M. Neu, J. Niedenführ, M. Ruben, and J. Repp, “High-resolution scanning tunneling and atomic force microscopy of stereochemically resolved dibenzo[a,h]thianthrene molecules,” *physica status solidi (b)*, vol. 250, no. 11, pp. 2424–2430, 2013.

[214] J. van der Lit, F. Di Cicco, P. Hapala, P. Jelinek, and I. Swart, “Submolecular Resolution Imaging of Molecules by Atomic Force Microscopy: The Influence of the Electrostatic Force,” *Phys. Rev. Lett.*, vol. 116, p. 096102, Mar. 2016.

[215] C.-S. Guo, M. A. Van Hove, X. Ren, and Y. Zhao, “High-Resolution Model for Noncontact Atomic Force Microscopy with a Flexible Molecule on the Tip Apex,” *J. Phys. Chem. C*, vol. 119, pp. 1483–1488, Jan. 2015.

[216] M. Ellner, N. Pavliček, P. Pou, B. Schuler, N. Moll, G. Meyer, L. Gross, and R. Peréz, "The Electric Field of CO Tips and Its Relevance for Atomic Force Microscopy," *Nano Lett.*, vol. 16, pp. 1974–1980, Mar. 2016.

[217] A. M. Sweetman, S. P. Jarvis, H. Sang, I. Lekkas, P. Rahe, Y. Wang, J. Wang, N. Champness, L. Kantorovich, and P. Moriarty, "Mapping the force field of a hydrogen-bonded assembly," *Nat Commun*, vol. 5, p. 3931, Sept. 2014.

[218] C. Moreno, O. Stetsovych, T. K. Shimizu, and O. Custance, "Imaging Three-Dimensional Surface Objects with Submolecular Resolution by Atomic Force Microscopy," *Nano Lett.*, vol. 15, pp. 2257–2262, Apr. 2015.

[219] K. Iwata, S. Yamazaki, P. Mutombo, P. Hapala, M. Ondráček, P. Jelínek, and Y. Sugimoto, "Chemical structure imaging of a single molecule by atomic force microscopy at room temperature," *Nat Commun*, vol. 6, p. 7766, Nov. 2015.

[220] M. Gajdo, A. Eichler, and J. Hafner, "CO adsorption on close-packed transition and noble metal surfaces: Trends from *ab initio* calculations," *J. Phys.: Condens. Matter*, vol. 16, pp. 1141–1164, Mar. 2004.

[221] J. P. Hardy, G. E. Ewing, R. Stables, and C. J. S. M. Simpson, "Thermodynamic measurements of adsorption of Xe and CO on NaCl(100)," *Surface Science Letters*, vol. 159, pp. L474–L482, 1985.

[222] K. Besocke, "An easily operable scanning tunneling microscope," *Surface Science*, vol. 181, pp. 145–153, 1987.

[223] G. Binnig and D. P. E. Smith, "Single-tube three-dimensional scanner for scanning tunneling microscopy," *Review of Scientific Instruments*, vol. 57, pp. 1688–1689, Aug. 1986.

[224] H. Hertz, "Ueber einen Einfluss des ultravioletten Lichtes auf die electrische Entladung," *Annalen der Physik und Chemie*, vol. 267, no. 8, pp. 983–1000, 1887.

[225] W. Hallwachs, "Über den Einfluß des Lichtes auf electrostatisch geladene Körper," *Annalen der Physik und Chemie*, vol. 17, pp. 301–312, 1888.

[226] "Table of physical and chemical constants (section 4.5.2): Attenuation lenght of electrons ins solids."

[227] A. Einstein, "Über einen die Erzeugung und Verwandlung des Lichtes betreffenden heuristischen Gesichtspunkt," *Annalen der Physik*, vol. 322, no. 6, pp. 132–148, 1905.

[228] F. Reinert and S. Hüfner, "Photoemission spectroscopy—from early days to recent applications," *New J. Phys.*, vol. 7, pp. 97–97, Apr. 2005.

[229] A. Damascelli, "Probing the electronic structure of complex systems by ARPES," *Physica Scripta*, vol. 2004, no. T109, p. 61, 2004.

[230] T. Wassmann, A. P. Seitsonen, A. M. Saitta, M. Lazzeri, and F. Mauri, "Clar's Theory, $\pi$-Electron Distribution, and Geometry of Graphene Nanoribbons," *Journal of the American Chemical Society*, vol. 132, pp. 3440–3451, Mar. 2010.

[231] L. Talirz and C. A. Pignedoli, "Electronic Structure of Atomically Precise Graphene Nanoribbons," *Handbook of Materials Modeling*, pp. 1–35, July 2018.

[232] L. Pauling, L. O. Brockway, and J. Y. Beach, "The Dependence of Interatomic Distance on Single Bond-Double Bond Resonance $^{1}$," *J. Am. Chem. Soc.*, vol. 57, pp. 2705–2709, Dec. 1935.

[233] A. Bostwick, T. Ohta, T. Seyller, K. Horn, and E. Rotenberg, "Experimental Determination of the Spectral Function of Graphene," *arXiv*, p. 10, 2006.

[234] R. Saito, G. Dresselhaus, and M. Dresselhaus, *Tight Binding Calculation of Molecules and Solids. In: Physical Properties of Carbon Nanotubes.*
Physical Properties of Carbon Nanotubes, London: Imperial College Press, 1998.

[235] S. Reich, J. Maultzsch, C. Thomsen, and P. Ordejón, "Tight-binding description of graphene," *Phys. Rev. B*, vol. 66, p. 035412, July 2002.

[236] S. Reich, J. Maultzsch, C. Thomsen, and P. Ordejón, "Tight-binding description of graphene," *Phys. Rev. B*, vol. 66, p. 035412, July 2002.

[237] K. Wakabayashi, K.-i. Sasaki, T. Nakanishi, and T. Enoki, "Electronic states of graphene nanoribbons and analytical solutions," *Science and Technology of Advanced Materials*, vol. 11, p. 054504, Oct. 2010.

[238] J. P. Perdew, "Density functional theory and the band gap problem," *International Journal of Quantum Chemistry*, vol. 28, no. S19, pp. 497–523, 1985.

[239] Y. Zhang, Y. Zhang, G. Li, J. Lu, X. Lin, S. Du, R. Berger, X. Feng, K. Müllen, and H.-J. Gao, "Direct visualization of atomically precise nitrogen-doped graphene nanoribbons," *Appl. Phys. Lett.*, vol. 105, p. 023101, July 2014.

[240] H. Zhang, L. Haiping, S. Kewei, L. Chen, Y. Zagranyarski, N. Aghdassi, S. Duhm, Q. Li, D. Zhong, Y. Li, K. Müllen, H. Fuchs, and L. Chi, "On-Surface Synthesis of Rylene-Type Graphene Nanoribbons.," *J. Am. Chem. Soc.*, vol. 137, no. 12, pp. 4022–4025, 2015.

[241] N. Kharche and V. Meunier, "Width and Crystal Orientation Dependent Band Gap Renormalization in Substrate-Supported Graphene Nanoribbons.," *J. Phys. Chem. Lett.*, vol. 7, pp. 1526–1533, 2016.

[242] P. Ruffieux, J. Cai, N. C. Plumb, L. Patthey, D. Prezzi, A. Ferretti, E. Molinari, X. Feng, K. Müllen, C. A. Pignedoli, and R. Fasel, "Electronic Structure of Atomically Precise Graphene Nanoribbons.," *ACSnano*, vol. 6, pp. 6930–6935, 2012.

[243] H. Söde, L. Talirz, O. Gröning, C. A. Pignedoli, R. Berger, X. Feng, K. Müllen, R. Fasel, and P. Ruffieux, "Electronic band dispersion of graphene nanoribbons via Fourier-transformed scanning tunneling spectroscopy.," *Physical Review B*, vol. 91, p. 045429, 2015.

[244] X. Wang, Y. Ouyang, X. Li, H. Wang, J. Guo, and H. Dai, "Room-Temperature All-Semiconducting Sub-10-nm Graphene Nanoribbon Field-Effect Transistors," *Physical Review Letters*, vol. 100, May 2008.

[245] M. Sprinkle, M. Ruan, Y. Hu, J. Hankinson, M. Rubio-Roy, B. Zhang, X. Wu, C. Berger, and W. A. de Heer, "Scalable templated growth of graphene nanoribbons on SiC," *Nature Nanotechnology*, vol. 5, pp. 727–731, Oct. 2010.

[246] Y. Zhu and J. M. Tour, "Graphene Nanoribbon Thin Films Using Layer-by-Layer Assembly," *Nano Letters*, vol. 10, pp. 4356–4362, Nov. 2010.

[247] A. Smolyanitsky and V. K. Tewary, "Atomistic simulation of a graphene-nanoribbon–metal interconnect," *Journal of Physics: Condensed Matter*, vol. 23, p. 355006, Sept. 2011.

[248] P. B. Bennett, Z. Pedramrazi, A. Madani, Y.-C. Chen, D. G. de Oteyza, C. Chen, F. R. Fischer, M. F. Crommie, and J. Bokor, "Bottom-up graphene nanoribbon field-effect transistors," *Applied Physics Letters*, vol. 103, p. 253114, Dec. 2013.

[249] Z. Johari, F. K. A. Hamid, M. T. Ahmadi, F. K. C. Harun, and R. Ismail, "The Effect of Interconnect on the Circuit Performance of 22 nm Graphene Nanoribbon Field Effect Transistor and MOSFET," *Journal of Computational and Theoretical Nanoscience*, vol. 10, pp. 1305–1309, June 2013.

[250] J. P. Llinas, A. Fairbrother, G. Borin Barin, W. Shi, K. Lee, S. Wu, B. Yong Choi, R. Braganza, J. Lear, N. Kau, W. Choi, C. Chen, Z. Pedramrazi, T. Dumslaff, A. Narita, X. Feng, K. Müllen, F. Fischer, A. Zettl, P. Ruffieux, E. Yablonovitch, M. Crommie, R. Fasel, and J. Bokor, "Short-channel field-effect transistors with 9-atom and 13-atom wide graphene nanoribbons," *Nature Communications*, vol. 8, p. 633, Dec. 2017.

[251] M. Ohtomo, Y. Sekine, H. Hibino, and H. Yamamoto, "Graphene nanoribbon field-effect transistors fabricated by etchant-free transfer from Au(788)," *Applied Physics Letters*, vol. 112, p. 021602, Jan. 2018.

[252] V. Passi, A. Gahoi, B. V. Senkovskiy, D. Haberer, F. R. Fischer, A. Grüneis, and M. C. Lemme, "Field-Effect Transistors Based on Networks of Highly Aligned, Chemically Synthesized N = 7 Armchair Graphene Nanoribbons," *ACS Applied Materials & Interfaces*, Mar. 2018.

[253] A. Basagni, G. Vasseur, C. A. Pignedoli, M. Vilas-Varela, D. Peña, L. Nicolas, L. Vitali, J. Lobo-Checa, D. G. de Oteyza, F. Sedona, M. Casarin, J. E. Ortega, and M. Sambi, "Tunable Band Alignment with Unperturbed Carrier Mobility of On-Surface Synthesized Organic Semiconducting Wires.," *ACSnano*, vol. 10, pp. 2644–2651, 2016.

[254] Y.-C. Chen, T. Cao, C. Chen, Z. Pedramrazi, D. Haberer, D. G. de Oteyza, F. R. Fischer, S. G. Louie, and M. F. Crommie, "Molecular bandgap engineering of bottom-up synthesized graphene nanoribbon heterojunctions.," *Nature Nanotechnology*, vol. 10, p. 156, 2015.

[255] S. Wang, L. Talirz, C. A. Pignedoli, X. Feng, K. Müllen, R. Fasel, and P. Ruffieux, "Giant edge state splitting at atomically precise graphene zigzag edges.," *Nature Communications*, vol. 7, p. 115107, 2016.

[256] A. D. Zdetsis and E. N. Economou, "Rationalizing and Reconciling Energy Gaps and Quantum Confinement in Narrow Atomically Precise Graphene Nanoribbons.," *Carbon*, vol. 116, pp. 422–434, 2017.

[257] M. Kertesz, C. H. Choi, and S. Yang, "Conjugated Polymers and Aromaticity," *Chemical Reviews*, vol. 105, pp. 3448–3481, Oct. 2005.

[258] J. Tesch, P. Leicht, F. Blumenschein, L. Gragnaniello, M. Fonin, L. E. M. STeinkasserer, B. Paulus, E. Voloshina, and Y. Dedkov, "Structural and electronic properties of graphene nanoflakes on Au(111) and Ag(111).," *Scientific Reports*, vol. 6, p. 23439, 2016.

[259] J. M. Wofford, E. Starodub, A. L. Walter, S. Nie, A. Bostwick, N. C. Bartelt, K. Thürmer, E. Rotenberg, K. F. McCarty, and O. D. Dubon, "Extraordinary epitaxial alignment of graphene islands on Au(111)," *New Journal of Physics*, vol. 14, p. 053008, May 2012.

[260] C. Enderlein, Y. S. Kim, A. Bostwick, E. Rotenberg, and K. Horn, "The formation of an energy gap in graphene on ruthenium by controlling the interface," *New Journal of Physics*, vol. 12, p. 033014, Mar. 2010.

[261] P. Leicht, L. Zielke, S. Bouvron, R. Moroni, E. Voloshina, L. Hammerschmidt, Y. S. Dedkov, and M. Fonin, "In Situ Fabrication Of Quasi-Free-Standing Epitaxial Graphene Nanoflakes On Gold," *ACS Nano*, vol. 8, pp. 3735–3742, Apr. 2014.

[262] Y. Wu, W. Jiang, Y. Ren, W. Cai, W. H. Lee, H. Li, R. D. Piner, C. W. Pope, Y. Hao, H. Ji, J. Kang, and R. S. Ruoff, "Tuning the Doping Type and Level of Graphene with Different Gold Configurations," *Small*, vol. 8, pp. 3129–3136, Oct. 2012.

[263] G. Giovannetti, P. A. Khomyakov, G. Brocks, V. M. Karpan, J. van den Brink, and P. J. Kelly, "Doping Graphene with Metals Contacts.," *Physical Review Letters*, vol. 101, p. 026803, 2008.

[264] P. A. Khomyakov, G. Giovannetti, P. C. Rusu, G. Brocks, J. van den Brink, and P. J. Kelly, “First-principles study of the interaction and charge transfer between graphene and metals,” *Physical Review B*, vol. 79, May 2009.

[265] J. Gebhardt, F. Viñes, and A. Görling, “Influence of the surface dipole layer and Pauli repulsion on band energies and doping in graphene adsorbed on metal surfaces,” *Physical Review B*, vol. 86, Nov. 2012.

[266] J. Hwang, A. Wan, and A. Kahn, “Energetics of metal-organic interfaces: New experiments and assessment of the field.,” *Materials Science and Engineering R*, vol. 64, pp. 1–31, 2009.

[267] C. A. Mead and W. G. Spitzer, “Fermi Level Position at Metal-Semiconductor Interfaces.,” *Physical Reviews*, vol. 134, p. A713, 1964.

[268] R. T. Tung, “Formation of an electric dipole at metal-semiconductor interfaces,” *Physical Review B*, vol. 64, p. 205310, Nov. 2001.

[269] G. Heimel, S. Duhm, I. Salzmann, A. Gerlach, A. Strozecka, J. Niederhausen, C. B?rker, T. Hosokai, I. Fernandez-Torrente, G. Schulze, S. Winkler, A. Wilke, R. Schlesinger, J. Frisch, B. Br?ker, A. Vollmer, B. Detlefs, J. Pflaum, S. Kera, K. J. Franke, N. Ueno, J. I. Pascual, F. Schreiber, and N. Koch, “Charged and metallic molecular monolayers through surface-induced aromatic stabilization,” *Nature Chemistry*, vol. 5, pp. 187–194, Feb. 2013.

[270] N. Merino-Díez, J. Lobo-Checa, P. Nita, A. Garcia-Lekue, A. Basagni, G. Vasseur, F. Tiso, F. Sedona, P. K. Das, J. Fujii, I. Vobornik, M. Sambi, J. I. Pascual, J. E. Ortega, and D. G. de Oteyza, “Switching from Reactant to Substrate Engineering in the Selective Synthesis of Graphene Nanoribbons,” *The Journal of Physical Chemistry Letters*, vol. 9, pp. 2510–2517, May 2018.

[271] S. Braun, W. R. Salaneck, and M. Fahlman, “Energy-Level Alignment at Organic/Metal and Organic/Organic Interfaces.,” *Advanced Materials*, vol. 21, no. 14-15, pp. 1450–1472, 2009.

[272] M. Corso, E. Carbonell-Sanromà, and D. G. de Oteyza, “Bottom-up fabrication of atomically precise graphene nanoribbons,” 2017.

[273] A. Narita, X.-Y. Wang, X. Feng, and K. Müllen, “New advences in nanographene chemistry.,” *Chem. Soc. Rev.*, vol. 44, p. 6616, 2015.

[274] N. Merino-Díez, J. Li, A. Garcia-Lekue, G. Vasseur, M. Vilas-Varela, E. Carbonell-Sanromà, M. Corso, J. E. Ortega, D. Peña, J. I. Pascual, and D. G. de Oteyza, “Unraveling the Electronic Structure of Narrow Atomically Precise Chiral Graphene Nanoribbons,” *The Journal of Physical Chemistry Letters*, vol. 9, pp. 25–30, Jan. 2018.

[275] S. Rousset, V. Repain, G. Baudot, Y. Garreau, and J. Lecoeur, “Self-ordering of Au(111) vicinal surfaces and application to nanostructure organized growth,” *Journal of Physics: Condensed Matter*, vol. 15, pp. S3363–S3392, Dec. 2003.

[276] B. Cirera, Y.-Q. Zhang, J. Björk, S. Klyatskaya, Z. Chen, M. Ruben, J. V. Barth, and F. Klappenberger, “Synthesis of Extended Graphdiyne Wires by Vicinal Surface Templating,” *Nano Letters*, vol. 14, pp. 1891–1897, Apr. 2014.

[277] A. Saywell, J. Schwarz, S. Hecht, and L. Grill, “Polymerization on Stepped Surfaces: Alignment of Polymers and Identification of Catalytic Sites,” *Angewandte Chemie International Edition*, vol. 51, pp. 5096–5100, May 2012.

[278] M. Corso, F. Schiller, L. Fernández, J. Cordón, and J. E. Ortega, “Electronic states in faceted Au(111) studied with curved crystal surfaces,” *Journal of Physics: Condensed Matter*, vol. 21, p. 353001, Sept. 2009.

[279] G. Vasseur, M. Abadia, L. A. Miccio, J. Brede, A. Garcia-Lekue, D. G. de Oteyza, C. Rogero, J. Lobo-Checa, and J. E. Ortega, "Pi Band Dispersion along Conjugated Organic Nanowires Synthesized on a Metal Oxide Semiconductor," *Journal of the American Chemical Society*, vol. 138, pp. 5685–5692, May 2016.

[280] J. A. Lipton-Duffin, O. Ivasenko, D. F. Perepichka, and F. Rosei, "Synthesis of Polyphenylene Molecular Wires by Surface-Confined Polymerization," *Small*, vol. 5, pp. 592–597, Mar. 2009.

[281] A. Neumann, K. Christmann, and T. Solomun, "Binding states and structural phase transformations upon iodine adsorption on a gold (100) surface," *Surface Science*, vol. 277-278, pp. 593–599, 1993.

[282] G. Vasseur, Y. Fagot-Revurat, M. Sicot, B. Kierren, L. Moreau, D. Malterre, L. Cardenas, G. Galeotti, J. Lipton-Duffin, F. Rosei, M. Di Giovannantonio, G. Contini, P. Le Fèvre, F. Bertran, L. Liang, V. Meunier, and D. F. Perepichka, "Quasi one-dimensional band dispersion and surface metallization in long-range ordered polymeric wires," *Nature Communications*, vol. 7, p. 10235, Jan. 2016.

[283] M. Chen, J. Xiao, H.-P. Steinrück, S. Wang, W. Wang, N. Lin, W. Hieringer, and J. M. Gottfried, "Combined Photoemission and Scanning Tunneling Microscopy Study of the Surface-Assisted Ullmann Coupling Reaction," *The Journal of Physical Chemistry C*, vol. 118, pp. 6820–6830, Apr. 2014.

[284] D. G. de Oteyza, A. García-Lekue, M. Vilas-Varela, N. Merino-Díez, E. Carbonell-Sanromà, M. Corso, G. Vasseur, C. Rogero, E. Guitián, J. I. Pascual, J. E. Ortega, Y. Wakayama, and D. Peña, "Substrate-Independent Growth of Atomically Precise Chiral Graphene Nanoribbons," *ACS Nano*, vol. 10, pp. 9000–9008, Sept. 2016.

[285] M. Abadía, M. Ilyn, I. Piquero-Zulaica, P. Gargiani, C. Rogero, J. E. Ortega, and J. Brede, "Polymerization of Well-Aligned Organic Nanowires on a Ferromagnetic Rare-Earth Surface Alloy," *ACS Nano*, vol. 11, pp. 12392–12401, Dec. 2017.

[286] P. Puschnig and D. Lüftner, "Simulation of angle-resolved photoemission spectra by approximating the final state by a plane wave: From graphene to polycyclic aromatic hydrocarbon molecules," *Journal of Electron Spectroscopy and Related Phenomena*, vol. 200, pp. 193–208, Apr. 2015.

[287] P. Puschnig, S. Berkebile, A. J. Fleming, G. Koller, K. Emtsev, T. Seyller, J. D. Riley, C. Ambrosch-Draxl, F. P. Netzer, and M. G. Ramsey, "Reconstruction of Molecular Orbital Densities from Photoemission Data," *Science*, vol. 326, pp. 702–706, Oct. 2009.

[288] M. Willenbockel, P. Puschnig, M. G. Ramsey, and F. S. Tautz, "The interplay between interface structure, energy level alignment and chemical bonding strength at organic-metal interfaces," *Physical Chemistry Chemical Physics*, vol. 17, pp. 1530–1548, 2015.

[289] H. Hayashi, J. Yamaguchi, H. Jippo, R. Hayashi, N. Aratani, M. Ohfuchi, S. Sato, and H. Yamada, "Experimental and Theoretical Investigations of Surface-Assisted Graphene Nanoribbon Synthesis Featuring Carbon–Fluorine Bond Cleavage," *ACS Nano*, vol. 11, pp. 6204–6210, June 2017.

[290] S. Kawai, S. Nakatsuka, T. Hatakeyama, R. Pawlak, T. Meier, J. Tracey, E. Meyer, and A. S. Foster, "Multiple heteroatom substitution to graphene nanoribbon," *SCIENCE ADVANCES*, vol. 4, p. 8, 2018.

[291] P. Han, K. Akagi, F. Federici Canova, H. Mutoh, S. Shiraki, K. Iwaya, P. S. Weiss, N. Asao, and T. Hitosugi, "Bottom-Up Graphene-Nanoribbon Fabrication Reveals Chiral Edges and Enantioselectivity," *ACS Nano*, vol. 8, pp. 9181–9187, Sept. 2014.

[292] F. Schulz, P. H. Jacobse, F. F. Canova, J. van der Lit, D. Z. Gao, A. van den Hoogenband, P. Han, R. J. Klein Gebbink, M.-E. Moret, P. M. Joensuu, I. Swart, and P. Liljeroth, “Precursor Geometry Determines the Growth Mechanism in Graphene Nanoribbons,” *The Journal of Physical Chemistry C*, vol. 121, pp. 2896–2904, Feb. 2017.

[293] X.-Y. Wang, J. I. Urgel, G. B. Barin, K. Eimre, M. Di Giovannantonio, A. Milani, M. Tommasini, C. A. Pignedoli, P. Ruffieux, X. Feng, R. Fasel, K. Müllen, and A. Narita, “Bottom-Up Synthesis of Heteroatom-Doped Chiral Graphene Nanoribbons,” *J. Am. Chem. Soc.*, vol. 140, pp. 9104–9107, July 2018.

[294] P. H. Jacobse, K. A. Simonov, M. J. J. Mangnus, G. I. Svirskiy, A. V. Generalov, A. S. Vinogradov, A. Sandell, N. Mårtensson, A. B. Preobrajenski, and I. Swart, “One Precursor but Two Types of Graphene Nanoribbons: On-Surface Transformations of 10,10′-Dichloro-9,9′-bianthryl on Ag(111),” *J. Phys. Chem. C*, p. 10, 2019.

[295] P. Han, K. Akagi, F. Federici Canova, H. Mutoh, S. Shiraki, K. Iwaya, P. S. Weiss, N. Asao, and T. Hitosugi, “Reply to ’Comment on Bottom-Up Graphene-Nanoribbon Fabrication Reveals Chiral Edges and Enantioselectivity’,” *ACS Nano*, vol. 9, pp. 3404–3405, Apr. 2015.

[296] K. A. Simonov, N. A. Vinogradov, A. S. Vinogradov, A. V. Generalov, E. M. Zagrebina, N. Mårtensson, A. A. Cafolla, T. Carpy, J. P. Cunniffe, and A. B. Preobrajenski, “Effect of Substrate Chemistry on the Bottom-Up Fabrication of Graphene Nanoribbons: Combined Core-Level Spectroscopy and STM Study,” *The Journal of Physical Chemistry C*, vol. 118, pp. 12532–12540, June 2014.

[297] K. A. Simonov, N. A. Vinogradov, A. S. Vinogradov, A. V. Generalov, E. M. Zagrebina, N. Mårtensson, A. A. Cafolla, T. Carpy, J. P. Cunniffe, and A. B. Preobrajenski, “Comment on “Bottom-up graphene-nanoribbon fabrication reveals chiral edges and enantioselectivity”,” *ACS nano*, vol. 9, no. 4, pp. 3399–3403, 2015.

[298] P. Han, K. Akagi, F. Federici Canova, R. Shimizu, H. Oguchi, S. Shiraki, P. S. Weiss, N. Asao, and T. Hitosugi, “Self-Assembly Strategy for Fabricating Connected Graphene Nanoribbons,” *ACS Nano*, vol. 9, pp. 12035–12044, Dec. 2015.

[299] P. H. Jacobse, A. van den Hoogenband, M.-E. Moret, R. J. M. Klein Gebbink, and I. Swart, “Aryl Radical Geometry Determines Nanographene Formation on Au(111),” *Angewandte Chemie International Edition*, vol. 55, pp. 13052–13055, Oct. 2016.

[300] A. Batra, D. Cvetko, G. Kladnik, O. Adak, C. Cardoso, A. Ferretti, D. Prezzi, E. Molinari, A. Morgante, and L. Venkataraman, “Probing the mechanism for graphene nanoribbon formation on gold surfaces through X-ray spectroscopy,” *Chem. Sci.*, vol. 5, pp. 4419–4423, July 2014.

[301] K. J. Shi, D. W. Yuan, C. X. Wang, C. H. Shu, D. Y. Li, Z. L. Shi, X. Y. Wu, and P. N. Liu, “Ullmann Reaction of Aryl Chlorides on Various Surfaces and the Application in Stepwise Growth of 2D Covalent Organic Frameworks,” *Organic Letters*, vol. 18, pp. 1282–1285, Mar. 2016.

[302] M. Di Giovannantonio, M. El Garah, J. Lipton-Duffin, V. Meunier, L. Cardenas, Y. Fagot Revurat, A. Cossaro, A. Verdini, D. F. Perepichka, F. Rosei, and G. Contini, “Insight into Organometallic Intermediate and Its Evolution to Covalent Bonding in Surface-Confined Ullmann Polymerization,” *ACS Nano*, vol. 7, pp. 8190–8198, Sept. 2013.

[303] H. Walch, R. Gutzler, T. Sirtl, G. Eder, and M. Lackinger, “Material- and Orientation-Dependent Reactivity for Heterogeneously Catalyzed Carbon-Bromine Bond Homolysis,” *The Journal of Physical Chemistry C*, vol. 114, pp. 12604–12609, July 2010.

[304] Y.-Q. Zhang, N. Kepčija, M. Kleinschrodt, K. Diller, S. Fischer, A. C. Papageorgiou, F. Allegretti, J. Björk, S. Klyatskaya, F. Klappenberger, M. Ruben, and J. V. Barth, "Homo-coupling of terminal alkynes on a noble metal surface," *Nature Communications*, vol. 3, Jan. 2012.

[305] A. R. Lahrood, J. Björk, W. M. Heckl, and M. Lackinger, "1,3-diiodobenzene on Cu(111) – an exceptional case of on-surface Ullmann coupling," p. 5, 2012.

[306] S. Blankenburg, J. Cai, P. Ruffieux, R. Jaafar, D. Passerone, X. Feng, K. Müllen, R. Fasel, and C. A. Pignedoli, "Intraribbon Heterojunction Formation in Ultranarrow Graphene Nanoribbons," *ACS Nano*, vol. 6, pp. 2020–2025, Mar. 2012.

[307] M. Treier, C. A. Pignedoli, T. Laino, R. Rieger, K. Müllen, D. Passerone, and R. Fasel, "Surface-assisted cyclodehydrogenation provides a synthetic route towards easily processable and chemically tailored nanographenes," *Nature Chemistry*, vol. 3, pp. 61–67, Jan. 2011.

[308] M. Xi and B. E. Bent, "Iodobenzene on Cu( 111): Formation and coupling of adsorbed phenyl groups," *Surface Science*, vol. 278, pp. 19–32, 1992.

[309] J. Eichhorn, D. Nieckarz, O. Ochs, D. Samanta, M. Schmittel, P. J. Szabelski, and M. Lackinger, "On-Surface Ullmann Coupling: The Influence of Kinetic Reaction Parameters on the Morphology and Quality of Covalent Networks," *ACS Nano*, vol. 8, pp. 7880–7889, Aug. 2014.

[310] C. Bronner, T. Marangoni, D. J. Rizzo, R. A. Durr, J. H. Jørgensen, F. R. Fischer, and M. F. Crommie, "Iodine versus Bromine Functionalization for Bottom-Up Graphene Nanoribbon Growth: Role of Diffusion," *The Journal of Physical Chemistry C*, vol. 121, pp. 18490–18495, Aug. 2017.

[311] M. Di Giovannantonio, O. Deniz, J. I. Urgel, R. Widmer, T. Dienel, S. Stolz, C. Sánchez-Sánchez, M. Muntwiler, T. Dumslaff, R. Berger, A. Narita, X. Feng, K. Müllen, P. Ruffieux, and R. Fasel, "On-Surface Growth Dynamics of Graphene Nanoribbons: The Role of Halogen Functionalization," *ACS Nano*, vol. 12, pp. 74–81, Dec. 2017.

[312] L. Lafferentz, V. Eberhardt, C. Dri, C. Africh, G. Comelli, F. Esch, S. Hecht, and L. Grill, "Controlling on-surface polymerization by hierarchical and substrate-directed growth," *Nature Chemistry*, vol. 4, pp. 215–220, Mar. 2012.

[313] G. Galeotti, M. Di Giovannantonio, J. Lipton-Duffin, M. Ebrahimi, S. Tebi, A. Verdini, L. Floreano, Y. Fagot-Revurat, D. F. Perepichka, F. Rosei, and G. Contini, "The role of halogens in on-surface Ullmann polymerization," *Faraday Discussions*, vol. 204, pp. 453–469, 2017.

[314] M. Kittelmann, M. Nimmrich, R. Lindner, A. Gourdon, and A. Kühnle, "Sequential and Site-Specific On-Surface Synthesis on a Bulk Insulator," *ACS Nano*, vol. 7, pp. 5614–5620, June 2013.

[315] V. V. Cherkez, V. V. Zheltov, C. Didiot, B. Kierren, Y. Fagot-Revurat, D. Malterre, B. V. Andryushechkin, G. M. Zhidomirov, and K. N. Eltsov, "Self-ordered nanoporous lattice formed by chlorine atoms on Au(111)," *Physical Review B*, vol. 93, p. 045432, Jan. 2016.

[316] V. V. Zheltov, V. V. Cherkez, B. V. Andryushechkin, G. M. Zhidomirov, B. Kierren, Y. Fagot-Revurat, D. Malterre, and K. N. Eltsov, "Structural paradox in submonolayer chlorine coverage on Au(111)," *Physical Review B*, vol. 89, p. 195425, May 2014.

[317] C. Bronner, J. Björk, and P. Tegeder, "Tracking and Removing Br during the On-Surface Synthesis of a Graphene Nanoribbon," *The Journal of Physical Chemistry C*, vol. 119, pp. 486–493, Jan. 2015.

[318] K. Fukui, T. Yonezawa, and H. Shingu, “A Molecular Orbital Theory of Reactivity in Aromatic Hydrocarbons,” *The Journal of Chemical Physics*, vol. 20, no. 722, p. 5, 1952.

[319] K. Fukui, T. Yonezawa, C. Nagata, and H. Shingu, “Molecular Orbital Theory of Orientation in Aromatic, Heteroaromatic, and Other Conjugated Molecules,” *The Journal of Chemical Physics*, vol. 22, p. 1453, 1954.

[320] S. S. Zade, N. Zamoshchik, A. R. Reddy, G. Fridman-Marueli, D. Sheberla, and M. Bendikov, “Products and Mechanism of Acene Dimerization. A Computational Study,” *J. Am. Chem. Soc.*, vol. 133, pp. 10803–10816, July 2011.

[321] S. S. Zade and M. Bendikov, “Reactivity of acenes: Mechanisms and dependence on acene length: REACTIVITY OF ACENES,” *J. Phys. Org. Chem.*, vol. 25, pp. 452–461, June 2012.

[322] J. Björk, F. Hanke, and S. Stafström, “Mechanisms of Halogen-Based Covalent Self-Assembly on Metal Surfaces,” *Journal of the American Chemical Society*, vol. 135, pp. 5768–5775, Apr. 2013.

[323] A. Mairena, M. Baljozovic, M. Kawecki, K. Grenader, M. Wienke, K. Martin, L. Bernard, N. Avarvari, A. Terfort, K.-H. Ernst, and C. Wäckerlin, “The fate of bromine after temperature-induced dehydrogenation of on-surface synthesized bisheptahelicene,” *Chemical Science*, 2019.

[324] C.-X. Wang, Q. Jin, C.-H. Shu, X. Hua, Y.-T. Long, and P.-N. Liu, “Dehydrogenative homocoupling of tetrafluorobenzene on Pd(111) via para-selective C–H activation,” *Chem. Commun.*, vol. 53, no. 47, pp. 6347–6350, 2017.

[325] L. Pasteur, “Ueber die Krystallisation des Schwefels,” *Annalen der Physik*, vol. 150, no. 5, p. 94, 1848.

[326] R. A. Hegstrom and D. K. Kondepudi, “The Handedness of the Universe,” *Scientific American*, vol. 262, no. 1, pp. 108–115, 1990.

[327] L. A. Nguyen, H. He, and C. Pham-Huy, “Chiral Drugs: An Overview,” *International Journal of Biochemical Science*, vol. 2, no. 2, pp. 85–100, 2006.

[328] J. E. Ridings, “The Thalidomide Disaster, Lessons from the Past,” in *Barrow P. (Eds) Teratogenicity Testing. Methods in Molecular Biology (Methods and Protocols)*, vol. 947, pp. 575–586, Totowa, NJ: Humana Press, 2012.

[329] H.-U. Blaser, “Enantioselective synthesis using chiral heterogeneous catalysts.,” *Tetrahedron: Asymmetry*, vol. 2, pp. 843–866, Jan. 1991.

[330] G. P. Lopinski, D. J. Moffatt, D. D. M. Wayner, and R. A. Wolkow, “Determination of the absolute chirality of individual adsorbed molecules using the scanning tunnelling microscope,” *Nature*, vol. 392, pp. 909–911, Apr. 1998.

[331] L. Atanasoska, J. Buchholz, and G. Somorjai, “Low-energy electron diffraction study of the surface structures of adsorbed amino acid monolayers and ordered films deposited on copper crystal surfaces,” *Surface Science*, vol. 72, pp. 189–207, Mar. 1978.

[332] Q. Chen, C. W. Lee, D. J. Frankel, and N. V. Richardson, “The formation of enantiospecific phases on a Cu(110) surface,” *Phys. Chem. Comm.*, vol. 9, 1999.

[333] F. Stevens, D. J. Dyer, and D. M. Walba, “Direct Observation of Enantiomorphous Monolayer Crystals from Enantiomers by Scanning Tunneling Microscopy,” *Angewandte Chemie International Edition in English*, vol. 35, pp. 900–901, May 1996.

[334] M. Böhringer, K. Morgenstern, W.-D. Schneider, R. Berndt, F. Mauri, A. De Vita, and R. Car, “Two-Dimensional Self-Assembly of Supramolecular Clusters and Chains,” *Physical Review Letters*, vol. 83, pp. 324–327, July 1999.

[335] K.-H. Ernst, M. Böhringer, C. F. McFadden, P. Hug, U. Müller, and U. Ellerbeck, "Nanostructured chiral surfaces," *Nanotechnology*, vol. 10, pp. 355–361, Sept. 1999.

[336] C. J. Eckhardt, N. M. Peachey, D. R. Swanson, J. M. Takacs, M. A. Khan, X. Gong, J.-H. Kim, J. Wang, and R. A. Uphaus, "Separation of chiral phases in monolayer crystals of racemic amphiphiles," *Nature*, vol. 362, pp. 614–616, Apr. 1993.

[337] R. Viswanathan, J. A. Zasadzinski, and D. K. Schwartz, "Spontaneous chiral symmetry breaking by achiral molecules in a Langmuir–Blodgett film," *Nature*, vol. 368, pp. 440–443, Mar. 1994.

[338] M. Parschau, D. Passerone, K.-H. Rieder, H. J. Hug, and K.-H. Ernst, "Switching the Chirality of Single Adsorbate Complexes," *Angewandte Chemie International Edition*, vol. 48, pp. 4065–4068, May 2009.

[339] K. E. Plass, A. L. Grzesiak, and A. J. Matzger, "Molecular Packing and Symmetry of Two-Dimensional Crystals," *Accounts of Chemical Research*, vol. 40, pp. 287–293, Apr. 2007.

[340] K.-H. Ernst, "Supramolecular Surface Chirality," in *Supramolecular Chirality* (M. Crego-Calama and D. N. Reinhoudt, eds.), vol. 265, pp. 209–252, Berlin/Heidelberg: Springer-Verlag, 2006.

[341] K.-H. Ernst, "Molecular chirality in surface science," *Surface Science*, vol. 613, pp. 1–5, July 2013.

[342] S. Barlow and R. Raval, "Complex organic molecules at metal surfaces: Bonding, organisation and chirality," *Surface Science Reports*, vol. 50, pp. 201–341, Aug. 2003.

[343] S. J. Jenkins, "Chirality at Solid Surfaces," p. 398, 2018.

[344] S. Dutta and A. J. Gellman, "Enantiomer surface chemistry: Conglomerate versus racemate formation on surfaces," *Chemical Society Reviews*, vol. 46, no. 24, pp. 7787–7839, 2017.

[345] V. Humblot, S. Barlow, and R. Raval, "Two-dimensional organisational chirality through supramolecular assembly of molecules at metal surfaces," *Progress in Surface Science*, vol. 76, pp. 1–19, Sept. 2004.

[346] R. Raval, "Chiral expression from molecular assemblies at metal surfaces: Insights from surface science techniques," *Chemical Society Reviews*, vol. 38, no. 3, p. 707, 2009.

[347] H. Zhang, Z. Gong, K. Sun, R. Duan, P. Ji, L. Li, C. Li, K. Müllen, and L. Chi, "Two-Dimensional Chirality Transfer via On-Surface Reaction," *Journal of the American Chemical Society*, vol. 138, pp. 11743–11748, Sept. 2016.

[348] C. Wäckerlin, J. Li, A. Mairena, K. Martin, N. Avarvari, and K.-H. Ernst, "Surface-assisted diastereoselective Ullmann coupling of bishelicenes," *Chemical Communications*, vol. 52, no. 86, pp. 12694–12697, 2016.

[349] A. Mairena, C. Wäckerlin, M. Wienke, K. Grenader, A. Terfort, and K.-H. Ernst, "Diastereoselective Ullmann Coupling to Bishelicenes by Surface Topochemistry," *Journal of the American Chemical Society*, vol. 140, pp. 15186–15189, Nov. 2018.

[350] A. Mairena, M. Parschau, J. Seibel, M. Wienke, D. Rentsch, A. Terfort, and K.-H. Ernst, "Diastereoselective self-assembly of bisheptahelicene on Cu(111)," *Chemical Communications*, vol. 54, no. 63, pp. 8757–8760, 2018.

[351] O. Stetsovych, M. Švec, J. Vacek, J. V. Chocholoušová, A. Jančařík, J. Rybáček, K. Kosmider, I. G. Stará, P. Jelínek, and I. Starý, "From helical to planar chirality by on-surface chemistry," *Nature Chemistry*, vol. 9, pp. 213–218, Mar. 2017.

[352] B. Andryushechkin, T. Pavlova, and K. Eltsov, "Adsorption of halogens on metal surfaces," *Surface Science Reports*, vol. 73, pp. 83–115, June 2018.

[353] P. Jelínek, “High resolution SPM imaging of organic molecules with functionalized tips,” *Journal of Physics: Condensed Matter*, vol. 29, p. 343002, Aug. 2017.

[354] D. Écija, R. Otero, L. Sánchez, J. M. Gallego, Y. Wang, M. Alcamí, F. Martín, N. Martín, and R. Miranda, “Crossover Site-Selectivity in the Adsorption of the Fullerene Derivative PCBM on Au(111),” *Angewandte Chemie International Edition*, vol. 46, pp. 7874–7877, Oct. 2007.

[355] Z. H. Cheng, L. Gao, Z. T. Deng, Q. Liu, N. Jiang, X. Lin, X. B. He, S. X. Du, and H.-J. Gao, “Epitaxial Growth of Iron Phthalocyanine at the Initial Stage on Au(111) Surface,” *The Journal of Physical Chemistry C*, vol. 111, pp. 2656–2660, Feb. 2007.

[356] M. Böhringer, K. Morgenstern, W.-D. Schneider, and R. Berndt, “Separation of a Racemic Mixture of Two-Dimensional Molecular Clusters by Scanning Tunneling Microscopy,” *Angewandte Chemie International Edition*, vol. 38, pp. 821–823, Mar. 1999.

[357] W. Chen, V. Madhavan, T. Jamneala, and M. F. Crommie, “Scanning Tunneling Microscopy Observation of an Electronic Superlattice at the Surface of Clean Gold,” *Physical Review Letters*, vol. 80, pp. 1469–1472, Feb. 1998.

[358] C. Moreno, M. Paradinas, M. Vilas-Varela, M. Panighel, G. Ceballos, D. Peña, and A. Mugarza, “On-surface synthesis of superlattice arrays of ultra-long graphene nanoribbons,” *Chemical Communications*, 2018.

[359] I. Fernandez-Torrente, S. Monturet, K. J. Franke, J. Fraxedas, N. Lorente, and J. I. Pascual, “Long-Range Repulsive Interaction between Molecules on a Metal Surface Induced by Charge Transfer,” *Physical Review Letters*, vol. 99, Oct. 2007.

[360] M. Kettner, V. V. Maslyuk, D. Nürenberg, J. Seibel, R. Gutierrez, G. Cuniberti, K.-H. Ernst, and H. Zacharias, “Chirality-Dependent Electron Spin Filtering by Molecular Monolayers of Helicenes,” *The Journal of Physical Chemistry Letters*, vol. 9, pp. 2025–2030, Apr. 2018.

[361] Y. Yang, R. C. da Costa, M. J. Fuchter, and A. J. Campbell, “Circularly polarized light detection by a chiral organic semiconductor transistor,” *Nature Photonics*, vol. 7, pp. 634–638, Aug. 2013.

[362] L. Gross, N. Moll, F. Mohn, A. Curioni, G. Meyer, F. Hanke, and M. Persson, “High-Resolution Molecular Orbital Imaging Using a p -Wave STM Tip,” *Physical Review Letters*, vol. 107, Aug. 2011.

[363] J. I. Pascual, Z. Song, J. J. Jackiw, K. Horn, and H.-P. Rust, “Visualization of surface electronic structure: Dispersion of surface states of Ag(110),” *Physical Review B*, vol. 63, p. 241103, June 2001.

[364] Boris V. Senkovskiy, Dmitry Yu. Usachov, A. V. Fedorov, Danny Haberer, Niels Ehlen, Felix R. Fischer, and Alexander Grüneis, “Finding the hidden valence band of N=7 armchair graphene nanoribbons with angle-resolved photoemission spectroscopy,” *2D Materials*, 2018.

# List of publications

**Substrate-Independent Growth of Atomically Precise Chiral Graphene Nanoribbons.** *ACSnano* **2016**, 10 (9), pp. 9000-9008.

**Width-Dependent Band Gap in Armchair Graphene Nanoribbons Reveals Fermi Level Pinning on Au(111).** *ACSnano* **2017**, 11 (11), pp. 11661-11668.

**Unraveling the Electronic Structure of Narrow Atomically Precise Chiral Graphene Nanoribbons.** *The Journal of Physical Chemistry Letters* **2018**, 9 (1), pp. 25-30.

**Switching from Reactant to Substrate Engineering in the Selective Synthesis of Graphene Nanoribbons.** *The Journal of Physical Chemistry Letters* **2018**, 9 (10), pp. 2510-2517.

**Hierarchy in the halogen activation during surface-promoted Ullmann coupling.** *ChemPhysChem* **2018**, 9 (10), pp. 2510-2517.

**Survival of spin state in magnetic porphyrins contacted by graphene nanoribbons.** *Science Advances* **2018**, 114, pp. 2510-2517.

# Other publications

**Symmetry, Shape, and Energy Variations in Frontier Molecular Orbitals at Organic/Metal Interfaces: The Case of F4TCNQ.** *The Journal of Physcial Chemistry C* **2017**, 121, pp. 28412-28419.

**Electrically Addressing the Spin of a Magnetic Porphyrin through Covalently Connected Graphene Electrodes.** *NanoLetters* **2019**, 19, pp. 3288-3294.

**Switching the Spin on a Ni Trimer within a Metal-Organic Motif by Controlling the On-Top Bromine Atom.** *ACSnano* **2019**, (accepted).

# Acknowlegdements

To begin with, one of the things that frightens me most is the fact that I know that is going to be really difficult to find such a charming and warming atmosphere as this one that I have enjoyed so much here, provided by all the people that has contributed to create this lovely environment. As well, although trying my best effort to avoid it, I would like to apologize in case that I am forgeting anybody that should be mentioned here. Those who know me well know that I do not particularly stand out due to my memory skills.

First of all, I would like to thank all the pain-sharing friends and workmates of San Sebastián who were there with me in the good and the bad moments, particularly to those who were in the bad ones. On the one hand, some of them already left San Sebastian, as their time here ended because of this or that reason. I am refering to such a lovely people as my beermates Jöerg, Alvaro and Okuda, my loved labmate and friend Luciano, Eduard, Carmen, Nieves, Bernard, Lei, David the most attractive technician in the world, Mikel, Iñaki, as well as the rest of the people/staff from Nanogune, CFM and DIPC, and my former (or current) flatmates, Bingen, Igor, Leire, Vero, Nico, David, Sebastián, etc. On the other hand, fortunately, most of the people who frame my time here within kind and enjoy stay still in San Sebastián. People who have been here from my very first day as Leire, or people who came after me, most of them working in my loved research teams and who fortunately I got to know well. Niklas, Alejandro, Mohammed, James, Stefano, Wen, and Paul, you will do great, just keep on doing like you are doing now. I would like to remark also the good atmosphere brought by the charming group emerged in the CFM this last year involving CheMikel, Jorge el tiburón, Dani, Charlie el cuate, Marina, Alejandro, Carmen, Fernando, Rodrigo, Paul, Martin, etc.

Among all of them, I would like to highlight the unvaluable constant support of two people. First of all, I would like to express my biggest feeling of luck due to the fact of sharing this period of my life with Javier Zaldivar, excellent researcher and better person. Being one of hte smartest, emphatic, pro-active, helpful, comprenhensive (and many others positive adjectives) person that I have ever known, meeting you in this experience has been one of my most satisfying achievements with no mere doubt. (If I were you the reader of these acknowlegdements, I will urgently try to contract this guy because he is going to be remarkably brilliant and succesful in whatever he will do). Next, I would like to remark the wide-ranged constructive influence (much more of what he could guess) of doctor Jincheng Li, not only in my professional carrer but also in my personal life, since I have learned from him how to think and behave as a mature person doing his life in and out of the laboratory. I am pretty sure that nobody will be surprised when I say that he is one the steadiest and kindest person that I have ever known. Although falling into the risk of being called cheesy, the time spent in the lab with you guys will be one of my sweetest memories and so I will always keep a piece of my heart for each of you.

Al mismo tiempo, me gustaría agradecer el impacto tan positivo que han tenido sobre mi tiempo aquí a mis siempre divertidos, golfos, queridos bastardos del gimnasio ‘Kuraia Martutene’, posiblemente el mejor gimnasio de artes marciales del mundo. Leo el catanepes, la loca Kevin, el bandido Ekaitz, Jaime el tigre de Zarautz, Jorge(s), Isaco, Brais, Gasol, Telle la batidora de Idiazabal y gigoló internacional, Julitus, CuLander, Giovanni el indio,

Kungfu Panda I, II Y III (que gran dinastía), GuArri, Juancar, Mario, Spartak el osito, Joseba el rey del postureo y capo del Antiguo, The Canarian un grande donde los haya, a mis encantadoras y letales compañeras Tala, Nekane, Aitana y Lina, a quien me pueda olvidar pero por supuesto, a los que han sido mis dos fantásticos senseis de las artes marciales, la vida y el amor, el maestro Mikelillo y el maestro Cortés (que majo es). Entrenar, bromear y en general disfrutar con vosotros tanto dentro como fuera del tatami, haciendome desconectar de en ocasiones difícil y absorbente etapa del doctorado, me ha ayudado enormemente a superar esta etapa de mi vida con mas gloria que pena. Vosotros habeis sido como mi segunda familia aquí y no os haceis a la idea de como os lo agradezco.

Time for the supervisors. I must say that it is really nice when you work with a person who cares about and try to guide you in the most fruitful and pleasant possible way in which they can along this sometimes complex and difficult but undoubtly enrichment experience as it is the PhD. It is even nicer when you meet such an experienced and talented people that you luckily learn attitudes useful for your personal growth even out of the research institute. It is even even nicer when you find his uncondicional support even with your problems are not related at all with science but with personal struggles, at the same time that you unfortunately hear from other PhD mates how distantly treated they are by their supervisors. Now ! Take all these marbellous facts and multiply them by two ! How else can it be better ?! Dimas and Nacho, I can not express with words how fortunate I feel because of you both being the captains of this fantastic and enjoyable adventure of my life. Once I heard a powerful speech based on personal and professional development saying that between your twenties and thirties more or less one should work for an excellent, brilliant and succesful person, so one learns how to become then in such a skilled person. I could not wonder such a similar description of my experience being a member of your teams. You like it or not, you both will have my unconditional gratitude forever.

Por último, por considerarlo el más importante, me gustaría agradecer a mi familia, especialmente a mis padres, el apoyo incondicional que he recibido por su parte siempre y cuando (y cuando no) lo he necesitado. De todo corazón os agradezco el haberme educado bajo los principios de trabajo humilde, esfuerzo y superación personal que me han convertido en la persona que soy ahora, así como por sacrificar vuestra comodidad personal a diario para que yo pueda tener las oportunidades de las que estoy disfrutando hoy en día.

For you all, my warmest acknowlegdements.